

國立交通大學

電子工程學系電子研究所

博士論文

室溫紅外線偵檢器與圓形極化天線在無線微感測器

應用上的設計, 製作與模擬分析

Design, Fabrication and Simulation of Uncooled Infrared  
Detectors and Circularly Polarized Antennas for Wireless  
Micro-Sensor Applications

研究生：林稔杰

指導教授：張國明 博士  
鄧一中 博士

中華民國九十六年七月

室溫紅外線偵檢器與圓形極化天線在無線微感測器應用上的設計, 製作與模擬分析

Design, Fabrication and Simulation of Uncooled Infrared Detectors and Circularly Polarized Antennas for Wireless Micro-Sensor Applications

研究生：林稔杰

Student : Da-Ming Fan

指導教授：張國明 博士

Advisor : Dr. Kow-Ming Chang

鄧一中 博士

Dr. I-Chung Deng

國立交通大學

電子工程學系電子研究所



A Dissertation

Submitted to Department of Electronics Engineering & Institute of Electronics

College of Electrical Engineering and Computer Science

National Chiao Tung University

In Partial Fulfillment of the Requirements

For the Degree of Doctor of Philosophy

In

Electronics Engineering

July 2007

Hsinchu, Taiwan, Republic of China

中華民國九十六年七月

# 室溫紅外線偵檢器與圓形極化天線在無線微感測器上的

## 設計, 製作與模擬分析

研究生：林稔杰

指導教授：張國明 博士

鄧一中 博士

國立交通大學

電子工程學系 電子研究所

### 摘要

一個無線微感測器主要可以分為三個部分：天線、積體電路以及感測器。一般而言, 由於積體電路以及感測器所占面積相對於天線尺寸顯得相當的微小, 因此, 一個無線微感測器所佔有的面積主要由天線的大小來做決定。此外, 對於一個無線微感測系統而言, 系統的功率損耗以及系統的傳輸距離在設計時都必須加以考慮進去。本論文主要針對如何製作用來感測物體溫度的室溫紅外線偵檢器以及如何製作一個可與積體電路與感測器整合的圓形極化天線, 此外對於無線微感測器的傳輸距離以及射頻訊號的轉換特性都做了一些評估。因此本論文主要分成三個部分: 第一部分為”無線微感測系統的效能評估”; 第二部分為”低溫 CMOS 製程相容之室溫紅線感測器的設計與模擬分析”; 第三部分為”適用於無線微感測器之圓形極化槽孔天線設計與模擬分析”。

在第一部分中, 為了降低系統的功率損耗以及有效利用接收到的電磁波能量, 我們利用無線射頻辨識技術(RFID)來製作一個零偏壓的天線整流器(rectenna), 此天線整流器的輸出受到訊號傳輸距離的影響, 為了精確評估電磁波能量的接收以及高頻訊號的轉換, 因此我們利用高頻 3D 電磁場軟體以及高頻電路軟體來模擬收發系統間的訊號傳輸特性。

在第二部分中，我們為了使積體電路與微感測器之間的訊號損耗降低以及增加感測訊號的靈敏度，我們採用在積體電路製作完成後於其上實現我們的紅外線微感測器。為了達到此一目標，我們必須將整個元件陣列的製程溫度限制在低於 400 °C，同時配合面型微細加工技術以及 CMOS 製程相容的方法來縮小每個紅外線感測陣列的像素面積以及降低元件的製作成本，進而提高系統的解析度以及增加陣列元件的積集度。在元件材料選擇上，我們採用二氧化矽當作元件的結構層、鋁當犧牲層、摻雜的非晶矽當作感測材料層、鈦用來當做金屬訊號傳導層，同時利用另一薄鋁層當作反射層來製作四分之一波長共振腔增加紅外線的吸收率，此元件的材料選擇可以達到幾乎百分之百的蝕刻選擇比，對於元件的製程上是相當穩定。此外，在元件最後乾燥過程中，我們也探討如何利用現有簡單的熱板設備取代目前常用的昂貴二氧化碳超臨界點來達到元件的高良率以及高可靠度，以利元件的進一步大量製造。對於元件的結構分析，我們使用 CoventorWare 軟體，在元件犧牲層釋放過程中，用來預測整個元件的浮板結構變形狀況，進一步用來判斷浮板懸浮與否。對於元件的熱分析，我們使用 Ansys 有限元素分析軟體來計算元件的溫度分布、熱時間常數以及熱流通量。

就天線而言，目前大部分的無線微感測器大都利用線性極化天線來傳輸感測訊號，線性極化天線往往因為傳輸端與接受端的天線角度誤差，而造成傳輸系統的極化損耗，最大損耗可達 30dB，然而對於圓形極化系統而言則可以避免此一損耗產生。圓形極化天線在設計上比線性極化天線困難很多，加上目前尚未有縮小化圓形極化天線出現過，因此對於圓形極化天線研究的人更少。目前大部分圓形極化天線主要以微帶天線居多，主要是因為微帶天線在設計上槽孔天線容易，然而槽孔天線卻有比微帶天線更寬的阻抗頻寬、圓形極化頻寬。在第三部分中，我們在目前常用的商業基板 FR4(介電常數 4.4，厚度 1.6 mm，基板損耗正切 0.0245)上創新設計出許多不同類型的圓形極化行波槽孔天線，有別於傳統的圓形極化共振型槽孔天線。這些圓形極化行波槽孔天線操作於 2.4 GHz ~2.5 GHz 頻段範圍，S 參數都低於 -30 dB，天線輻射增益都在 3 dBi 以上，天線輻射效率大於 85%，以及 3 dB 圓形極化軸

比在空間分部至少涵蓋正負 30 度以上的俯角，而饋入的方式有微帶線訊號饋入以及共平面波導訊號饋入兩種，天線輸入阻抗匹配到射頻系統的 50 歐姆。我們藉由電磁模擬軟體 Zeland IE3D 來進行 2.5D 的天線設計與模擬分析，接著利用 Ansoft HFSS 來觀察天線 3D 結構的電磁分佈，這是因為 IE3D 對於開發平板天線的時效上有其優勢，而 HFSS 對於空間中的電磁分佈有其獨到之處。天線阻抗量測部分使用網路分析儀，而輻射場形部分使用 HP85301C 於無反射波量測實驗室進行。

關鍵字：無線微感測器、紅外線感測器、CMOS 製程相容、圓形極化天線、行波天線、槽孔天線



# **Design, Fabrication and Simulation of Uncooled Infrared Detectors and Circularly Polarized Antennas for Wireless Microsensor Applications**

**Student: Ren-Jie Lin**

**Advisor: Dr. Kow-Ming Chang**

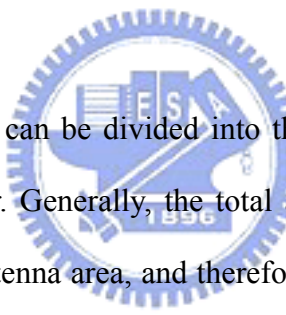
**Dr. I-Chung Deng**

*Department of Electronics Engineering & Institute of Electronics*

*National Chiao-Tung University*

*HsinChu, Taiwan R.O.C.*

## **Abstract**



A wireless microsensor can be divided into three main parts: Antenna, integrated circuit (IC), and micro-sensor. Generally, the total area of IC and micro-sensor is very little as compared with the antenna area, and therefore the area of a wireless microsensor is dependent on the antenna area. Besides, for a wireless microsensing system, the power loss of a system and the transmission distance must be taken into account during the system design. The purpose of this dissertation focus on how to fabricate the uncooled infrared detector array using to sense the infrared from objects and how to develop the circularly polarized slot antenna using to integrate with IC and micro-sensor. Besides, we also evaluate the transmission distance and the RF signal conversion characteristics of the wireless microsensing system. Consequently, this dissertation includes three parts: Part I “Performance evaluation of wireless microsensing system”; Part II “Design and simulation of an uncooled microbolometer with low temperature CMOS-process compatibility”, Part III “Design and simulation of circularly polarized slot antennas for wireless micro-sensor applications”.

In Part I, in order to decrease the system power loss and increase efficiently the use of the received electromagnetic power, we use the radio frequency identification technology (RFID) to design a zero-bias rectenna (antenna and rectifier). The output of the rectenna is affected by the signal transmission distance. In order to exactly estimate the received EM power and RF signal conversion, we use a 3-D high frequency EM software and a high frequency circuit software to simulate the signal transmission characteristics between the transmitter and the receiver.

In Part II, in order to reduce the signal loss and increase the sensing signal sensitivity between IC and micro-sensor, we implement our infrared micro-sensor directly fabricated on the top of IC. Achieving the preceding purpose, the whole processing temperature must be limited to below 400 degrees. At the same time, the surface micromachining technology and CMOS-process compatible method used to reduce the pixel size of infrared sensor array and lower the device-processing cost can further improve the system resolution and increase the device fill factor. With respect to material selection, we use silicon dioxide as the structural layer, Al as sacrificial layer, doped amorphous silicon as the sensitive layer, and Ta as the signal conducting line. Besides, we also use aluminum as a mirror layer to develop a quarter-wavelength resonator to increase infrared absorption. These materials providing nearly 100% etching selectivity is very stable during device fabrication. In addition, we also discuss how to use simple and cheap hot plate instead of expensive apparatus of CO<sub>2</sub> supercritical to achieve high yield and high reliability during device drying step. This is a great benefit to mass production. Considering device structural analysis, we use CoventorWare simulator to predict the status of the device structure deformation to further determine whether the membrane is suspend or collapsed during device releasing step. With respect to thermal simulation, Ansys which is a FEM simulator is used to estimate the temperature distribution, thermal time constant, and heat flux distribution of the device.

In terms of antenna, nowadays the most use of antenna communicating signal for wireless micro-sensor is the linearly polarized antenna. However, the polarization misalignment between the antennas of the transmitter and receiver always results in polarization loss, the maximum loss being 30dB possible. But with respect to circularly polarized (CP) system, the polarization loss can be alleviated. Only a few of the studies related to circularly polarized antenna are done due to the difficulty of the CP antenna. In addition, the compact size of CP antenna is never presented. Because the CP microstrip antennas are easier design than the CP slot antennas, the most of CP antennas are microstrip antenna. However, the slot antenna has wider impedance bandwidth, axial-ratio bandwidth over the microstrip antenna. In Part III, we develop several novel design CP traveling wave slot antennas on the common use substrate of FR4 (dielectric constant of 4.4, height of 1.6 mm, and loss tangent of 0.0245), and these proposed slot antennas are different from other traditional CP resonator slot antenna. These proposed slot antennas have several characteristics such as the operating frequency of 2.4 ~2.5 GHz, the S parameter of lower than -30 dB, the antenna gain above 3 dBi, the antenna radiation efficiency of above 85 %, and the 3 dB Axial-ratio at least cover the 30 degrees at the elevation direction. The feed types of the proposed antennas include microstrip feed and coplanar waveguide (CPW) feed. The Antenna input impedance also matches to 50 Ohm of the general RF system. We use electromagnetic simulator of Zeland IE3D to design and simulate the 2.5D antenna structure followed by using Ansoft HFSS to observe the 3D electromagnetic distribution. This is because the IE3D is superior to HFSS in analyzing time. However, the HFSS can exactly display the 3D electromagnetic distribution in the free space. The antenna impedance is measured by network analyzer, and the radiation pattern is measured by HP 85301C in the non-reflection chamber.

**Keyword: Wireless micro-sensor, Infrared detector, CMOS process compatible, circularly polarized antenna, traveling wave antenna, slot antenna**



## 致謝 (Acknowledgements)

首先誠摯的感謝指導教授張國明博士多年來的悉心指導與照顧，使我得以相繼完成碩士與博士學位，在這段攻讀博士學位的過程中，深刻的體會到老師的淵博學識、廣闊的學術視野、嚴謹認真的致學態度，這些不僅令我在學術上有所精進，在待人處事上更是受益良多。在這求學七年期間，老師能夠讓我盡情發揮自己的研究理念與擴展多方位的研究領域，讓我得以沉醉在研究的喜悅之中，讓我了解到自由發揮創意所帶來的無限空間，同時也很感激老師在學生低潮時期的拉拔與提攜，讓學生重獲研究的動力。此外，也誠摯的感謝共同指導教授鄧一中博士在研究資源上與研究方法建言上提供莫大的幫助與方便。

修業期間，特別感謝實驗室一同打拼的學長、學弟，尤其是已畢業學長羅俊傑在紅外線感測器上對我的協助與解惑，也感謝學弟黃士軒、林建宏與陳博寧在這段時間一起努力於學術研究與空閒時間的團隊激戰。另外，對於國家奈米元件實驗室、交大奈米中心的技術員徐秀鑾、范秀蘭、陳悅婷與黃月美小姐以及葉雙得先生多年來在半導體製程設備上的幫助與方便，讓我可以順利的將論文完成。

最後，必須感謝我的家人，感激你們這麼多年來的支持與幫忙，讓我無後顧之憂的在學術研究上努力，在我失意的時候也給我適時的鼓勵，真的感激你們。

## Contents

<b>Part I</b> .....	<b>10</b>
<b>Part II</b> .....	<b>10</b>
<b>Part III</b> .....	<b>13</b>
<b>Introduction</b> .....	<b>17</b>
<b>Part I</b> .....	<b>21</b>
<b>Chapter 1</b>	
<b>Electromagnetic power transmission</b> .....	<b>22</b>
<b>Chapter 2</b>	
<b>Rectifier of a wireless microsensor</b> .....	<b>28</b>
<b>Part II</b> .....	<b>40</b>
<b>Chapter 1</b>	
<b>Introduction</b> .....	<b>41</b>
<b>1.1 Characteristics of infrared</b> .....	<b>41</b>
<b>1.2 Infrared (IR) detector</b> .....	<b>42</b>
<b>1.3 Micromachining technology with integrated circuits for micro-sensor applications</b> .....	<b>43</b>
<b>1.4 Surface micromachining on top of IC for bolometer detector applications</b> .....	<b>46</b>
<b>1.5 In our research</b> .....	<b>48</b>
<b>Chapter 2</b>	
<b>Bolometer Operation and Theory</b> .....	<b>49</b>
<b>2.1 Bolometer operation</b> .....	<b>49</b>
<b>2.2 General performance concepts [23]</b> .....	<b>51</b>
<b>2.3 Analysis of heat transfer mechanisms for bolometer structures</b> .....	<b>55</b>
<b>2.4 Material property control</b> .....	<b>58</b>
<b>Chapter 3</b>	
<b>Structure design and related considerations</b> .....	<b>59</b>
<b>3.1 General considerations</b> .....	<b>59</b>
<b>3.2 Consideration about material of sensing layer</b> .....	<b>61</b>
<b>3.3 Consideration about micromachining technology</b> .....	<b>66</b>
<b>3.4 Consideration about material of sacrificial layer</b> .....	<b>67</b>
<b>Chapter 4</b>	
<b>Device thermal simulation</b> .....	<b>70</b>
<b>Chapter 5</b>	
<b>Device fabrication</b> .....	<b>93</b>
<b>5.1 Processes of bolometer array</b> .....	<b>93</b>



## Figure Captions

### *Part I*

Figure 1-1-1 Electromagnetic transmission simulations by DataLink method.....	24
Figure 1-1-2 The calculated and simulated results of the received power varying with distances .....	26
Figure 1-1-3 Calculation of receiving power .....	27
Figure 1-2-1 Equivalent model of HSMS 2850.....	28
Figure 1-2-2 Impedance matching circuit of voltage doubler @ 2.4 GHz.....	30
Figure 1-2-3 Matching circuit between receiver antenna and rectifier .....	31
Figure 1-2-4 The rectenna circuit @ 2.4 GHz .....	31
Figure 1-2-5 Return loss of the rectenna circuit .....	32
Figure 1-2-6 Transfer simulation of the rectenna circuit .....	34
Figure 1-2-7 Transfer curve of the rectenna circuit.....	34
Figure 1-2-8 Voltage sensitivity varying with frequency of the rectenna circuit for different input power.....	35
Figure 1-2-9 Transfer curves of the rectenna circuit for single, double and triple schottky diodes .....	35
Figure 1-2-10 Voltage sensitivity varying with frequency of the single diode rectenna circuit for different input power.....	36
Figure 1-2-11 Voltage sensitivity varying with frequency of the triple diode rectenna circuit for different input power.....	36
Figure 1-2-12 Transfer simulation of the rectenna circuit with the microstrip line ..	38
Figure 1-2-13 Transfer curve of the rectenna circuit with the microstrip line.....	38
Figure 1-2- 14 Photograph of the real rectenna circuit for the frequency of 2.4 GHz .....	39
Figure 1-2- 15 Measured results of the output voltage against transmission distance .....	39

### *Part II*

Figure 2-1-1 Spectral dependence of radiation on temperature.....	41
Figure 2-1-2 Atmospheric transmission characteristics .....	42
Figure 2-1-3 Vertical wafer-level MEMS-IC integration.....	46

Figure 2-2-1 Pixel structure of a microbolometer.....	49
Figure 2-2-2 (a) Schematic illustration of bolometer operation (b) Bolometer bias circuit .....	50
Figure 2-3- 1 Figure 3.1 Proposed structure configuration of bolometer detector....	60
Figure 2-3-2 (a)120 x 160 a-Si microbolometer array with 46.8 $\mu\text{m}$ pixels (b) Cross section of microbolometer structure .....	64
Figure 2-3- 3 pixel absorptance measurements show >80% absorptance over the 8-12 $\mu\text{m}$ spectral band. ....	65
Figure 2-4-13D solid model of bolometer pixel .....	70
Figure 2-4-2 Solid 90 geometry.....	70
Figure 2-4-3 Shell 131 geometry .....	71
Figure 2-4-4(a) 2D model, (b) 3D model, and (c) finite element model.....	72
Figure 2-4-5(a) TE3 temperature, (b) TTop temperature, and (c) Temperature Gradient distribution in the vacuum package condition .....	79
Figure 2-4-6(a) Thermal flux distribution on nodal plane, and (b) 3D thermal flux distribution on each node.....	80
Figure 2-4-7(a) Vector plot of thermal flux on nodal plane, and (b) enlargement of the submodel .....	81
Figure 2-4-8 (a) TE3 temperature and (b) TTop temperature distribution in the air condition .....	82
Figure 2-4-9(a) Thermal flux distribution on nodal plane, and (b) 3D thermal flux distribution on each node in the air condition .....	83
Figure 2-4-10(a) TTop temperature, and (b) Temperature Gradient distribution in the vacuum package condition .....	84
Figure 2-4-11 (a) Thermal flux distribution on nodal plane, and (b) 3D thermal flux distribution on each node in the vacuum package.....	85
Figure 2-4-12(a) TTop temperature, and (b) Temperature Gradient distribution in the air condition .....	86
Figure 2-4-13(a) Thermal flux distribution on nodal plane, and (b) 3D thermal flux distribution on each node in the air condition .....	87
Figure 2-4-14 (a) TTop temperature distribution, (b) Thermal flux distribution on nodal plane, and (c) Thermal flux distribution on each element for the vacuum condition .....	88
Figure 2-4-15(a) TTop temperature distribution, (b) Thermal flux distribution on nodal plane, and (c) Thermal flux distribution on each element for the Air	

condition .....	90
Figure 2-4-16 Transient of temperature and thermal flux of the central node on the top of bolometer pixel in air and vacuum conditions for using (a) Ta, (b) Ni/Cr, and (c) Metal line .....	92
Figure 2-5-1(a) ~ (e) Processing flow of bolometer .....	96
Figure 2-5-2 Three various drying procedures .....	98
Figure 2-5-3 Evaporation drying of short cantilever.....	100
Figure 2-5-4 Evaporation drying of long cantilever .....	101
Figure 2-5-5 Temperature dependence of surface tension for water and methanol	102
Figure 2-5-6 Fluid forces acting on a cantilever beam during drying process.....	104
Figure 2-5-7 Drying process for (a) rigid beams and (b) non-rigid beams.....	105
Figure 2-6-1 Definition of sidewall conformal factor (SCF). .....	111
Figure 2-6-2 Simulation results of z displacement against SCF with the sidewall angle of 75 degrees for the 75 $\mu$ m x 75 $\mu$ m test structure with annealing process for one hours .....	111
Figure 2-6-3 SEM images (a) The upper side is the pixel size of 75 $\mu$ m x 75 $\mu$ m, and the lower side is 50 $\mu$ m x 50 $\mu$ m. (b) The SCF of these test structures is about 0.3 .....	112
Figure 2-6-4 SEM images (a) The upper side is the pixel size of 75 $\mu$ m x 75 $\mu$ m. (b) The SCF of these test structures is about 1 on the sidewall angle of 75 degrees. ....	113
Figure 2-6-5 Simulation results of z displacement against SCF for the test structure with non-annealing sacrificial layer. ....	114
Figure 2-6-6 SEM image of the test membrane structure having the SCF of one and the sidewall angle of 75 degrees without annealing process.....	114
Figure 2-6-7 SEM images (a) The microbolometer arrays with the pixel size of 50 $\mu$ m x 50 $\mu$ m having fillet angle design. (b) The membrane structure with the pixel size of 100 $\mu$ m x 100 $\mu$ m having rectangle angle design. ....	115
Figure 2-6-8 SEM images (a) The enlarged image of the test microstructure includes mirror layer and sensing layer. (b) The microbolometer including mirror layer, sensing layer and metal line has a flat suspension structure. ....	116
Figure 2-6-9 (a) Z-Displacement and (b) Nodal-Displacement for the test structure (75 $\mu$ m x 75 $\mu$ m) with SCF of 0.4, sidewall slope of 80 degree, and thickness of 0.8 $\mu$ m while the supporting layer has the residual stress of 150 MPa .....	117
Figure 2-6-10 (a) Z-Displacement and (b) Nodal-Displacement for the test structure	

(75 $\mu\text{m}$ x 75 $\mu\text{m}$ ) with SCF of 0.4, sidewall slope of 80 degree, and thickness of 0.8 $\mu\text{m}$ while the supporting layer has the residual stress of -150 MPa.....	118
Figure 2-6-11 Nodal-Displacement of the whole microbolometer structure with SCF of 0.4 and sidewall slope of 80 degree for (a) positive and (b) negative gradient stress imposed on the supporting layer.....	119
Figure 2-6-12 SEM images (a) The single test microstructure with the pixel size of 75 $\mu\text{m}$ x 75 $\mu\text{m}$ . (b) The test microstructure arrays with the pixel size of 75 $\mu\text{m}$ x 75 $\mu\text{m}$ .....	120

### *Part III*

Figure 3-2-1 Dual-fed (a) circular and (b) square patch antennas.....	135
Figure 3-2-2 singly fed (a) circular and (b) square patch antennas .....	136
Figure 3-2-3 Amplitude and phase of orthogonal modes for singly fed patch antennas .....	137
Figure 3-2-4 Geometry of a circular loop antenna loaded at $\phi = 45^\circ$ with impedance $Z_L$ .....	139
Figure 3-2-5 Equivalent model of current distribution .....	139
Figure 3-2-6 Radiation mechanism of the proposed CP slot antenna.....	140
Figure 3-2-7 Polarization ellipse.....	141
Figure 3-2-8 Antenna measurement setup for measuring polarization pattern .....	142
Figure 3-2-9 Measurement of the polarization pattern .....	143
Figure 3-3-1 Geometry of the proposed CPW-fed circularly polarized slot antenna .....	148
Figure 3-3-2 Return loss against frequency for the proposed antenna with different signal strip length ( $L_C$ ) as the length of $L_4 = W_4 = 10\text{mm}$ and $g_2 = 1.35\text{ mm}$ ....	148
Figure 3-3-3 (a) Return loss against frequency and (b) axial ratio against frequency for the proposed antenna with different ground size ( $L_4 = W_4$ ) as the length of $L_C = 10\text{ mm}$ , and $g_2 = 1.35\text{ mm}$ .....	149
Figure 3-3-4(a) Return loss against frequency and (b) axial ratio against frequency for the proposed antenna with different gap space ( $g_2$ ) as the length of $L_C = 10\text{ mm}$ , and $L_4 = W_4 = 10\text{ mm}$ .....	150
Figure 3-3-5 Axial ratio against elevation angle ( $\theta$ ) at the resonant frequency of 2.44 GHz for the proposed antenna with the different azimuthal angle as the length of $L_C = 10\text{ mm}$ , $L_4 = W_4 = 10\text{ mm}$ , $g_2 = 1.35\text{ mm}$ .....	151
Figure 3-3-6 Radiation patterns on the (a) elevation plane and (b) azimuthal plane at the.....	152

<b>Figure 3-3-7 Geometry of the proposed CPW-fed CP square slot antenna.....</b>	<b>160</b>
<b>Figure 3-3-8(a) Simulated return loss and (b) simulated axial ratio against frequency for the proposed antenna geometry on three different substrates. ....</b>	<b>161</b>
<b>Figure 3-3-9 Simulated axial ratio against frequency for the proposed antenna geometry on two different substrates.....</b>	<b>162</b>
<b>Figure 3-3-10(a) Simulated return loss and (b) simulated axial ratio against frequency for the proposed slot antenna with different protruded strip length (Lc) .....</b>	<b>163</b>
<b>Figure 3-3-11(a) Simulated return loss and (b) simulated axial ratio against frequency for the proposed slot antenna with different grounded plane width (W1).....</b>	<b>164</b>
<b>Figure 3-3-12 Measured and simulated (a) return loss and (b) axial ratio against frequency for the optimum proposed slot antenna.....</b>	<b>165</b>
<b>Figure 3-3-13 Simulated circularly polarized radiation patterns for the optimum proposed slot antenna at the frequency of 2.45 GHz.....</b>	<b>165</b>
<b>Figure 3-3-14 Measured radiation patterns at the frequency of (a) 2.4 GHz, (b) 2.5 GHz, and (c) 2.6 GHz by the rotating source method. ....</b>	<b>167</b>
<b>Figure 3-3-15 Axial ratio against elevation angle calculated from the measured CP radiation patterns .....</b>	<b>167</b>
<b>Figure 3-3-16 Simulated electric-current distributions on the proposed slot antenna at the frequency of 2.45 GHz. ....</b>	<b>168</b>
<b>Figure 3-3-17 Measured and simulated antenna gain against frequency for the proposed antenna.....</b>	<b>168</b>
<b>Figure 3-4-1 Configuration of the proposed microstrip-fed circularly polarized slot antenna .....</b>	<b>173</b>
<b>Figure 3-4-2 Simulated and measured results of return loss against frequency for the proposed antenna.....</b>	<b>174</b>
<b>Figure 3-4-3 Simulated polarization patterns at the frequency of 2.4 GHz for the proposed antenna.....</b>	<b>174</b>
<b>Figure 3-4-4 Simulated results of axial-ratio and CP gain against frequency for the proposed antenna.....</b>	<b>175</b>
<b>Figure 3-4-5 Measured polarization patterns at different frequencies of 2.3, 2.4 and 2.5 GHz for the proposed antenna.....</b>	<b>176</b>
<b>Figure 3-4-6 Axial ratio against elevation angle calculated from the measured polarization patterns .....</b>	<b>177</b>
<b>Figure 3-4-7 Simulated axial ratio against elevation angle at the frequency of 2.4 GHz for the proposed antenna (a) with and (b) without three small triangles.</b>	



.....	178
<b>Figure 3-5-1 Photograph of microstrip fed slot antenna.....</b>	<b>183</b>
<b>Figure 3-5-2 3D solid model of microstrip fed slot antenna.....</b>	<b>183</b>
<b>Figure 3-5-3 Simulation of (a) S parameter, (b) Axial ratio, and (c) CP radiation pattern by using Ansoft HFSS simulator.....</b>	<b>184</b>
<b>Figure 3-5-4 Measurement of polarization patterns of microstrip-fed CP slot antenna at different frequency.....</b>	<b>188</b>
<b>Figure 3-5-5 Electrical field distributions on the x-y plane as feed signal phase from 0 to 180 by step of 90 .....</b>	<b>189</b>
<b>Figure 3-5-6 Magnetic field distributions on the x-y plane as feed signal phase from 0 to 180 by step of 90 .....</b>	<b>190</b>
<b>Figure 3-5-7 Vector plot of electrical field distribution on the top of Air box as the feed phase from 0 to 180 by step of 90 .....</b>	<b>191</b>
<b>Figure 3-5-8 Vector plot of magnetic field distribution on the top of Air box as the feed phase from 0 to 180 by step of 90 .....</b>	<b>192</b>
<b>Figure 3-5-9 Photograph of CPW-fed square-ring slot antenna .....</b>	<b>193</b>
<b>Figure 3-5-10 3D solid model of microstrip fed slot antenna.....</b>	<b>193</b>
<b>Figure 3-5-11 Simulation of (a) S parameter, (b) Axial ratio, and (c) CP radiation pattern by using Ansoft HFSS simulator.....</b>	<b>194</b>
<b>Figure 3-5-12 Measurement of polarization patterns of CPW-fed CP slot antenna at different frequency.....</b>	<b>197</b>
<b>Figure 3-5-13 Electrical field distributions on the x-y plane as feed signal phase from 0 to 180 by step of 90 .....</b>	<b>198</b>
<b>Figure 3-5-14 Magnetic field distributions on the x-y plane as feed signal phase from 0 to 180 by step of 90 .....</b>	<b>199</b>
<b>Figure 3-5-15 Vector plot of electrical field distribution on the top of Air box as the feed phase from 0 to 180 by step of 90 .....</b>	<b>200</b>
<b>Figure 3-5-16 Vector plot of magnetic field distribution on the top of Air box as the feed phase from 0 to 180 by step of 90 .....</b>	<b>201</b>
<b>Figure 3-5-17 Photograph of microstrip-fed square-ring slot antenna .....</b>	<b>202</b>
<b>Figure 3-5-18 Measured and simulated results of the microstrip-fed square-ring slot antenna .....</b>	<b>202</b>
<b>Figure 3-5-19 Simulated results of axial ratio against frequency and against elevation angle by IE3D simulator for microstrip-fed square-ring slot antenna .....</b>	<b>203</b>
<b>Figure 3-5-20 Measurement of polarization patterns of microstrip-fed square-ring slot antenna at different frequency.....</b>	<b>204</b>

**Figure 3-5-21 Photograph of CPW-fed square-ring slot antenna .....205**  
**Figure 3-5-22 Simulated result of return loss for CPW-fed slot antenna with two slits  
.....205**  
**Figure 3-5-23 Simulated results of (a) axial ratio against frequency and (b) axial  
ratio against elevation angle .....206**  
**Figure 3-5-24 Measured results of polarization pattern at various frequencies.....208**



## Introduction

A wireless sensor network (WSN) is a wireless network consisting of spatially distributed autonomous devices using sensors to cooperatively monitor physical or environmental conditions, such as temperature, sound, vibration, pressure, motion or pollutants, at different locations [1,2]. The development of wireless sensor networks was originally motivated by military applications such as battlefield surveillance. However, wireless sensor networks are now used in many civilian application areas, including environment and habitat monitoring, healthcare applications, home automation, and traffic control [1,3]. In addition to one or more sensors, each node in a sensor network is typically equipped with a radio transceiver or other wireless communications device, a small microcontroller, and an energy source, usually a battery. The size of a single sensor node can vary from shoebox-sized nodes down to devices the size of grain of dust. The cost of sensor nodes is similarly variable, ranging from hundreds of dollars to a few cents, depending on the size of the sensor network and the complexity required of individual sensor nodes. Size and cost constraints on sensor nodes result in corresponding constraints on resources such as energy, memory, computational speed and bandwidth.

Generally, a wireless microsensor (that is a sensor node) can be divided into three main parts: Antennas, integrated circuits (IC), and micro-sensors. The total area of ICs and micro-sensors is very little as compared with the antenna area, and therefore the area of a wireless microsensing system is dependent on the antenna area. Besides, for a wireless microsensing system, the power loss of a system and the transmission distance must be taken into account during the system design.

The purpose of this dissertation focuses on the design of the key components and the performance evaluation of a wireless microsensor. Here, we develop an uncooled

infrared detector array using to sense the infrared from objects and also develop a circularly polarized slot antenna using to receive the input RF power. Besides, we also evaluate the transmission distance and the RF signal conversion characteristics of the wireless microsensing system.

Consequently, this dissertation includes three parts: Part I “Performance evaluation of wireless microsensing system”; Part II “Design and simulation of an uncooled microbolometer with low temperature CMOS-process compatibility”, Part III “Design and simulation of circularly polarized slot antennas for wireless micro-sensor applications”.

In Part I, in order to decrease the system power loss and increase efficiently the use of the received electromagnetic power, we use the radio frequency identification technology (RFID) to design a zero-bias rectenna (antenna and rectifier). The output of the rectenna is affected by the signal transmission distance. In order to exactly estimate the received EM power and RF signal conversion, we use a 3-D high frequency EM software and a high frequency circuit software to simulate the signal transmission characteristics between the transmitter and the receiver.

In Part II, in order to reduce the signal loss and increase the sensing signal sensitivity between IC and micro-sensor, we implement our infrared micro-sensor directly fabricated on the top of IC. Achieving the preceding purpose, the whole processing temperature must be limited to below 400 degrees. At the same time, the surface micromachining technology and CMOS-process compatible method used to reduce the pixel size of infrared sensor array and lower the device-processing cost can further improve the system resolution and increase the device fill factor. With respect to material selection, we use silicon dioxide as the structural layer, Al as sacrificial layer, doped amorphous silicon as the sensitive layer, and Ta as the signal conducting line. Besides, we also use aluminum as a mirror layer to develop a quarter-wavelength resonator to increase

infrared absorption. These materials providing nearly 100% etching selectivity is very stable during device fabrication. In addition, we also discuss how to use simple and cheap hot plate instead of expensive apparatus of CO<sub>2</sub> supercritical to achieve high yield and high reliability during device drying step. This is a great benefit to mass production. Considering device structural analysis, we use CoventorWare simulator to predict the status of the device structure deformation to further determine whether the membrane is suspend or collapsed during device releasing step. With respect to thermal simulation, Ansys which is a FEM simulator is used to estimate the temperature distribution, thermal time constant, and heat flux distribution of the device.

In Part III, nowadays the most use of antenna communicating signal for wireless micro-sensor is the linearly polarized antenna. However, the polarization misalignment between the antennas of the transmitter and receiver always results in polarization loss, the maximum loss being 30dB possible. But with respect to circularly polarized (CP) system, the polarization loss can be alleviated. Only a few of the studies related to circularly polarized antenna are done due to the difficulty of the CP antenna. In addition, the compact size of CP antenna is never presented. Because the CP microstrip antennas are easier design than the CP slot antennas, the most of CP antennas are microstrip antenna. However, the slot antenna has wider impedance bandwidth, axial-ratio bandwidth over the microstrip antenna. In Part II, we develop several novel design CP traveling wave slot antennas on the common use substrate of FR4 (dielectric constant of 4.4, height of 1.6 mm, and loss tangent of 0.0245), and these proposed slot antennas are different from other traditional CP resonator slot antenna. These proposed slot antennas have several characteristics such as the operating frequency of 2.4 ~2.5 GHz, the S parameter of lower than -30 dB, the antenna gain above 3 dBi, the antenna radiation efficiency of above 85 %, and the 3 dB Axial-ratio at least cover the 60 degrees at the elevation direction. The feed types of the proposed antennas include microstrip feed and

coplanar waveguide (CPW) feed. The Antenna input impedance also matches to 50 Ohm of the general RF system. We use electromagnetic simulator of Zeland IE3D to design and simulate the 2.5D antenna structure followed by using Ansoft HFSS to observe the 3D electromagnetic distribution. This is because the IE3D is superior to HFSS in analyzing time. However, the HFSS can exactly display the 3D electromagnetic distribution in the free space. The antenna impedance is measured by network analyzer, and the radiation pattern is measured by HP 85301C in the non-reflection chamber.



- [1] Cauligi S. Raghavendra (Editor), Krishna M. Sivalingam (Editor), Taieb Znati, "Wireless Sensor Networks".
- [2] Edgar H. Callaway, Jr., "Wireless Sensor Networks: Architectures and Protocols," CRC Press, August 2003, ISBN 0-8493-1823-8.
- [3] Feng Zhao and Leonidas Guibas, Morgan Kaufmann, "Wireless Sensor Networks: An Information Processing Approach," 2004. ISBN 1-55860-914-8.

# *Part I*

## *Performance evaluation of wireless microsensing system*



## Chapter 1

### Electromagnetic power transmission

A wireless microsensing system consists of two parts which are a Reader and a wireless microsensor. The RF signal (electromagnetic power) is transmitted from the reader and received by the wireless microsensor. When the microsensor receives the request signal, it returns the sensing data stored in the memory of the microsensor to the reader. Because the sensing and signal processing circuits need power supply to drive active devices, the microsensor has an embedded battery. Thus, the microsensor life is dependent on the battery life. In order to prolong the microsensor life, the low power consumption is very important to design a wireless microsensor.

In our proposed wireless microsensing system, the slot antenna with magnetic-current excitation with circularly polarized radiation is used as the transmitter and receiver antennas. Here, we can also use linearly polarized antenna in the wireless microsensor. The different between those antennas is the efficiency of the received EM power. We assume the input power of 1 Watt imposing on the input-end of the reader antenna, and calculate the receiving power at the output-end of the microsensor antenna. The received power is well known dependence on the transmission distance. The theoretical estimation of the transmission distance (Friis equation) is shown as (1-1). Especially, the first term of the right side of the equation is known as free space attenuation. Table 1.1 lists the parameters of the Friis equation.

In our proposed slot antenna, the antenna must have antenna gain above 3 dB and scattering parameter below -30 dB at the frequency of 2.4 GHz. Besides, we assume the polarization loss is zero and the input power of 1 Watt. In this case, the calculated free space attenuation with the distance of 1 meter is -40.5 dB, and thus we can obtain the receiving power of -34 dB, that is also -34 dBw in the power point of view. However, this



equation is a very rough estimation for the case in most wireless microsensing situations. A full system simulation including reader, tag and the environment is needed.

$$\frac{P_R}{P_T} = \left(\frac{\lambda}{4\pi R}\right)^2 G_T G_R |\vec{\rho}_T \cdot \vec{\rho}_R|^2 (1 - |\Gamma_T|^2)(1 - |\Gamma_R|^2) \quad (1-1)$$

	Transmitter antenna	Receiver antenna
Gain	$G_T$	$G_R$
Polarization vector	$\vec{\rho}_T$	$\vec{\rho}_R$
Reflection coefficient	$\Gamma_T$	$\Gamma_R$
Distance	R	
Wavelength	$\lambda$	

Table 1.1 Parameters of Friis equation

We use Ansoft HFSS software to simulate the electromagnetic transmission phenomena. In order to reduce the need of computer resource, the DataLink function only supported by HFSS 10 version is used to simulate the electromagnetic transmission between two or more RF antenna systems. The conventional EM transmission simulation needs to develop full system model including every components and a very large air space. If the interesting distance between the transmitter and receiver is long, the full model is very large and needs very large amount of computer resource to accurately calculate. Generally, the conventional approach is more accurate than the DataLink approach, but it is not suitable for us due to the limitation of computer resource. In the DataLink procedures, we firstly use the 3D field results from the developing and simulating the source antenna system which can be seen as a transmitter, and then develop the target antenna system which can be seen as a received antenna of the

microsensor. The target system is simulated with dynamic link to the source target system. In this case, we simulate larger structures without increasing hardware capacity. Besides, these two antenna systems can be placed anywhere with respect to each other by using the translation and Euler rotation method.

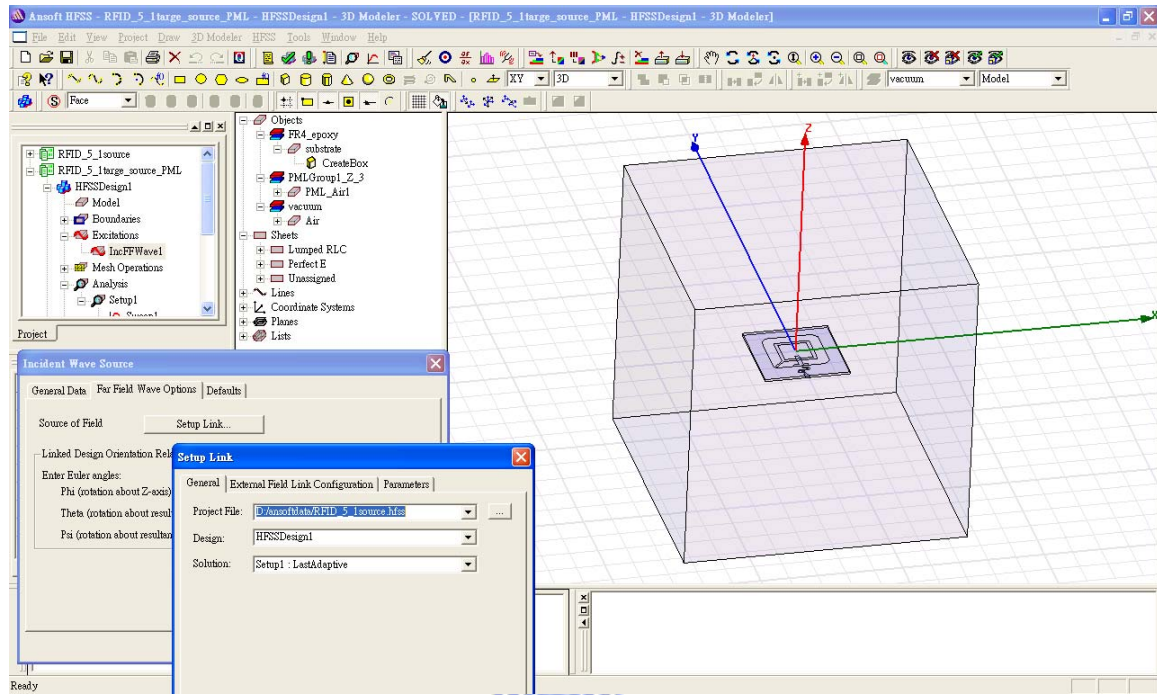


Figure 1-1-1 Electromagnetic transmission simulations by DataLink method

Figure 1-1-1 shows the electromagnetic transmission simulations by DataLink method of Ansoft HFSS. In this simulation, the source antenna system adopts the lump-port at the RF input terminal with one watt, and then the target antenna system uses the lump impedance of 50 ohm at the output terminal to calculate the received power. The radiation boundaries are assigned on the surface of the air box, which has the dimension of  $200 \times 200 \times 200$  (mm<sup>3</sup>), and these radiation boundaries have the distances larger than the quarter-wavelength from the radiation slot antenna. In order to increase the simulation accuracy of RF power transmission, we use perfect matched layer (PML) to substitute for the conventional radiation boundary condition (B.C.) due to the PML B.C. nondependent

on RF power incident angle. The conventional radiation boundary will reflect varying amounts of energy depending on the incident angle. The best performance is achieved at normal incidence. Avoid angles greater than 30 degrees. The calculated and simulated results of the received power varying with the distances between transmitter and receiver are presented in Figure 1-1-2 and lists in Table 1.2. These results are at the frequency of 2.4 GHz. It can be seen that the received power is about 6.13E-4 (watt) and 4.10E-6 (watt) for the distance of 1 m and 10 m, respectively. These simulated data are very useful to decide the transmission distance of the wireless microsensor system, and it can be used as the input power of the rectenna in the next chapter. Especially, the simulated result takes the substrate loss, polarization mismatch and impedance mismatch into account. These effects are not evaluated in the calculated result. In order to further improve the simulation exactitude, we use the full system model simulation for the distance of below 2 meters and use the DataLink method for above 5 meters. At the long distance, the calculated results are in good agreement with the simulated results because the Friis equation is enough exact for long-distance transmission.

Here, we use the induced complex current calculated from the complex magnetic field by the equation of (1-2) to evaluate the received power. It must be noted that we cannot only consider the real part of the magnetic field to evaluate the received power. The integration line in this equation is illustrated in Figure 1-1-3, and it is perpendicular to the conduction line. The integration line cannot be set too large, or we will obtain error calculated receiving power.

$$Power = \frac{50 * [\oint real(\vec{H}) \cdot dl + j * \oint imag(\vec{H}) \cdot dl] * [\oint real(\vec{H}) \cdot dl + j * \oint imag(\vec{H}) \cdot dl]^*}{1} \quad (1-2)$$

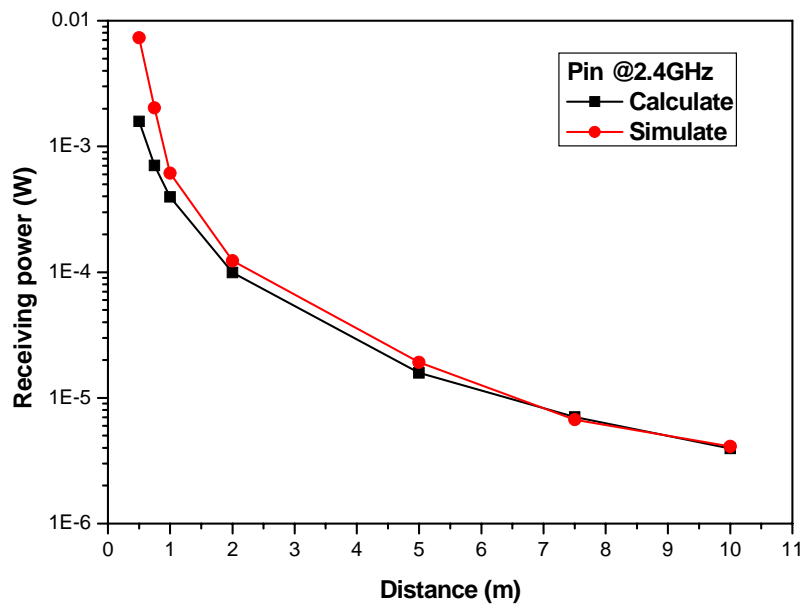


Figure 1-1-2 The calculated and simulated results of the received power varying with distances

Distance (m)	0.5	0.75	1	2	5	7.5	10
Calculated (Watt)	1.58E-3	7.0362E-4	3.95786E-4	9.89465E-5	1.58314E-5	7.0362E-6	3.95786E-6
Simulated (Watt)	7.32E-3	2.03E-3	6.13E-4	1.23E-4	1.914E-5	6.72E-6	4.10E-6
C/S value	0.204	0.3466	0.6456	0.8044	0.8271	1.047	0.9653

Table 1.2 The calculated and simulated results of the received power varying with distances.

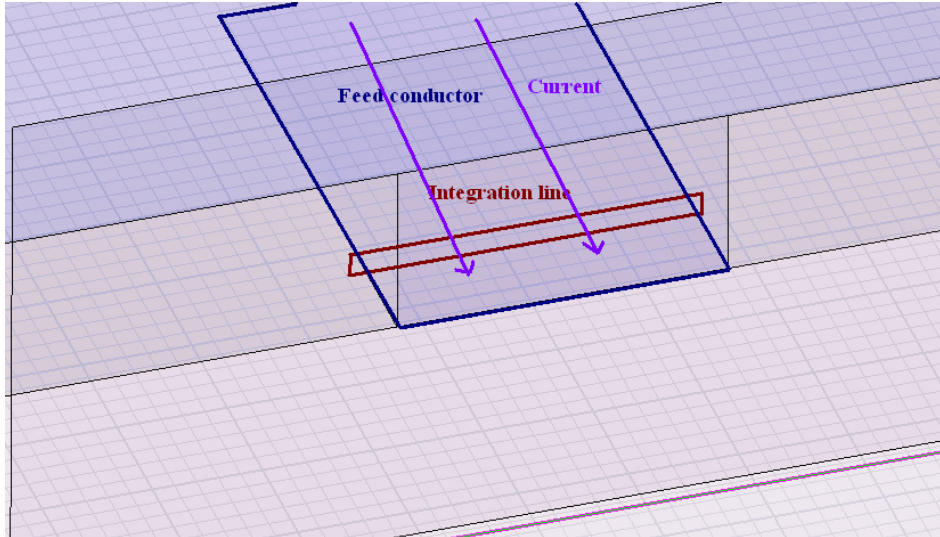


Figure 1-1-3 Calculation of receiving power



## Chapter 2

### Rectifier of a wireless microsensor

The received power of a wireless microsensor depends on the distance between the transmitter and receiver. Generally, the received power is about -10 ~ -20 dBm at the distance of 1 meter while the transmitting power is one watt. In order to efficiently use the input RF power for microsensor applications, the rectenna composed of an antenna and a rectifier is used to convert the RF power to DC voltage. In this research, we use two zero bias schottky diodes (HSMS-2850) to form a voltage doubler. The HSMS-2850 is designed and optimized for use in small signal applications. They are ideal for RFID and RF tag applications where primary (DC bias) power is not available. The zero bias schottky diode is modeled as Figure 1-2-1. The equivalent model includes the parasitic effect due to the device package. Table 2.1 shows the spice parameters for the HSMS-2850. These spice parameters are provided by Agilent manufacturer. Here, the advanced design system (ADS) software is used to simulate the RF circuit performance.

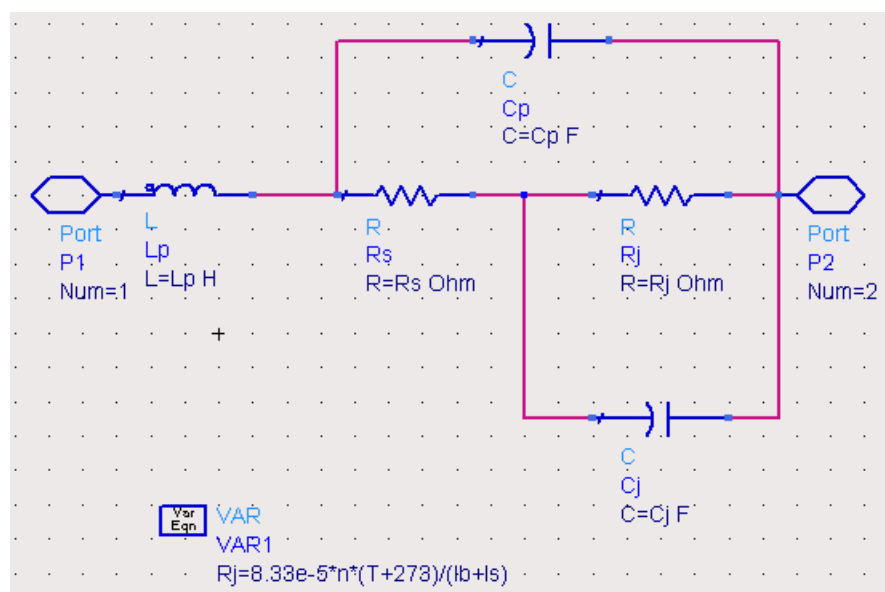


Figure 1-2-1 Equivalent model of HSMS 2850

	B <sub>v</sub>	C <sub>j0</sub>	E <sub>G</sub>	I <sub>BV</sub>	I <sub>S</sub>	N	R <sub>S</sub>	P <sub>B</sub>	P <sub>T</sub>	M
Units	V	pF	eV	A	A		Ω	V		
2850	3.8	0.18	0.69	3E-4	3E-6	1.06	25	0.35	2	0.5

Table 2.1 Spice parameters for HSMS 2850

In the equivalent model, R<sub>s</sub> is parasitic series resistance of the diode, the sum of the bondwire and leadframe resistance, the resistance of the bulk layer of silicon. RF energy coupled into R<sub>s</sub> is lost as heat- it does not contribute to the rectified output of the diode. C<sub>j</sub> is parasitic junction capacitance of the diode, controlled by the thickness of the epitaxial layer and the diameter of the schottky contact. R<sub>j</sub> is the junction resistance of the diode, a function of the total current flowing through it.

$$R_j = \frac{8.33 * 10^{-5} * n * (T + 273)}{I_s + I_b} \quad (2-1)$$

Where

n = ideality factor

T = temperature

I<sub>s</sub> = saturation current

I<sub>b</sub> = externally applied bias current

I<sub>s</sub> is a function of diode barrier height, and can range from picoamps for high barrier diodes to as much as 5 uA for very low barrier diodes. In general, very low barrier height diode (with high values of I<sub>s</sub>, suitable for zero bias applications) are realized on p-type silicon. Such diodes suffer from higher values of R<sub>s</sub> than do the n-type. Besides, L<sub>p</sub> is about 2 nH, C<sub>p</sub> is 0.08 pF, R<sub>s</sub> is 25 ohm, and C<sub>j</sub> is about 0.18 pF. The most difficult part of the design of a rectified circuit is the input impedance matching network. The input

impedance of the voltage doubler at the frequency of 2.4 GHz as shown in Figure 1-2-2 is about  $9.668 - j*113.449$ . Because the input impedance of the receiving antenna is designed as 50 ohm, the matching network must be designed between the rectifier and the antenna, the impedance matching is done from 50 ohm to  $9.668 - j*113.449$ . The impedance matching circuit including an inductor of 7.535 nH and a resistance of 40.33 ohm is shown in Figure 1-2-3. Because the RF system is operated at the frequency of 2.4 GHz, the rectenna circuit is optimized at the operational frequency and shown in Figure 1-2-4. In the circuit, the two capacitances have the values of 100 pF, and the load resistance is 100 kOhm. Besides, the Smith Chart tool is used to match the receiver antenna and the rectifier presented as Figure 1-2-3. The return loss of the rectenna circuit is presented in Figure 1-2-5.

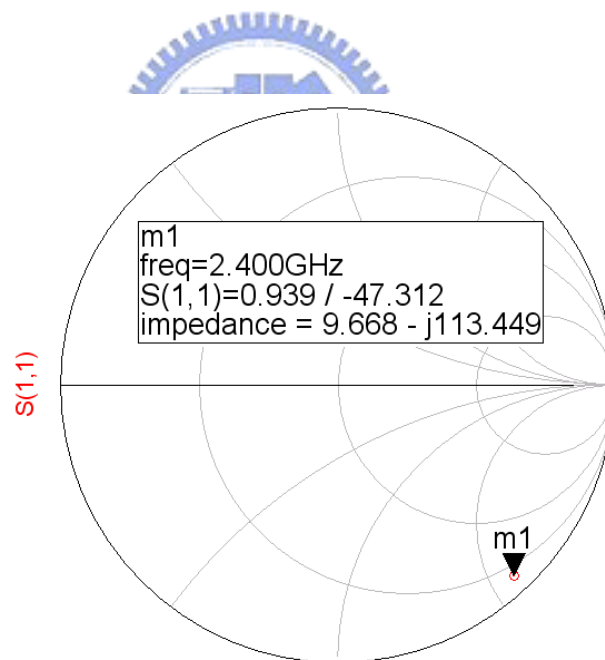


Figure 1-2-2 Impedance matching circuit of voltage doubler @ 2.4 GHz



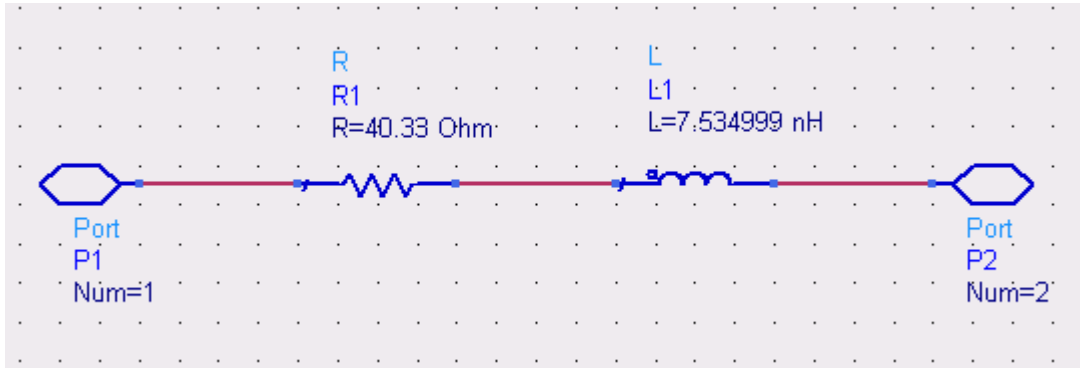


Figure 1-2-3 Matching circuit between receiver antenna and rectifier

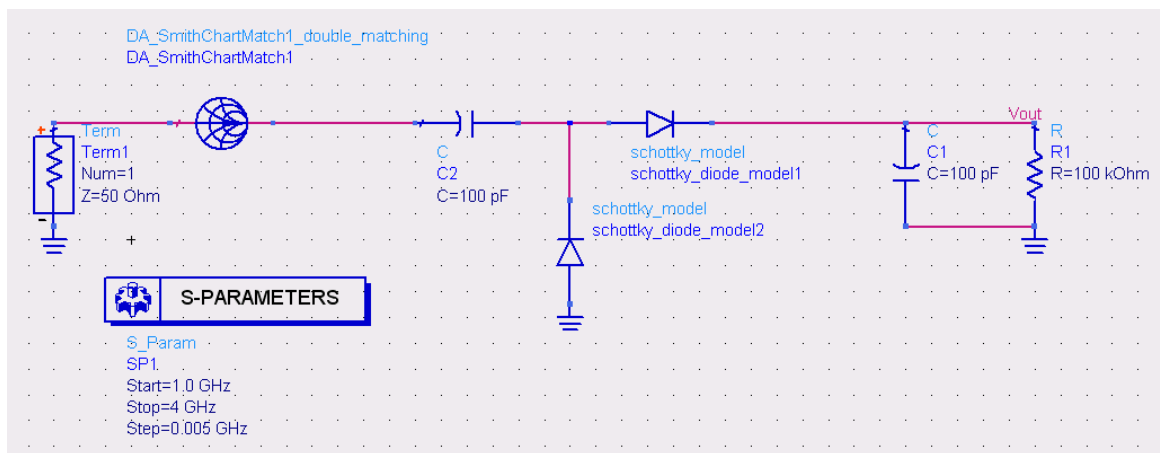


Figure 1-2-4 The rectenna circuit @ 2.4 GHz

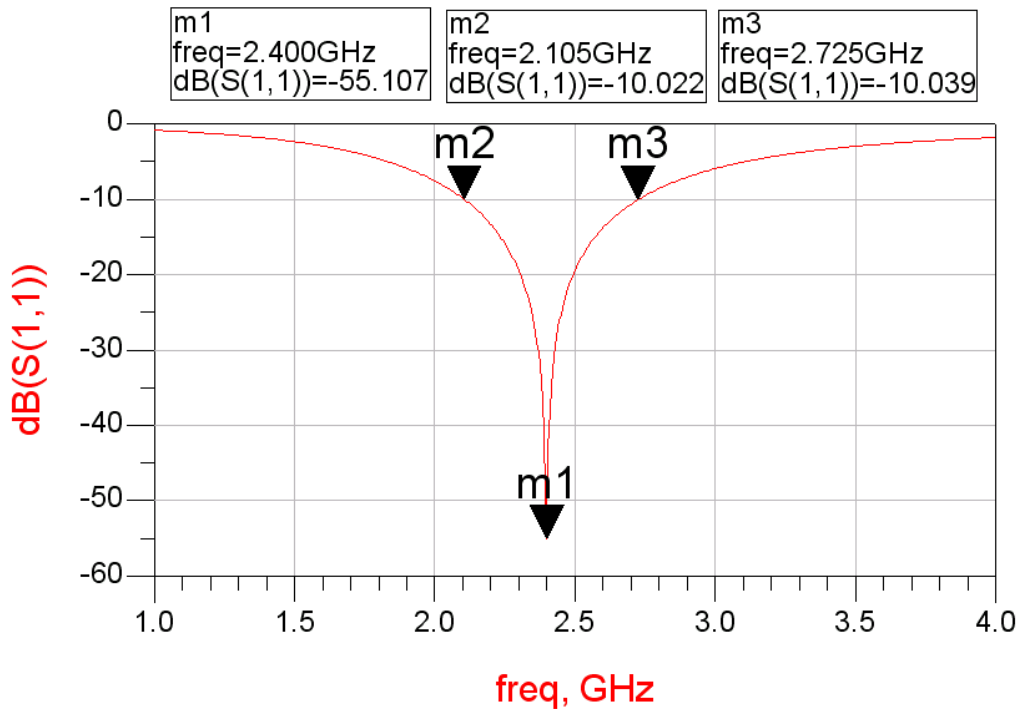


Figure 1-2-5 Return loss of the rectenna circuit

From Figure 1-2-5, it can be noted that the rectenna circuit has the return loss of -55.107 dB at the frequency of 2.4 GHz and the impedance bandwidth of 0.62 GHz from the frequency of 2.105 GHz to 2.725 GHz. The transfer simulation of the rectenna circuit is developed in Figure 1-2-6. We use harmonic balance approach to simulate the transfer characteristics, and the first third order harmonic modes of the operational frequency of 2.4 GHz are considered. The RF input (Pin) simulated the receiving power from the antenna sweeps from -50 dBm to 30 dBm. Besides, the noise effect on all components is also considered in this simulation. The transfer curve of the rectenna circuit is shown in Figure 1-2-7. If the RF input power is -30, -20, -10 dBm, we can achieve a DC output voltage of 11.629 mV, 87.050 mV, and 415.183 mV. It can be noted that the transfer curve shows two regions of square law response and the linear law response. The boundary of the two regions is about at the input power of -15 dBm. The region above the boundary is the linear law response, and the region below the boundary has the square law response.

In the RFID application, the square law region is the better operational region due to its large voltage sensitivity. The voltage sensitivity varying with frequency of the rectenna circuit for different input power is shown in Figure 1-2-8. The input power varies from -50 dBm to -20 dBm. It can be seen that the maximum voltage sensitivity occurs at the frequency of 2.65 GHz for the input power of -50 ~ -30 dBm and the maximum sensitivity for the input power of -20 dBm is at the frequency of 2.7 GHz. In order to compare with the rectifier with single schottky diode, we have also implemented the single diode rectenna circuit. The transfer curves of the rectenna circuits with single, double and triple schottky diodes are shown in Figure 1-2-9, and it can be noted that the single diode rectenna has larger output voltage than the double and triple diode ones below the input power of -30 dBm, but it has less output voltage than double and triple diode rectenna circuit above the input power of -30 dBm. This can be explained by the series resistance and parasitic resistance of the rectenna circuit. Besides, the voltage sensitivity varying with frequency of the single diode rectenna circuit for different input power is presented in Figure 1-2-10. The maximum voltage sensitivity at the input power from -50 dBm to -30 dBm occurs at the frequency of 2.95 GHz higher than that of the double diode rectenna circuit, and the sensitivity decreases as the input power increases due to the operation from the square law response to the linear law response as shown in Figure 1-2-11.

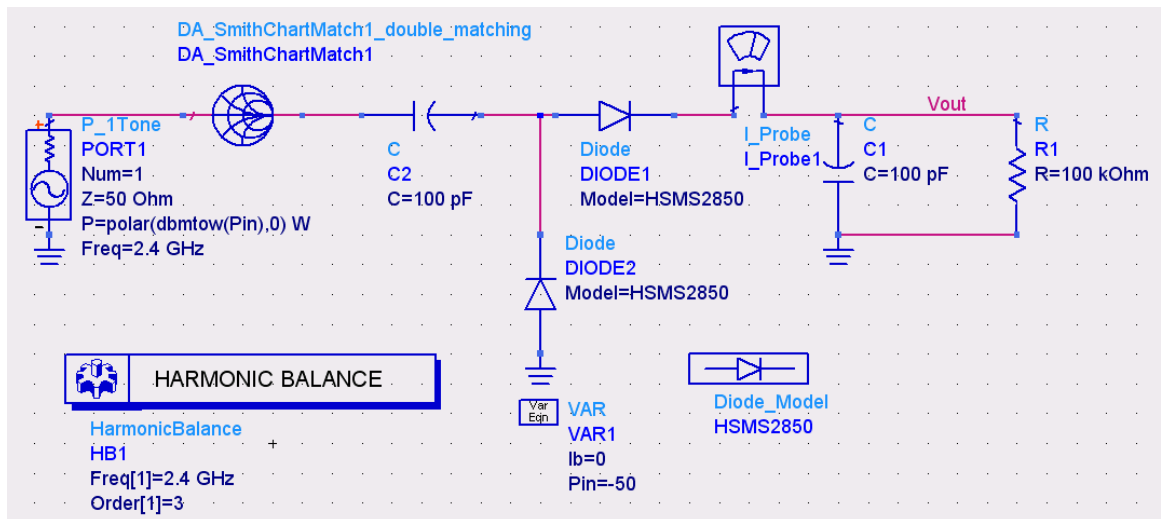


Figure 1-2-6 Transfer simulation of the rectenna circuit

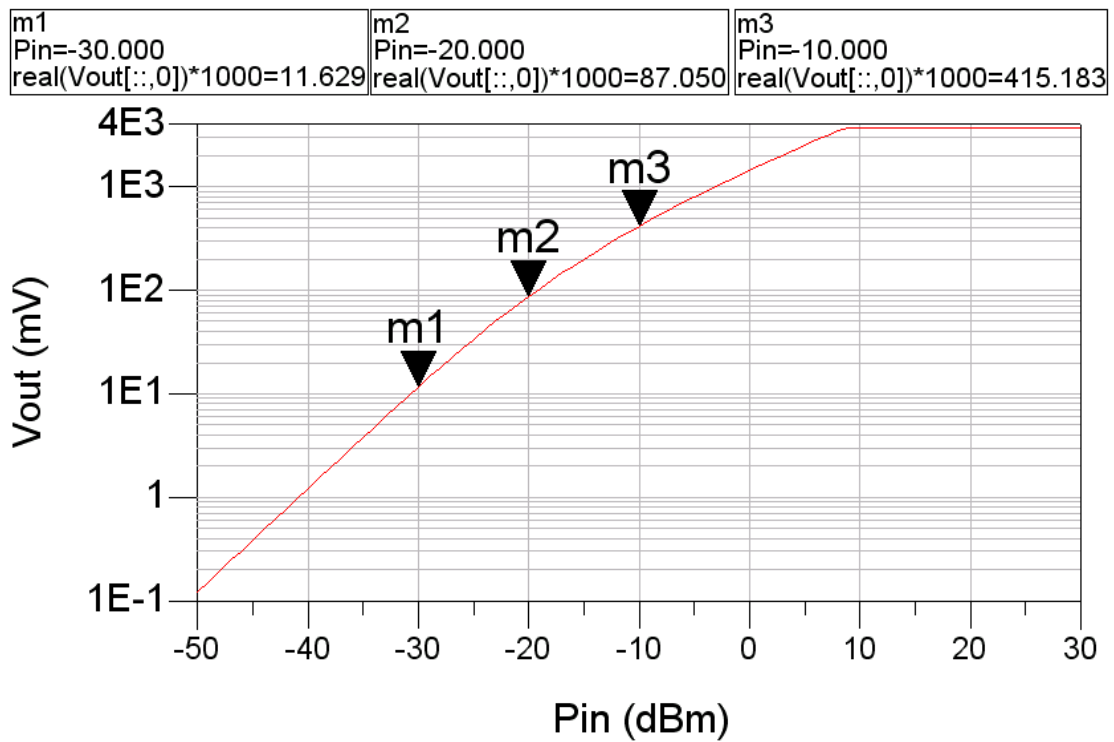


Figure 1-2-7 Transfer curve of the rectenna circuit

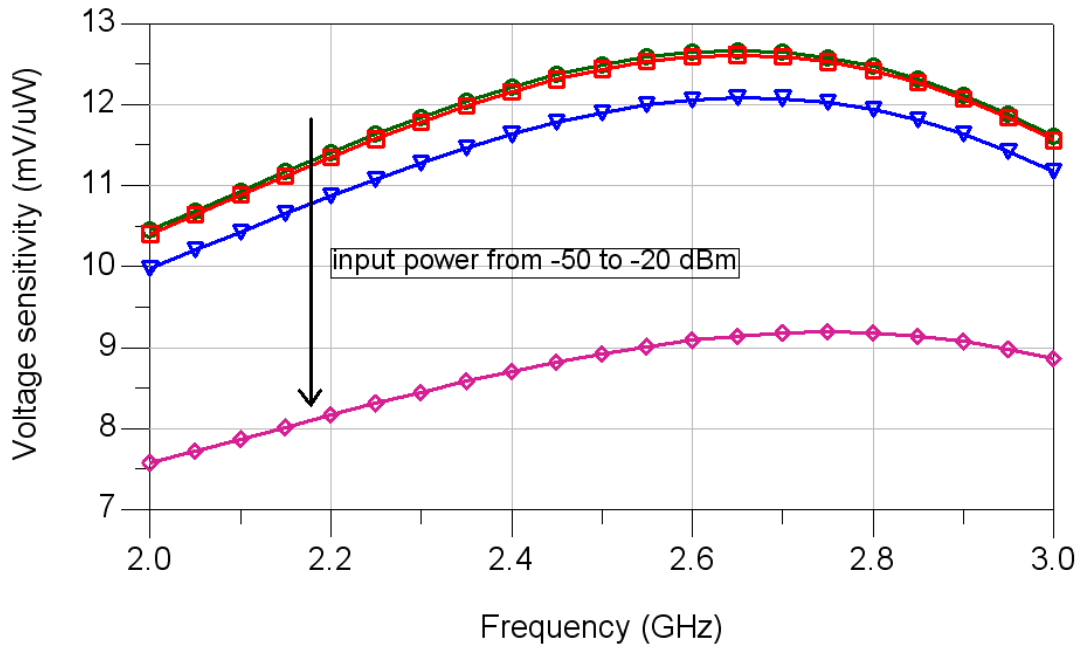


Figure 1-2-8 Voltage sensitivity varying with frequency of the rectenna circuit for different input power

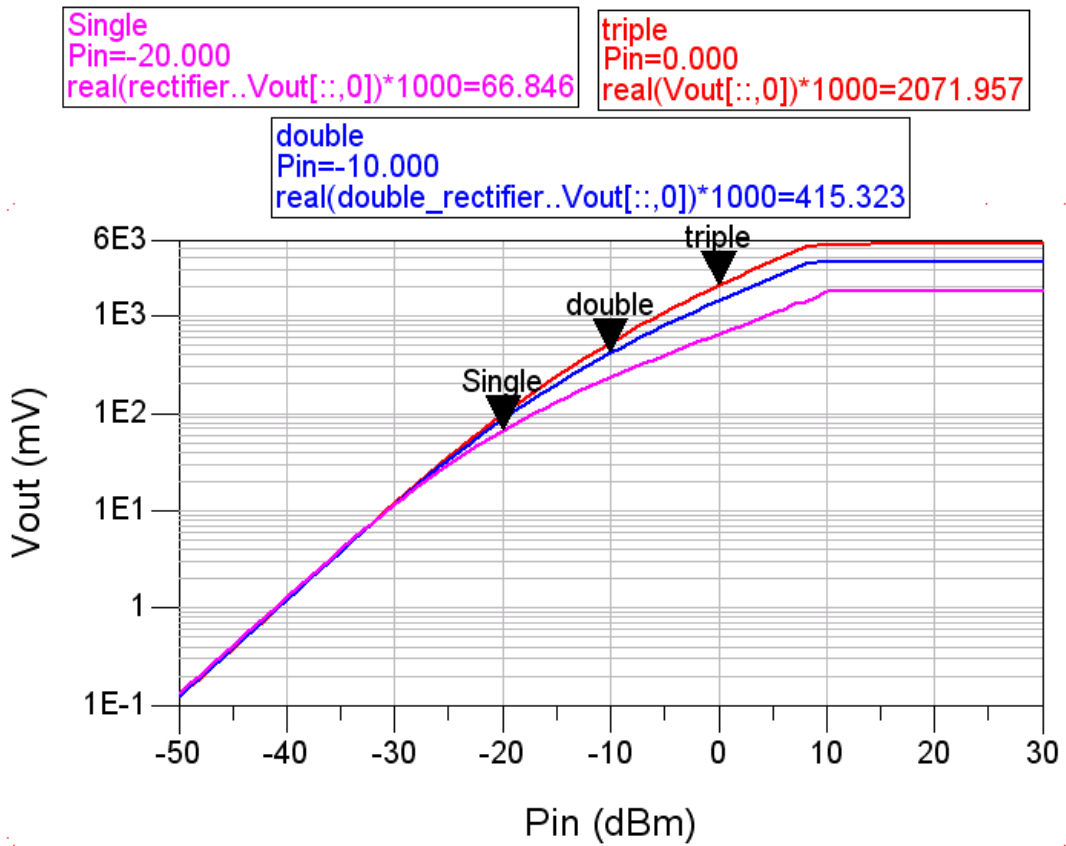


Figure 1-2-9 Transfer curves of the rectenna circuit for single, double and triple schottky diodes

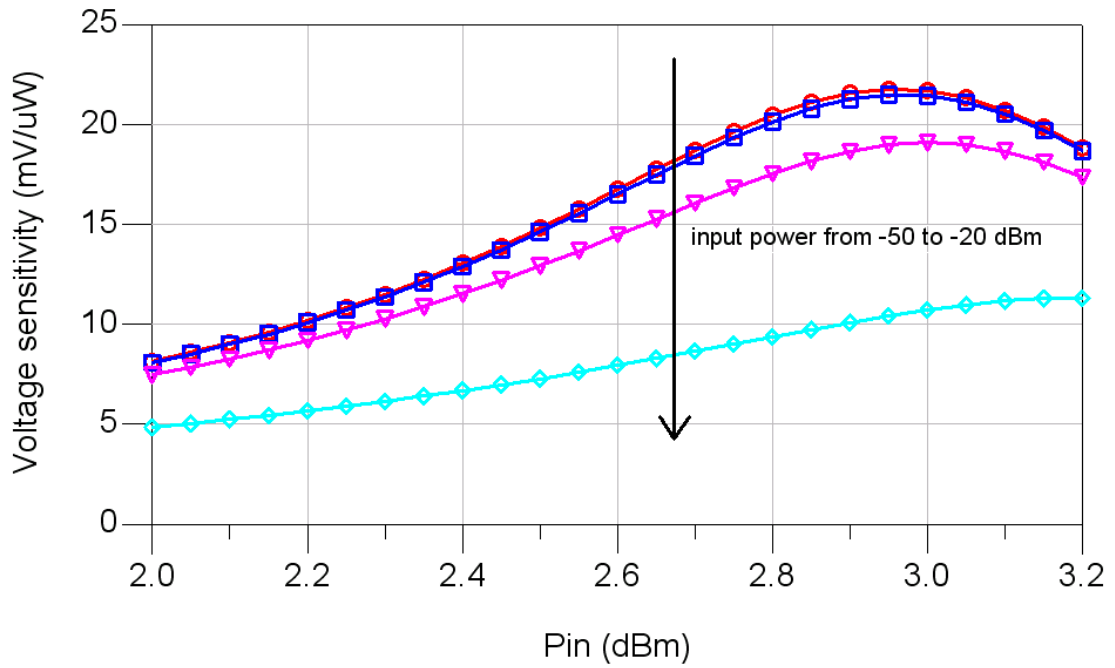


Figure 1-2-10 Voltage sensitivity varying with frequency of the single diode rectenna circuit for different input power

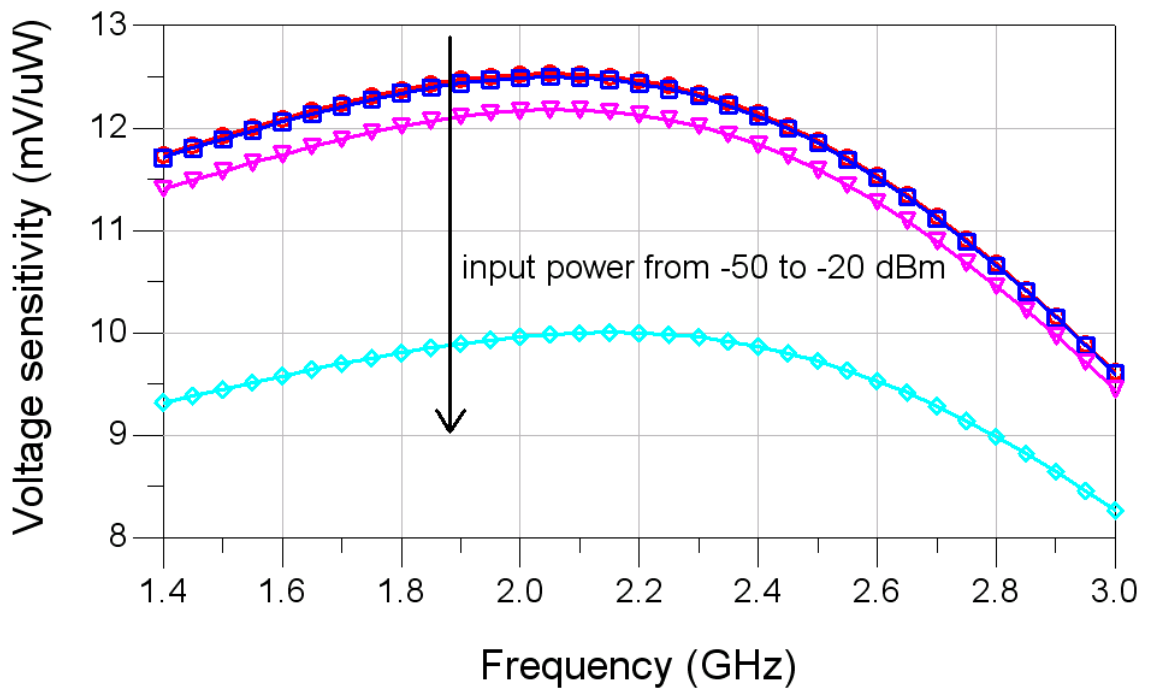


Figure 1-2-11 Voltage sensitivity varying with frequency of the triple diode rectenna circuit for different input power

In order to further improve the simulated exactness, we use microstrip lines to implement the matching circuit and also include the package influence of the HSMS-2862 by including capacitances and inductances. Because the vendor does not give us the zero-bias schottky diodes of HSMS-2850 yet, we use HSMS-2862 instead of HSMS-2850. The HSMS-2862 have been designed and optimized for use from 915 MHz to 5.8 GHz. It is ideal for RFID and RF tag applications. In small signal detector applications ( $P_{in} < -20$  dBm ), this diode is used with DC bias at frequencies above 1.5 GHz. In larger signal power applications (  $P_{in} > -20$  dBm), it is used without bias at frequencies above 4 GHz. When DC bias is available, Schottky diode detector circuits can be used to create low cost RF and microwave receivers with a sensitivity of -55 dBm to -57 dBm. Figure 1-2-12 shows the configuration of the rectenna circuit whose matching network is made by microstrip line. The transfer curve of the rectenna circuit with the microstrip line is presented in Figure 1-2-13. The output voltage with the received RF power of -30 dBm and -20 dBm at the frequency of 2.4 GHz are about 64.932 mV and 185.867 mV, respectively. The photograph of the real rectenna circuit is shown in Figure 1-2- 14. We use chip resistance, chip capacitance and HSMS-2862 to implement the circuit, and the measured results of output voltage against transmission distance are shown in Figure 1-2- 15. From these, it can be noted that the measured output voltage is less than the predicted result due to the fabrication tolerance and the RF property of these passive chip devices. The RF input power of the transmitting antenna is 13 dBm which is the limitation of our equipments.

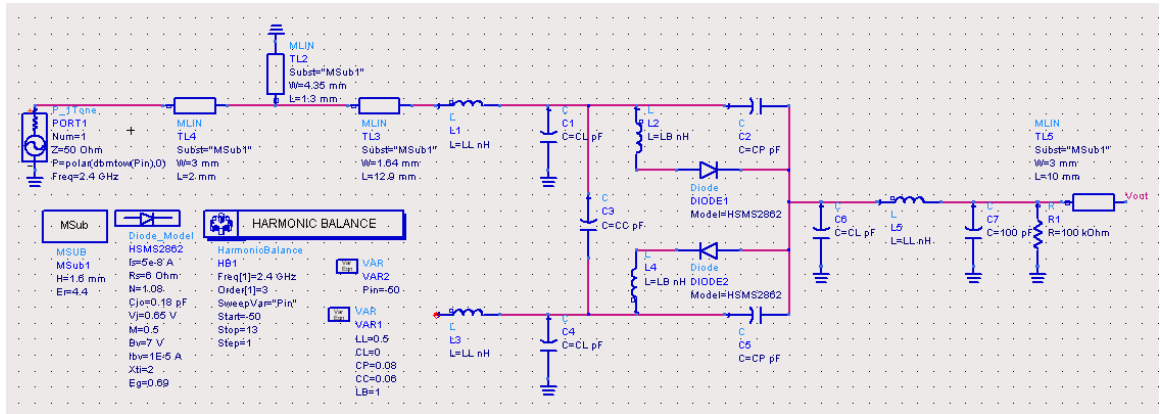


Figure 1-2-12 Transfer simulation of the rectenna circuit with the microstrip line

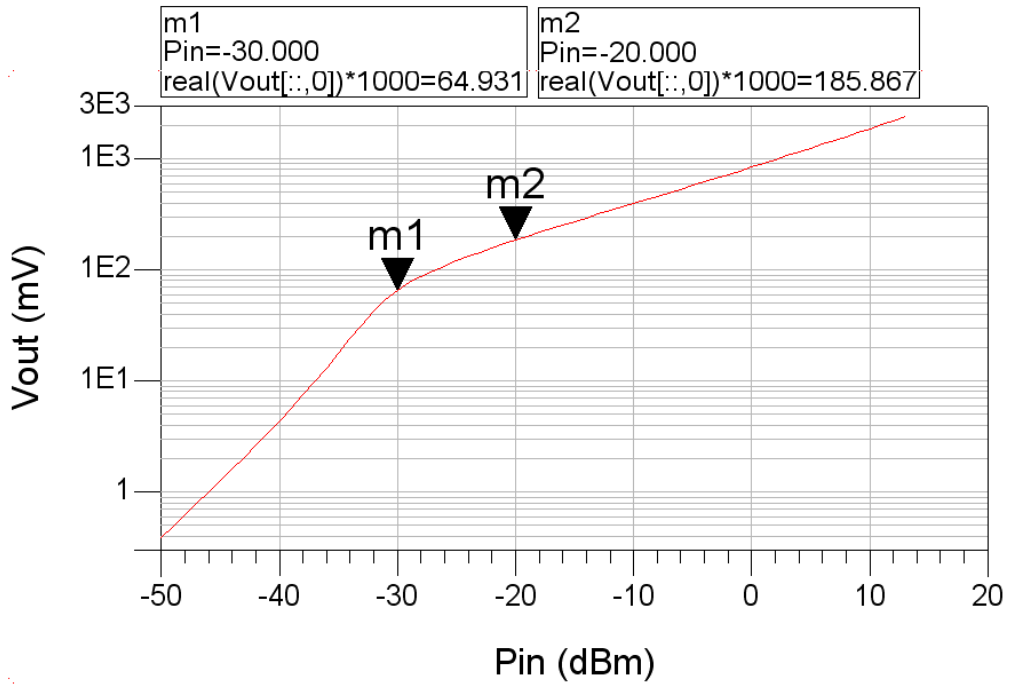


Figure 1-2-13 Transfer curve of the rectenna circuit with the microstrip line



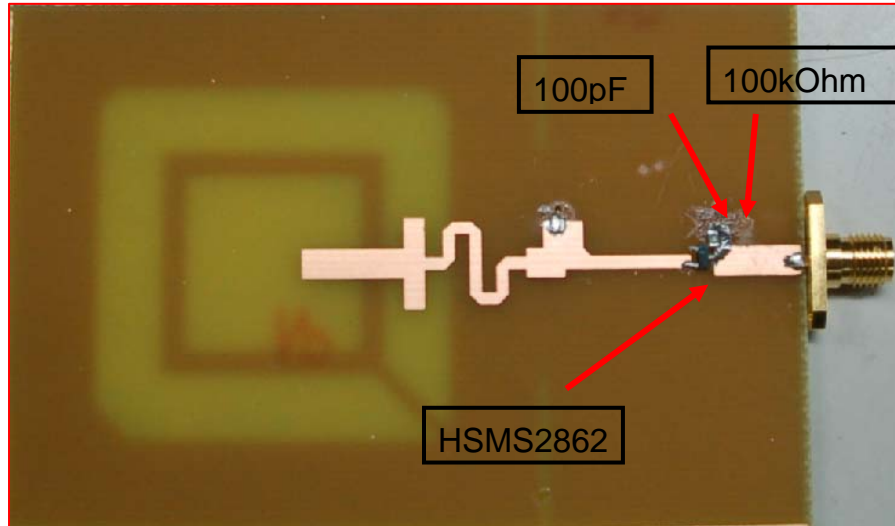


Figure 1-2- 14 Photograph of the real rectenna circuit for the frequency of 2.4 GHz

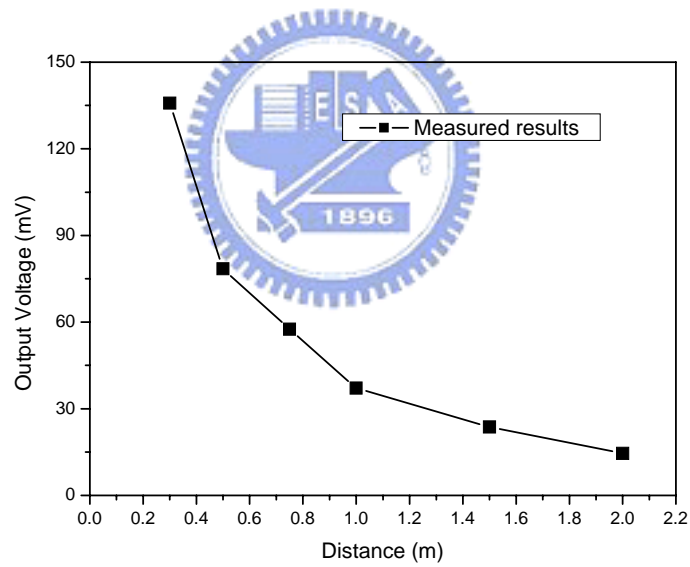


Figure 1-2- 15 Measured results of the output voltage against transmission distance

## *Part II*

*Design and simulation of an uncooled  
microbolometer with low temperature  
CMOS-process compatibility*



# Chapter 1

## Introduction

### 1.1 Characteristics of infrared

The range of infrared wavelengths is from 0.76  $\mu\text{m}$  to 1000  $\mu\text{m}$ . It can be divided into four groups which are near infrared (0.76  $\mu\text{m}$ ~1.5  $\mu\text{m}$ ), middle infrared (1.5  $\mu\text{m}$ ~5.6  $\mu\text{m}$ ), far infrared (5.6  $\mu\text{m}$ ~25  $\mu\text{m}$ ), and extra far infrared (25  $\mu\text{m}$ ~1000  $\mu\text{m}$ ). Crawford F.J. [1] presented the spectral dependence of radiation on temperature shown as Figure 2-1-1. Every object that is not at absolute zero emits and reflects electromagnetic radiation. The wavelength of the radiation is a function of the temperature of the object. Shorter wavelengths are emitted by higher temperatures and longer wavelengths are emitted by cooler objects. The short wavelengths between 0.45  $\mu\text{m}$  to 1  $\mu\text{m}$  used by visible cameras are emitted by very hot sources, such as the sun or incandescent light bulbs. However, the longer infrared wavelengths between 3 and 14  $\mu\text{m}$  are emitted by objects at temperatures around 300 K or 25  $^{\circ}\text{C}$ .

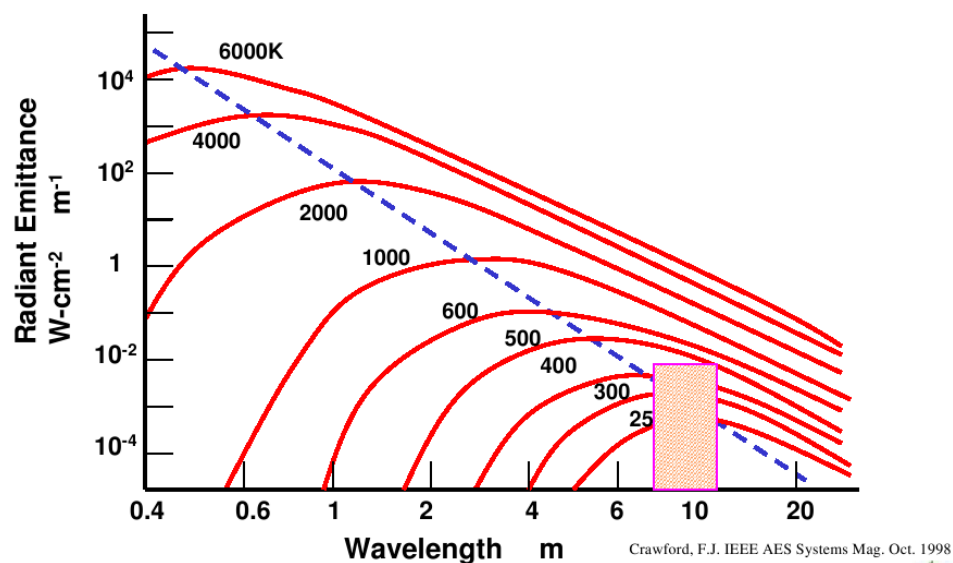


Figure 2-1-1 Spectral dependence of radiation on temperature

Radiation is either scattered or absorbed by gas molecules, rain, and snow as it propagates through the atmosphere. Figure 2-1-2 shows the atmospheric transmission characteristics from visible to 14  $\mu\text{m}$ . It can be noted that the two infrared transmission windows at 3 to 5  $\mu\text{m}$  and 8 to 12  $\mu\text{m}$  are the wavelengths encompassed by terrestrial temperatures. These transmission windows dictate the choice of wavelengths used in the infrared sensor design.

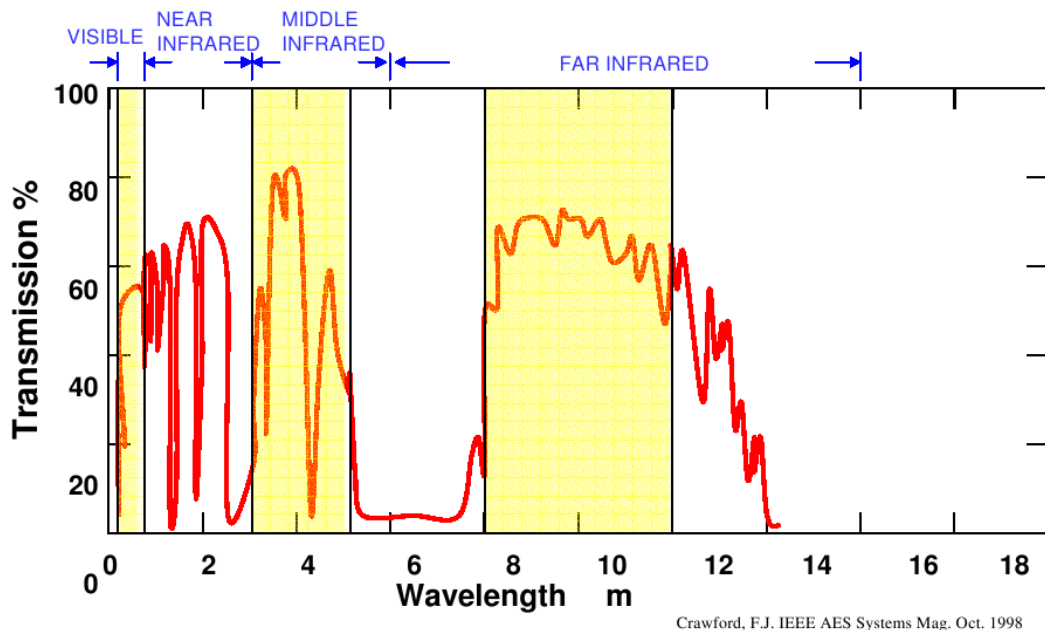


Figure 2-1-2 Atmospheric transmission characteristics

## 1.2 Infrared (IR) detector

Over the past several years, uncooled infrared (IR) radiation detectors have been rapidly developed into a large size of focal plane arrays (FPA). IR detectors have been an important technology for both military and civilian application, such as night vision, surveillance, detection of gas leakage, fire rescue operation, manufacturing quality control, early fire detection, and missile tracking, guidance, discrimination, and interception [2-5]. There are basically two types of IR detectors: photon and thermal detectors [6]. Traditionally, photon detectors are preferred primarily due to their superior

sensitivity. However, the photon detectors must be cooled to approximately the temperature of liquid nitrogen, with the cooling apparatus typically which is the most expensive component in a photon detector's IR camera. Most thermal detectors, on the other hand, don't need such an apparatus, and they are uncooled and comparatively inexpensive. In addition, the recent advances in micromachining technology have made it possible to fabricate highly sensitive thermal IR detectors. Hence it can decrease the cost of the system, offer improved reliability and mean-time-before failure (MTBF), instant operation, sensitivity in the spectral region of 8  $\mu\text{m}$  to 12  $\mu\text{m}$ . Conventional uncooled IR detectors, which have long been used for human image detection and temperature measurements, have a very small number of elements, sometimes only one. This is insufficient for tracking moving IR images; here, it is necessary to increase the number of elements and to integrate them into a two dimensional (2 D) array. Such an array sensor is called a focal plane array (FPA), or an array image sensor. Three different types of uncooled FPA have been developed. They are bolometer detectors [3, 7], thermopile detectors [8], and pyroelectric detectors [9-10]. Bolometers are generally easier to fabricate than pyroelectric detectors and have better responsibility than thermopiles [6]. The bolometer detectors are adopted in this dissertation.

### **1.3 Micromachining technology with integrated circuits for micro-sensor**

#### **applications**

In recent years, microelectromechanical systems (MEMS) have emerged as a very promising field of researches and applications. There is a tendency towards developing a smart sensor which is a combination of sensors and integrated circuits (ICs) in the same chip. Practical implementation of smart sensors has still a lot of problems to be solved such as the difficulty in integrating different fabrication technologies.

From the very beginning, integration of microelectromechanical systems (MEMS) with integrated circuits (ICs) was a major attraction of silicon micromachining

technology. Practical implementation has not been easy. While the first pressure sensors reached the market in the 1960s, many first integration efforts failed, yielding the first practical, integrated pressure sensors in the 1980s [11]. The 1990s brought multiple product launches of integrated MEMS-IC devices, such as acceleration sensors, ink jet print heads, and display chips. In the current decade, integrated gyro sensors entered the market. All these efforts focused on integrating MEMS processes and IC processes on the same wafer. Incompatibilities forced long and expensive development cycles. Several approaches of process integration between IC and MEMS were developed over the past two decades. Generically, they classify into three categories as the following:

- (a) Integration of MEMS on Top of IC
- (b) Lateral (side-by-side) MEMS and IC integration
- (c) Vertical wafer-level MEMS-IC integration.

➤ Integration of MEMS on Top of IC

The most straightforward method of integration is to build the MEMS device directly on top of the CMOS wafers. This has the severe disadvantage of requiring strict process compatibility. MEMS structures are limited to those that can be surface micromachined within the CMOS thermal budget ( $<400\text{ }^{\circ}\text{C}$ ). It rules out LPCVD polysilicon and silicon fusion bonding, a staple for many MEMS devices. Another restriction is that the exposed materials, a low-temperature oxide and aluminum, limit the chemical means available for processing.

➤ Lateral (Side-by-Side) MEMS and IC Integration

This approach overcomes some process incompatibilities between MEMS and CMOS. This method fabricates any CMOS incompatible processes first and then can do both bulk and surface micromachining.

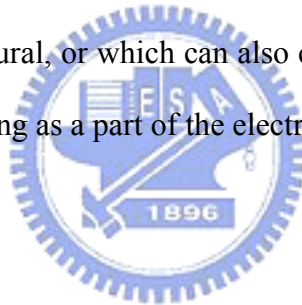
➤ Vertical Wafer-Level MEMS-IC Integration

This approach bonds together two or more wafers. At least one wafer is MEMS and at least one other is CMOS. Each is fabricated in a dedicated foundry. Vertical wafer level integration of circuits and MEMS has several advantages over integrating MEMS

and active circuitry at the process level:

- (1) It lacks the restriction of process compatibility.
- (2) It does not suffer the real estate penalty and inefficiency of lateral integration techniques.
- (3) Because the MEMS and CMOS are fabricated separately prior to integration, it affords the designer absolute flexibility in the choice of active circuit process options. High-density digital, mixed signal, high voltage (HV), BiCMOS, and RF can all be integrated using the same process steps.

The example of the wafer-level MEMS and IC integration is shown in Figure 2-1-3 [11]. Two wafers are preprocessed to fabricate the bond metallization. The bonding recipe requires a precise bonding pressure and temperature profile. It is possible to create bonds which are purely structural, or which can also conduct signals between the MEMS and the CMOS, thus functioning as a part of the electrical circuit.



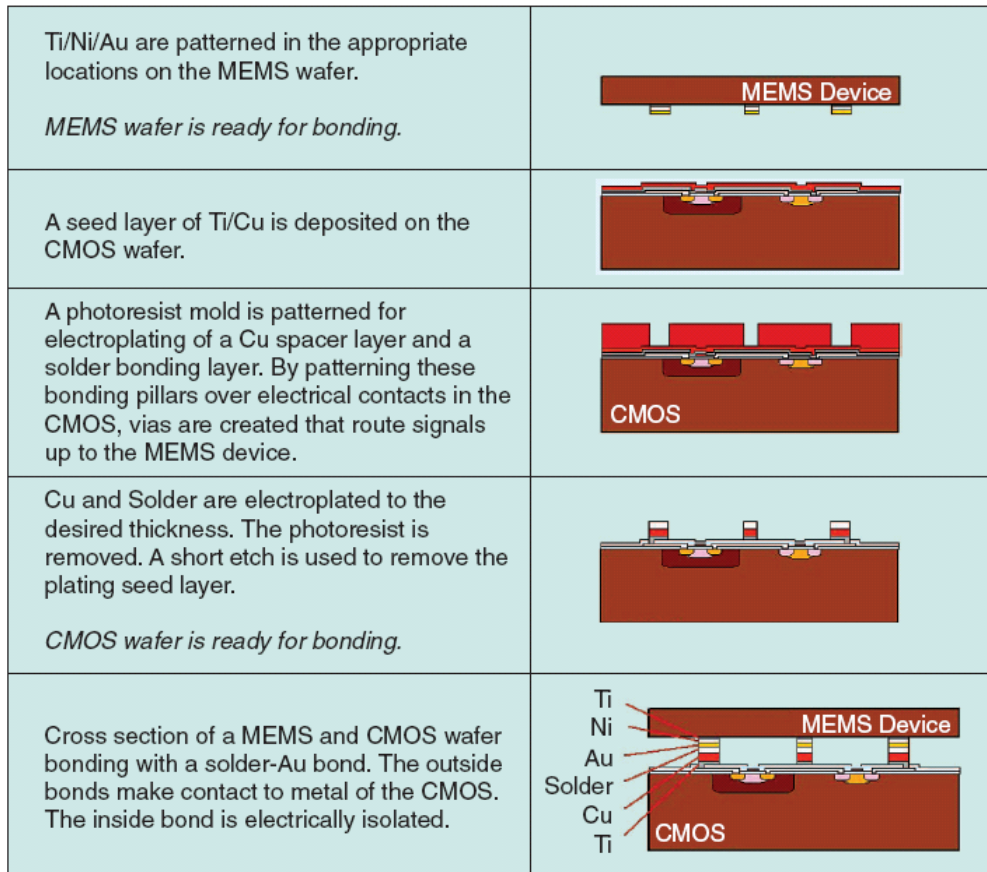


Figure 2-1-3 Vertical wafer-level MEMS-IC integration

#### 1.4 Surface micromachining on top of IC for bolometer detector applications

Although the technology of vertical wafer-level MEMS-IC integration provides many advantages over MEMS on top of IC and lateral MEMS-IC integration, it may not be the best choice for the IRFPA applications, which require a large number of elements and are very susceptible to environmental thermal noise and electrical noise. In order to obtain the best device performance of IR detectors, the surface micromachining on top of IC is the promising candidate for infrared detector applications.

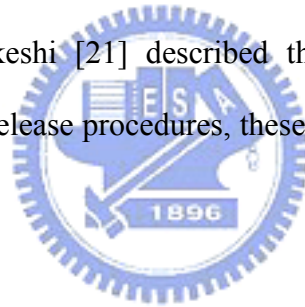
Hence, a low-thermal budget (<math><400^{\circ}\text{C}</math>), CMOS-process compatible, surface micromachining process becomes more and more attractive, and it is widely applied to commercial products and consumer goods due to its benefit of easy integration with ICs.



In addition, a low temperature ( $<400^{\circ}\text{C}$ ) process makes MEMS sensors be able to fabricate directly on ICs as a post-process. This is a very convenient approach to integrate MEMS devices with driving and sensing circuits into a chip, and this integration can improve immunity against noise and increase sensing sensitivity. The primary structures of the surface micromachining are suspension structures such as cantilever beam, bridge, diaphragm, and membrane [12]-[15]. In these structures, flatness of a freestanding diaphragm or a cantilever beam is an important issue for optical applications which are like optical switches and micro-mirrors [15]. However, the flatness and long-legs of membranes are even more a challenge than other devices to design and fabricate for thermally isolated applications, especially as low cost uncooled IR (infrared) microbolometers [16], [17].

The IR microbolometers are radiation sensors with an infrared absorber. Under IR illumination, the temperature of the absorbing layer increases and then the resistivity of the sensitive material changes. In order to acquire a microbolometer with high responsivity, the thermally isolated structure of the device is vital to ensure a maximum increase of temperature due to the absorption of IR radiation [16]. The most important part of the whole microbolometer is the suspension membrane serving as a structural layer on which the sensing material and the signal metal lines are located. Besides, regarding thermal isolation of the microbolometer, many microfabrication approaches have been presented to reduce the thermal losses and thermal mass of the membranes of the microbolometer structures. These approaches contain the use of low thermal conductivity materials and thermally isolated structures obtained by surface or bulk micromachining techniques [17]. In order to integrate easily with CMOS sensing circuits, the surface micromachining technique is preferable due to its small feature size and CMOS compatible processes. However, in the surface micromachining technique, the sticking effect and residual stress play an important role in determining whether the

microstructures are suspended or collapse during the release process. In general, the released microstructures are apt to be attached to the underlying layers. There have been many studies about sticking effect and residual stress with regard to the cantilevered beam structures by developing several different models [18]-[19]. However, no research has been done on the influence of the anchor profile of the membrane microstructure with residual stress. In addition, during the release process, drying of the delicate microstructures is another important issue for whether the device is successful or failure. Many release methods have been presented and compared [20]. To date, most drying methods of release apply CO<sub>2</sub> supercritical point to overcome the sticking effect, but this method leads to low throughput, high cost and expensive apparatus. In this dissertation, we used hot plate to dry the release-etch microstructure to substitute for CO<sub>2</sub> supercritical point method. Although Takeshi [21] described the effects of elevated temperature treatments in microstructure release procedures, these effects were only been investigated for cantilever.



### **1.5 In our research**

We first develop the test microbolometer structure from two aspects including structural design and material selection to obtain high thermal isolation structures. Then, the structure fabrication has been developed to reach the aims of lower processing cost, higher fabricating reliability, and compatible with CMOS processes. The design of the test microstructure by controlling the anchor profile containing sidewall conformal factor (SCF) and sidewall angle is investigated. In addition, the temperature effect during release procedures for single membrane and membrane array is also discussed.

## Chapter 2

### Bolometer Operation and Theory

#### 2.1 Bolometer operation

In general, the IR microbolometers are radiation sensors with an infrared absorber. Under IR illumination, the temperature of the absorbing layer increases and then the resistivity of the sensitive material changes. In this research, the proposed pixel structure of a microbolometer is presented in Figure 2-2-1. The operation of the device is based on three steps as the following:

- (1) Distant objects that are not at absolute zero temperature emit thermal radiation and impact on the thermal absorbing layer of a microbolometer device. This is the first step that optical signal is converted into heat flux.
- (2) The absorbed thermal energy increases the temperature of the sensing layer. This is the second step that heat flux is converted into temperature difference.
- (3) The increasing temperature results in the resistance change of the sensing layer. This is the third step that temperature difference is converted into electrical signals.

In order to obtain the largest temperature difference on the basis of these three steps, the absorbed efficiency and the thermal isolation of the microbolometer device must keep as good as possible.

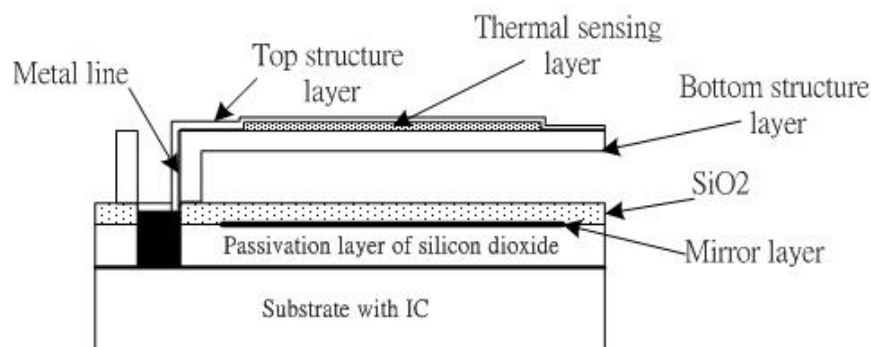


Figure 2-2-1 Pixel structure of a microbolometer

For the sake of making bolometer operation more clear, we further consider the input bias and heat-sink phenomenon [22]. A bolometer measures changes in the heat input from the surroundings and converts this into a measurable quantity such as a voltage or current. A bolometer therefore typically consists of an absorber and a thermometer of heat capacity  $C$ , connected by a small thermal conductance  $G$ , to a heat sink held at a fixed temperature  $T_0$  (it is usually 300 K) as demonstrated in Figure 2-2-2(a). The energy  $P$  of the incident radiation is converted into heat in the absorber, leading to a temperature rise  $\Delta T = T - T_0 = P/C$ , until the radiation power flowing into the absorber is equal to the power flowing into the heat sink through the weak thermal link. The temperature rise is subsequently measured and is directly proportional to the deposited energy.

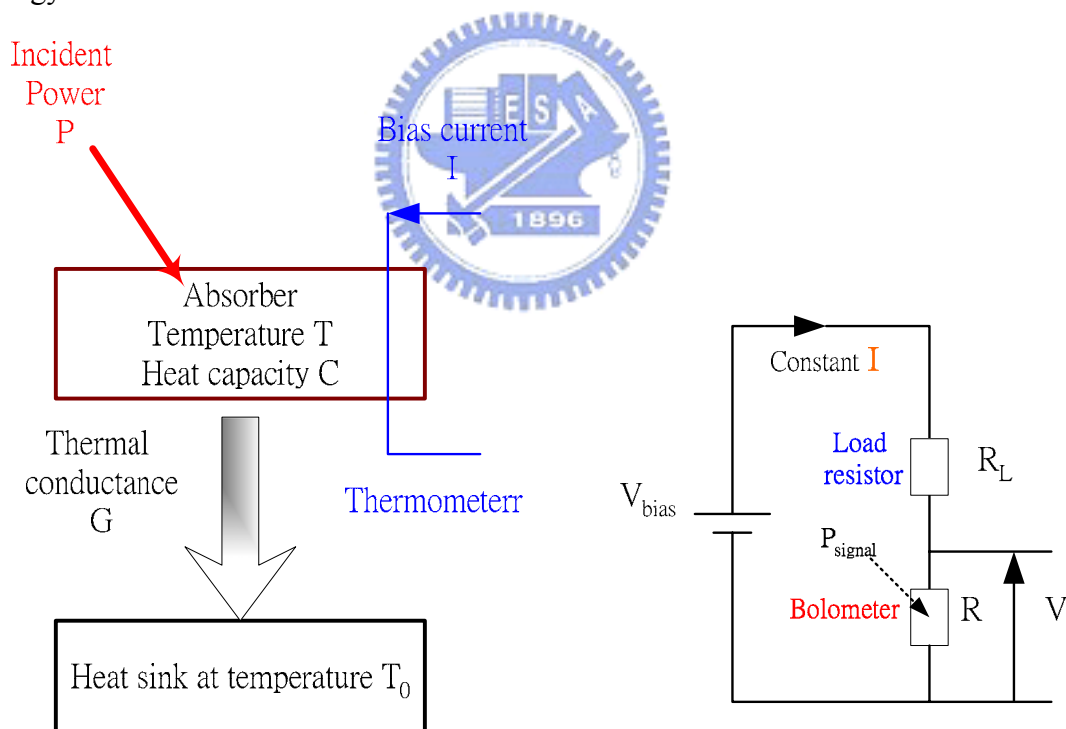


Figure 2-2-2 (a) Schematic illustration of bolometer operation (b) Bolometer bias circuit

The bolometer is in general placed in a bias circuit with a voltage source and load resistor as shown in Figure 2-2-2(b). A constant current  $I$ , generated from the load resistor

$R_L$  and bias voltage  $V_{bias}$ , flows through the bolometer. Provided this bias power ( $P_{bias} = V_{bias}I$ ) remains constant, the incoming signal power ( $P_{signal}$ ), collected by the detector, will cause the bolometer temperature  $T$  to increase according to:

$$T = T_0 + (P_{signal} + P_{bias})/G \quad (2-1)$$

The temperature rise causes a change in the resistance of the bolometer and consequently in the voltage across it. This change in voltage is amplified and measured. The thermometer is therefore made of a material that ideally has a large change in resistivity for a small change in temperature.

## 2.2 General performance concepts [23]

The important figure of merit for a bolometer is the sensitivity ( $S$ ), detectivity ( $D$ ), noise equivalent power (NEP) and time constant ( $\tau$ ). The NEP is a measure of the sensitivity of a bolometer, and is defined as the power absorbed that produces a signal to noise of unity at the output. NEP can also be defined as the minimum incident radiation power necessary to obtain a signal to noise of unity.

Radiation incident on a solid state device will cause the absorption of photons and the creation of lattice vibrations or phonons. This will act to increase the resistivity of a solid state device. Two parameters are convenient to define before stating an expression for a bolometer's voltage signal. The first is the heat conductance of  $G$  defined as  $dP/dT$  where  $P$  is the radiative power lost or absorbed by the device and  $T$  is temperature. The second parameter is the temperature coefficient of resistance,  $\alpha$ , where  $\alpha = (1/R)dR/dT$  is the fractional change in resistance per degree Kelvin. We now assume the device is driven by a constant current  $I$ , and is enclosed in a chamber at temperature  $T_0$ . Since the current through the resistor heats it slightly, we define the temperature of the detector element as

T and assume  $(T-T_0) \ll T_0$ . The signal voltage becomes

$$V_s = I\Delta R = I\alpha R\Delta T = I\alpha R \frac{P_s}{G} \quad (2-2)$$

It follows that bolometer sensitivity,  $S=V_s/P_s$ , is given by

$$S = \frac{I\alpha R}{G} \quad (2-3)$$

For high sensitivity, one requires a large electrical resistance, a large current, a large temperature coefficient of resistance and a small heat conductance. In order to obtain a large temperature coefficient of resistance is accomplished by choosing the proper material. The bolometer's resistance is controlled by maintaining a small film thickness and a large length to width ratio. The latter requirement, however, conflicts the need for resistance uniformity across an array of bolometers for infrared video imaging. In such cases, it may be necessary to sacrifice the benefits of a large resistance. Minimizing the heat conduction is probably the most interesting aspect of bolometer design. The large thermal conductance provided by a bulk substrate will draw heat from the temperature sensing element too fast and lower the sensitivity. A large thermal conductance, however, may be desirable in the construction of very high speed bolometer if a reduction in sensitivity is tolerable. By quickly drawing the excess heat from the bolometer resistance element, fast changes in temperature or infrared images can be detected.

To quantify the speed of a bolometer, consider a detector element with heat capacity C defined as  $C = dE/dT$  where E is the total internal energy of the element. The bolometer time constant is then  $\tau = C/G$  in analogy to a single time constant circuit. It should be noted that optimizing the sensitivity by lowering G and optimizing the speed by increasing G cannot be done without simultaneously lowering the heat capacity. Intuitively, the need for a small C by considering that a smaller change in the bolometer internal energy is needed to create an appreciable change in temperature. Therefore a

small incident energy can be used to cause a change in the voltage signal.

Equation (2-3) can be further modified to include the effect of illumination chopping frequency,  $\omega$ , as the following:

$$S = \frac{\eta I \alpha R}{G \sqrt{1 + \omega^2 \tau^2}} \quad (2-4)$$

A factor,  $\eta$ , has also added to account for incomplete optical absorption by the absorbing layer. The factor is called the coefficient of absorptance.

In terms of noise figure for a bolometer, the three dominant noise factors must be considered. All solids at a finite temperature suffer from temperature fluctuations and Johnson noise. The third noise source arises from the electrical noise in the amplifier electronics. The mean-square fluctuation in the voltage signal per unit of bandwidth is obtained by summing the square of the two independent factors. The first factor is the amplifier noise and the second factor arises from the temperature fluctuations in the bolometer resistive element.

$$\overline{V_N^2} = 4kT_N R + I^2 \alpha^2 R^2 \overline{\Delta T^2} \quad (2-5)$$

Where  $k$  is Boltzmann's constant and  $T_N$  is the effective input noise temperature of the amplifier. Because the body has a conductance  $G$  and capacity  $C$  with time constant  $\tau$ , we know from basic network theory that the power spectrum of such a body is of the form

$$\overline{\Delta T^2(f)} = \frac{K}{1 + \omega^2 \tau^2} \quad (2-6)$$

where  $K$  is a constant of proportionality found by considering the entire temperature fluctuation over all frequencies. Besides, from Boltzmann's relationship, the probability of the resistive element has energy  $E_i$  and can be expressed

$$p(E_i) = A e^{-E_i / kT} \quad \text{with} \quad \sum_i A e^{-E_i / kT} = 1 \quad (2-7)$$

The average energy of the body is

$$\bar{E} = \frac{\sum_i E_i e^{-E_i / kT}}{\sum_i e^{-E_i / kT}} \quad (2-8)$$

From the definition of heat capacity,

$$C = \frac{dE}{dT} = \frac{1}{kT^2} (\overline{E^2} - \bar{E}^2) = \frac{1}{kT^2} \overline{\Delta E^2} \quad (2-9)$$

$$\overline{\Delta T^2} = \frac{\overline{\Delta E^2}}{C^2} = \frac{kT^2}{C} \quad (2-10)$$

Combining the above with equation (2-6), we have,

$$\frac{K}{2\pi} \int_0^\infty \frac{d\omega}{1 + \omega^2 \tau^2} = \frac{kT^2}{C} \quad (2-11)$$

Solving for K yields the noise spectral density,

$$\overline{\Delta T^2}(f) = \frac{4kT^2}{G} \left( \frac{1}{1 + \omega^2 \tau^2} \right) \quad (2-12)$$

For frequencies much less than  $1/\tau$ , the final temperature fluctuation of the sensor, per unit of bandwidth, is

$$\overline{\Delta T^2} = \frac{4kT^2}{G} \quad (2-13)$$

For a body in thermal equilibrium, one-half of the fluctuation is due to emission of radiation while the other half is due to absorption. It follows that the mean-square temperature fluctuation per unit of bandwidth is

$$\overline{\Delta T^2} = \left( \frac{2kT_0}{G} + \frac{2kT^2}{G} \right) = \frac{4kT_0^2}{G} \left( 1 + \frac{\Delta T}{T_0} \right) \quad (2-14)$$

This equation can be rewritten as

$$\overline{\Delta T^2} = \frac{4kT_0^2}{G} \left( 1 + \frac{I^2 R}{GT_0} \right) \quad (2-15)$$

The resultant voltage fluctuation is

$$\overline{V_N^2} = 4kT_N R B + \frac{4I^2 \alpha^2 R^2 kT_0^2}{G} \left( 1 + \frac{I^2 R}{GT_0} \right) \quad (2-16)$$

and the signal to noise ratio is



$$\frac{S}{N} = \frac{V_S^2}{V_N^2} = \frac{\frac{I^2 \alpha^2 R^2 P_s^2}{G^2}}{4kT_N RB + \frac{4I^2 \alpha^2 R^2 kT_0^2}{G} \left(1 + \frac{I^2 R}{GT_0}\right)} \quad (2-17)$$

The NEP is defined as the minimum incident radiation power,  $P_s$ , necessary to produce  $S/N = 1$ . From the latter equation we therefore have the noise equivalent power in units of watts per  $\text{Hz}^{1/2}$ ,

$$NEP^2 = 4kT_0^2 G + 4kT_0 I^2 R + \frac{4kT_N G^2}{I^2 \alpha^2 R} \quad (2-18)$$

The second term indicated an increasing NEP with bias current. The third term is the Johnson noise and indicates a decreasing NEP with bias current, associated with the increased signal response. It can be written in terms of the sensitivity, using equation (2-2),

$$\frac{4kT_N G^2}{I^2 \alpha^2 R} = \frac{4kT_N R}{S^2} \quad (2-19)$$

It is convenient to define a figure of merit which accounts for the device area.

The specific detectivity,  $D^*$ , is defined as

$$D^* = \frac{\sqrt{A(BW)}}{NEP} \quad (2-20)$$

Where  $A$  is the device area and  $BW$  is the bandwidth of the noise power. The detectivity  $D^*$  is less sensitive to the detector area  $A$ .

### 2.3 Analysis of heat transfer mechanisms for bolometer structures

The main structure of the microbolometer consists of two parts; one is the thin film resistor, another is the membrane structure. The membrane structure offers a excellent thermal isolation and supports the whole device with two narrow legs. The basic principle of microbolometer is that raising material temperature by absorbing IR radiant energy, and when temperature changes, the electrical resistance will be change. The heat balance

equation is expressed by mathematically as follows:

$$C \frac{d\Delta T}{dt} + G\Delta T = \varepsilon\Phi_e \quad (2-21)$$

C: Thermal capacitance

G: Thermal conductance

$\varepsilon$  : Emissivity

We assume that the radiant power is

$$\Phi_e = \Phi_{e0} e^{j\omega t} \quad (2-22)$$

$\Phi_{e0}$  : The amplitude of sinusoidal radiation

The boundary condition is  $t = 0, \Delta T = 0$ , and the solution of the differential heat equation is

$$\Delta T = \frac{\varepsilon\Phi_{e0}}{G\sqrt{1 + \omega^2\tau^2}} \quad (2-23)$$

$$\tau = \frac{C}{G} \quad (2-24)$$

This thermal time constant  $\tau$  determines the speed of response of the microbolometer. In order to get more sensitivity of microbolometer, thermal capacitance must be smaller and thermal conductance must be larger. However, the larger thermal conductance will bring about increasing heat loss of microbolometers, and it also reduces temperature difference at the same absorbed thermal energy. From Figure 2.1, it can be noted that the total thermal conductance of the microbolometer can be expressed as

$$G = G_{leg} + G_{gap} + G_{rad} \quad (2-25)$$

where  $G_{leg}$  : Thermal conductance due to two supporting legs

$G_{gap}$  : Thermal conductance due to surrounding gas

$G_{rad}$  : Thermal conductance due to sensing layer and supporting layer

The optical radiation falling on the detectors goes into heating the bolometer. Hence, heat

flows from the bolometer to the surrounding via three heat-transfer mechanisms, conduction, convection, and radiation. The conduction mechanism occurs through the supporting legs and the surrounding air. Therefore, the supporting legs must be carefully designed to reduce the thermal conductance path and to meet the thermal time response requirements. The IR sensitive element must be thermally isolated from its surroundings to reduce the rate of heat loss and, hence, increase the sensitivity of the detector. Therefore, the bolometer arrays must be packaged in vacuum. The convection mechanism occurs in the presence of a surrounding atmosphere. If the principal heat loss mechanism is radiative, then the detector is at the background limit. In this design, the detector will be packaged in vacuum. Therefore, the thermal conductance of the microbolometers is mainly due to the heat flow via the supporting legs. The thermal conductance was estimated from the calculated thickness, width and length of the supporting legs simulated in the solid model.

Since the thermal conductance of the individual components making up the supporting legs were in parallel, the total thermal conductance was determined by the summation of the individual thermal conductance of all layers. The total thermal conductance is given by:

$$G = \sum_m \frac{K_m W_m t_m}{L_m}$$

where  $K_m$  is the thermal conductivity of each component, and  $W_m$ ,  $t_m$ , and  $L_m$  correspond to width, length, and thickness of each component. The thermal time constant was calculated from the ratio of the device's thermal mass to its thermal conductance. A low thermal time constant was targeted for high-speed camera applications.

The thermal mass of the microbolometer can be calculated from the specific heat capacity and volume of each layer forming the micro-bridge, namely amorphous silicon layer, silicon dioxide layer, tantalum layer. The thermal mass is given by

$$C = \sum_m W_m L_m t_m c_m$$

Where,  $W_m$ ,  $L_m$ ,  $t_m$ ,  $c_m$  a correspond to width, length, thickness, and specific heat of each layer.

## 2.4 Material property control

The material of membrane is important in a bolometer. The mechanical deformation may cause thermal isolation failure. The Young's modulus of a material affects its mechanical deformation with respect to applied stress,  $E = \sigma / \varepsilon$ , where  $\sigma$  is normal stress and  $\varepsilon$  is strain. The total stress of a micro-structure is expressed by following equation,

$$\sigma_{total} = \sigma_i + \sigma_e + \sigma_{th} \quad (2-26)$$

Where  $\sigma_i$  is internal stress,  $\sigma_e$  is external stress, and  $\sigma_{th}$  is thermal stress. Besides, thermal stress can be estimated by equation.

$$\sigma_{th} = E_y \Delta T (\alpha_{film} - \alpha_{sub}) \quad (2-27)$$

$\alpha_{film}$  : Thermal expansion coefficient of thin film

$\alpha_{sub}$  : Thermal expansion coefficient of substrate

Assuming that the substrate is flat and from biaxial stress analysis, after depositing film on the substrate, the stress can be expressed as

$$\sigma = \frac{E_{sub} t_{sub}^2}{6R t_{film}} \frac{1}{1-\nu} \quad (2-28)$$

$\nu$  : Poisson ratio

$E_{sub}$  : Young's modulus of substrate

## Chapter 3

### Structure design and related considerations

#### 3.1 General considerations

In order to design thermally isolated membrane structures of the microbolometers, we develop the microbolometer structure from two aspects including structural design and material selection.

In respect of structural design, longer legs are preferable due to reducing thermal losses and increasing device responsivity. To date, the most usual pixel size of microbolometers for commercial applications is about  $50\mu\text{m} \times 50\mu\text{m}$  or less. Though the larger test structure size is not suitable for applying to microbolometer, in this study, it is still considered and discussed for the sake of the comparison with different simulation conditions. In addition, it can also prove that the design approach well applies to develop other devices that need larger membranes such as tunable capacitor [24] and Fabry-Perot filter [25]. In this research, we propose a new microbolometer structure directly fabricated on ICs. Figure 2-3- 1 illustrates a new structure of a microbolometer having 52% fill factor and low effective thermal conductivity due to its longer support legs and very low thermal conductivity of the silicon dioxide structural layer. In order to obtain the highest fill factor of the microbolometer arrays, each pixel size must be square shape. Moreover, a quarter-wavelength resonance is also attained using appropriate air gap space and mirror layer to improve efficiency of IR absorption. For the purpose of lower effective thermal conductivity and prevention of thermal losses from the structure layer by thermal conduction, the supporting legs of the microbolometer are designed to longer lengths, and each of those legs has to be two right angle corners to retain the high fill factor. This proposed microbolometer includes mainly five parts that are mirror layer (reflecting IR), contact hole, structure layer (membrane), sensing layer (TCR material), and metal line (delivering signal).

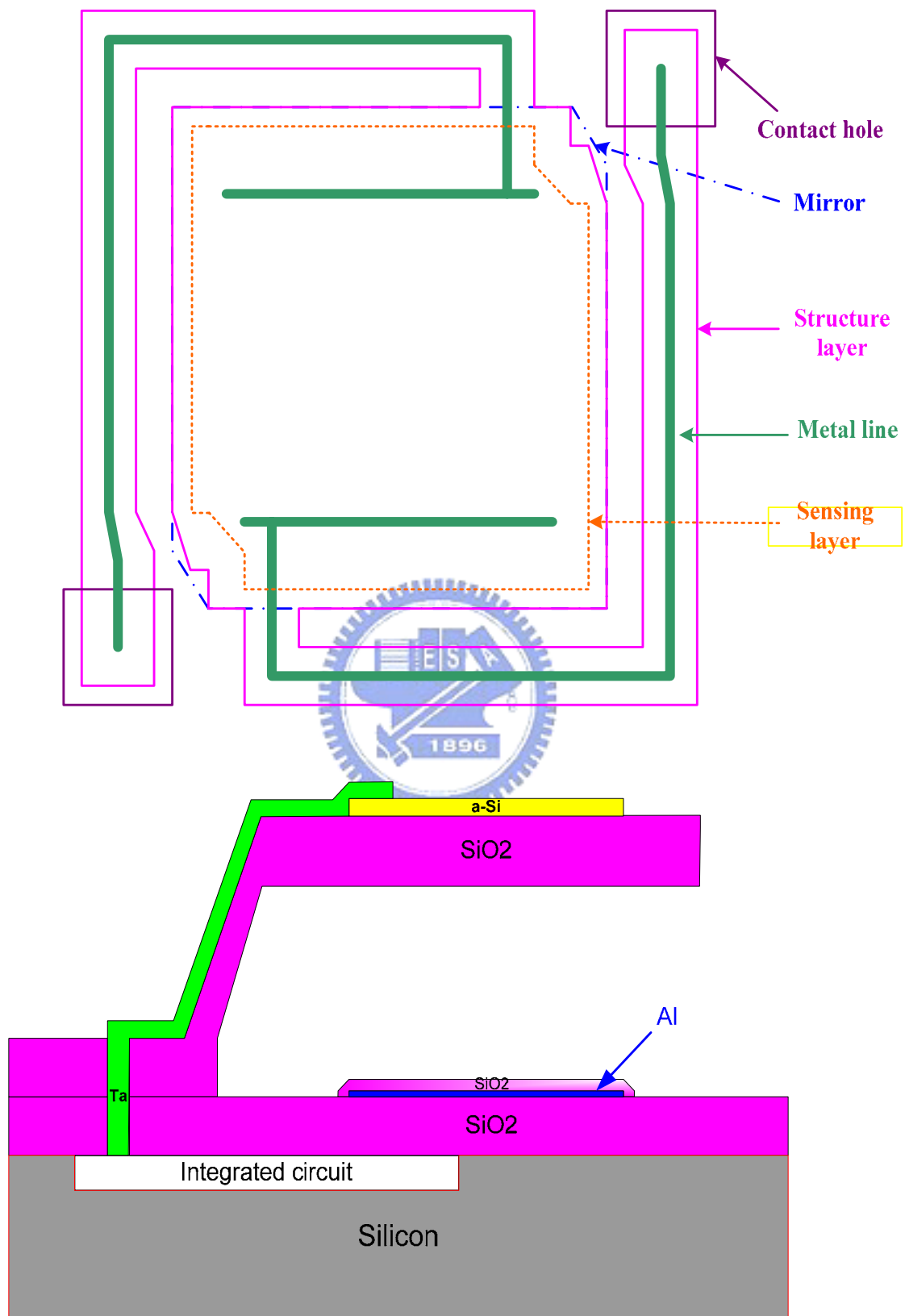


Figure 2-3- 1 Figure 3.1 Proposed structure configuration of bolometer detector

Because the resolution limitation of our lithography equipments is the smallest line width of  $2\mu\text{m}$  and the alignment tolerance must also be considered, the width of the metal lines is designed to  $2\mu\text{m}$ , and each of the legs of the structure layer is  $5\mu\text{m}$  for  $50\mu\text{m} \times 50\mu\text{m}$  pixel size. However, in order to prevent the fragile anchor part from being destroyed during release-etch processes, the width of the anchor translates from  $8\mu\text{m}$  to  $5\mu\text{m}$  at the beginning section of the anchor region. In this proposed microbolometer structure, we used aluminum as the sacrificial layer [26~28], and mirror layer owing to its easily depositing thick film, larger etching rate, and very high etching selectivity with dielectric layers. Besides, amorphous silicon or silicon germanium oxide is used as the sensing layer as they have higher temperature coefficient of resistance (TCR), lower depositing temperature, and showing very high resistance for aluminum etchants. The metal line adopts tantalum (Ta) due to its lower thermal conductivity ( $57.5\text{W/m/K}$ ) than chromium ( $93.7\text{ W/m/K}$ ) and nickel ( $90.7\text{W/m/K}$ ), and, furthermore, tantalum has not bad electric conductivity and very high resistance for aluminum etchants. Up to now, this is the first time using Ta to substitute for Cr and Ni as a metal line for the microbolometer application. Silicon dioxide by plasma enhanced chemical vapor deposition (PECVD) is deposited to serve as an isolation layer and structural layer due to its very low thermal conductivity than other conventional dielectric layers such as silicon nitride, polysilicon etc. Besides, Silicon dioxide deposited by PECVD is easier to fabricate lower stress thin film than silicon nitride by PECVD.

### **3.2 Consideration about material of sensing layer**

Material of sensing layer plays an important role in significantly affecting device performance. A bolometer at temperature  $T$  is a thermal sensor that uses a material with a temperature dependent resistance  $R(T)$  to measure the heating effect of absorbed IR

radiation. The parameter used to quantify the temperature dependence of R is the temperature coefficient of resistance (TCR), defined as

$$\alpha = \frac{1}{R} \frac{dR}{dT} \quad (3-1)$$

Metals shows little change in free carrier density with temperature, but the mobility of free carrier decreases with temperature, producing a positive TCR, typically about  $+0.2\% \text{ K}^{-1}$ . Thin metal films usually have a TCR less than the bulk value, and the TCR of metal films varies slightly with temperature. The first microbolometer arrays [29] employed nickel-iron (NiFe) metal films with a TCR of  $+0.0023 \text{ K}^{-1}$ , and achieved NETD of  $0.25 \text{ }^\circ\text{C}$ . Because the resistivity of metal is low, serpentine resistors about 100 squares long were used to form the bolometer resistors. The principal attractions of metal TCR materials are the ease of achieving controllable deposition and low 1/f noise in metal films and contacts [30]. Semiconductor materials have mobile carrier densities that increase with increasing temperature, as well as carrier mobility that changes with temperature [31], producing a high negative TCR that is generally temperature dependent. A typical R(T) behavior for a semiconductor whose mobile carrier density is controlled by thermal excitation across a bandgap is

$$R(T) = R_0 \exp\left(\frac{E_a}{kT}\right) \quad (3-2)$$

where  $E_a$  is activation energy and equals to half the bandgap  $E_g$ . Combining equation (3-1) and (3-2), we can obtain the expression as following:

$$\alpha = \frac{1}{R} \frac{dR}{dT} = -\frac{E_a}{kT^2} \quad (3-3)$$

For example, if  $E_g$  is 0.6eV and T is 300K,

$$\alpha = -\frac{0.3}{8.625 \times 10^{-5} \times 300^2} = -3.86\% / K$$

Since the number of mobile carriers decreases as  $E_a$  increase, the general trend is for higher resistance materials to have higher  $\alpha$ . Unfortunately, higher resistivity materials



also tend to have great excess noise (1/f noise).

For uncooled microbolometer applications, a wide variety of materials are candidates for TCR material, such as amorphous silicon [32-33], amorphous silicon germanium [34-35] and amorphous  $\text{Ge}_x\text{Si}_{1-x}\text{O}_y$  [36-37]. They are compatible for semiconductor process and among these, amorphous  $\text{Ge}_x\text{Si}_{1-x}\text{O}_y$  has the highest TCR value. Vanadium oxide [38-39] and YBaCuO [40-43] are mostly used for sensing layer of microbolometer. However, Vanadium oxide is not compatible for CMOS process as it is easy to hydrolyze. Besides, YBaCuO is superconductor material and must be operated at cooling environment [44-45]. Table 1 lists the TCR values of usual use of sensitive element for bolometer applications from literatures.

	$\text{VO}_x$	Poly-Si	YBCO	Poly-SiGe	Ti
TCR (%/K)	-2	-1~-2	-3.1	-0.75~-2	0.2~0.25
		$\alpha - \text{Si}$		$\alpha - \text{SiGe}$	
TCR (%/K)		-1.3~-3.2		-2.8~-3.8	

Table 1 TCR of sensitive film

In this research, we choose n-type doping amorphous silicon layer used to sensitive material. This is based on several reasons: First, in order to fabricate microbolometer directly on the top of IC, the whole post-processing temperature must be limited to below 400 degrees C. Second, although sputtering silicon-germanium oxide has very good TCR value and is suitable for low temperature processing, but it cannot be deposited by our apparatuses. Even if the chemical-vapor-depositing (CVD) silicon-germanium oxide can be deposited in our laboratory, its processing temperature is higher than 550 degrees C. Third, the processing temperature of amorphous silicon by

PECVD is about 250 degrees C. However, the resistance of undoping amorphous silicon is too high to suit bolometer applications even though it has higher TCR value than that of doped amorphous silicon. Fourth, the doped amorphous silicon structures can achieve good radiation absorptance and good TCR value. An example is described in the reference [46]. T. Schimert used p-type doped amorphous silicon as sensitive layer of microbolometer array. The proposed pixel structure array and pixel cross section view are shown in Figure 2-3-2 (a) and (b), respectively. The microbolometer pixel parameters are also listed in Table 2. Besides, the proposed bolometer structure is very simple compared to other bolometer structures, and, even though it has very simple structure, it can also achieve good radiation absorptance ( $> 80\%$ ) within the wavelength of  $6 \sim 15 \mu\text{m}$  as shown in Figure 2-3- 3.

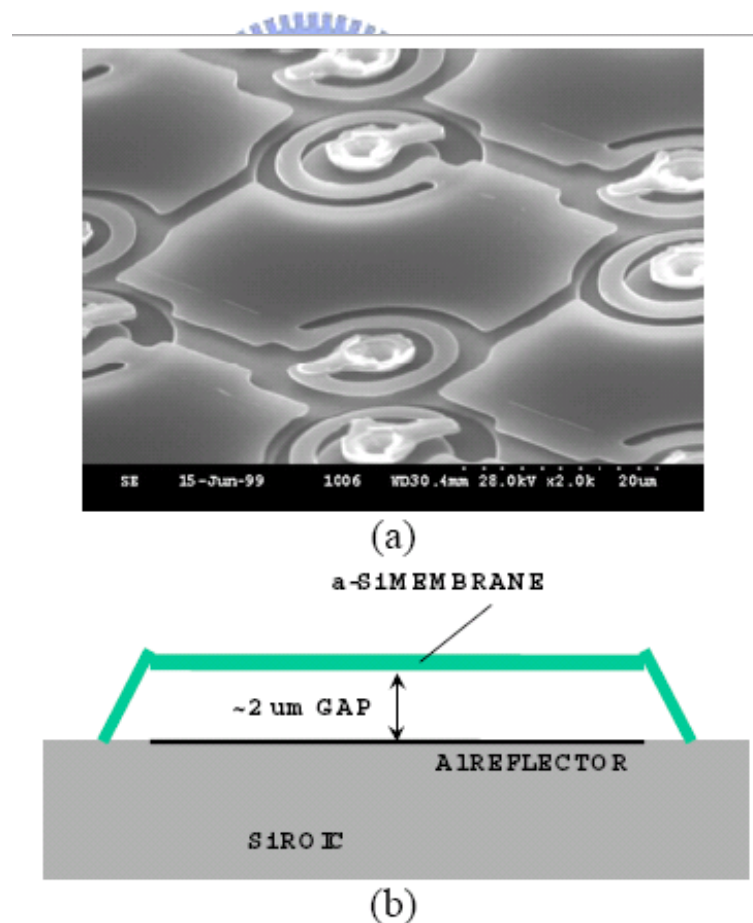


Figure 2-3-2 (a) 120 x 160 a-Si microbolometer array with 46.8  $\mu\text{m}$  pixels (b) Cross section of microbolometer structure

PARAMETER	UNITS	MEASURED VALUE
PIXEL SIZE	$\mu\text{m}^2$	46.8X46.8
FILL FACTOR	%	58
IR ABSORPTANCE ( $\epsilon$ )	%	>80
THERMAL RESISTANCE (RTH)		$4 \times 10^7$
THERMAL CONDUCTANCE (GTH)	K/W	
MEMBRANE THICKNESS	W/K	$2.5 \times 10^{-8}$
THERMAL TIME CONSTANT ( $\tau_{\text{TH}}$ )	A	
	ms	~2000
		~11
DC PIXEL BIAS (VBIAS)	V	1
PIXEL RESISTANCE (R)	M $\Omega$	30

Table 2 Amorphous silicon pixel parameters

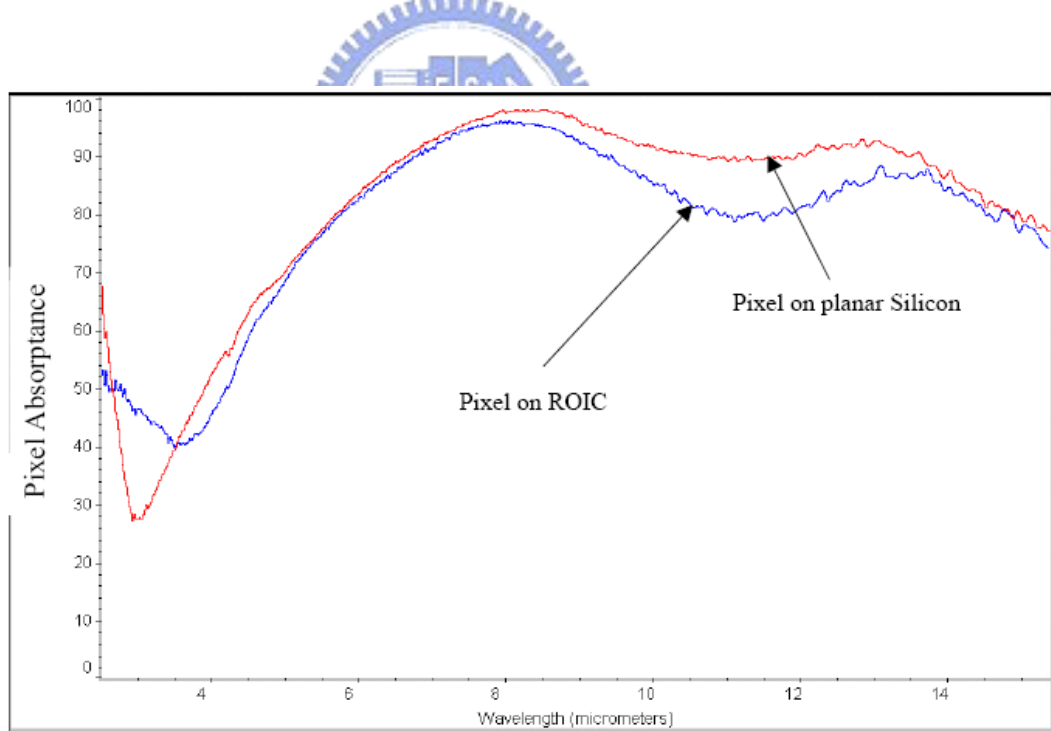


Figure 2-3- 3 pixel absorbance measurements show >80% absorbance over the 8-12  $\mu\text{m}$  spectral band.

### 3.3 Consideration about micromachining technology

The main method of fabricating micro bolometer in MEMS often employs poly silicon [33], silicon nitride [35], and silicon dioxide [36] to serve as structural layer. The key consideration of selecting the material of the structural layer is thermal conductance as we hope the heat absorbed by the sensing layer can be preserved on sensing layer to improve the responsibility of the device. Polysilicon, silicon nitride, and silicon dioxide are suitable for structural layer due to their low thermal conductance which can provide less thermal losses. In bulk micromachining, most fabrication methods employ silicon dioxide or silicon nitride to do structural layer and use TMAH or KOH to etch silicon substrate. Disadvantages in this method are difficult to control the etching depth and to reduce device dimension and less compatible to CMOS processes.

In surface micromachining, the sticking effect and residual stress play an important role in determining whether the microstructures are suspension or collapse during the release process. High compressive stress results in bending structure, so the structure might stick to substrates, thus losing its thermal isolation. On the other hand, high tensile stress might cause cracks in suspended structure. Ideally, the stress must be zero, or practically, it must be low. The most fabrication methods employ polysilicon for the main structure layer and use high temperature annealing to release the stress of whole structure. But the high temperature process also increases the thermal budget of processing and it cannot be used in post processing after IC has finished.

In terms of infrared focal plane array (IRFPA) applications, it requires high fill factor, a large number of pixels, and minimum pixel size to increase array sensitivity and resolution. As the bulk micromachining needs to remove substrate material, the pixel area is inherently large and hard to reduce the pixel size due to fabricating limitation, and the overall area of bolometer array is usually larger than that by surface micromachining.

Thus, surface micromachining is the best candidate than bulk micromachining. In addition, we intend to fabricate bolometer array directly on the top of IC, so surface micromachining becomes the only choice, and, furthermore, the processing temperature is limited to below 400 degrees C.

### 3.4 Consideration about material of sacrificial layer

The sacrificial layer and structural layer in surface micromachining technology are related intimately to each other. They form the main supporting structure of a micro device, and these two layers are also the most important factor for determining whether the whole floating structure is success or failure. The fabricating processes of these layers are necessary to be compatible with each other. Considerations about these two layers are listed below:

➤ Structural Layer

1. Must have good mechanical properties
2. Depending on the application it must have good electrical and thermal properties
3. Resistant to sacrificial layer etchants
4. IC compatible

➤ Sacrificial Layer

1. Must be stable during structural layer deposition and processing
2. Fast etch rate with high selectivity
3. IC compatible

According to preceding statement, the most common combinations of materials for sacrificial and structural layers, and the etchants of sacrificial layers can be chosen and are shown in Table 3.

Microstructure	Sacrificial layer	Etchant
Poly-Si	PSG, BPSG	BOE, HF
CVD Tungsten	LPCVD SiO <sub>2</sub>	RIE
Si <sub>3</sub> N <sub>4</sub>	Poly-Si	KOH
Polyimide	PSG	HF
SiO <sub>2</sub>	Poly-Si	EDP, XeF <sub>2</sub>
Aluminum	Photoresist	O <sub>2</sub> Plasma

Table 3 Most common combinations of materials for structure and sacrificial layers, and sacrificial-layer etchants

Sacrificial Aluminum Etching (SALE) has recently been introduced as a variant fully compatible with standard IC processes. Sacrificial aluminum has been removed for the fabrication of electroplated nickel microstructures [47] or polyimide based thermal microactuators [48-49]. These techniques are IC-compatible in that the structures (including the sacrificial layer) can be built on top of IC substrates. SALE goes one step further in its IC compatibility by exploiting the aluminum based metallization of standard IC processes as the sacrificial material. So far we investigated the application of SALE to commercial ASIC processes of EM Microelectronic Marin SA (EM), ATMEL-ES2, and Austria Mikro Systeme (AMs). The potential of SALE was recently highlighted with the CMOS integration of a thermal pressure sensor microsystem [50] and a miniaturized CMOS-compatible fluid density sensor [51].

Because the sacrificial layer is removed during releasing process, the etching time of the necessity to remove completely the sacrificial layer is always long due to the sacrificial layer covered by large area structural layer. The etchants must diffuse to the under part of the floating membrane and react with the rest of sacrificial layer, and then

the produced reactant must diffuse to outside of the membrane. The etching time is dominated by diffusion mechanism, and it is a waste-time process. We apply wet etching to remove the sacrificial aluminum layer due to its high etching speed as shown in Table 4. Because of diffusion mechanism, the etching speed tends to decrease with the etching time continuing increase. In addition, the etching speed also rises with etching temperature.

The polyimide or photoresist are also popular materials for sacrificial layer, but it must be removed by dry etching, which is a very slowly processing than wet etching and cannot be done by batch mode. Since the longer etching time is necessary for dry etching, the long-term plasma damage on microstructures always occurs, and it also leads to structure bending or plasma charging.



Name	Components, Proportion	T [°C]	r <sub>0</sub> [μm/min]	t <sub>50</sub> [h]	t <sub>150</sub> [h]	t <sub>250</sub> [h]	RPM	t <sub>HB</sub> [min.]
1. Etch No. 11940, Soprelec SA, France	H <sub>3</sub> PO <sub>4</sub> 72.88 w%	30	6.8	7	24	-	3000-4000	5-10
	HNO <sub>3</sub> 2.29 w%	50	68	1	5	14	3000-4000	5-10
	CH <sub>3</sub> COOH 11.37 w%	65	170	0.3	2.5	8	-	-
	H <sub>2</sub> O 13.46 w%	80	340	0.2	1.6	6	-	-
2. Krumm etch	H <sub>3</sub> PO <sub>4</sub> (85%) 80 v%	50	44	1.3	6	12	3000	10
	H <sub>2</sub> O <sub>2</sub> (30%) 10 v%	80	108	0.3	1.7	6	-	-
3. HCl /H <sub>2</sub> O <sub>2</sub>	H <sub>2</sub> O 10 v%	30	500	0.1	0.6	2	3000	5
	HCl(32%) 80 v%	50	600	< 0.1	0.4	1.1	-	-

Table 4 Sacrificial aluminum etchants which processing conditions for reliable purposes

## Chapter 4

### Device thermal simulation

In this section, we used finite element simulator of ANSYS to conduct thermal analysis. First, we used Solid 90 element to build the 3D solid model of bolometer pixel as shown in Figure 2-4-1. The Solid 90 element has 20 nodes with a single degree of freedom, temperature, at each node. The 20-node elements have compatible temperature shapes and are well suited to model 3D geometry. Figure 2-4-2 demonstrates Solid 90 geometry.

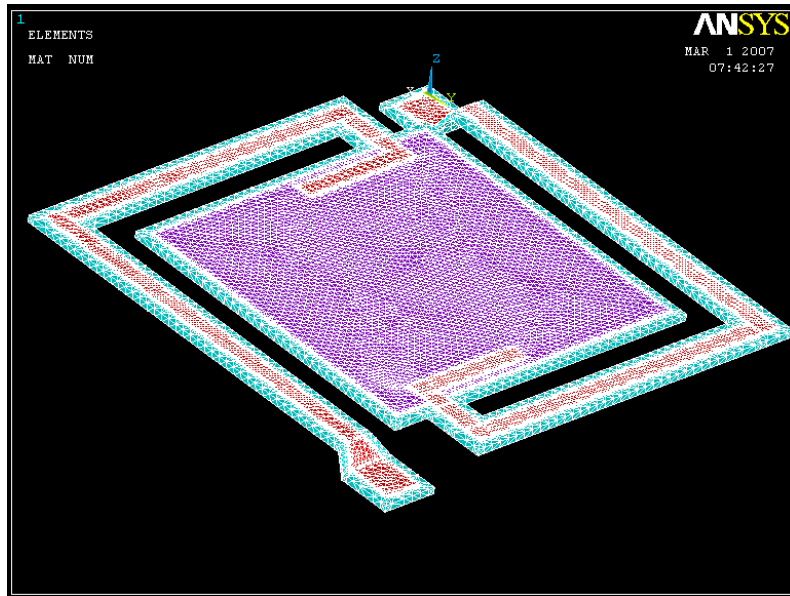


Figure 2-4-13D solid model of bolometer pixel

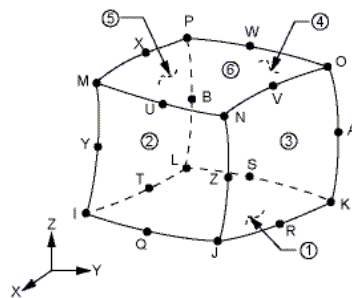


Figure 2-4-2 Solid 90 geometry



The finite element model must be refined enough to accurately model the temperature distribution of the bolometer pixel. To do this, the total number of finite element for the bolometer is larger than 130,000. In addition, we used Radiosity Solver method of ANSYS to simulate object radiation illuminating the bolometer pixel. The Radiosity Solver method works for generalized radiation problems involving two or more surfaces receiving and emitting radiation. However, the calculation of view factor by Radiosity Solver for this 3D finite element model of bolometer pixel needs a very large number of computer resource. This is not efficient in simulating different thermal conditions. In order to simplify this 3D problem and save computer resource, we use 2D element to model 3D structure. In this case, we can achieve more efficient simulation, and the results by 2D model are also accurate as well as that by 3D model. The Shell 131 element is adopted to analyze thermal distribution of the bolometer pixel. Figure 2-4-3 shows the Shell 131 geometry. SHELL131 is a 3-D layered shell element having in-plane and thru-thickness thermal conduction capability. The element has four nodes with up to 32 temperature degrees of freedom at each node. The conducting shell element is applicable to a 3-D, steady-state or transient thermal analysis. The quadratic variation in temperature through each layer of shell 131 is chosen to exactly estimate the thermal distribution. The 2D model, induced 3D model, and 3D finite element model are illustrated in Figure 2-4-4 (a), (b), and (c), respectively.

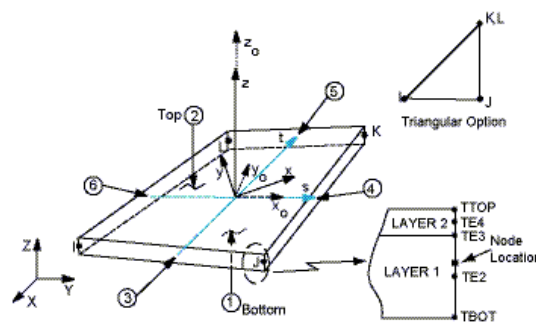
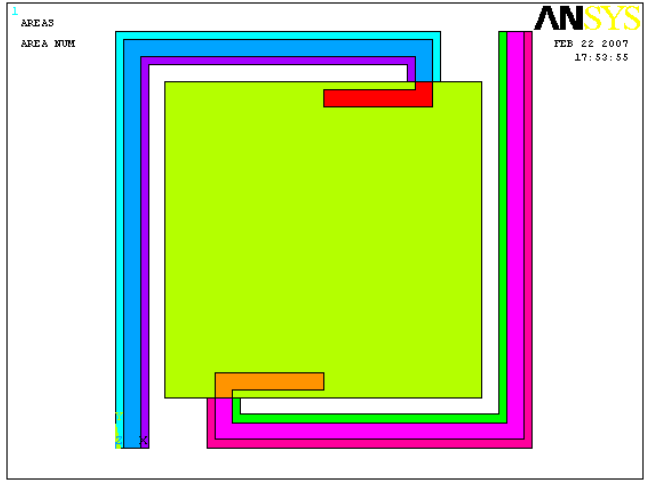
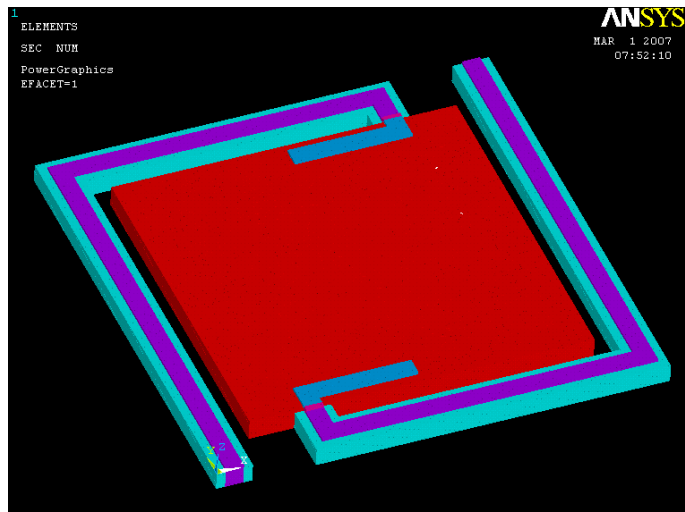


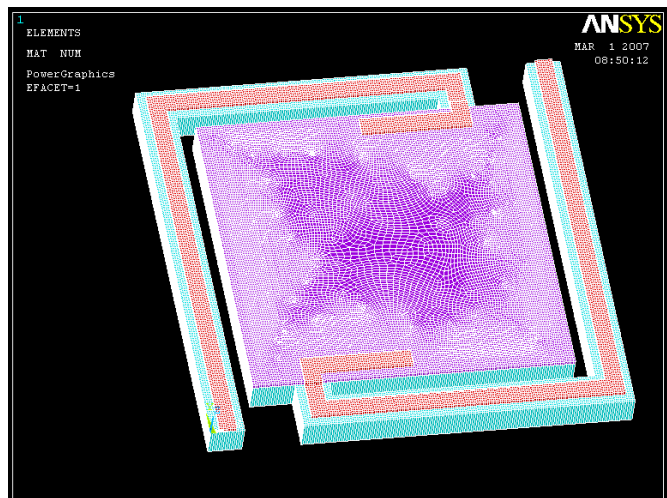
Figure 2-4-3 Shell 131 geometry



(a)



(b)



(c)

Figure 2-4-4(a) 2D model, (b) 3D model, and (c) finite element model

In 2D model, we divided the bolometer into five regions to model different layers as listed in Table 5.1.

Section	Thickness (um)	Material	Section)offset	Element type
Region 1	0.7	SiO <sub>2</sub>	0.35	Type 1
Region 2	0.1	Ta	0.3	Type 2
	0.7	SiO <sub>2</sub>		
Region 3	0.1	$\alpha$ -Si	0.3	Type 3
	0.7	SiO <sub>2</sub>		
Region 4	0.1	Ta	0.25	Type 4
	0.1	$\alpha$ -Si		
	0.7	SiO <sub>2</sub>		
Region 5	0.2	Ta	0.25	Type 2
	0.7	SiO <sub>2</sub>		

Table 5.1 Five regions of bolometer pixel

The nodal plane controlled by section offset parameters is designed on the top surface of the silicon dioxide layer. In this condition, these different layers can correctly connect with each other. Besides, the position of nodal plane is very important to calculate derived solutions. If the nodal plane position is set incorrectly, we may get some erroneous data. The material parameters of different layers used in this solid model adopt um-SI unit and are listed in Table 5.2.

	SiO <sub>2</sub>	$\alpha$ -Si	Ta
Density (Kg/um <sup>3</sup> )	$2.2 \times 10^{-15}$	$2.33 \times 10^{-15}$	$1.66 \times 10^{-14}$
Specific heat (J/Kg.K)	1000	753	140
Thermal conductivity (W/um.K)	$1.1 \times 10^{-6}$	$3 \times 10^{-6}$	$5.75 \times 10^{-5}$

Table 5.2 material parameters for different layers

With respect to loading and boundary conditions, we apply the heat flux ( $1e-9$  W/ $\mu\text{m}^2$ ) to the top of sensing layer instead of radiation input, and also apply the temperature of  $300^\circ\text{C}$  to the two leg ends. The uniform temperature is set to  $300^\circ\text{C}$  to simulate background temperature effect and serve as initial condition of thermal simulation. From chapter 2 discussion, the heat convection and heat conduction of thermal transferences dominate the thermal characteristics of bolometer devices. If radiation effect must be included, we can set the emissivity of sensing layer to 0.8 within the wavelength of  $6 \sim 15$   $\mu\text{m}$  obtained from Figure 2-4-3. However, the radiation effect is neglected here due to its very slight influence. We also simulated the bolometer pixel in two different environments such as air condition and vacuum package, and set the simulation load time schedule as Table 5.3. It should be noted that the load step 1 is designed to obtain the stationary temperature after loading heat flux on the top of sensing layer. The load step 3 is designed to simulate the transient effect after stop loading heat flux, and, in this step, we can observe the variation of the temperature and thermal flux distribution on the solid model due to heat conduction and convection. In addition, the load step 2 must be involved in the air condition due to the transition of changing load, or you will get some error messages.

In air environment, the air convection coefficient applied to all surfaces of the bolometer pixel is set to  $20e-12$  W/ $\mu\text{m}^2/\text{K}$ . In order to compare with other reports, these several preceding simulation parameters are referred to several related literatures [52-54].

Environment	Load step 1 (s)	Load step 2 (s)	Load step 3 (s)
	10 time steps	10 time steps	25 time steps
Vacuum	5		5~5.005
Air	5	5~5.000005	5.000005~5.005

Table 5.3 Simulation load time schedule

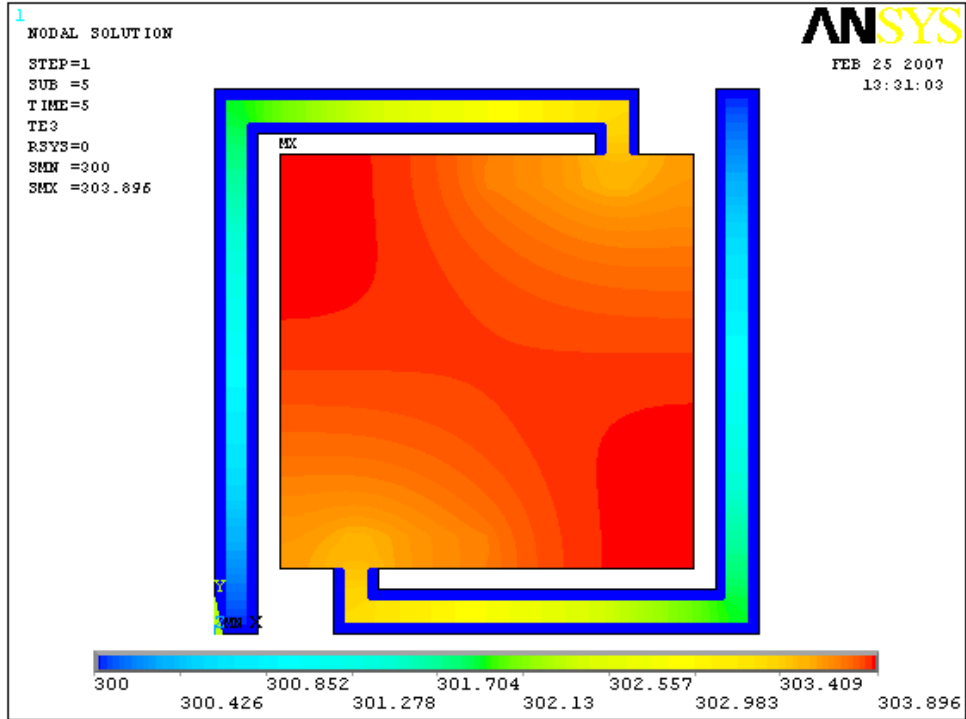
From our several thermal simulations, the global mesh size of 0.5  $\mu\text{m}$  is not enough to exactly estimate the temperature distribution, so the mesh size of 0.25  $\mu\text{m}$  is adopted in the following simulations. The contour plots of TE3 and TTop temperature distribution are shown in Figure 2-4-5 (a) and (b), respectively. The TE3 indicates the temperature distribution at the location of 0.1  $\mu\text{m}$  above the silicon dioxide surface. And the TTop indicates the temperature distribution on the top of the bolometer pixel. The maximum increasing temperature while applying heat flux on the sensing layer is 3.896 K. Figure 2-4-5 (c) shows the vector plot of the temperature gradient distribution on the nodal plane. The arrow direction of the temperature gradient is from high temperature to low. It should be noted that the four parts with red circular mark have the highest temperature gradient due to the occurrence with the largest thermal flux. The thermal flux distributions on nodal plane and overall nodes are presented in Figure Figure 2-4-6 (a) and (b), respectively. The minimum and maximum values of thermal flux on nodal plane are  $3.82\text{e-}10$  ( $\text{W}/\mu\text{m}^2$ ) and  $1.51\text{e-}7$  ( $\text{W}/\mu\text{m}^2$ ), and the maximum value is less than that of overall nodes which is  $5.39\text{e-}6$  ( $\text{W}/\mu\text{m}^2$ ). It means that most heat is conducted by the meat line of the tantalum and less heat is conducted by supporting layer. The four inner corners of two legs have the largest heat flux, but the four outer corners have the less one. This is because, at the inner corners, the conduction path is shorter than that at outer part. The vector plots of thermal flux on nodal plane and enlargement of sub model are plotted in Figure 2-4-7 (a) and (b). We can observe the main conduction path on the top of silicon dioxide layer. With respect to air condition, the contour plot of the TE3 and TTop temperature distribution are shown in Figure 2-4-8 (a) and (b), respectively. The maximum increasing temperature in the air condition is 3.544 K which is less than that in vacuum package by 0.352 K. The maximum temperature is lower due to the air convection and conduction. Besides, thermal flux distribution on nodal plane, and 3D thermal flux distribution on each node are demonstrated in Figure 2-4-9(a) and (b). The

maximum value of thermal flux on nodal plane in air condition is less than that in vacuum package by  $1.1e-8 \text{ W/um}^2$ , and the maximum thermal flux of overall node in air condition is also less than that in vacuum package by  $3.9e-7 \text{ W/um}^2$ . Because the air convection takes some portion of heat from the bolometer surface away, the thermal flux of the metal layer is reduced.

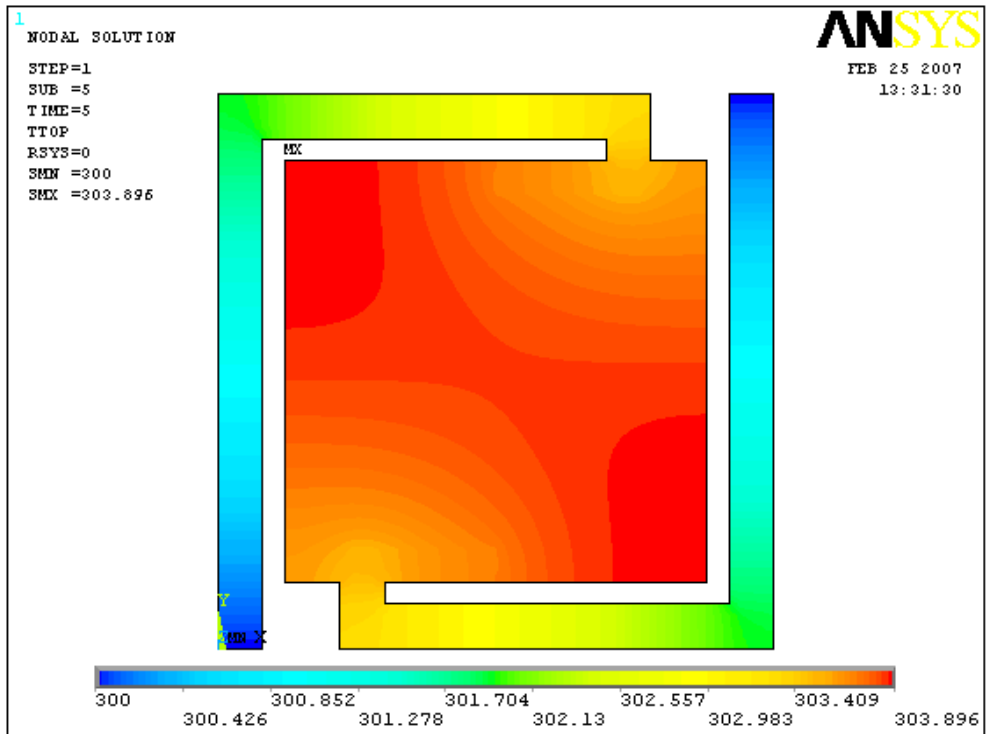
So far, the most use of metal line in bolometer applications is Cr/Ni. Some literals [52] adopt the thermal conductivity of  $13 \text{ W/mK}$  for Cr/Ni, but some literals [53] adopt the value of  $90.7 \text{ W/mK}$ . From our survey, the thermal conductivity of chromium and nickel are  $93.7 \text{ W/mK}$  and  $90.7 \text{ W/mK}$ . Thus we take the value of  $90.7 \text{ W/mK}$  to be the thermal conductivity of the metal line in the following thermal simulation in comparison with the preceding simulation using tantalum metal line. Figure 2-4-10 (a) and (b) show the TTop temperature and Temperature Gradient distribution in the vacuum package condition for Ni/Cr metal line. And Figure 2-4-11 (a) and (b) present the Thermal flux distribution on nodal plane, and 3D thermal flux distribution on each node in the vacuum package. The increasing temperature in this condition is about  $2.765 \text{ K}$  which is less than that in using Ta metal line by  $1.131 \text{ K}$ . The maximum thermal flux in using Ni/cr metal line is larger than that using Ta by  $6.7e-7 \text{ W/um}^2$  due to Ni/Cr having higher thermal conductivity. In respect of including air convection for Ni/Cr case, Figure 2-4-12 (a) and (b) show the TTop temperature and Temperature Gradient distribution in the air condition. And Figure 2-4-13(a) and (b) present the Thermal flux distribution on nodal plane, and 3D thermal flux distribution on each node. We also observe that most portion of thermal flux is on the metal layer and fewer portions are on other layers. This phenomenon is similar to the case of using Ta metal line. Besides, we take the central node of the top surface of the bolometer to estimate the thermal time constant of the device at various conditions. If the thermal conductivity of the metal line is less than that of Ta, e.g.  $1.3E-5 \text{ W/um K}$  in [52], the values of thermal time constant in the Vacuum package and Air

condition are 10.21 ms and 6.55 ms, respectively. The  $T_{Top}$  temperature distribution, thermal flux distribution on nodal plane, and thermal flux distribution on each element in Vacuum and Air condition are shown in Figure 2-4-14 and Figure 2-4-15, respectively. In Figure 2-4-14 (c) and Figure 2-4-15, we can observe that the maximum thermal flux occurs at the part1 in vacuum package and at the part2 in air condition. The part 1 is located at the first rectangular inner corner, and the part2 is at the second one. Besides, it should be noted that the thermal loss of the supporting layer using metal line with lower thermal conductivity is larger than that using larger thermal conductivity of metal line. This is because the thermal loss of the supporting layer is large enough and cannot be neglected. Consequently, the thermal loss by the supporting layer and air convection has larger influence on device thermal characteristics for lower metal thermal conductivity than for higher thermal conductivity of metal.

The comparison of the thermal time constant at different conditions is shown in Table 4. In addition, the Transient of temperature and thermal flux of the central node on the top of bolometer pixel in air and vacuum conditions are also shown in Figure 2-4-16.



(a)



(b)



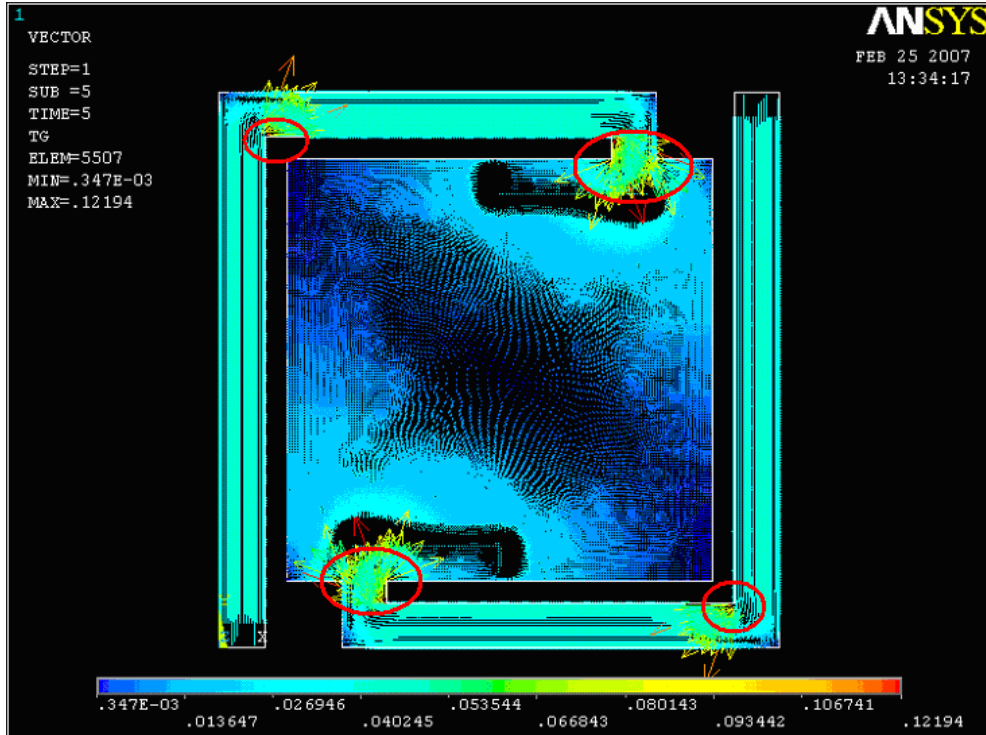
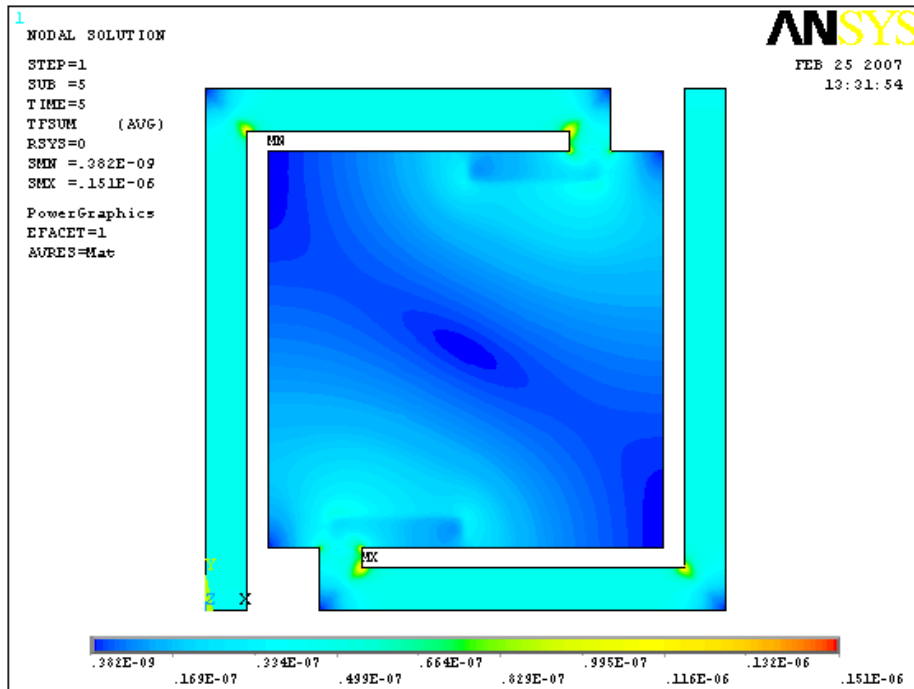


Figure 2-4-5(a) TE3 temperature, (b) TTop temperature, and (c) Temperature Gradient distribution in the vacuum package condition



(a)

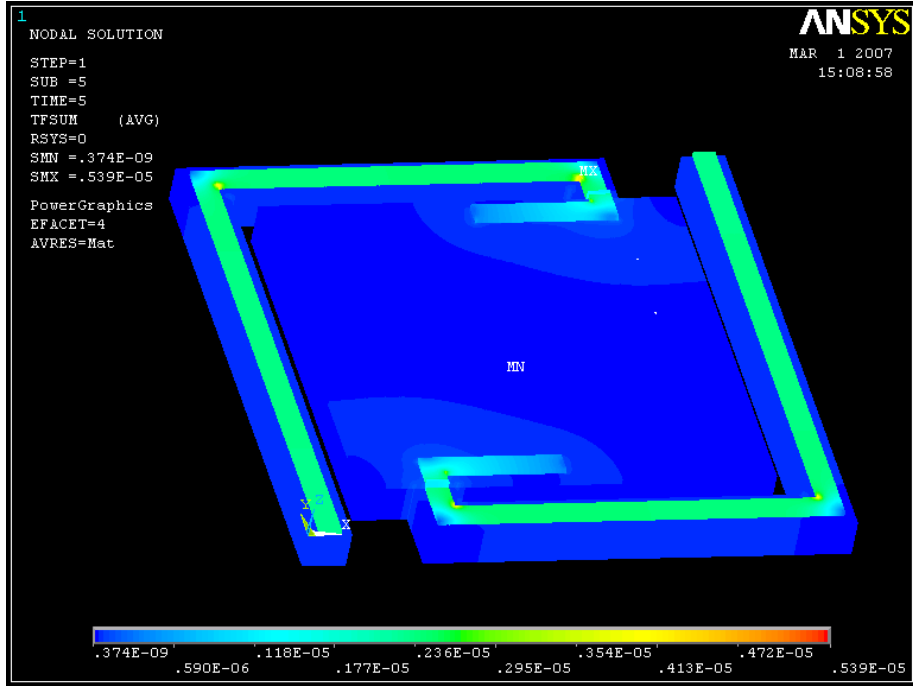
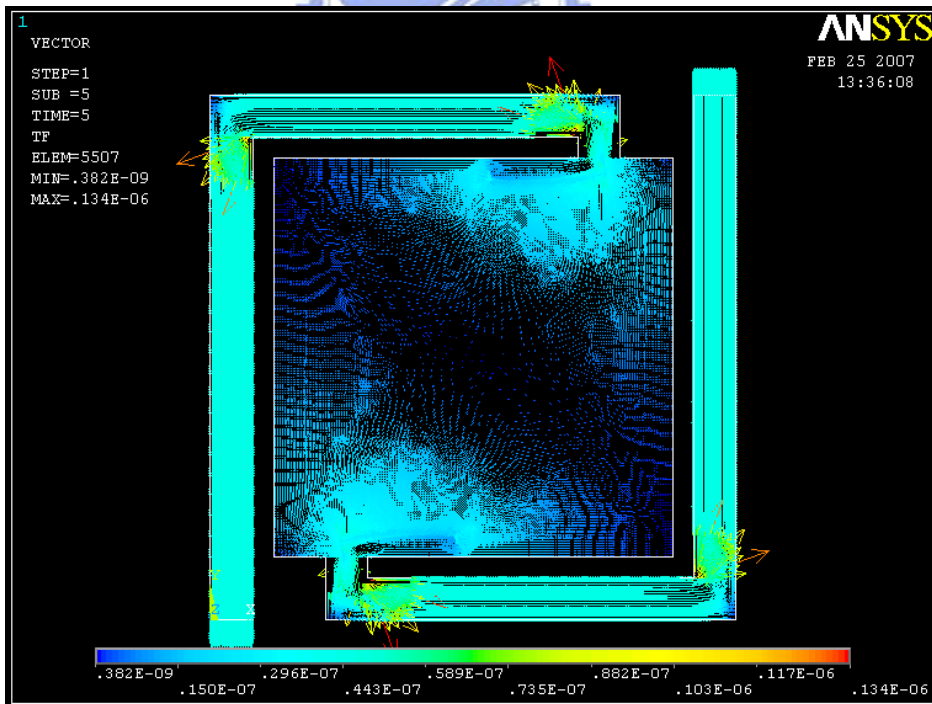


Figure 2-4-6(a) Thermal flux distribution on nodal plane, and (b) 3D thermal flux distribution on each node



(a)

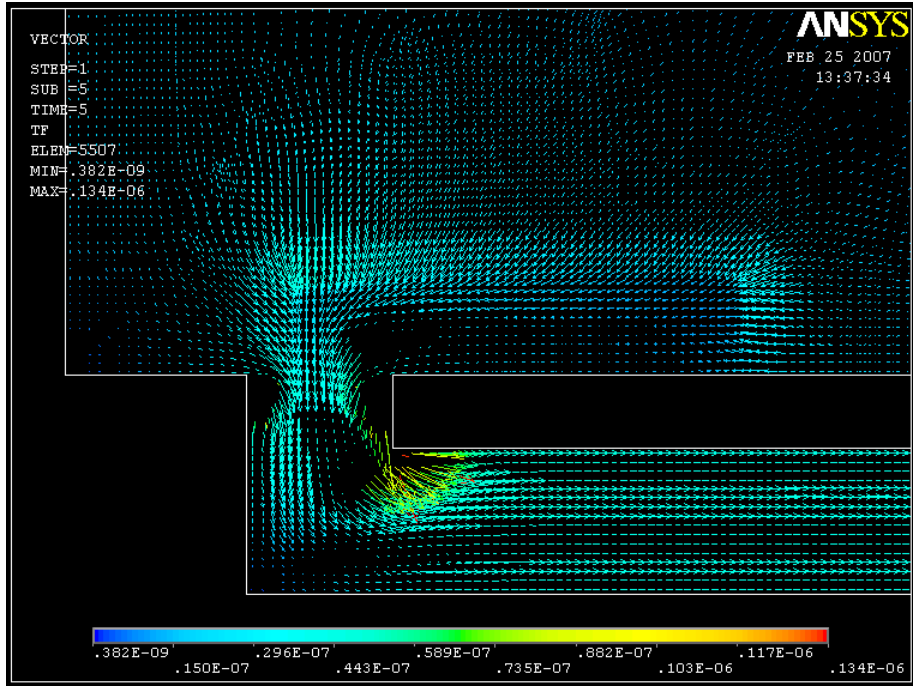
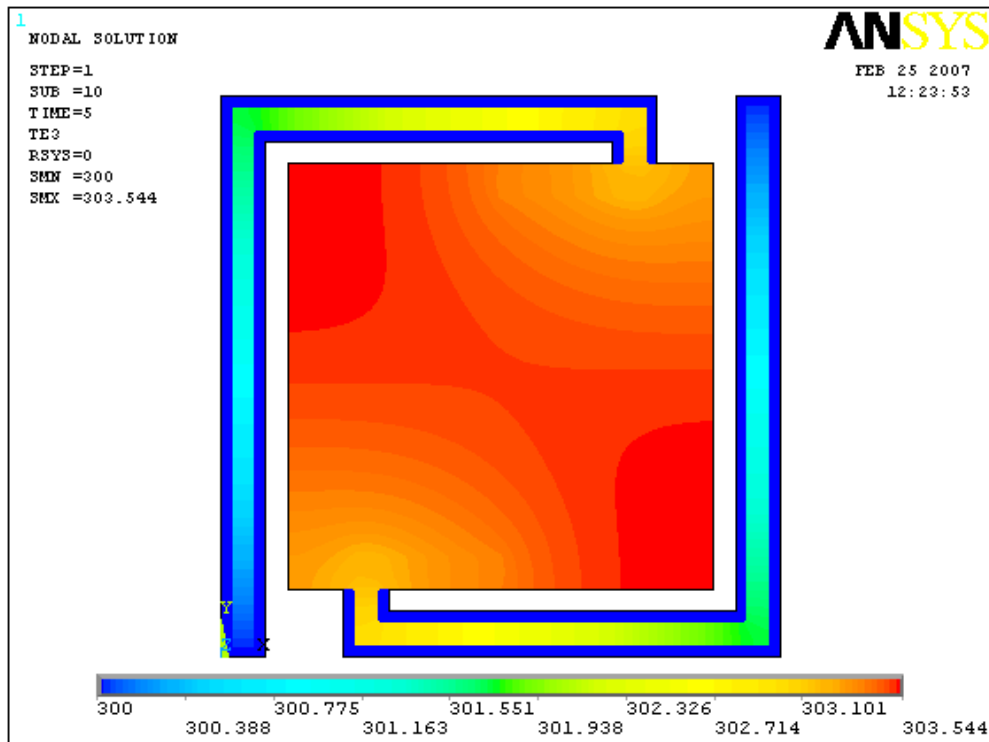


Figure 2-4-7(a) Vector plot of thermal flux on nodal plane, and (b) enlargement of the submodel



(a)

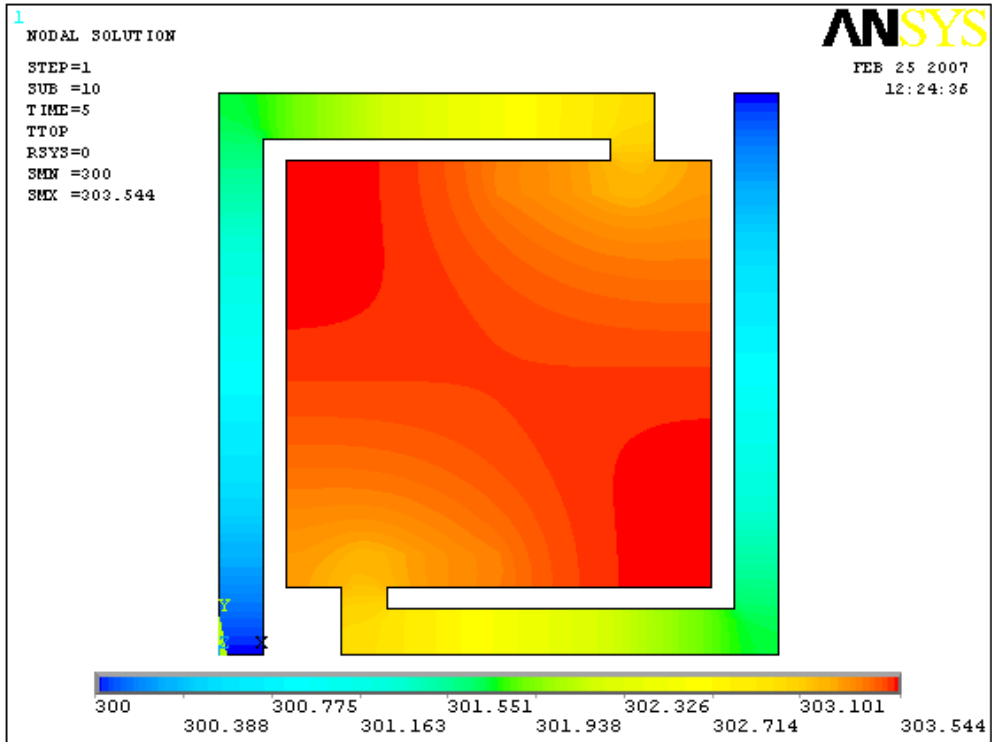
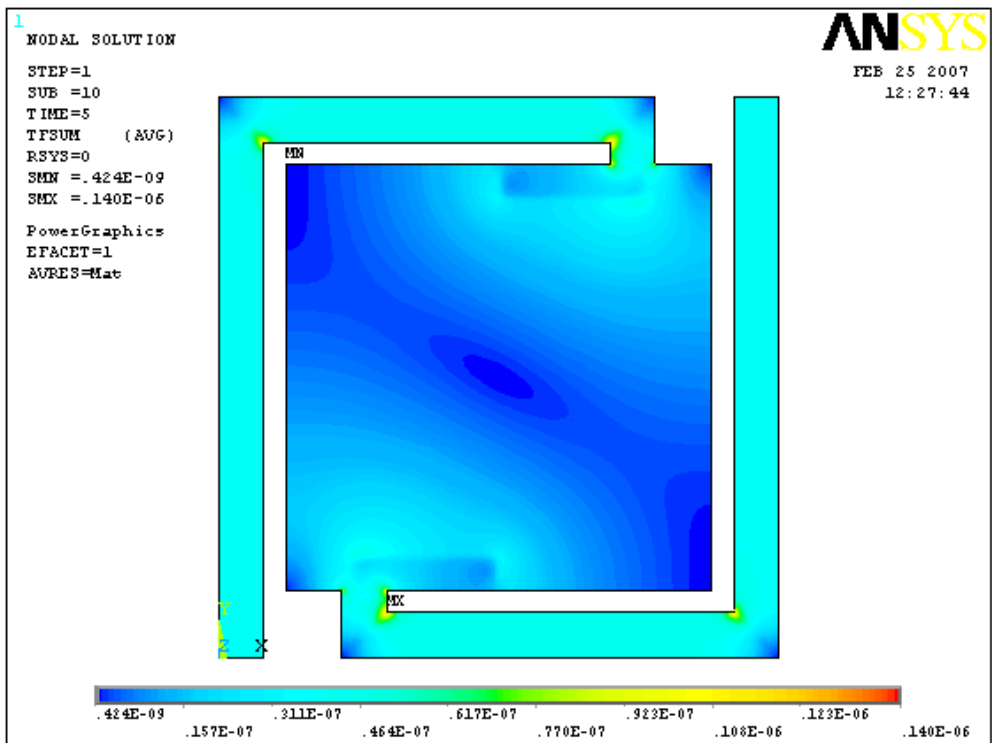


Figure 2-4-8 (a) TE3 temperature and (b) TTop temperature distribution in the air condition



(a)

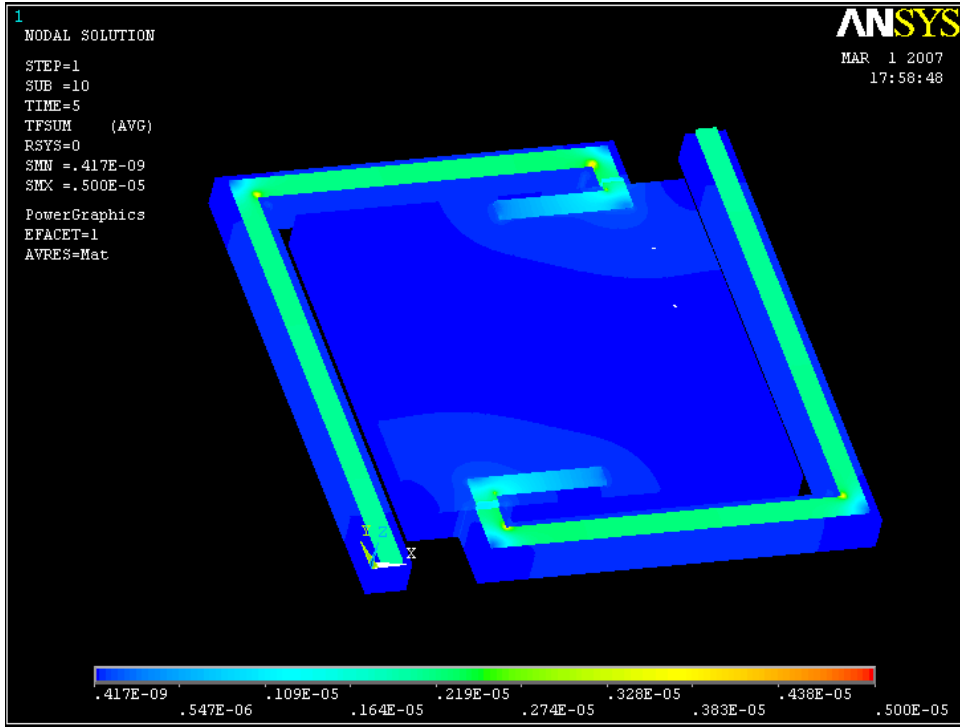
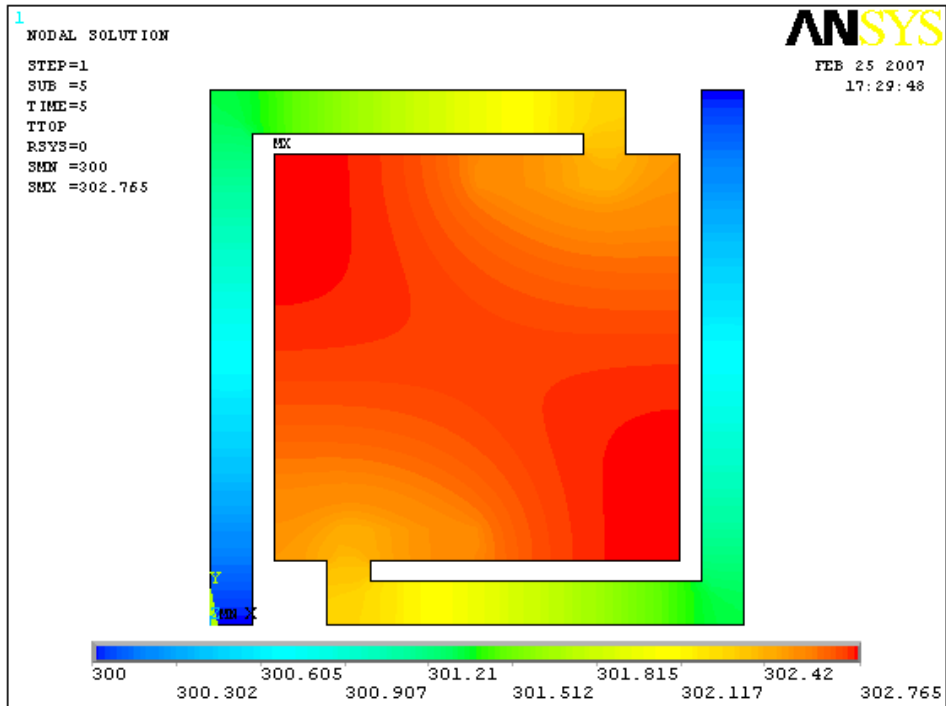


Figure 2-4-9(a) Thermal flux distribution on nodal plane, and (b) 3D thermal flux distribution on each node in the air condition



(a)

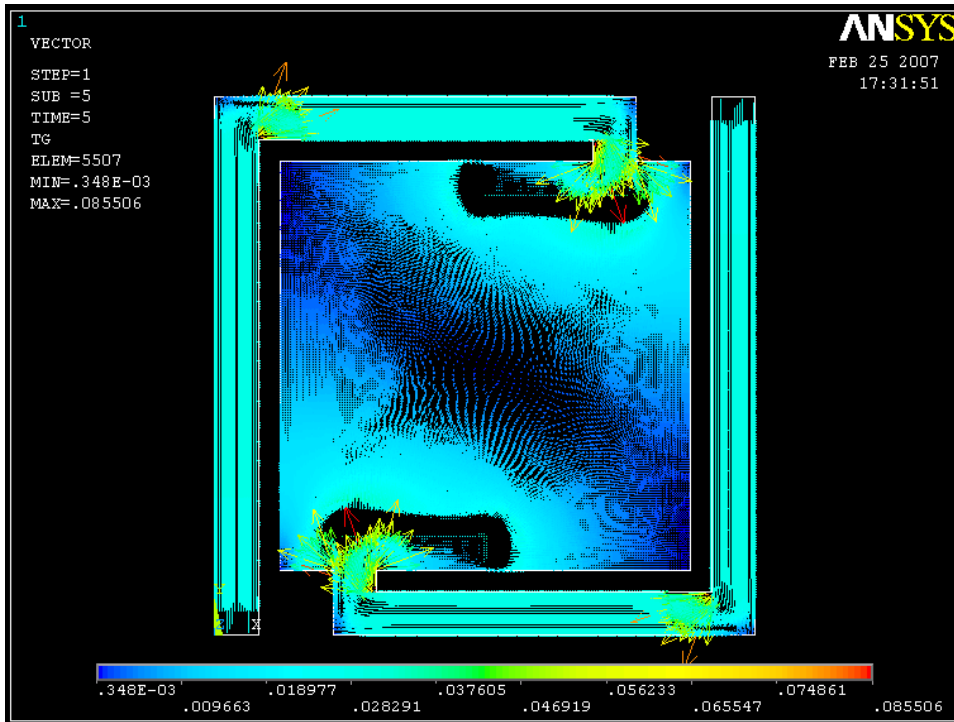
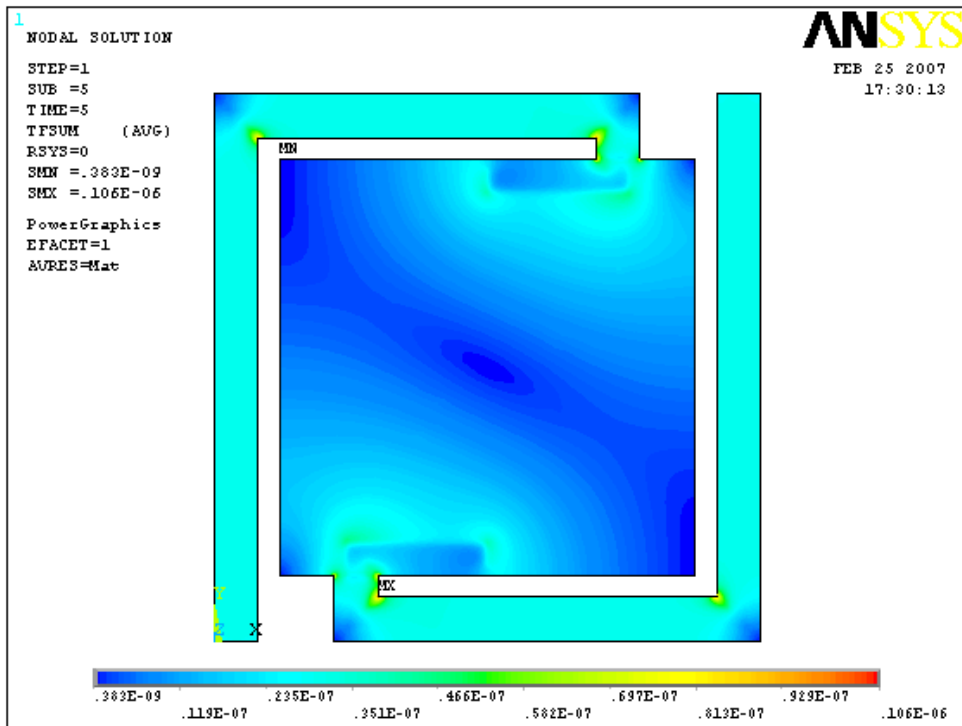


Figure 2-4-10(a) TTop temperature, and (b) Temperature Gradient distribution in the vacuum package condition



(a)

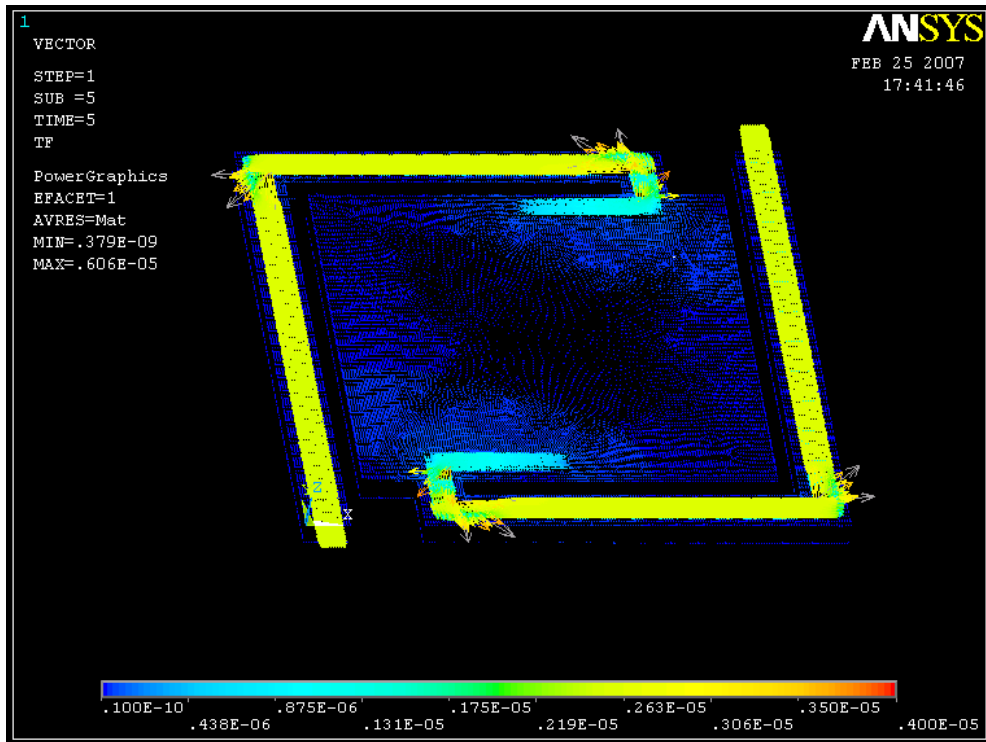
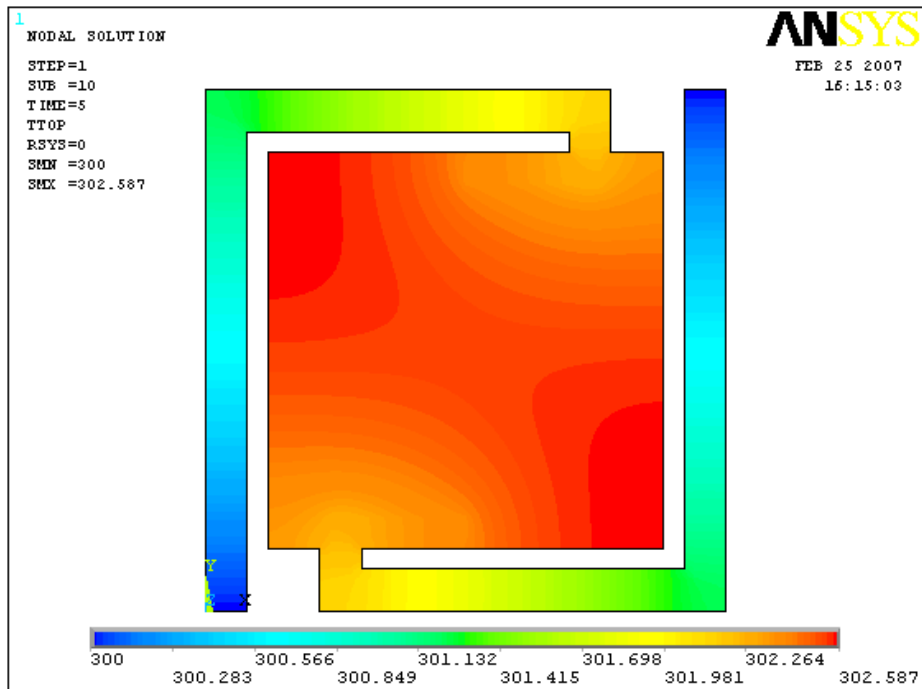


Figure 2-4-11 (a) Thermal flux distribution on nodal plane, and (b) 3D thermal flux distribution on each node in the vacuum package



(a)

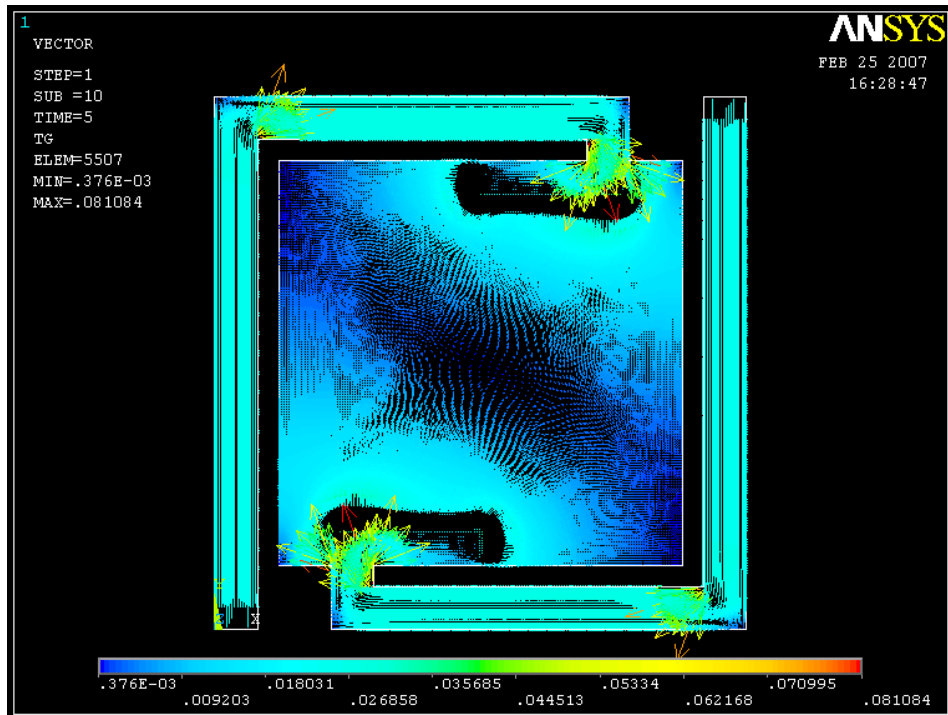
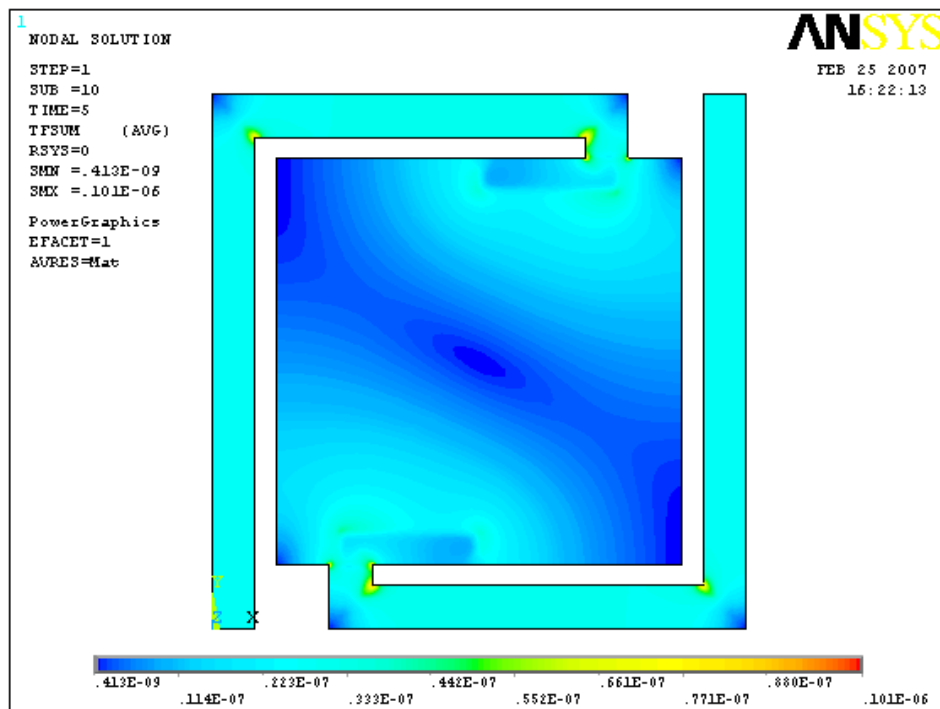


Figure 2-4-12(a) TTop temperature, and (b) Temperature Gradient distribution in the air condition



(a)



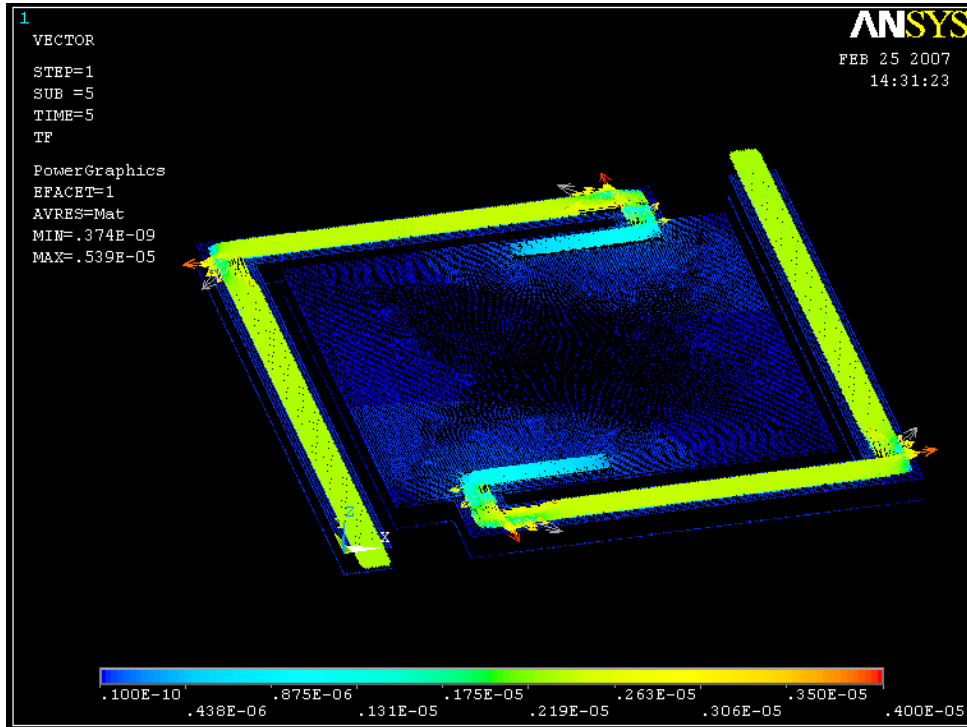
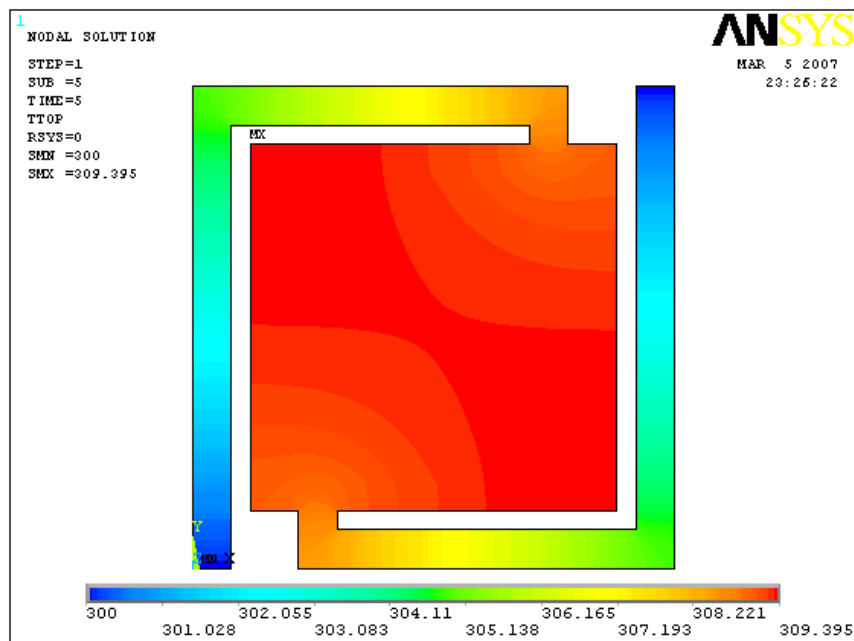
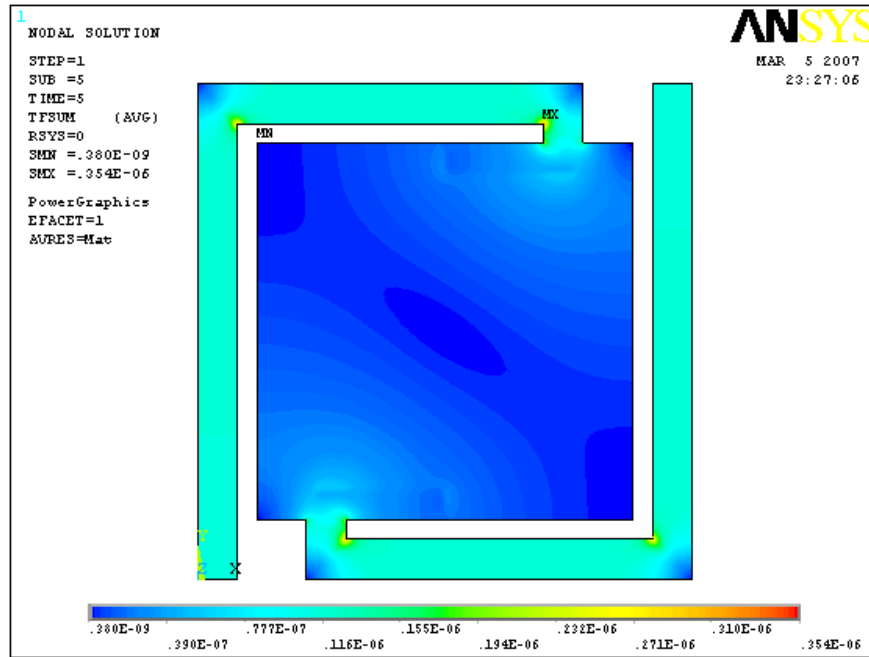


Figure 2-4-13(a) Thermal flux distribution on nodal plane, and (b) 3D thermal flux distribution on each node in the air condition



(a)



(b)

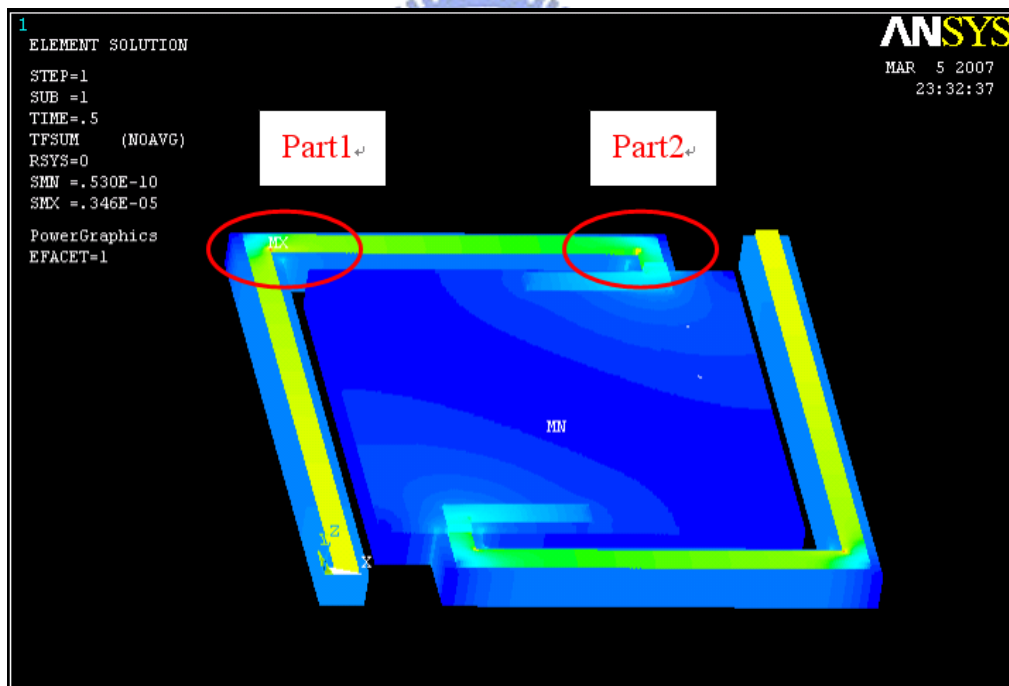
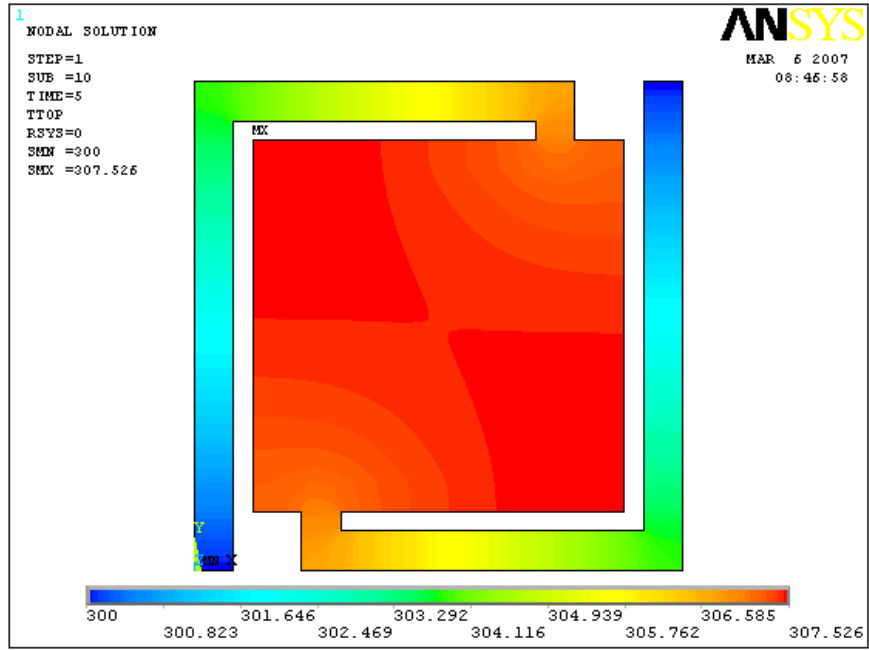
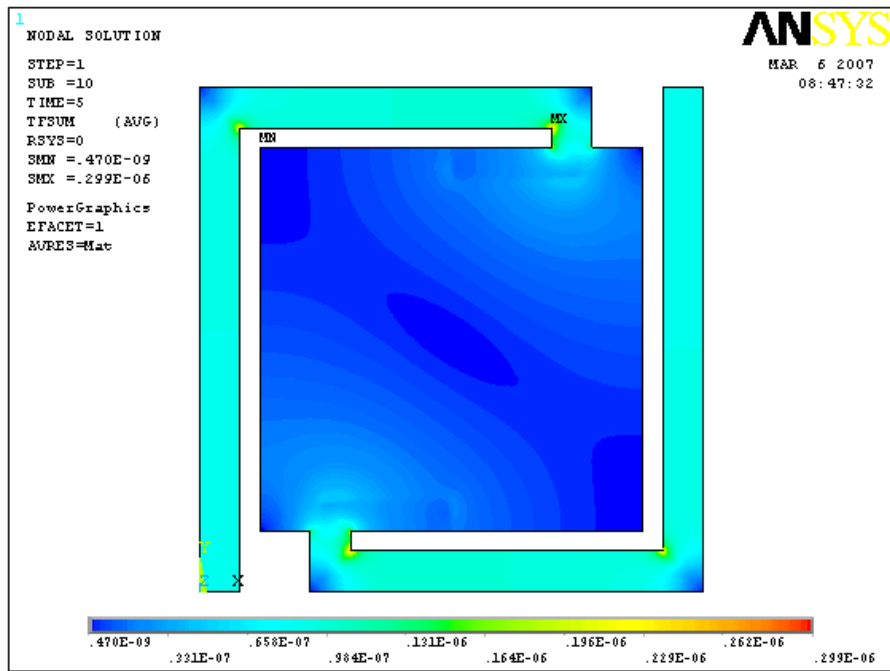


Figure 2-4-14 (a) TTop temperature distribution, (b) Thermal flux distribution on nodal plane, and (c) Thermal flux distribution on each element for the vacuum condition



(a)



(b)

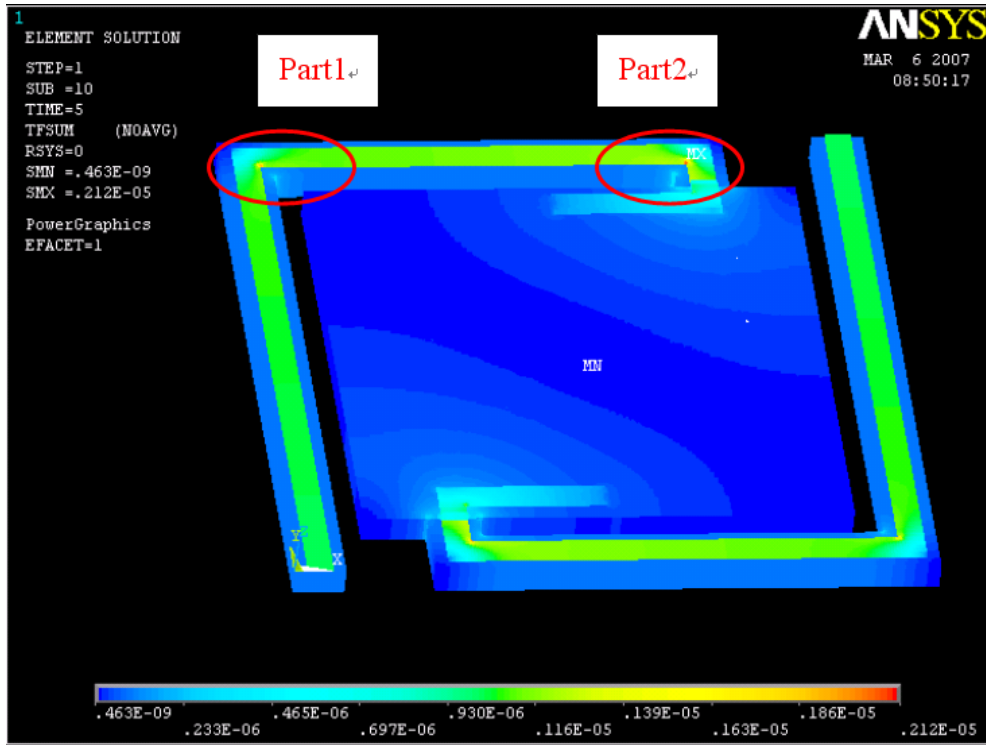
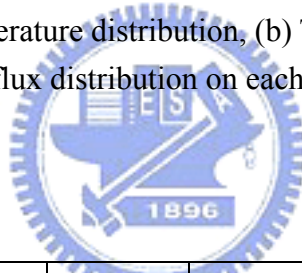
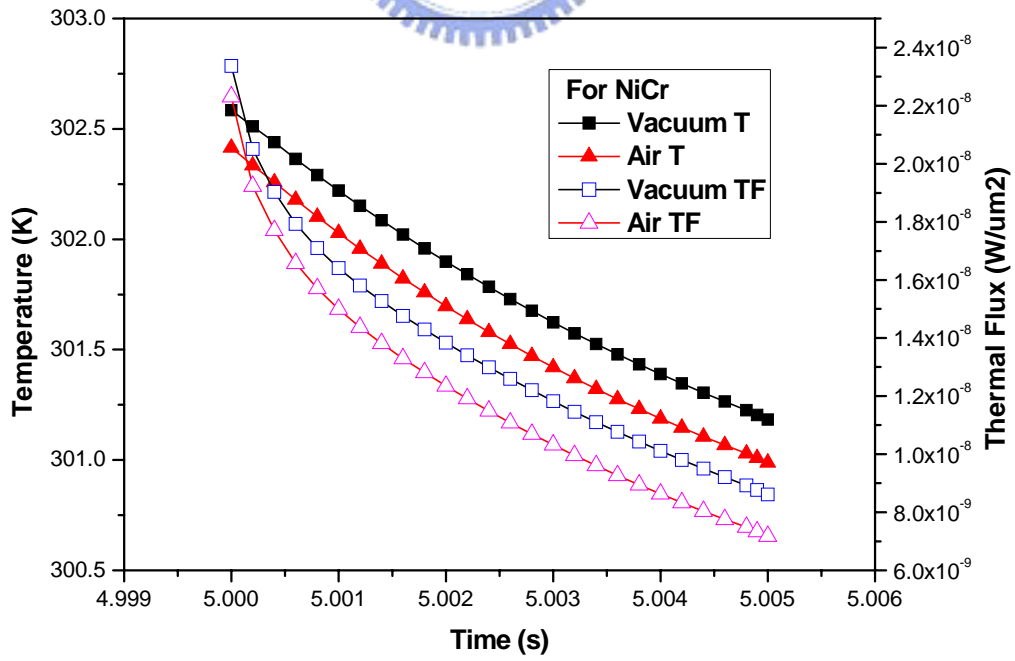
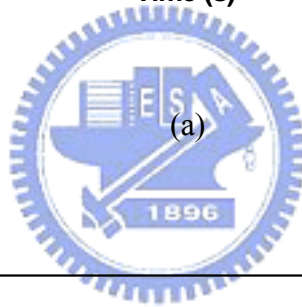
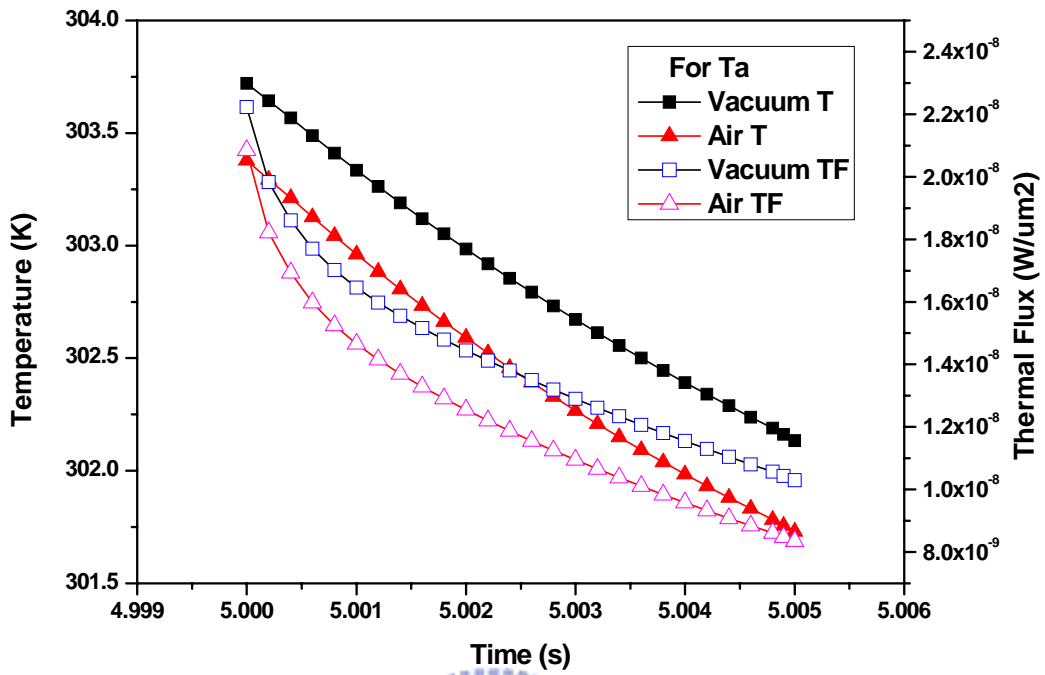


Figure 2-4-15(a) TTop temperature distribution, (b) Thermal flux distribution on nodal plane, and (c) Thermal flux distribution on each element for the Air condition



	Thermal Conductivity (W/um.K)	Density (Kg/um <sup>3</sup> )	Specific heat (J/Kg.K)	Environment	Thermal time Constant (ms)	Temperature Increase (2657 node) At steady state
Hear flux loading of 1E-9 W/um <sup>2</sup> , Air convection 20E-12 W/um <sup>2</sup>						
Ta	5.75E-5	1.66E-14	140	Vacuum	4.15	3.720
Ta	5.75E-5	1.66E-14	140	Air	3.45	3.379
Cr/Ni	9.07E-5	8.9E-15	440	Vacuum	2.97	2.584
Cr/Ni	9.07E-5	8.9E-15	440	Air	2.60	2.415
Metal	1.3E-5	1.66E-14	140	Vacuum	10.21	9.233
Metal	1.3E-5	1.66E-14	140	Air	6.55	7.386

Table 4



(b)

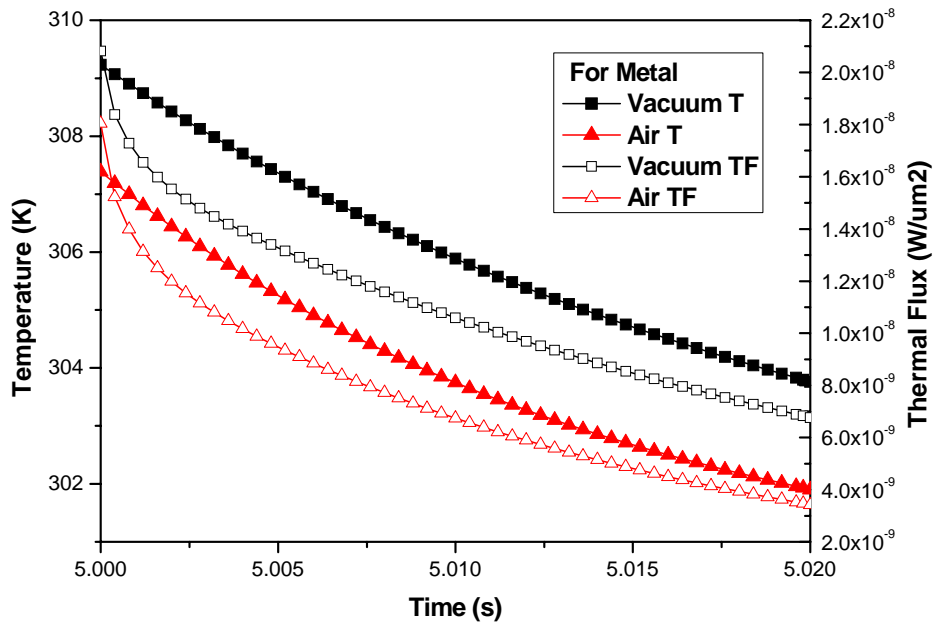
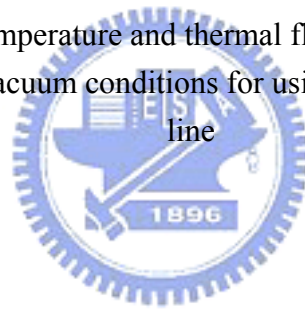


Figure 2-4-16 Transient of temperature and thermal flux of the central node on the top of bolometer pixel in air and vacuum conditions for using (a) Ta, (b) Ni/Cr, and (c) Metal line



## Chapter 5

### Device fabrication

#### 5.1 Processes of bolometer array

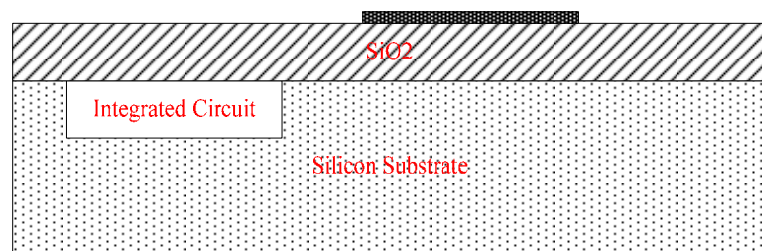
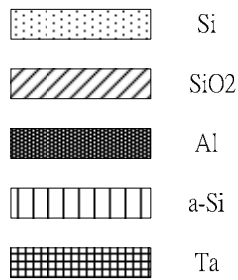
To integrate with CMOS circuits, the temperature of the whole fabricating process must be below 400°C. In this research, we proposed a new fabrication process that had the lower processing cost, the higher processing reliability, and the less processing steps than that of other present microbolometers. The basic process steps necessary to fabricate the microbolometer are briefly described in the following and shown in Figure 2-5-1. First, 500nm-thick PECVD silicon dioxide is grown on silicon wafer as an isolation layer. Next, 30nm-thick aluminum deposited by thermally evaporating approach is formed and patterned to serve as a mirror layer. Before next step, the mirror layer has to be annealed at 350°C to alleviate thermal stress during sequential depositing dielectric layers. In this processing step, the surface of the mirror layer is still smooth. Then, 50nm-thick PECVD silicon dioxide is grown on mirror layer as a passivation layer protecting mirror layer from being etched during release-etching process. Before the following step, the sputtered thick aluminum to a thickness of about 2.5μm is implemented and patterned to make a connection between the substrate contact (anchor) and the active region on the thermally isolated membrane, and this aluminum film also serves as a sacrificial layer due to its good wet-etching selectivity with semiconductor dielectric film [26]. In addition, the suspension gap of 2.5μm-height is designed to make an optical quarter wavelength cavity which increases the IR absorption in the range of 8~14 μm. Before the next thermal procedure, the annealing process with the temperature of 350°C for one hours must be conducted to decrease the non-uniform residual stress of the microbolometer structure and to alleviate the thermal stress during the following dielectric film depositing processes. Next, 500nm-thick PECVD silicon dioxide is deposited and patterned on the sacrificial layer as a structural layer, and the processing temperature of the PECVD oxide

is about 300°C. Then, 50nm-thick PECVD n+ amorphous silicon deposited using the mixture gases of PH<sub>3</sub>, SiH<sub>4</sub> and H<sub>2</sub> at the temperature of 250°C is made for the sensing layer. Besides, sputtered silicon germanium oxide is another candidate for TCR materials, and it can substitute for amorphous silicon in this proposed microbolometer structure. In the next step, we use lift-off lithography technique to define the metal line locations, and then sputtered tantalum of a 100nm thickness is deposited. The metal line pattern is formed after using acetone to remove photo-resist.

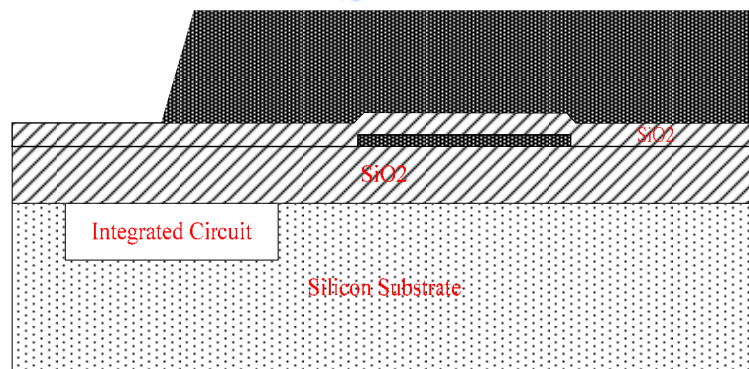
Finally, the microstructures are released by a three-steps process [27],[55] : (1) Etching of the sacrificial layer of aluminum, (2) Rinsing, and (3) Drying. Wet aluminum etchants use the weight proportion of HCl:H<sub>2</sub>O<sub>2</sub> = 10:1 due to its several advantages of high etching rate at room temperature and high wet-etch selectivity with dielectric materials. In order to guarantee the sacrificial aluminum layer to be fully removed and prove the excellent wet-etching selectivity, these microstructures are immersed in the aluminum etchants for six hours with respect to the pixel size of 50µm x 50µm, and it can be seen that the whole structure does not be destroyed absolutely. Next, rinsing the microstructures in acetone (ACE) solution effectively removes the etchants from the under membranes. However, the elimination of etchants from inside the microstructures relies on diffusion mechanism, which is a slow process. In our experience, ten minutes is enough for the proposed structure. After that, for the sake of alleviating the sticking effect, isopropyl alcohol (IPA) solution having lower surface tension replaces ACE. Drying of the delicate microstructures is an important issue for whether the device is successful or failure. In order to obtain high throughput and low cost, this study used hot plates to heat and dry the microstructures in this drying step and also obtained very high yield. From our experience, the temperature of hot plate about 70°C ~ 80°C for IPA or methanol solution can achieve the best results, reaching the yield of 99% or more. If the drying temperature is too high, too much vapor of IPA or methanol under the membranes



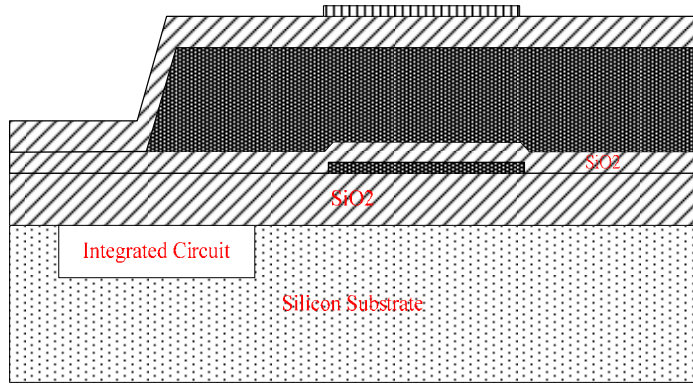
produces at a very short time and then causes serious destruction to the membrane structure or it distorts the microbolometer structures. On the contrary, the lower drying temperature gives rise to the membrane being apt to stick the substrate due to sticking effect.



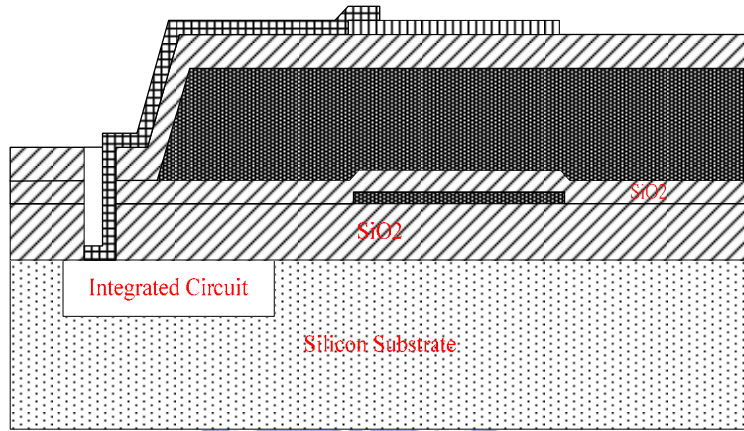
(a)



(b)



(C)



(d)

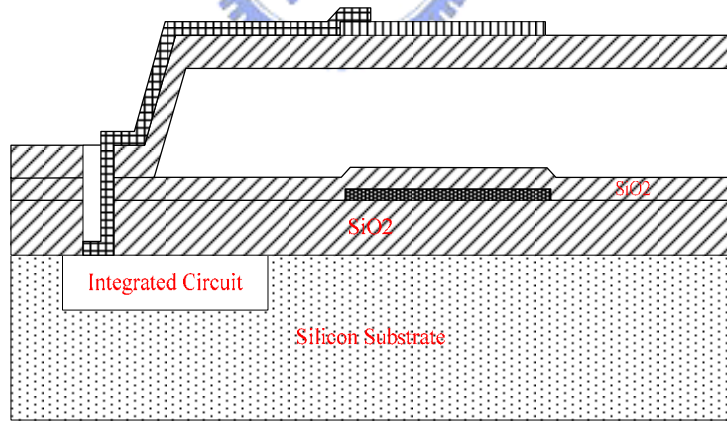


Figure 2-5-1(a) ~ (e) Processing flow of bolometer

## 5.2 Detailed processing list

1. (100) orientation silicon wafer
2. Initial cleaning
3. 500nm SiO<sub>2</sub> was grown by PECVD at temperature of 300°C
4. 30nm aluminum was deposited by thermal coater at 30 ~ 40 °C
5. Mask #1: define mirror region
6. Aluminum of mirror was etched by wet etching  
(HNO<sub>3</sub> : CH<sub>3</sub>COOH : H<sub>3</sub>PO<sub>4</sub> : H<sub>2</sub>O = 2 : 9 : 50 : 10)
7. Sample annealed in furnace at temperature 350 °C for one half hour
8. 50nm SiO<sub>2</sub> was deposited by PECVD at temperature 300°C
9. 2.5um aluminum was deposited by sputter approach at 30 ~ 40 °C
10. Mask # 2: defined sacrificial layer region
11. Aluminum of sacrificial layer was etched by wet etching
12. 400°C anneal in furnace about one hour
13. 500nm SiO<sub>2</sub> was deposited by PECVD at temperature 300°C
14. Mask # 3: defined structural layer region
15. SiO<sub>2</sub> was etched by HDPRIE
16. 50nm n+ amorphous silicon was deposited by PECVD at 250°C
17. Mask # 4: define sensing layer region
18. Amorphous silicon was etched by HDPRIE
19. Mask # 5: defined metal line region
20. 100nm tantalum was deposited by sputter
21. Lift off by ACE
22. Release processes
  - a. Etch sacrificial layer (Al) → b. ACE substitution → c. Methanol substitution
  - d. Hot plate drying

### 5.3 Some important considerations about drying process

#### 5.3.1 Methods of suppressing the sticking effect during release process

Five different procedures commonly used to rinse and dry released microstructures are compared: evaporation drying with deionized (DI) water or methanol, sublimation drying with t-butyl alcohol or p-dichlorobenzene, and supercritical drying with CO<sub>2</sub> [56]. The three various drying procedures can be depicted in Figure 2-5-2. Chang-Jin Kim's study reveals, for the first time, that the maximum beam length obtainable increases as the beam width increases for the cases of sublimation and supercritical drying, opposite to the previously known case of evaporation drying. Both sublimation drying methods as well as supercritical drying rendered good results, releasing cantilevers up to 700  $\mu\text{m}$  in length without stiction.

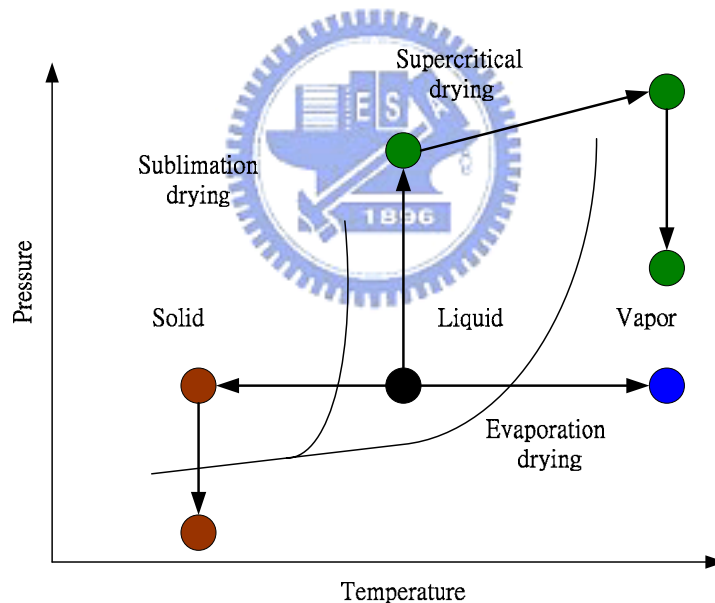


Figure 2-5-2 Three various drying procedures

In our research, we employed evaporation method to rinse and dry our samples due to our apparatus deficiency, and this method is also very much cheaper than other methods. Besides, evaporation approach is the most suitable for mass production among these methods. In this section, the basic evaporation concept and standard procedures are presented for cantilever beams as follows:

After etching completely sacrificial layer, the sample is immersed in a large volume of continuously flowing DI water for 30 minutes. Long rinsing in high-quality DI water helps to reduce the accumulation of residual particles under the beam and the effect of solid bridging. Careful handling of the sample is critical for all of the procedures tested due to the presence of many unusually long and flexible beams. Agitation in liquid could significantly deform or even break the longer and more flexible cantilevers, causing the deformed or broken beams to land on other structures. For methanol evaporation drying, DI water was replaced with methanol by three steps, each time immersing the chip in fresh methanol for 10 min. Samples from DI water or methanol were then placed inside a 100°C oven for approximately 20 minutes to ensure complete removal of the liquid from the samples. The sequence leading to stiction starts first by a liquid droplet in the gap pulling down the beam to the substrate. If the beam is stiff (i.e., short) enough, the beam would not bend much, and drying proceeds from the tip of the beam to the base as depicted in Figure 2-5-3. Stiction would not occur in this case. On the other hand, a flexible (i.e., long) beam will bend down enough so that a droplet is formed near the tip as depicted in Figure 2-5-4. As rinsing liquid starts to evaporate (Figure 2-5-4(a) and (b)), necking of the liquid occurs near the base (Figure 2-5-4 (c)), and as time proceeds a discontinuous droplet is formed below the tip of the beam (Figure 2-5-4(d) and (e)). As this droplet evaporates it may pull down the beam into contact with the substrate, after which it remains pinned down if the surface adhesion force is greater than the elastic restoring force of the beam.

Since capillary pressure is the dominant component [57], the pull down force is approximately proportional to the projected area of the droplet. Due to the tendency of the droplet to be circular (to minimize the free surface area), it is expected that the liquid area is proportional to approximately the square of the beam width. On the other hand, the restoring elastic energy stored in the beam is linearly proportional to the beam width.

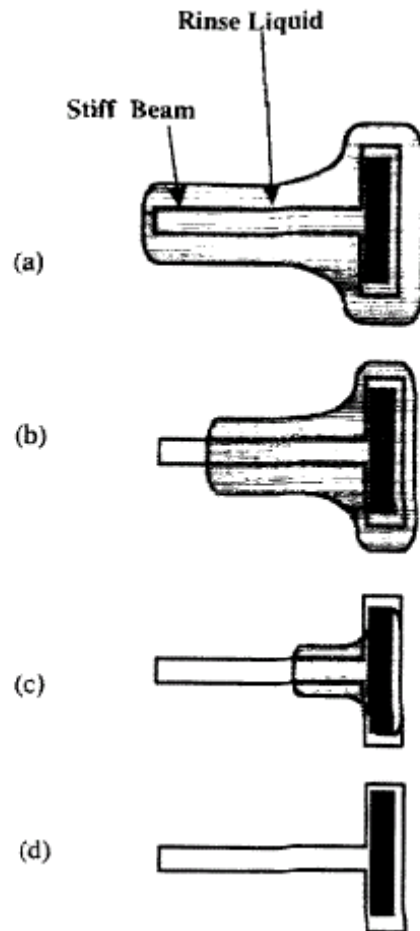


Figure 2-5-3 Evaporation drying of short cantilever

Hence the liquid pull-down energy increases at a greater rate than the restoring elastic energy as the beam width increases. Assuming the contact area is proportional to the droplet area, a similar trend is expected between the surface adhesion energy and beam restoring energy. For this reason, the detachment length decreases as the beam width increases for evaporation drying. The above argument of droplet area being proportional to the square of the beam width assumes the beam is long and flexible enough to have the tip of the pulled-down beam reasonably flat on the substrate. The assumption does not extend to shorter beams, however, which start to exhibit the effect of tip slope. For short cantilevers, the droplet area and the resulting pull-down force become more sensitive to the beam length than width.

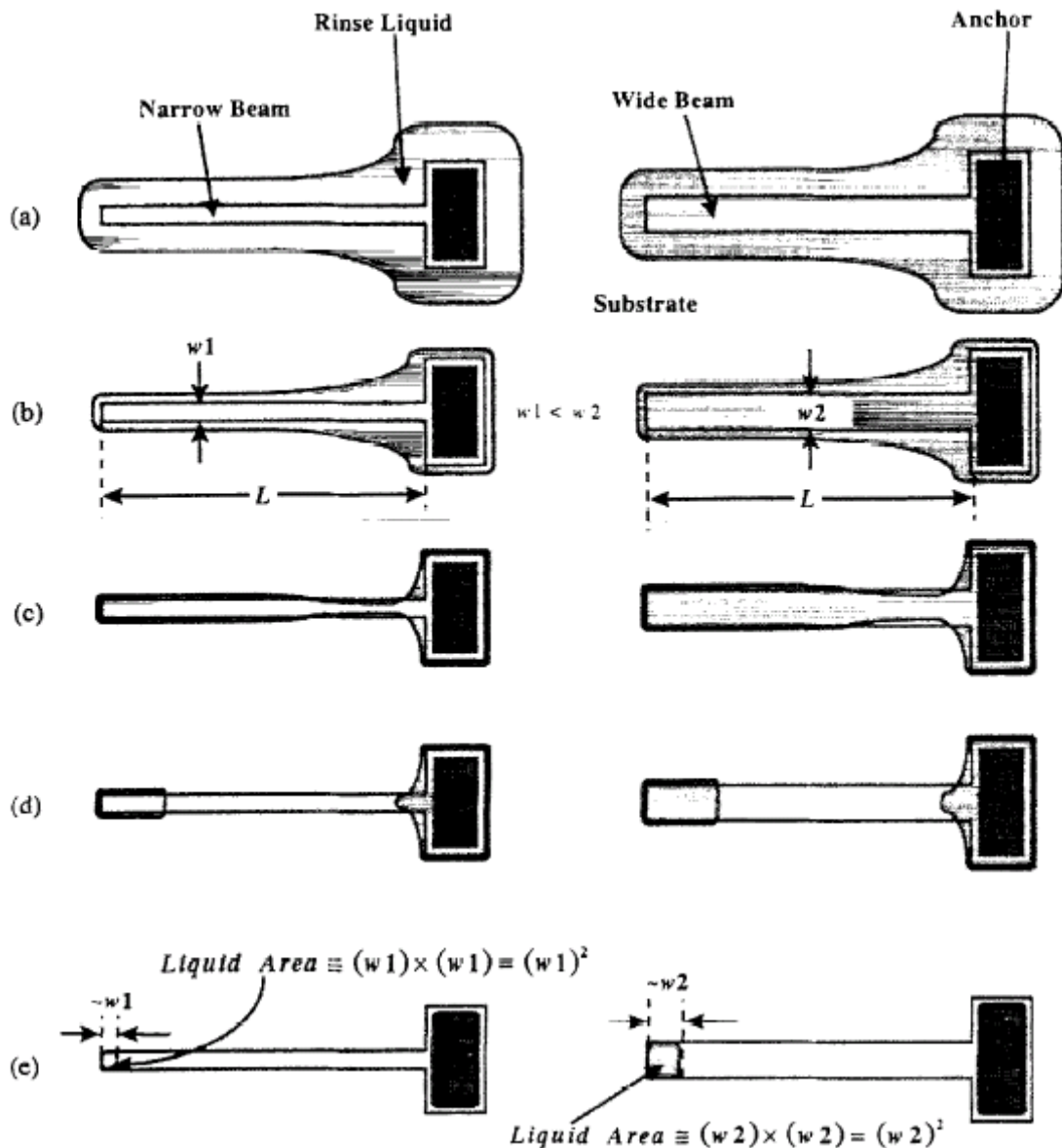


Figure 2-5-4 Evaporation drying of long cantilever

The general procedures of CO<sub>2</sub> supercritical drying is described as follows. The released sample was placed on a boat filled with methanol before placing it inside the setup. Carbon dioxide filling and methanol flushing were repeated 10 times to ensure complete removal of methanol from the chamber. The chamber pressure rises from 800 psi to 1350 psi when the temperature, initially about 17°C is brought above the supercritical temperature (~40°C) of carbon dioxide. As carbon dioxide is vented out of the chamber slowly, maintaining the temperature roughly constant, the pressure lowered back to the atmospheric pressure without condensation. This method can avoid stiction

influence and obtain very high good yield for cantilever beam, but the production cost is more expensive than that by evaporation method.

### 5.3.2 Modeling the drying process

Bending of microstructures resulting from trapped rinse liquids can be reduced by lowering the liquid surface tension. Methanol has approximately one-third of the surface tension of water. Figure 2-5-5 [21] shows that further reduction in surface tension can be realized by raising the temperature. It may therefore be possible to reduce the incidence of stiction by performing post-release etch rinses in hot solvents.

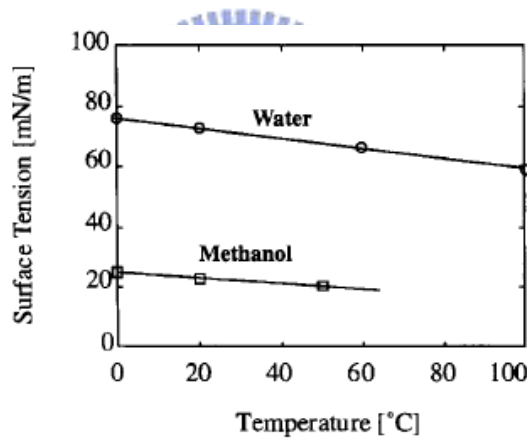


Figure 2-5-5 Temperature dependence of surface tension for water and methanol

From Figure 2-5-6, fluid forces acting on a cantilever beam during drying process can be expressed as:

$$f_s = 2\gamma \cos\theta = 2\gamma \frac{\sqrt{d(2r_{\parallel} - d)}}{r_{\parallel}} \quad (5-1)$$

$$f_l = \gamma b \left( \frac{1}{r_{\parallel}} + \frac{1}{r_{\perp}} \right)$$

where  $f_s$  is the surface tension force per unit length along the beam;  $f_l$  is the Laplace



pressure force per unit length along the beam;  $\gamma$  is liquid-gas surface tension;  $d$  is the gap distance;  $b$  is the beam width; and  $\theta$  is the contact angle defined as Figure 2-5-6(c) During the drying process, the meniscus radius of curvature continuously changes from larger values toward smaller values. As the meniscus curvature becomes tighter, the force acting on the beam increases due to both the surface tension force and the Laplace pressure component

At a certain radius, however, the surface tension force begins to decrease; this corresponds to the transition where the meniscus transforms from an “outside” to an “inside” meniscus. Once an “inside” meniscus forms, only the Laplace pressure term acts to pull the beam down. Figure 2-5-7 presents the application of above stated concept to rigid and non-rigid beams [21].



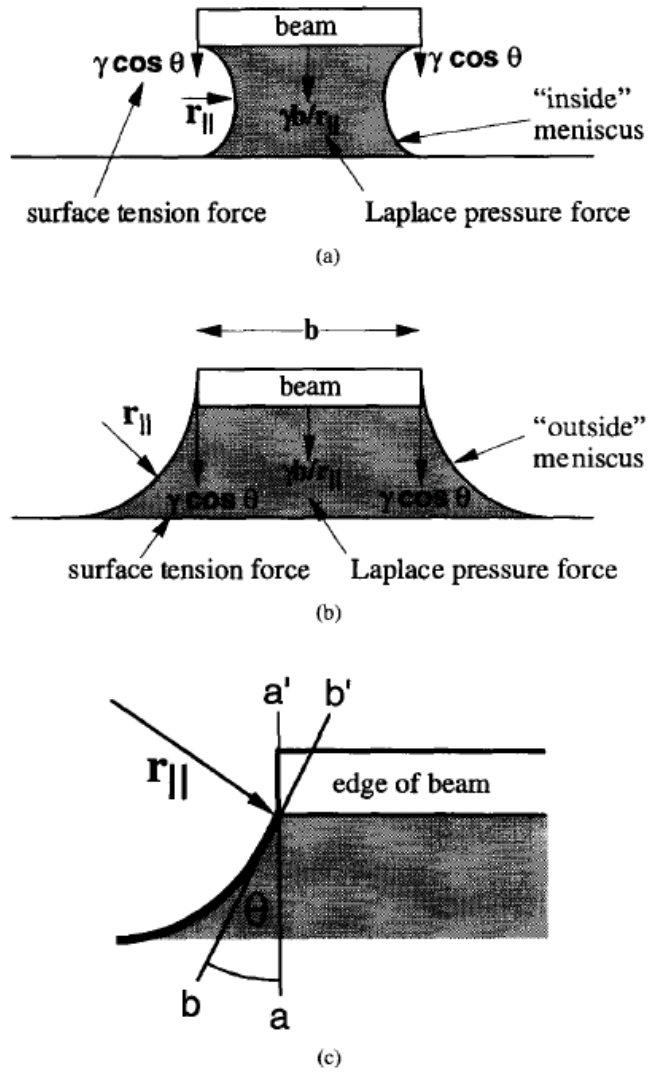


Figure 2-5-6 Fluid forces acting on a cantilever beam during drying process

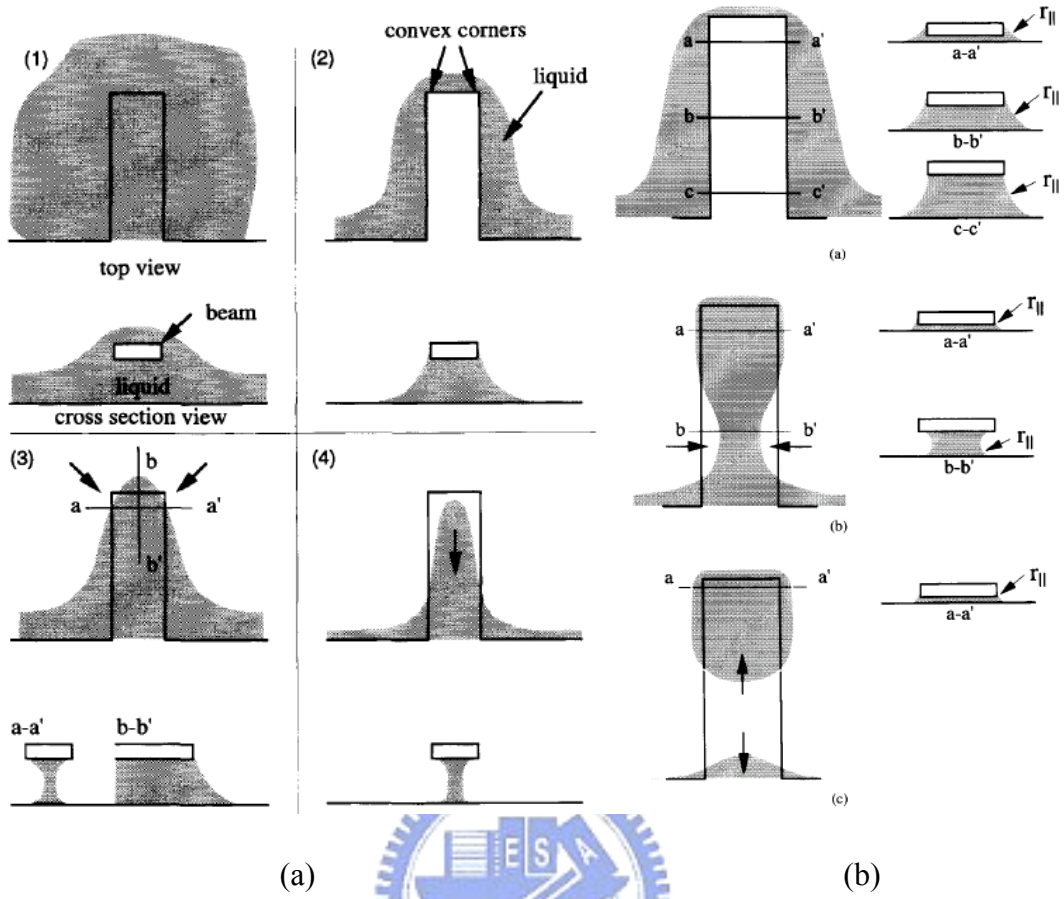


Figure 2-5-7 Drying process for (a) rigid beams and (b) non-rigid beams

## Chapter 6

### Results and Discussion

In general, an arbitrary stress profile can be thought as a sum of uniform stress and nonuniform stress across thickness direction. In the case of a cantilevered beam, uniform residual stress is released, and only the nonuniform stress determines the deformation of the beam [58]. However, for a membrane structure, the uniform residual stress and gravity effect cannot be neglected due to its very large suspended area and only two small supports. The average residual stress of the membrane structure containing the sacrificial layer without annealing is measured about -285MPa by using the stress measurement apparatus of FLX-2320. On the contrary, the average residual stress is about +140MPa for the membrane structure with the annealed sacrificial layers. This phenomenon of residual stress changing from compressive stress to tensile stress can be explained that the annealing process with the temperature of 350°C for one hour makes aluminum layer have lower thermal expansion coefficient than oxide layer during PECVD deposition with 300°C depositing temperature. Consequently, after depositing oxide layer and then unloading sample from chamber, the oxide layer will have much more shrinkage than that of the aluminum layer and this effect results in the oxide layer upward bending. In the surface micromachining technology, the suspended microstructures are favorable to have tensile stress less than 100MPa in order to reduce sticking effect during release process. Due to our PECVD apparatus limitation, it can only deposit compressive oxide film, so annealing aluminum sacrificial layer is conducted to change the PECVD oxide film from compressive stress to tensile stress.

In addition, because the sacrificial layer has a thickness of 2.5 $\mu$ m and is wetly etched, the sidewall angle of the anchor profile is about 75~85 degrees and must be taken into account during structural simulation. From structural simulation results with the

constant sidewall angle of  $75^\circ$ , the SCF plays an important role in determining whether the microstructure is suspended or collapse during the drying step of the release process.

Regarding computer aided design for the released structure prediction, the test microbolometer structures containing material properties, residual stress, gravity effect and anchor profile are evaluated and optimized by using Coventorware simulation which is developed for MEMS applications. In this simulation, the pixel size of  $75\mu\text{m} \times 75\mu\text{m}$ , which structure dimension is one half times of  $50\mu\text{m} \times 50\mu\text{m}$ , is used to verify our design due to its larger influence by residual stress. The effect of anchor profile includes the sidewall angle of the anchor part of the microstructure and the sidewall conformity factor (SCF) which is defined as the ratio of the thickness of the vertical part of the deposit with respect to one of the horizontal deposit at the anchor region. In Figure 2-6-1, it illustrates the definition of SCF and also indicates the sidewall angle  $\theta$ . Figure 2-6-2 shows the simulation results of the displacement of the Z direction (vertical) of the  $75\mu\text{m} \times 75\mu\text{m}$  test structure with the variances in SCF on the sidewall angle of  $75^\circ$  for the sacrificial layer with annealing process for one hours. In simulation aspect, because the anchor part is boundary condition and it can not be moved, the  $Z_{\text{max}}$  is defined as the absolute value of the maximum displacement of the whole membrane, and the  $Z_{\text{min}}$  is defined as the value of the minimum displacement of the whole membrane. From this figure, when the SCF is below 0.4, the  $Z_{\text{min}}$  of the microbolometer membrane equals zero and the  $Z_{\text{max}}$  displacement is above zero. This indicates that the position of the whole membrane is higher than the anchor parts, so the whole microstructure upward bends and then suspends due to the sticking effect release. This can be explained by the following. Due to  $2.5\mu\text{m}$  height of the gap between the suspended membrane and substrate, the solvent moves quickly to the anchor part which results from surface tension force and then vaporizes during the dry step of the release process. In Figure 2-6-3 (a) and (b), the influence of the anchor profile is shown for the SCF of 0.3 and the sidewall angle of  $75^\circ$ .

It is worth noticing that the leg of the membrane bends slightly upward and the center part of the membrane is flat. However, in the case of the SCF above 0.5, the  $Z_{\min}$  is negative and the  $Z_{\max}$  equals zero. This indicates the position of the whole membrane is lower than the anchor parts, so the solvent moves separately to the center part of the membrane and the anchor parts during the drying step [11]. The solvent underneath the membrane pulls down the membrane towards the substrate owing to sticking effect happened under the center part during the drying step, and the microstructure tends to be downward and then collapses. This phenomenon has less influence on  $50\mu\text{m} \times 50\mu\text{m}$ , but it has a great effect on larger membrane structures. This phenomenon must be considered, as the larger membrane is necessary to apply to other applications. Figure 2-6-4 (a) and (b) show SEM photographs of the pixel size of  $75\mu\text{m} \times 75\mu\text{m}$ , when the value of the SCF is one and the sidewall angle of the anchor part is about  $75^\circ$ . As demonstrated in the Figure 2-6-4 (a), the microstructure collapses at the center part of the membrane. Besides, in the Figure 2-6-3 (a) and Figure 2-6-4 (a), these legs demonstrating monotonically upward and downward deformation due to only uniform stress can prove the annealing process being capable of reducing nonuniform stress. The simulation results without annealing process are depicted in Figure 2-6-5 and have opposite phenomenon as compared with Figure 2-6-2. Figure 2-6-6 shows the SEM photographs of the test microstructure with the pixel size of  $75\mu\text{m} \times 75\mu\text{m}$  and without annealing process. From this figure, the legs showing seriously upward bending curve is observed and can be explained by the nonuniform residual stress of the PECVD oxide film without implementing annealing treatment. These SEM photographs are in good agreement with the preceding Coventorware simulations. From these figures, the measured RMS surface roughness of the microbolometers is about  $0.1\mu\text{m}$  and results from the process of the annealing  $2.5\mu\text{m}$ -thick aluminum by using AFM measurement of Digital Instruments DI 5000. Some large surface roughness (about  $1\mu\text{m}$ ) of annealing aluminum thickness of  $2.5\mu\text{m}$  is

not observed for the annealing aluminum in standard CMOS processes which the aluminum thickness is less than 1.5 $\mu\text{m}$ , and this phenomenon can be explained by Classical Homogeneous 3D Nucleation Theory [59]. As the thickness of aluminum is over the critical value, it has larger volume energy than surface energy during thermal process and results in precipitation occurrence. The precipitation occurs at random location, but it can be improved by using rapid thermal annealing (RTA) substituted for furnace annealing to reducing thermal processing time..

By appropriately controlling the SCF and sidewall angle, the successful suspended surface micromachining membranes can be accomplished. The SCF related to step coverage of depositing thin film can be controlled by process parameters such as chamber pressure, gas flow rate and process temperature. In order to obtain higher SCF, we can decrease chamber pressure to increase deposited atom mean free time, and increase process temperature to increase deposited atom mobility. In regard to sidewall angle, we can control the temperature of aluminum etchants. If the etching temperature is higher, the sidewall angle becomes lower due to larger undercut. In Figure 2-6-7 (a), the test structure arrays with the pixel size of 50 $\mu\text{m}$  x 50 $\mu\text{m}$  are demonstrated and have nearly 100% yields. In this figure, the fillet-angle design of the legs conduces to alleviate the concentration stress of these right-angle corners and the sticking effect during the drying step. From Figure 2-6-7 (b), the microstructure with the pixel size of 100 $\mu\text{m}$  x 100 $\mu\text{m}$  is successfully developed for rectangle angle design if the fabrication processes well design and control. Figure 2-6-8 (a) is the enlarged picture of the single microstructure including mirror layer and sensing layer. Basing on the successful design and fabrication, the microbolometer including mirror layer, sensing layer and metal line has a flat suspension structure and is demonstrated in Figure 2-6-8 (b). From our experience, if we can develop a flat membrane of the microbolometer, the stress of the sensing layer and metal line only slightly affects the whole microbolometer structure due

to low temperature processing ( $< 250^{\circ}\text{C}$ ) and thin films (about 50nm). Besides, we use Coventorware to simulate some test structures with residual stress or gradient stress to represent the distinction between them. The Z-displacement and Nodal-displacement of the test structure having the residual stress of 150 MPa, the dimension of 75um x 75 um, the SCF of 0.4, the sidewall slope of 80 degrees, and the supporting-layer thickness of 0.8 um are evaluated and shown in Figure 2-6-9 (a) and (b), respectively. The displacement for the uniform-stress structure is monotonously increasing from the two anchor parts toward the central structure. Besides, it can be noted that the asymmetry of the displacement distribution comes from the spatial-dependent mesh of the simulator, but the deviation of the distribution is little and able to tolerate. On the contrary, Figure 2-6-10 (a) and (b) show that the displacement of the uniform-stress structure (-150MPa) is monotonously decreasing from the two anchor parts toward the central structure. From the Figure 2-6-9 and Figure 2-6-10, it can be seen that the four rectangular corners on the two legs have the largest displacement. The stiction effect often occurs in these parts. The displacement distributions of the whole microbolometer structure with the supporting layer having nonuniform stress of 1MPa per 1um and the residual stress of 150MPa or -150MPa are also shown in Figure 2-6-11. We can observe the curve displacement of the two legs and much larger deformation due to the existence of the gradient stress. These results are again in agreement with the preceding discussion.

In comparison with Figure 2-6-12 (a), Figure 2-6-12 (b) demonstrated a microbolometer array having a seriously upward deformation, especially at the first right-angle corner parts, but they are fabricated on the same wafer. This difference can be explained as follows. During drying step, much more vapor produces suddenly below the array structure than in the single structure due to liquid surface tension. By decreasing the drying temperature of hot plate, the flat suspension structures of the microbolometer array can be achieved due to the appropriate vaporizing velocity.



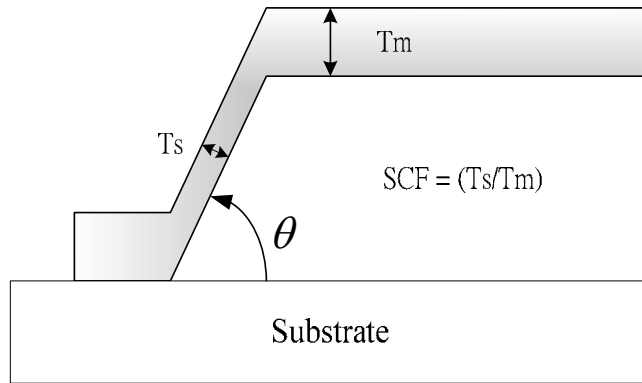


Figure 2-6-1 Definition of sidewall conformal factor (SCF).

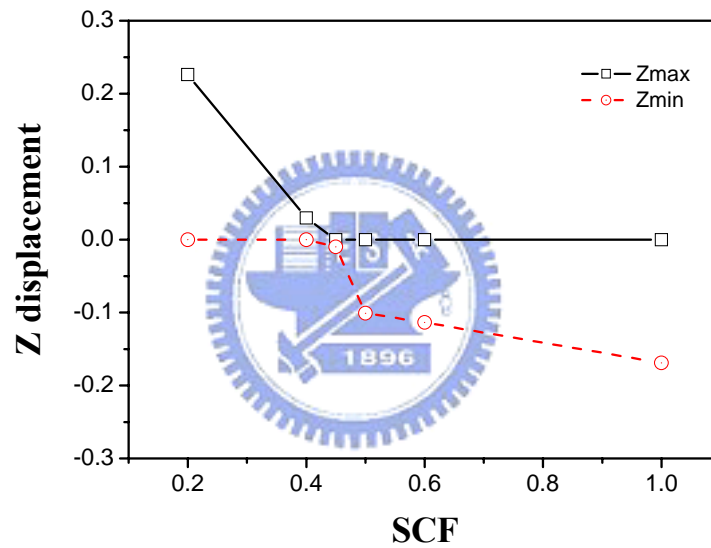
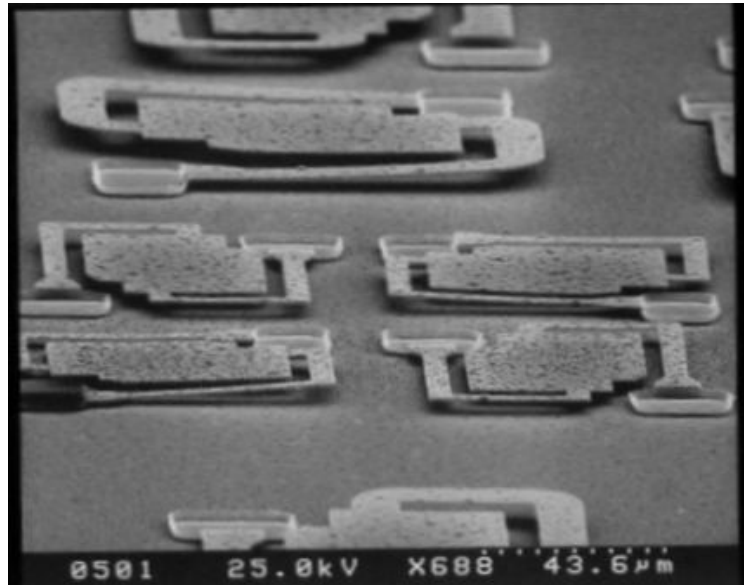
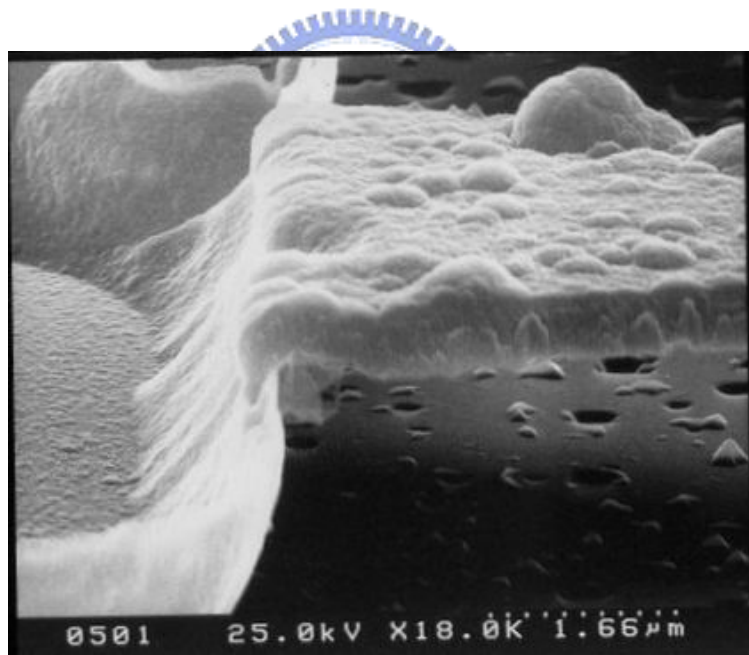


Figure 2-6-2 Simulation results of z displacement against SCF with the sidewall angle of 75 degrees for the 75 $\mu$ m x 75 $\mu$ m test structure with annealing process for one hours

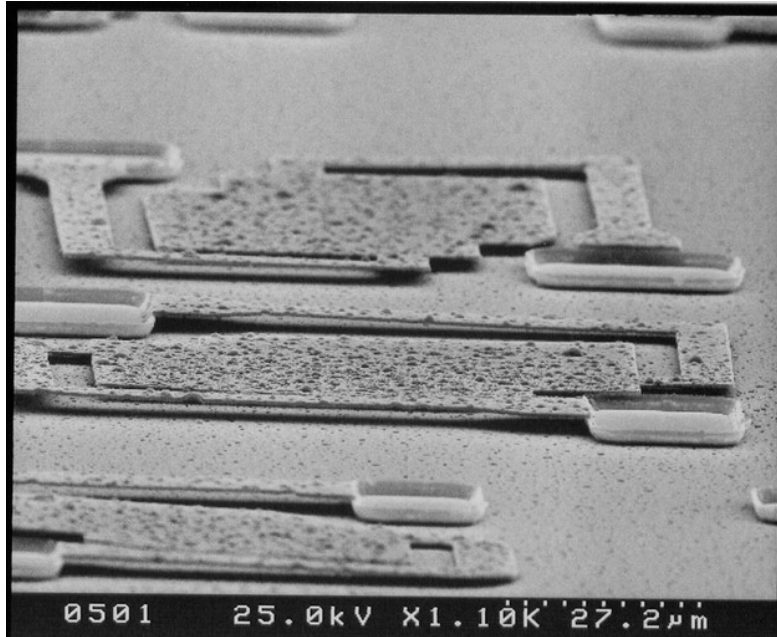


(a)

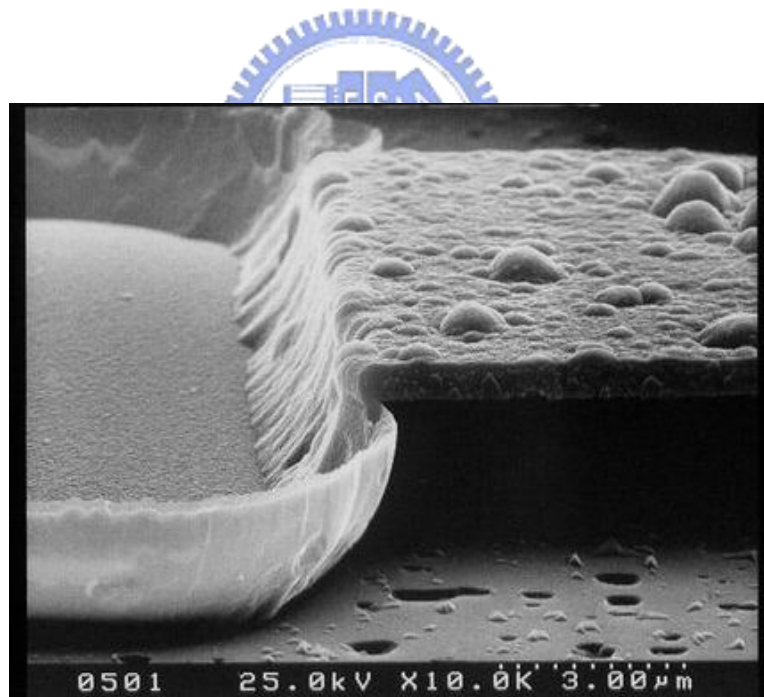


(b)

Figure 2-6-3 SEM images (a) The upper side is the pixel size of  $75\mu\text{m} \times 75\mu\text{m}$ , and the lower side is  $50\mu\text{m} \times 50\mu\text{m}$ . (b) The SCF of these test structures is about 0.3



(a)



(b)

Figure 2-6-4 SEM images (a) The upper side is the pixel size of  $75\mu\text{m} \times 75\mu\text{m}$ . (b) The SCF of these test structures is about 1 on the sidewall angle of 75 degrees.

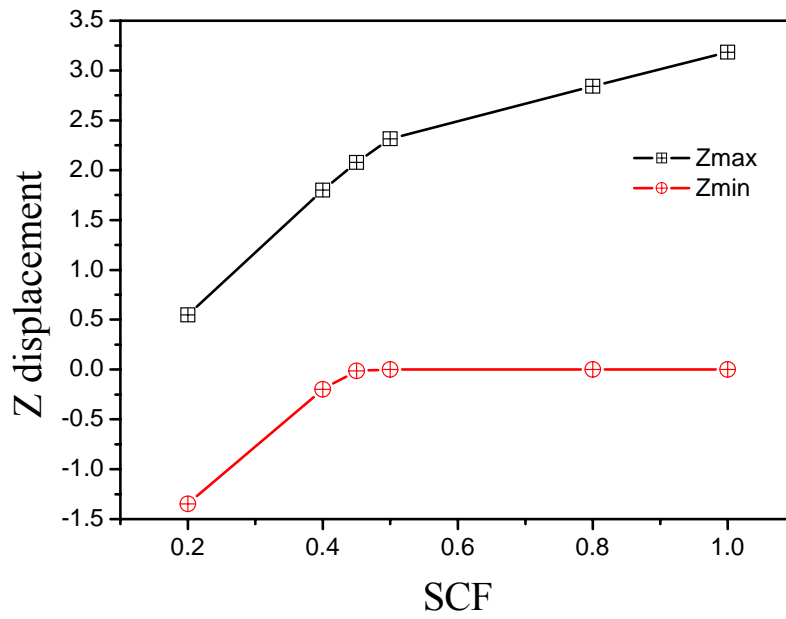


Figure 2-6-5 Simulation results of z displacement against SCF for the test structure with non-annealing sacrificial layer.

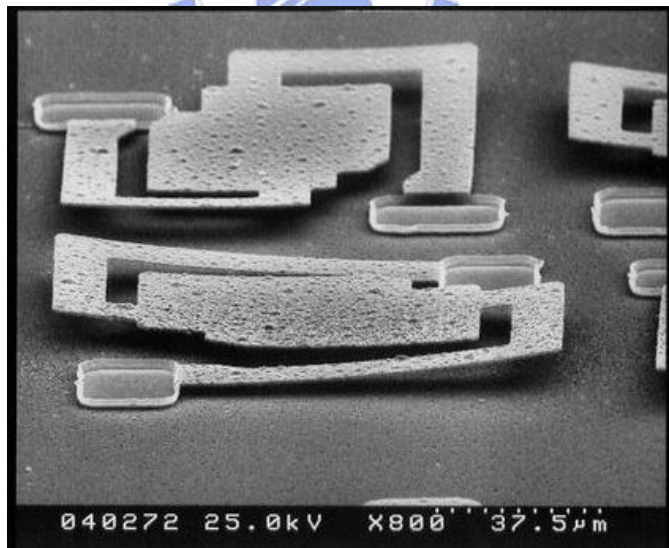
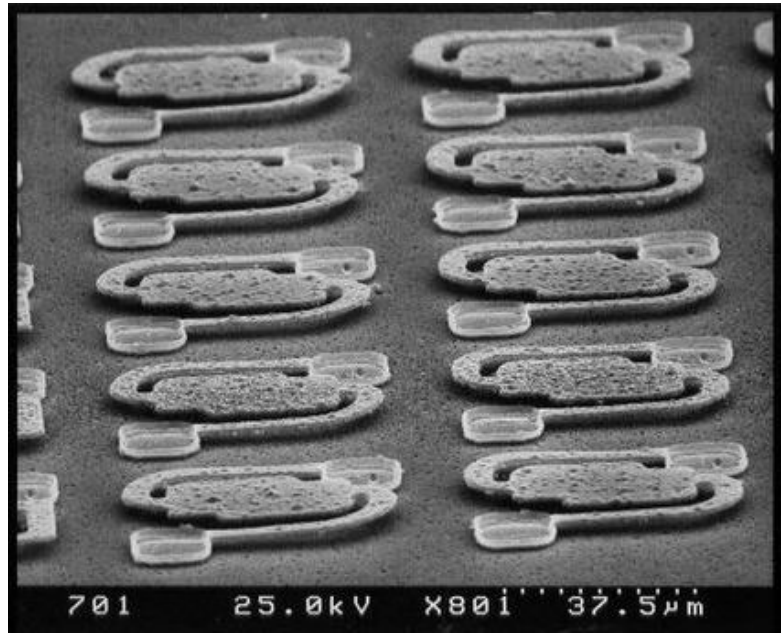
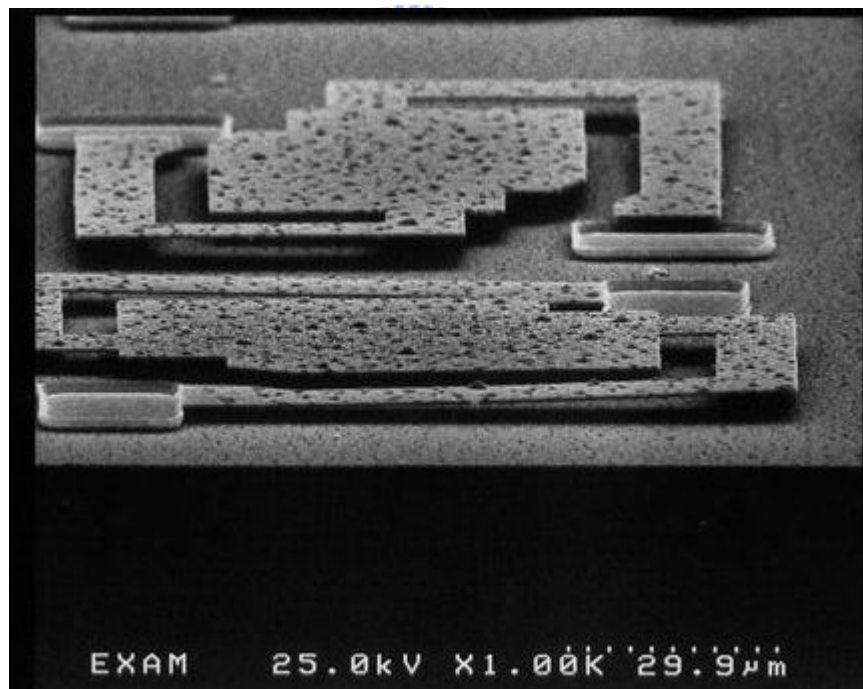


Figure 2-6-6 SEM image of the test membrane structure having the SCF of one and the sidewall angle of 75 degrees without annealing process.

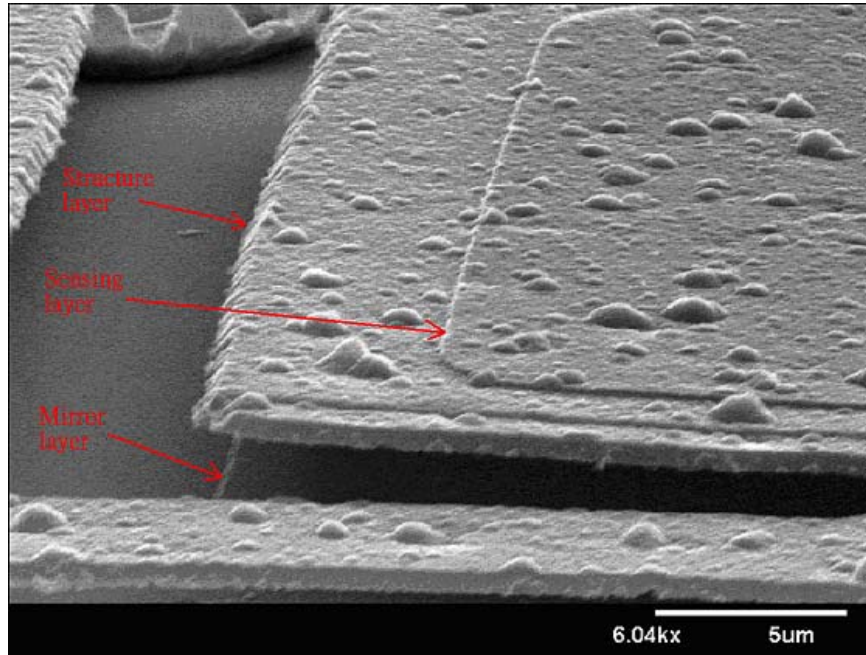


(a)

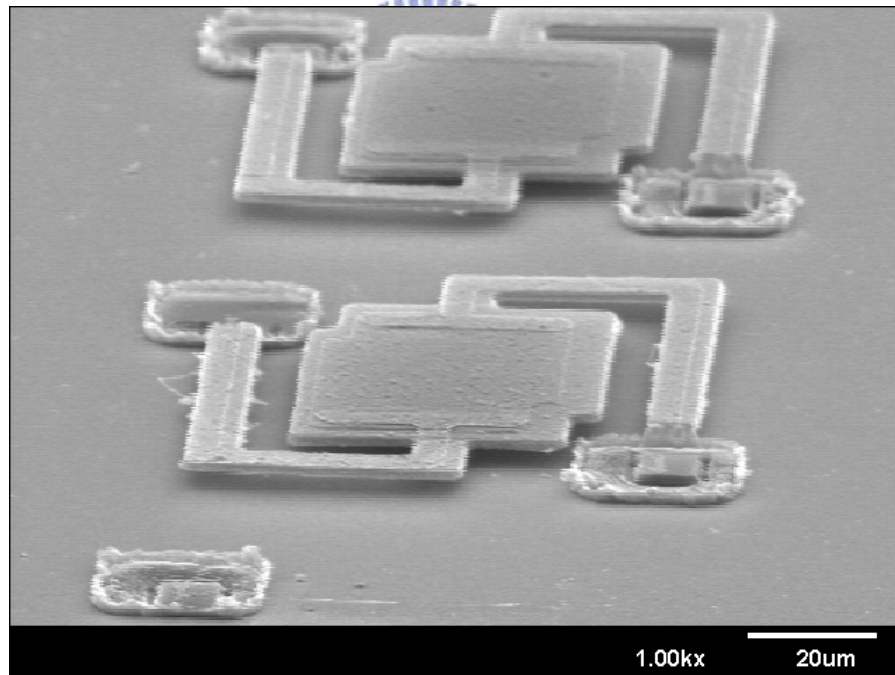


(b)

Figure 2-6-7 SEM images (a) The microbolometer arrays with the pixel size of  $50\mu\text{m} \times 50\mu\text{m}$  having fillet angle design. (b) The membrane structure with the pixel size of  $100\mu\text{m} \times 100\mu\text{m}$  having rectangle angle design.



(a)



(b)

Figure 2-6-8 SEM images (a) The enlarged image of the test microstructure includes mirror layer and sensing layer. (b) The microbolometer including mirror layer, sensing layer and metal line has a flat suspension structure.

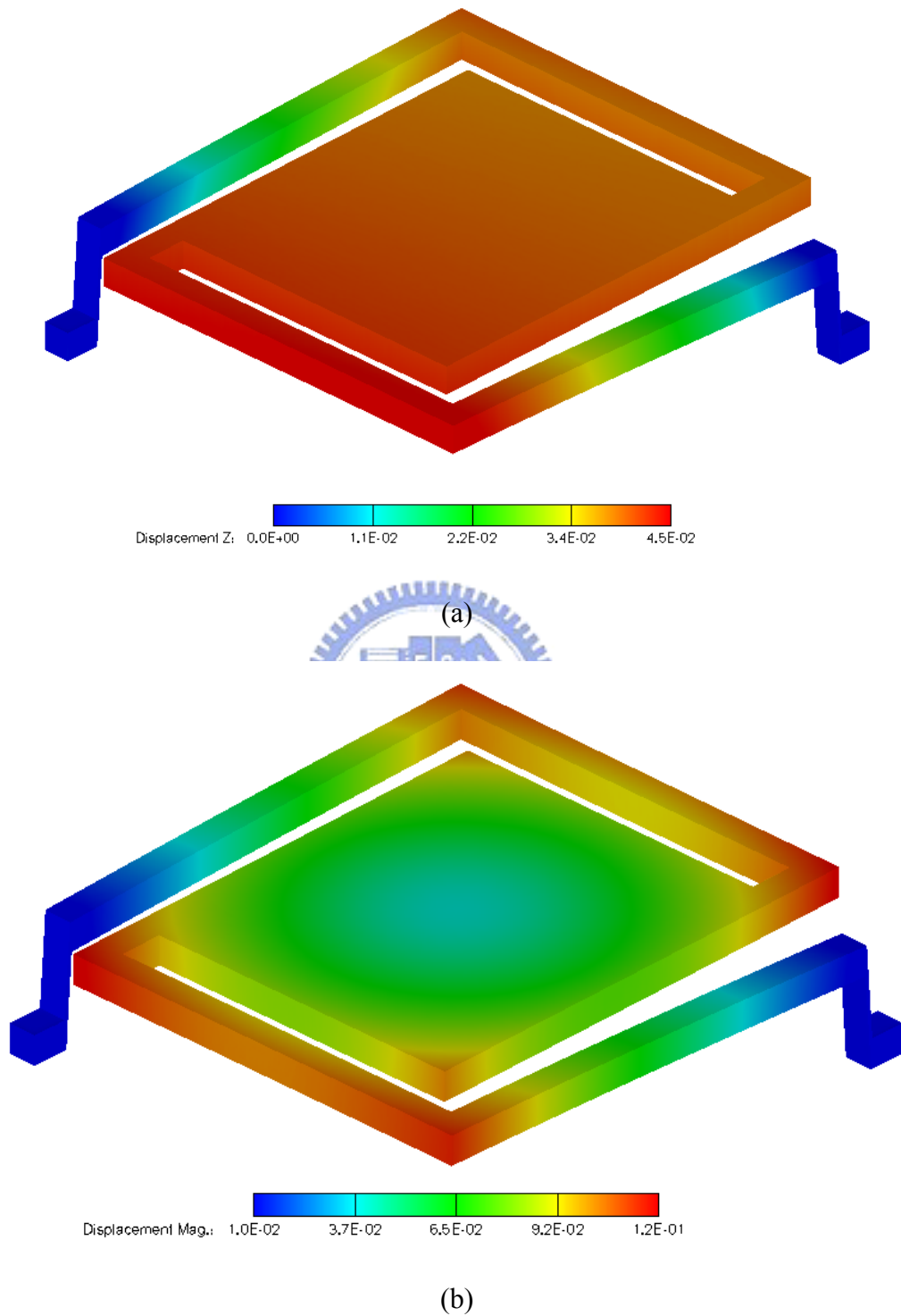
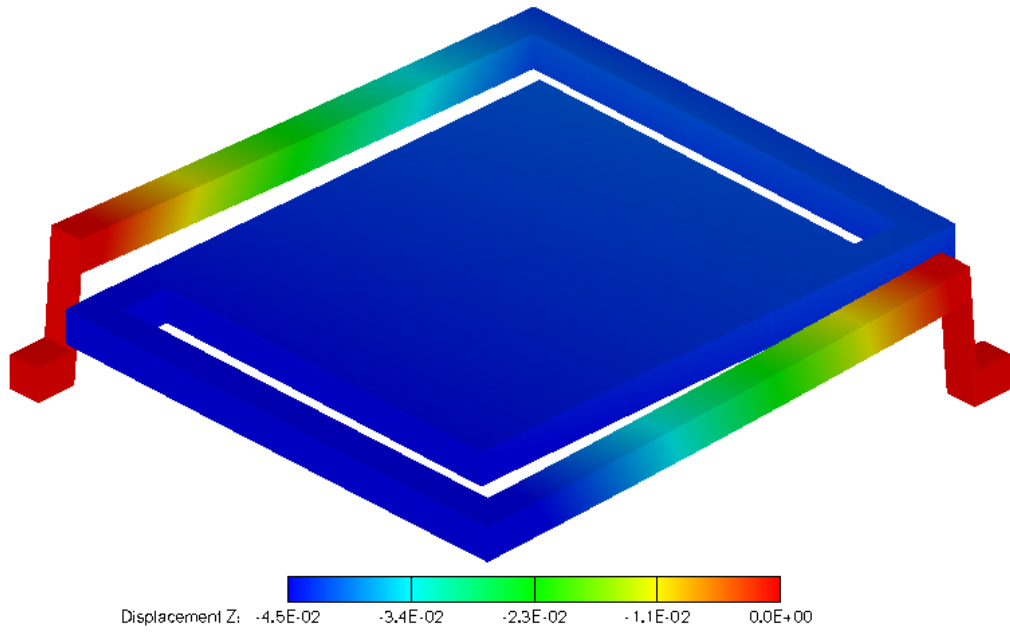
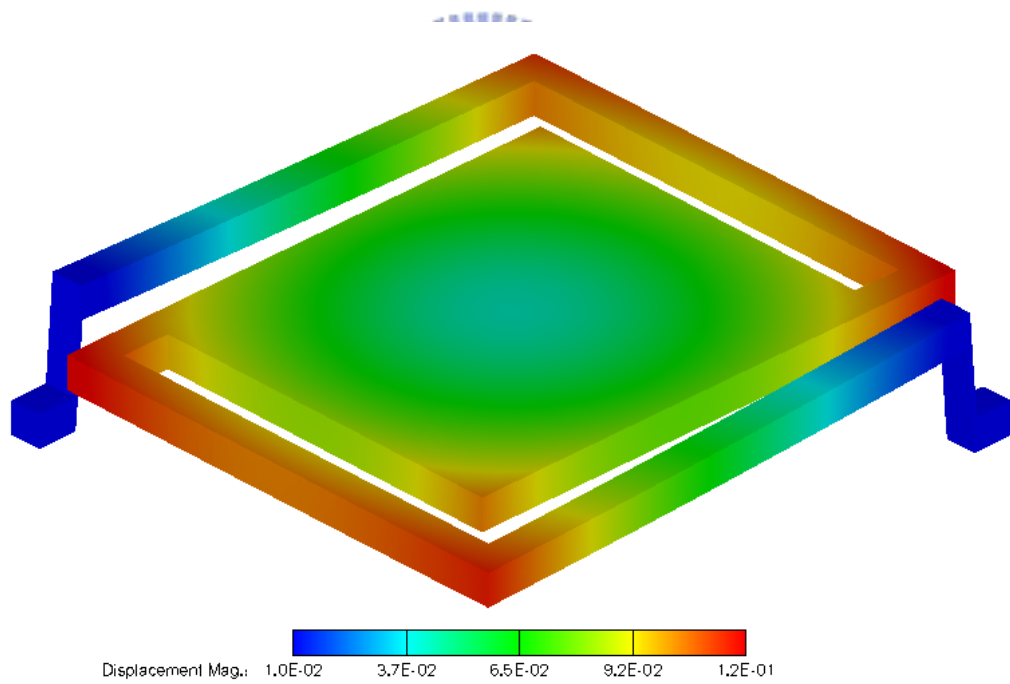


Figure 2-6-9 (a) Z-Displacement and (b) Nodal-Displacement for the test structure (75  $\mu\text{m}$  x 75  $\mu\text{m}$ ) with SCF of 0.4, sidewall slope of 80 degree, and thickness of 0.8 $\mu\text{m}$  while the supporting layer has the residual stress of 150 MPa



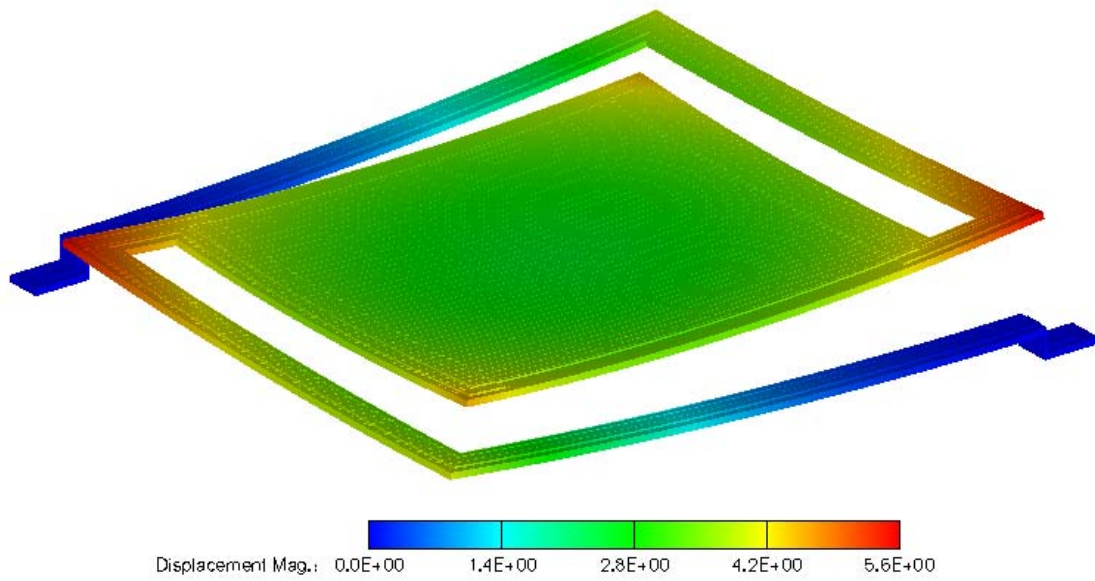
(a)



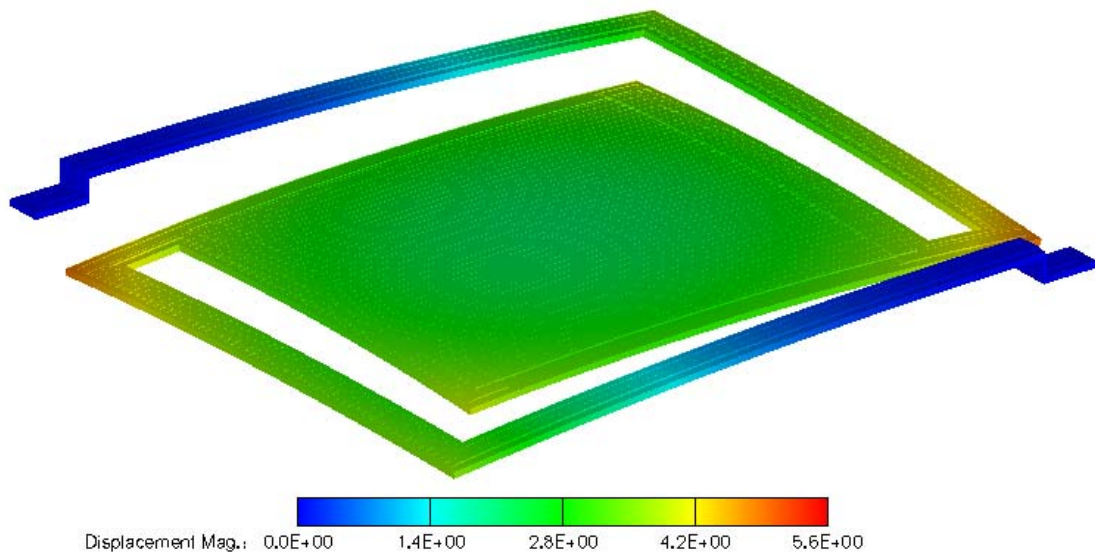
(b)

Figure 2-6-10 (a) Z-Displacement and (b) Nodal-Displacement for the test structure (75  $\mu\text{m}$  x 75  $\mu\text{m}$ ) with SCF of 0.4, sidewall slope of 80 degree, and thickness of 0.8 $\mu\text{m}$  while the supporting layer has the residual stress of -150 MPa



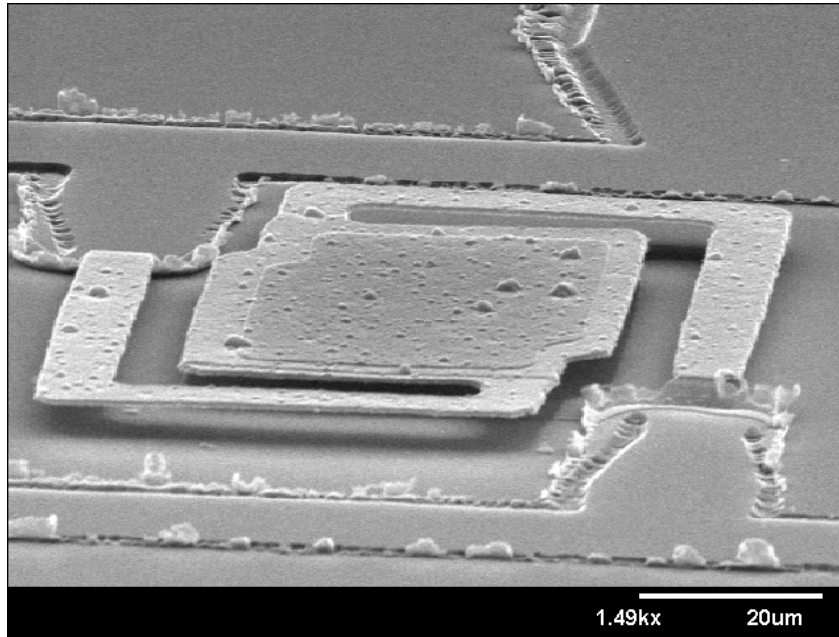


(a)

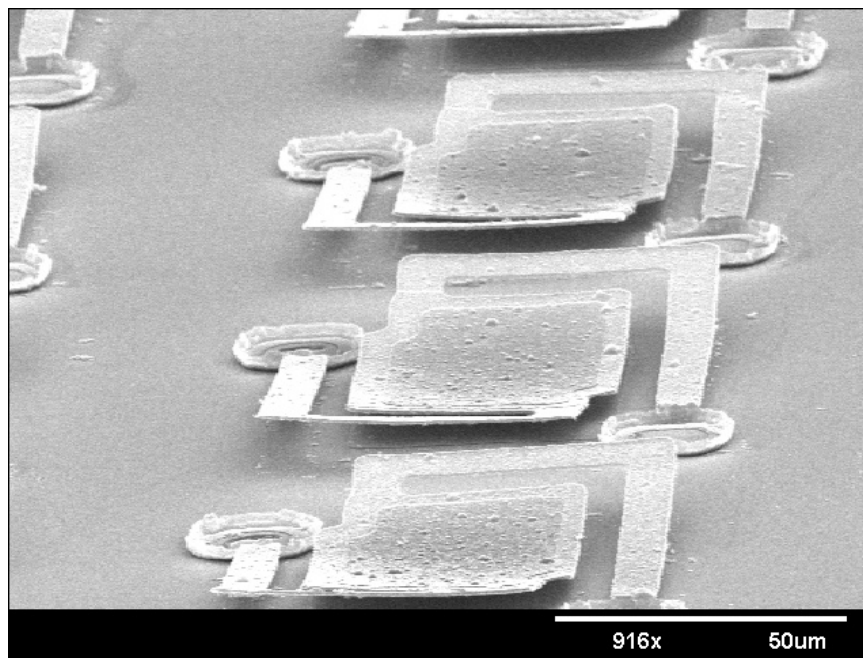


(b)

Figure 2-6-11 Nodal-Displacement of the whole microbolometer structure with SCF of 0.4 and sidewall slope of 80 degree for (a) positive and (b) negative gradient stress imposed on the supporting layer.



(a)



(b)

Figure 2-6-12 SEM images (a) The single test microstructure with the pixel size of  $75\mu\text{m} \times 75\mu\text{m}$ . (b) The test microstructure arrays with the pixel size of  $75\mu\text{m} \times 75\mu\text{m}$ .

## Chapter 7

### Summary

In this research, we have successfully accomplished a simpler method, a low-cost, high yield fabrication for making thermal isolation membranes. We also use Ansys FEM simulator to analyze the thermal characteristics of the device using three different thermal conductivity of metal line. The thermal time constant and heat flux of the bolometer device are also extracted. Once the residual stress of a membrane microstructure is known, the optimal design of a suspended membrane by controlling the SCF and sidewall angle has been successfully developed. Using Coventorware simulations to predict the z displacement of the structure, we can modify the structure and fabrication to have the zero minimum displacement of z direction and then alleviate the sticking effect. Therefore, these proposed approaches are very promising to predict a successful structure and provide a low-thermal budget, CMOS-process compatible fabrication with higher yield, cheaper apparatus and less process steps.

In this research, we don't actually measure the uncooled microbolometer due to the limitation of apparatuses. In the future, we can assemble a simple apparatus to actually measure the thermal characteristics of the uncooled microbolometer device. Besides, we can also improve the TCR value of the sensing layer by using amorphous silicon germanium oxide with low temperature fabrication. We must also account for self heating effect and external signal sensing circuits to exactly estimate the actual electrical and thermal performance of the device.

## References:

- [1] Crawford, F.J., "Electro-optical sensors overview", Aerospace and Electronic system Mag. IEEE, vol. 13, (1998), pp.17-24
- [2] Neli, R.R., Melo, A.M., Arbex, C.J.N. Zakia, M.B.P., "A submm-wave/far IR uncooled bolometer system and applications" IEEE MTT-S vol. 2, (2003), pp.785-789
- [3] R.A. Wood, "Uncooled thermal imaging with monolithic silicon focal planes", Proceedings of SPIE infrared Technology XIX, vol. 2020, (1993), pp.322-329
- [4] Z. Mai, X. Zhao, F. Zhou, and W. Song, "Infrared radiation detector linear arrays of high T superconducting thin films," Infrared Phys. Technol., vol. 38, (1997), pp.13-16
- [5] Tomohiro Ishikawa," Low cost 320x240 uncooled IRFPA using conventional silicon IC process", Proceedings of SPIE infrared Technology and applications XXV, vol. 3698, (1999), pp.556-564
- [6] Akio tanaka, Shouhei Matsumoto, Nanao Tsukamoto, Nobukazu Teranishi, "Infrared Focal Plane Array Incorporating Silicon IC Process Compatible bolometer", IEEE Transactions Electron Devices, vol. 43, (1996), pp. 1844-1850
- [7] M. H. Unewisse, S. J. Passmore, K. C. Liddiard, and R. J. Watson, "Performance of uncooled semiconductor Micro bolometer infrared detectors,"in Proc. SPIE, (1994), vol. 2269, pp. 43-52.
- [8] I.H. Choi and K.D. Wise, "A silicon thermopile based infrared sensing array for use in automated manufacturing," IEEE Trans. Electron Devices, vol. 33, (1986), pp.72-79
- [9] H. Beratan, C. Hanson, and E.G. Meissner, " Low cost uncooled ferroelectric detector," proc. SPIE, vol. 2274, (1994), pp.147-156
- [10] R. Watton, "Ferroelectric materials and IR bolometer arrays: From hybrid arrays toward integration," Inter. Ferroelectrics, vol.4, (1994), pp.175-186
- [11] Bryzek, J., Flannery, A., Skurnik, D, Integrating microelectromechanical systems

- with integrated circuits, *Instrumentation & Measurement Magazine, IEEE*, vol. 7, (June 2004) pp.51 – 59
- [12] Robertson, T.J., Neild, A., Hutchins, D.A., Radiated fields of rectangular air-coupled micromachined transducers, *Ultrasonics Symposium, 2001 IEEE*, vol.2, (Oct. 2001) pp.891 – 894
- [13] Jun-Bo, Yun-Seok Choi, CMOS compatible surface micromachined suspended spiral inductors for multi-GHz silicon RF ICs, *IEEE Electron device letters*, vol.23 (Oct. 2002) pp. 591-593.
- [14] Fritschi, R., Hibert, C., High tuning range AlSi RF MEMS capacitors fabricated with sacrificial amorphous silicon surface micromachining, *Microelectronic engineering*, vol. 73-74 (June 2004), pp. 477-451.
- [15] J.W. Graff, E.F. Schubert, Flat free-standing silicon diaphragms using silicon on insulator wafers, *Sensor and actuator A: Physical*, vol.84, Issue.3 (2000), pp276-279.
- [16] Christine M. Travers, Agha Jahanzeb, Donald P. Butler, Zeynep, Celik-Butler, Fabrication of semiconducting YBaCuO surface-micromachined bolometer arrays, *IEEE J. of Microelectromech. Syst.*, vol. 6, no. 3 (1997) pp.271 - 276
- [17] Deniz Sabuncuoglu Tezcan, Selim Eminoglu, Tayfun Akin, A Low-Cost Uncooled Infrared Microbolometer Detector in Standard CMOS Technology, *IEEE trans. Electron Devices*, vol. 50, no. 2 (2003) pp.494 – 502
- [18] C. H. Mastrangelo and C. H. Hsu, mechanical stability and adhesion of micro-structures under capillary forces-Part I: Basic theory, *IEEE J. Microelectromech. Syst.*, vol. 2, no. 1 (1993), pp. 33-43
- [19] C. H. Mastrangelo and C. H. Hsu, mechanical stability and adhesion of micro-structures under capillary forces-Part II: Experiments, *IEEE J. Microelectromech. Syst.*, vol. 2, no. 1 (1993), pp. 44-55
- [20] John Y. Kim, Chang-in Kim; Comparative study of various release methods for

polysilicon surface micromachining, MEMS '97, Proceedings, IEEE, Jan. 1997  
pp.66 – 75

- [21] Takeshi Abe, Willam C. Messner; Effects of elevated temperature treatments in microstructure release procedures, IEEE J. Microelectromech. Syst., vol. 4, no. 2 (1998) pp. 339-344
- [22] Holland Wayne, Duncan Willian, Griffin Mathew, "Bolometers for submillimeter and millimeter astronomy", ASP Conference Proceedings, vol. 278, (2002), pp. 463~491
- [23] Greenspan, Jonathan Edward, "The fabrication and characterization of metal thin film bolometers", (1998), thesis.
- [24] Jinghong Chen; Jun Zou; Chang Liu, Design and modeling of a micromachined high-Q tunable capacitor with large tuning range and a vertical planar spiral inductor, Electron Devices, IEEE Transaction, vol.50, Issue.3, (March 2003)  
pp.730 – 739.
- [25] Muller, R.; Manea, E.; Kusko, M., Thin membranes obtained by surface micromachining Preliminary study for a Fabry-Perot interferometer, Semiconductor Conference, CAS 2001 Proceedings. Vol.1, 9-13 (Oct. 2001)  
pp.193 –196.
- [26] Martin Hill, Conor O'Mahony, "Test structures for a MEMS SiO<sub>x</sub>/metal process," Proc. IEEE 2002 Int. Conference on Microelectronic Test Structures, vol. 15, April 2002.
- [27] O. Paul, D. Westberg, M. Hournung, V. Ziebart, "Sacrificial Aluminum Etching For CMOS Microstructures", Micro Electro Mechanical Systems, Proceedings, IEEE., 26-30 Jan. 1997 pp:523 ~ 528
- [28] O. Paul, H. Baltes, "Novel fully CMOS-compatible vacuum sensor", Sensor and Actuators, A46 (1995), 143~146

- [29] Wood, R. A. (1983).Honeywell Research Memorandum.
- [30] Voss, R. F., and Clarke, J.(1976). Phys. Rev. B13, 556-573.
- [31] Fisher, B (1982).J. Chem. Phy.Solids 43, 205-211.
- [32] E. Mottin, J. Martin, J. Ouvrier-Buffet, M. Vilain, A. Bain, J. Yon, J. L. Tissot,and J. P. Chatard, “Enhanced amorphous silicon technology for 320 x 240 microbolometer arrays with a pitch of 35  $\mu\text{m}$ ,” Proc. SPIE, vol. 4369, pp. 250–256, 2001
- [33] Sherif Sedky, Paolo Fiorini, and Chris Baert, “IR bolometers made of polycrystalline silicon germanium”, Sensors and Actuators A 66 (1998) 193-199
- [34] T. Ichihara, Y. Watabe, Y. Honda, and K. Aizawa, “A high performance amorphous Si C :H thermistorC bolometer based on micro-machined structure,” in Proc. 1997 Int. onf. Solid State Sensors Actuators, vol.1253.
- [35] M. Garcia, R. Ambrosio, A. Torres, A. Kosarev, “IR bolometers based on amorphous silicon germanium alloys,” Journal of Non-Crystalline Solids 338–340 (2004) 744–748
- [36] Enrique Iborra, Marta Clement, Lucía Vergara Herrero, and Jesús Sangrador , “IR Uncooled Bolometers Based on Amorphous  $\text{Ge}_x\text{Si}_{1-x}\text{O}_y$  on Silicon Micromachined Structures,” Journal of Micromechanical Systems, vol. 11, no. 4, august 2002
- [37] M. Clement, E. Iborra, J. Sangrador, and I. Barberán, “Amorphous Ge Si O sputtered thin films for integrated sensor applications,” J.Vac. Sci. Technol. B, vol. 19, no. 1, pp. 294–298, 2001.
- [38] Yong-Hee Han and In-Hoon Choi , “ Fabrication of vanadium oxide thin film with high-temperature coefficient of resistance using  $\text{V}_2\text{O}_5/\text{V}/\text{V}_2\text{O}_5$  multi-layers for uncooled microbolometers”, Thin Solid Films 425 (2003) 260.264
- [39] R.J. Herring, P.E. Howard, Design and performance of the ULTRA 320x240 uncooled focal plane array and sensor, SPIE 2746 (1996) 2-12.

- [40] B. Johnson, T. Ohnstein, C. Han, R. Higashi, P. Kruse, R. Wood, H. Marsh, and S. Dunham, "YBaCuO superconductor microbolometer arrays fabricated by silicon micromachining," *IEEE Trans. Appl. Superconduct.*, vol. 3, pp. 2856–2859, Mar. 1993.
- [41] M. Fardmanesh, A. Rothwarf, and K. Scoles, "Low and midrange modulation frequency response for YBCO infrared detectors: Interface effects on the amplitude and phase," *IEEE Trans Appl. Superconductivity*, vol. 5, no. 1, pp. 7–13, Mar. 1995.
- [42] Christine M. Travers, Agha Jahanzeb, Donald P. Butler, Zeynep, Celik-Butler," Fabrication of semiconducting YBaCuO surface-micromachined bolometer arrays", *IEEE J. of Microelectromech. Syst.*, vol. 6, no. 3 (1997) pp.271 – 276
- [43] F. Bertrand, J.L. Tissot, G. Destefanis, "Second generation cooled infrared detectors state of the art and prospects", 4th International workshop on advanced infrared technology and applications, Florence - Italie
- [44] Leila R.Vale and R.H.Ono," Small area Y-Ba-CU-O thin films for applications in hot-electron bolometers", *IEEE Transaction on Applied Superconductivity*.vol.11. NO.1 March 2001
- [45] M. Fardmanesh, A. Rothwarf, and K. Scoles, "Low and midrange modulation frequency response for YBCO infrared detectors: Interface effects on the amplitude and phase," *IEEE Trans Appl. Superconductivity*, vol. 5, no. 1, pp. 7–13, Mar. 1995.
- [46] TR Schimert, N Cunningham, G Francisco, R Gooch," Low-cost low-power uncooled 120x160 a-Si-based microinfrared camera for law enforcement applications", *Proc. SPIE*, 2001
- [47] W.M. Putty, K. Najafi," Micronachined vibrating ring gyroscope", *IEEE Hilton Head '94 Workshop, Technical Digest* (1994) 213-220.
- [48] G. Lin, C.J. Kim, S. Konishi." Design, fabrication, and testing of a C-shaped actuator", *Transducers '95 Digest of Tech. Papers*, Vol. 2, (1995), pp.416-419



- [49] J.W. Suh, C.W. Stormer," Characterization of multi-segment organic thermal actuators", Transducers '95 Digest of Tech. Papers, Vol. 2 (1995), pp. 333-336
- [50] A. Haberli, O. Paul, P. Malcovati," CMOS Integration of a thermal pressure sensor system", Proc. IEEE ISCAS'96, vol. 1, (1996) pp. 377-380
- [51] D. Westberg, O. Paul, G. Anderson, and H. Baltes," A CMOS compatible device for fluid density measurements", Proc. IEEE MEMS '97 (1997)
- [52] Ge Li, Ningyi Yuan, Jinhua Li, and Xiaoshuang Chen," Thermal simulation of micromachined bridge and self-heating for uncooled VO<sub>2</sub> infrared microbolometer", Sensor and actuators A, vol. 126, (2006) pp. 430~435.
- [53] Biao Li," Design and simulation of an uncooled double cantilever microbolometer with the potential for ~mK NETD", Sensor and actuator A, vol.112, (2004), pp. 351~359
- [54] Mahmoud Almasri, Bai Xu, and James Castracane," Amorphous silicon two color microbolometer for uncooled IR detection", IEEE sensors journal, vol. 6, April 2006, pp.293~300
- [55] O. Paul, H. Baltes, "Novel fully CMOS-compatible vacuum sensor", Sensor and Actuators, A46 (1995), 143~146
- [56] Chang-Jin Kim, John Y. Kim and Balaji Sridharan ," Comparative evaluation of drying techniques for surface micromachining," Sensors and Actuators A: Physical, Volume 64, Issue 1, 1 January 1998, Pages 17-26
- [57] B. Bhushan (ed.), Handbook of Micro/Nano Tribology, CRC Press, 1995.
- [58] Youngjoo Yee, Myoungkyu Park and Kukjin Chun, A sticking Model of Suspended Polysilicon Microstructure Including Residual stress Gradient and Postrelease Temperature, IEEE J. Microelectromech. Syst., vol. 7, no. 3 (1998) pp. 339-344
- [59] Stanley Wolf, Richard N. Tauber, "Silicon processing for the VLSI era: part 1", Sunset Beach, California, pp.49~51.

# *Part III*

*Design and simulation of circularly  
polarized slot antennas for wireless  
microsensor applications*



# Chapter1

## Introduction

### 1.1 Antenna polarization review for signal communication

Antenna polarization is a very important consideration when choosing and installing an antenna. Most communications systems use vertical, horizontal or circular polarization. Knowing the difference between polarizations and how to maximize their benefit is very important for the antenna design.

An antenna is a transducer that converts radio frequency electric current to electromagnetic waves that are then radiated into space. The electric field or "E" plane determines the polarization or orientation of the radio wave. In general, most antennas radiate either linear or circular polarization. A linear polarized antenna radiates wholly in one plane containing the direction of propagation. In a circular polarized antenna, the plane of polarization rotates in a circle making one complete revolution during one period of the wave. If the rotation is clockwise looking in the direction of propagation, the sense is called right-hand-circular (RHC). If the rotation is counterclockwise, the sense is called left-hand-circular (LHC). An antenna is said to be vertically polarized (linear) when its electric field is perpendicular to the Earth's surface. An example of a vertical antenna is a broadcast tower for AM radio antenna. Horizontally polarized (linear) antennas have their electric field parallel to the Earth's surface. Television transmissions in the USA use horizontal polarization.

However, a circular polarized wave radiates energy in both the horizontal and vertical planes and all planes in between. The difference, if any, between the maximum and the minimum peaks as the antenna is rotated through all angles, is called the axial ratio or ellipticity and is usually specified in decibels (dB). If the axial ratio is near 0 dB,

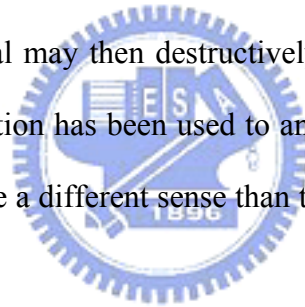
the antenna is said to be circular polarized. If the axial ratio is greater than 1 ~ 2 dB, the polarization is often referred to as elliptical polarization. Polarization is an important design consideration. The polarization of each antenna in a system should be properly aligned. Maximum signal strength between stations occurs when both stations are using identical polarization.

Besides, on line-of-sight (LOS) paths, it is most important that the polarization of the antennas at both ends of the path use the same polarization. In a linearly polarized system, a misalignment of polarization of 45 degrees will degrade the signal up to 3 dB and if misaligned 90 degrees the attenuation can be 20 dB or more. Likewise, in a circular polarized system, both antennas must have the same sense. If not, an additional loss of 20 dB or more will be incurred. Also note that linearly polarized antennas will work with circularly polarized antennas and vice versa. However, there will be up to a 3 dB loss in signal strength. In weak signal situations, this loss of signal may impair communications. Cross polarization is another consideration. It happens when unwanted radiation is present from a polarization which is different from the polarization in which the antenna was intended to radiate. For example, a vertical antenna may radiate some horizontal polarization and vice versa. However, this is seldom a problem unless there is noise or strong signals nearby. Vertical polarization is most often used when it is desired to radiate a radio signal in all directions such as widely distributed mobile units. Vertical polarization also works well in the suburbs or out in the country, especially where hills are present. As a result, nowadays most two-way Earth to Earth communications in the frequency range above 30 MHz use vertical polarization. Horizontal polarization is used to broadcast television in the USA. Some say that horizontal polarization was originally chosen because there was an advantage to not have TV reception interfered with by vertically polarized stations such as mobile radio. Also, man made radio noise is predominantly vertically polarized and the use of horizontal polarization would provide

some discrimination against interference from noise.

Circular polarized is most often use on satellite communications. This is particularly desired since the polarization of a linear polarized radio wave may be rotated as the signal passes through any anomalies (such as Faraday rotation) in the ionosphere. Furthermore, due to the position of the Earth with respect to the satellite, geometric differences may vary especially if the satellite appears to move with respect to the fixed Earth bound station. Circular polarization will keep the signal constant regardless of these anomalies. As stated earlier, for best performance, it is desirable to use an antenna with the same polarization on both ends of a communications path.

On another note, when radio waves strike a smooth reflective surface, they may incur a 180 degree phase shift, a phenomenon known as specular or mirror image reflection. The reflected signal may then destructively or constructively affect the direct LOS signal. Circular polarization has been used to an advantage in these situations since the reflected wave would have a different sense than the direct wave and block the fading from these reflections.



## **1.2 Microstrip antenna for circular polarization (CP)**

So far, the most common use in circularly polarized wireless communication applications is microstrip-type antenna. In general, the feeding method of circularly polarized antenna mainly includes two categories which are dual-feed and single-feed. The major advantage of single-feed, circularly polarized microstrip antennas is their simple structure, which does not require an external polarizer. They can, therefore, be realized more compactly by using less board space than do dual-feed, circularly polarized microstrip antennas. Many designs of single-feed, circularly polarized microstrip antennas with square or circular patches are known [1]. Recently, various CP designs

with a compact patch size at a fixed operating frequency have been reported. In these designs, the compact CP techniques used include embedding a cross-slot of unequal arm lengths [2, 3], embedding a Y-shaped slot of unequal arm lengths [4], inserting slits or spur lines at the patch boundary [5–13], truncating patch corners or tips [14–17], introducing small peripheral cuts at the boundary of a circular patch [18], adding a tuning stub [19–21] or a bent tuning stub [22], among others. For feeding these compact CP designs, a probe feed or an edge-fed microstrip-line feed can be used. A compact CP design using a  $50\Omega$  inset microstrip-line feed has also been developed. In this case, the main problem to be solved arises from the perturbation effects caused by the inset microstrip line on the excited patch surface currents, which makes it difficult for the excitation of two orthogonal near-degenerate resonant modes for CP radiation. Several possible designs for solving this problem have been reported [23].



### **1.3 Coplanar waveguide fed slot antenna**

Coplanar waveguide (CPW) was widely studied as an alternate to microstrip line for feeding square slot antenna in past few years, because they are compatible with the monolithic microwave integrated circuits (MMIC) and active device applications [24-27]. Besides, the CPW-fed slot antenna can also have relatively much wider impedance bandwidth than the conventional microstrip antenna [28, 29]. They have enough bandwidth to support modern wireless communication. Thus, the designs of the CPW-fed slot antennas have recently received much attention, especially for the circularly polarized CPW-fed slot antenna. In order to obtain circularly polarized (CP) radiation by a single feed, many microstrip antenna designs have been reported [30]. However, the obtained CP bandwidth of the conventional microstrip antenna determined by 3-dB axial-ratio (AR) is usually narrow and less than 2%. It is also noted that most of the

available circularly polarized slot antennas are designed by a microstrip feed. K.L. Wong et al. [31] proposed the microstrip-line-fed ring slot antennas with 3-dB AR bandwidth of only about 4.3% and 3.5% for square and annular ring slot antennas, respectively. However, few studies have been done on the design of CPW-fed CP slot antennas [32, 33]. It is well known that CPW-fed slot antennas have the advantage of uniplanar geometry and are easier to fabricate than the design with a microstrip feed. In addition, the CPW-fed CP slot antennas have also wider impedance bandwidth than microstrip-fed CP slot antenna. The best case of the 3-dB and 1-dB AR bandwidths at the center frequency of 2 GHz in Ref. [32] can reach as large as 18% and 13%, respectively, but the antenna size is  $70 \times 70 \text{ mm}^2$  and the length of the square slot is 40 mm. Besides, Y.B. Chen [33] presented a CPW-fed circularly polarized square slot antenna which has 3-dB AR bandwidth of 17% and input return-loss bandwidth of 43% with respect to the center frequency 2.6 GHz, but the presented antenna size is large to  $100 \times 100 \text{ mm}^2$ .

In this research, we propose a new design of a CPW-fed CP square slot antenna using a square ring with a gap. This new slot antenna resembles the presented antenna geometry of these literatures [34-36] which include two rhombic or rectangular loop wire antennas. The presented antennas in these literatures have several disadvantages such as larger structure, more difficult fabrication, and narrower AR bandwidth than our proposed antenna. The proposed antenna improves these drawbacks and shows good circularly polarized radiation performances.

## Chapter 2

### Theory of circularly polarized antenna

In general, an antenna will radiate an elliptical polarization, which is defined by three parameters: axial ratio, tilt angle, and sense of rotation [57, 58]. When an axial ratio is infinite or zero, the polarization becomes linear with the tilt angle defining the polarization. Sense is not applicable in this case. The quality of a linear polarization is usually indicated by the level of the cross polarization. For a unity axial ratio, a perfect circular polarization (CP) results and the tilt angle is not applicable. The axial ratio is generally used to specify the quality of the circularly polarized waves [59]. Antennas produce circularly polarized waves when two orthogonal field components with equal amplitude but in phase quadrature are radiated. Various printed antennas are capable of satisfying these requirements. They can be classified as resonator and traveling wave types. A resonator-type antenna consists of a single patch antenna that is capable of simultaneously supporting two orthogonal modes in phase quadrature or an array of linearly polarized resonating patches with proper orientations and phasings. A traveling wave type of antenna is usually constructed from a microstrip transmission line.

#### 2.1 dual-fed CP patch antenna

The fundamental configurations of a dual-orthogonal fed circularly polarized patch using an external power divider are shown in Figure 3-2-1. The patch is usually square or circular. The dual-orthogonal feeds excite two orthogonal modes with equal amplitude but in-phase quadrature. Several power divider circuits that have been successfully employed for CP generation include the quadrature hybrid, the ring hybrid, the Wilkinson power divider, and the T-junction power splitter. The quadrature hybrid splits the input



into two outputs with equal amplitude but  $90^\circ$  out of phase. Other types of dividers, however, need a quarter-wavelength line in one of the output arms to produce a  $90^\circ$  phase shift at the two feeds. Consequently, the quadrature provides a broader axial ratio bandwidth. These splitters can be easily constructed from various planar transmission lines.

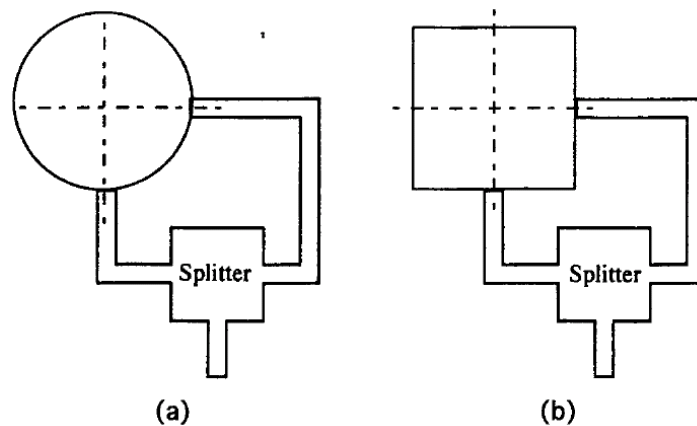


Figure 3-2-1 Dual-fed (a) circular and (b) square patch antennas



## 2.2 singly fed CP patch antenna

Typical configurations for singly fed CP microstrip antennas are shown in Figure 3-2-2. A single point feed patch capable of producing CP radiation is very desirable in situations where it is difficult to accommodate dual orthogonal feed with a power network. Because a patch with a single point feed generally radiates linear polarization, in order to radiate CP, it is necessary for two orthogonal patch modes with equal amplitude and in-phase quadrature to be induced. This can be accomplished by slightly perturbing a patch at appropriate locations with respect to the feed. Although various perturbation configurations for generating CP have been reported [61], they operate on the same principle of detuning degenerate modes of symmetrical patch by perturbation segments as

illustrated in Figure 3-2-3. The fields of a singly fed patch can be resolved into two orthogonal degenerate modes, 1 and 2. Proper perturbation segments will detune the frequency response of and 2 such that, at the operating frequency  $f_0$ , it is of the same amplitude but  $90^\circ$  out of phase with respect to mode 1. Hence, the two modes satisfy the required condition for CP radiation. As the frequency moves away from  $f_0$ , the axial ratio rapidly degrades while the input match usually remains acceptable. The actual detuning occurs either for one or both modes depending on the placement of perturbation segments.

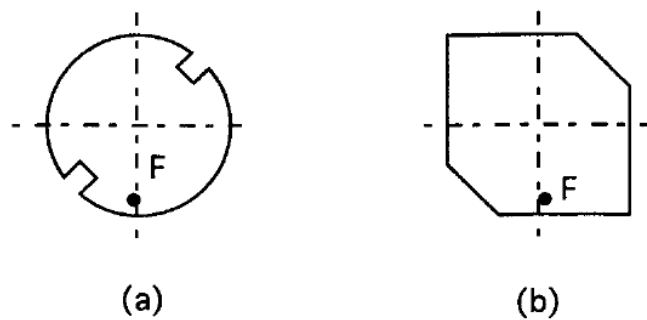


Figure 3-2-2 singly fed (a) circular and (b) square patch antennas

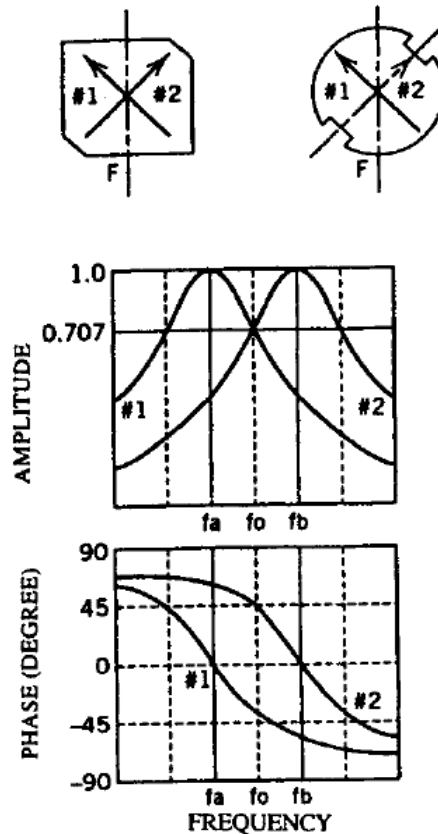


Figure 3-2-3 Amplitude and phase of orthogonal modes for singly fed patch antennas

### 2.3 Circularly polarized loop antennas with traveling wave current distribution

It is well-known that a single-fed circular wire loop antenna of one-wavelength circumference (called one-wavelength loop in short) creates a standing-wave current distribution and thus radiates a linearly polarized wave in the far-field zone [42]–[44]. It is also easy to understand that a one-wavelength circular loop can radiate perfectly circularly polarized waves in the direction perpendicular to the plane of the loop if a uniform traveling-wave current distribution is generated [45]. A common way to produce a uniform traveling-wave current distribution is to feed the loop antenna with two 90 phase shifted generators which are located 90 (or a quarter-wavelength) apart along the loop so that a superposition of two standing-wave current distributions with equal amplitude, 90 phase shift in time, and a quarter-wavelength difference in space results in

a perfectly uniform traveling-wave current distribution [46]. The disadvantage of this approach is the need for two sources or a 90 hybrid coupler. Another commonly used technique for achieving a traveling-wave current distribution is to load the antenna with resistors [47]. Obviously the main problem of this method is that it leads to low antenna efficiency since the resistors absorb the majority of fed power. It was demonstrated that a traveling-wave current distribution could be obtained if a circular loop is reactively loaded at a position of  $45^\circ$  away from the feed point [47].

However, it was shown in [48] that the obtained traveling-wave current distributions were far from uniform due to the high-value ( $300\ \Omega$ ) of the used reactance. (High-value impedance loading usually tends to block the flowing of current, thus causing a dip in the magnitude of the current distribution.) In addition, the loaded loop antenna usually needs to be placed at a considerable height above a ground plane (e.g., at a height of more than a quarter-wavelength considered in [48]) and results in a high input impedance (e.g., input resistance  $> 200\ \Omega$  and input reactance  $< 200\ \Omega$ ), thus causing difficulties in matching the antenna to the feeding system. Most importantly, no theoretical prediction has been given in [48] for the value of the loading reactance; therefore it was not clear why a traveling-wave current distribution could be achieved by the reactive load. However, RongLin Lin [49] resolved this problem and presented a method to determine the reactance loading for CP loop antenna with a uniform traveling wave current distribution. The geometry of a circular loop antenna loaded at  $\phi$  of  $45^\circ$  degrees with impedance  $Z_L$  is shown in Figure 3-2-4. The loop antenna has a height of  $h$  above the ground plane, and the current distribution on a loaded circular loop antenna is equal to a superposition of the currents generated by the feeding voltage  $V_o$  and the loading voltage  $V_L$  as shown in Figure 3-2-5.

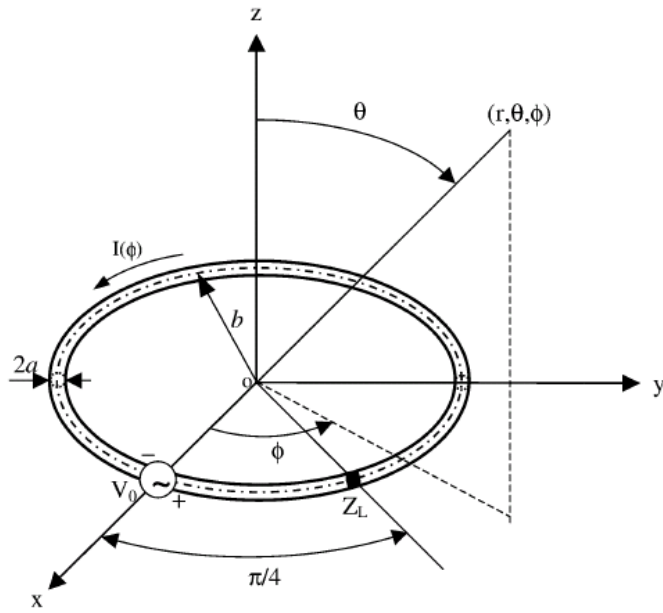


Figure 3-2-4 Geometry of a circular loop antenna loaded at  $\phi = 45^\circ$  with impedance  $Z_L$

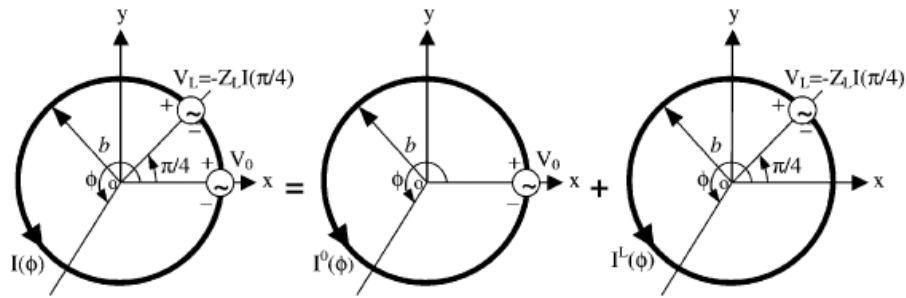


Figure 3-2-5 Equivalent model of current distribution

Besides, the uniform current distribution of this type of CP antenna is dependent on loading reactance varying with substrate height. In this research, we proposed a new design of a CPW-fed slot antenna for circular polarization. This type of slot antenna originates from the above antenna configuration and operational mechanism, but it provides simpler geometry, easier fabrication, smaller antenna size, and more integrable with other active devices. Circular polarization of the traveling-wave slot antenna can radiate by two mechanisms which are electric current excitation and magnetic current excitation. Figure 3-2-6 demonstrates the radiation mechanism of our proposed square slot antennas, and, of course, it is also applicable to circular slot antennas for CP

applications. In this figure, the four red arrows represent the electric or magnetic current. The direction of the arrows indicates the vector direction of the electric or magnetic current. It should be noted that the shading region can be strip line or slot line with respect to electric current or magnetic current, respectively. In this case as shown in Figure 3-2-6, the current at the left and right sides has the same direction and amplitude, and similarly the current at the upper and lower sides also has the same direction and amplitude. These two types of current will excite circularly polarized wave because they have equal amplitude and in-phase quadrature. The shorted strip or open slot with the included angle of  $45^\circ$  along the feed line is served as reactively loading similar to preceding statement.

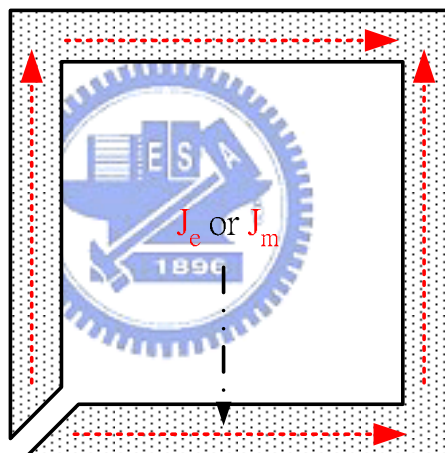


Figure 3-2-6 Radiation mechanism of the proposed CP slot antenna

## 2.4 The measurement of circular polarization

For many communication systems, it is preferable to operate in the circular polarization mode, where the trajectory of the tip of the E vector rotates about the propagation axis as a function of time. Such operation is the case for satellite and ground station antennas, since circular polarization (CP) operation removes the need to continuously align the two apertures, which would otherwise be required to maximize the

receive power. In addition, CP signals are not subject to the Faraday rotation effect [50], which causes the linear-field vectors to rotate as a consequence of interaction with static magnetic fields along the propagation path. Therefore, again, the polarization match between the antennas can be maintained without the use of complex tracking systems. A perfectly circularly polarized wave is generated by an antenna that simultaneously excites two orthogonal vectors of equal amplitude and in phase quadrature. Formal definitions for this mode of propagation are given in the IEEE Standard Test Procedures for Antennas [51], where the sense of polarization is given by the direction of the rotation of the vector describing a circle for an observer looking in the direction of propagation as shown in Figure 3-2-7.

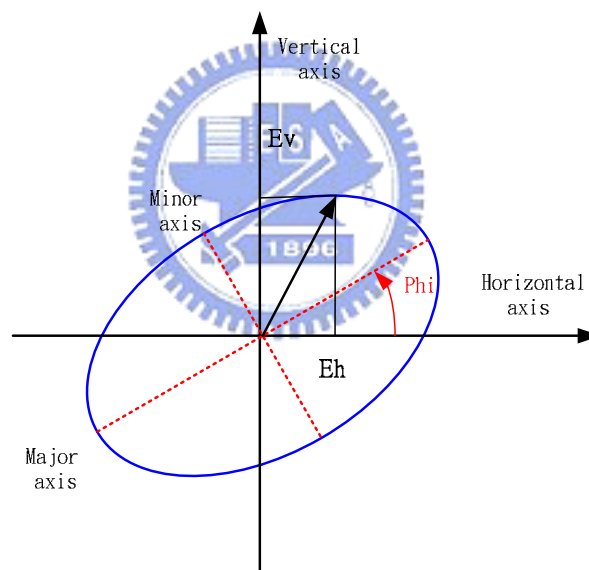


Figure 3-2-7 Polarization ellipse

IF the complex voltage terms in the horizontal and vertical planes (or any two orthogonal cuts)  $E_H$  and  $E_V$  are of equal amplitude and in phase quadrature, these terms may be combined to express either the RHCP or LHCP wave components [52] as follows:

$$E_{RHCP} = \frac{1}{\sqrt{2}}(E_H + jE_V)$$

$$E_{LHCP} = \frac{1}{\sqrt{2}}(E_H - jE_V)$$

$$E_H = E_{Hr} + jE_{Hi} \tag{2-1}$$

where  $E_{Hr} = H_A \cos(H_p), E_{Hi} = H_A \sin(H_p)$

$$E_V = E_{Vr} + jE_{Vi}$$

where  $E_{Vr} = V_A \cos(V_p), E_{Vi} = V_A \sin(V_p)$

The horizontal and vertical amplitude ( $H_A, V_A$ ) and phase components ( $H_p, V_p$ ) are quantities that are measured at each angle  $\theta$  in the far field of the antenna, which source horn orientated at angles  $\phi = 0^\circ$  and  $\phi = 90^\circ$  as presented in Figure 3-2-8.

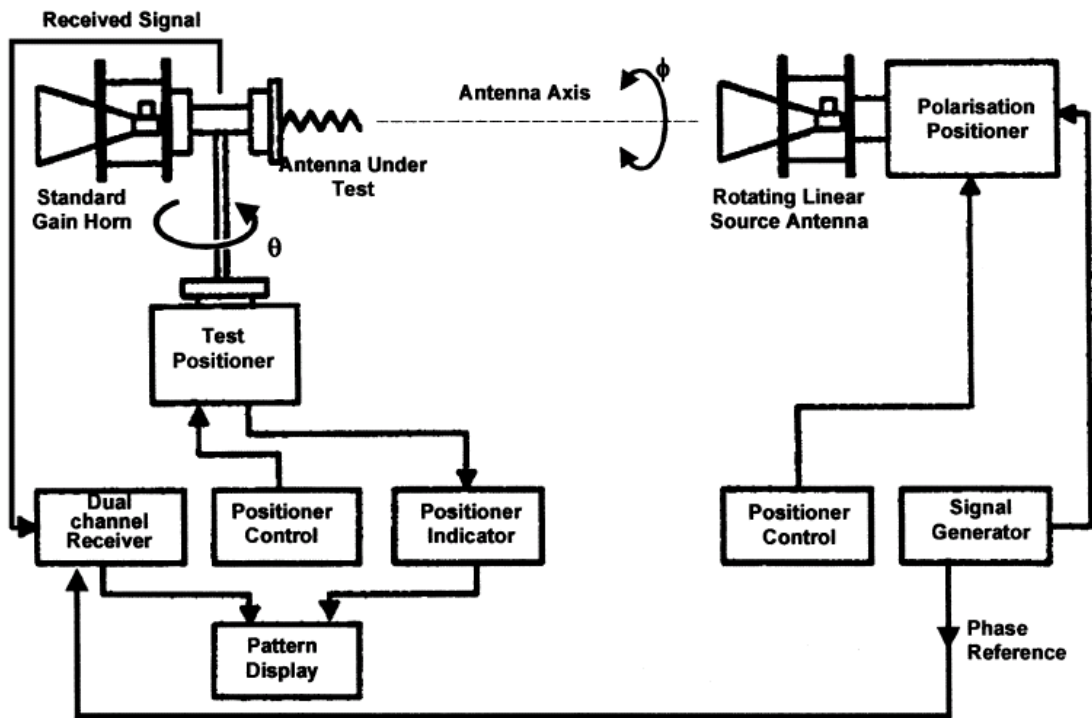


Figure 3-2-8 Antenna measurement setup for measuring polarization pattern



Besides, inserting above equations into estimating the two hands of polarization:

$$E_{RHCP} = \frac{1}{\sqrt{2}} \{ [H_A \cos(H_p) - V_A \sin(V_p)] + j[H_A \sin(H_p) + V_A \cos(V_p)] \}$$

$$E_{LHCP} = \frac{1}{\sqrt{2}} \{ [H_A \cos(H_p) + V_A \sin(V_p)] + j[H_A \sin(H_p) - V_A \cos(V_p)] \}$$
(2-2)

In each hand of polarization, the power can be expressed by

$$P(dB) = 10 \log_{10} \left( \frac{E^2}{120\pi} \right)$$
(2-3)

where  $120\pi$ : the wave impedance of free space.

From our measurement of antenna polarization patterns, the definition of axial ratio can be modified from  $AR(dB) = 20 \log \left( \frac{Major - axis}{Minor - axis} \right)$  to as follows:

$$AR(dB) = 10 \log \left( \frac{E_{RHCP} + E_{LHCP}}{E_{RHCP} - E_{LHCP}} \right)^2 = 10 \log \left\{ \frac{H_A \cos(H_p) + jH_A \sin(H_p)}{j[V_A \cos(H_p) + V_A \sin(H_p)]} \right\}^2 =$$

$$10 \log \left( \frac{E_H}{jE_V} \right)^2 = P_{EH}(dB) - P_{EV}(dB)$$
(2-4)

We will use the preceding formulas to predicate and simulate the polarization pattern as shown in Figure 3-2-9, and thus the simulated data will be also in comparison with the measuring results. This is the first time to present the polarization patterns by simulations.

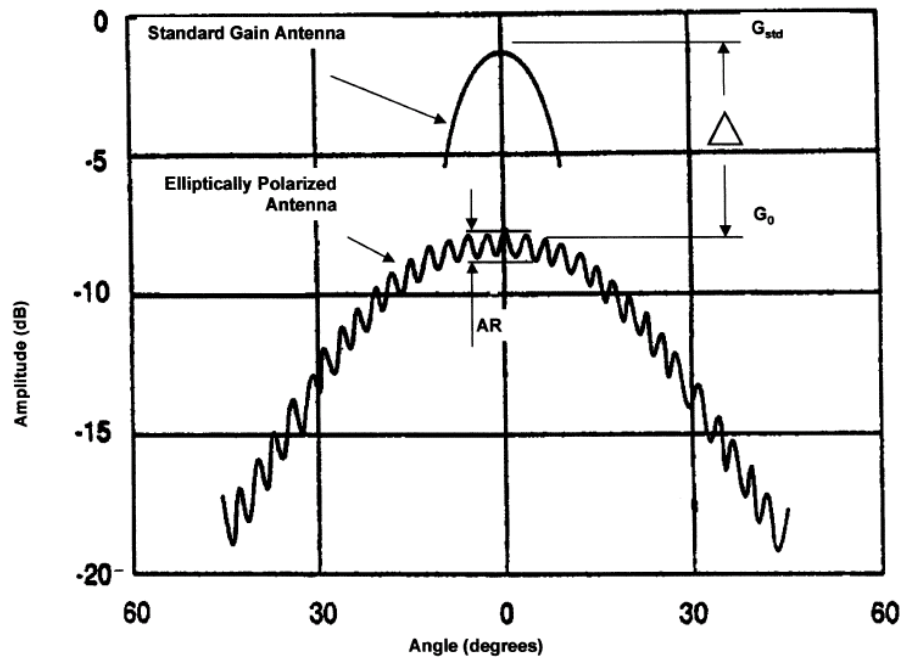


Figure 3-2-9 Measurement of the polarization pattern

From above figure, we can observe that a practical antenna normally generates a desired reference polarization in addition to an undesirable cross-polar component, which is polarized in opposite hand. The reference and cross-polar spatial patterns can also be retrieved from an AR plot, which is generated using a linearly polarized spinning source antenna. This information requires the source horn to be continuously rotated about its axis ( $\phi$ ) while moving the antenna under test in azimuthal ( $\theta$ ). The ripples in the polarization pattern are a consequence of the beam ellipticity, which occurs when a finite cross-polar component exists. Thus, the depth of the nulls defines the AR.



## Chapter 3

### Electric current excited CP slot antenna

In this research, we proposed several different circularly polarized slot antennas. They are mainly divided into two different mechanisms which are electric current excitation and magnetic current excitation. In this chapter, only the CP slot antennas by electric current excitation are discussed, and the antennas by magnetic current excitation are presented in the next chapter.

#### 3.1 Type 1

##### 3.1.1 Antenna Configurations

The geometry of the proposed CPW-fed circularly polarized slot antenna is depicted in Figure 3-3-1. The substrate used an inexpensive FR4 dielectric substrate with a thickness of 1.6 mm, a relative permittivity of 4.4, and a loss tangent of 0.0245. In this suggested antenna, the lengths of  $L_1$ ,  $L_2$ ,  $L_3$ ,  $L_f$  are fixed to be 49 mm, 29 mm, 17 mm, 11mm respectively, and the widths of  $W_1$ ,  $W_2$ ,  $W_3$ ,  $W_5$ ,  $W_6$  are fixed to be 49 mm, 23 mm, 17 mm, 15 mm, 10 mm respectively. A 50 ohm CPW transmission line, having a protruded single strip of width  $W_f = 6.3$  mm and a gap of distance  $g_1 = 0.5$  mm between the signal strip and the ground plane, is used to feed the proposed antenna. By adjusting the length of the protruded strip  $L_C$ , the impedance matching of the slot antenna can be easily controlled, and its width of the protruded strip is fixed to be 1 mm. Besides, for the proposed antenna, an outer rectangular ring is printed on the center of the slot antenna, and it has a gap ( $g_2$ ) to excite circularly polarized radiation. If the gap is located at the lower-left corner of the rectangular ring, the slot antenna excites a left hand circular polarization (LHCP). However, if the gap is located at the lower-right corner, the slot antenna generates a right hand circular polarization (RHCP). From the empirical

experiences, the circumference of the midline of the outer rectangular ring is about  $1.03 \lambda$  ( $\lambda$  is the wavelength of operational frequency) for the sake of achieving the desirable operational frequency as the width of the outer rectangular ring is chosen to be 1mm. In order to improve the 3dB AR bandwidth and the impedance bandwidth, an inner rectangular ring has been implemented. The space between inner ring and outer ring is 1 mm, and the width of both rings is 1 mm.

### 3.1.2 Summary

The length of the protruded signal strip ( $L_C$ ) in the proposed antenna is varied and the influence on the impedance matching is investigated. Figure 3-3-2 shows the return loss against frequency for the proposed antenna with different signal strip length of  $L_C = 9, 8, 7, 6, 5$  mm when  $g_2 = 1.35$  mm and  $L_4 = W_4 = 10$  mm. It is apparent that as the length of  $L_C$  decreases, the fundamental resonant frequency increases, and the return loss decreases and then increases. The minimum value of return loss occurs as  $L_C = 7$  mm. It presents a fundamental resonant frequency of 2.44GHz with a return loss of -40.93 dB, and has the impedance bandwidth of 880 MHz or 36.07% which is from 2.19 GHz to 3.07 GHz. Besides, from the analysis of AR against frequency with the variation of  $L_C$ , the fundamental resonant frequency consisting with the frequency of minimum AR value only occurs in the condition of  $L_C = 7$ mm. The return loss against frequency and AR against frequency for the proposed antenna with different ground size ( $W_4, L_4$ ) as  $L_C = 7$  mm and  $g_2 = 1.35$  mm are demonstrated in Figure 3-3-3(a), Figure 3-3-3(b) respectively. It is evident that the ground size has less influence on the fundamental resonant frequency, but has larger effect on the value of return loss. Besides, the ground size also affects the AR profile, and it is obvious that as  $W_4 = L_4 = 12, 11, 10$  mm, the minimum AR value for the proposed antenna occurs at the frequency of 2.44 GHz. However, as  $W_4 = L_4 = 9, 8$  mm, the minimum AR value occurs at 2.34 GHz and 2.24 GHz respectively, but they

does not meet the fundamental resonant frequency. In comparison with these different ground sizes, the proposed antenna with the length of  $L_4 = W_4 = 10$  mm has the widest 3dB AR bandwidth of 420 MHz or 17.21% which is from 2.23 GHz to 2.65 GHz, the minimum AR value of 0.54 dB, and the fundamental resonant frequency of 2.44GHz.

Figure 3-3-4(a) and Figure 3-3-4(b) present respectively the return loss against frequency and the AR against frequency with different gap ( $g_2$ ) located at the lower-left corner of the outer rectangular ring as the length of  $L_4 = W_4 = 10$  mm and  $L_C = 7$  mm. It is apparent that as the space of  $g_2$  decreases, both the fundamental resonant frequency and the return loss value decrease. As the space of  $g_2 = 1.35$  mm, the proposed antenna has the maximum 3dB AR bandwidth of 420 MHz or 17.21% which is from 2.23 GHz to 2.65 GHz within the impedance bandwidth (-10 dB return loss), and its minimum value of axial ratio is about 0.54dB at the frequency of 2.44GHz.

From above discussions, the best condition for the proposed antenna is the length of  $L_C = 7$ mm,  $L_4 = W_4 = 10$  mm, and  $g_2 = 1.35$  mm. Figure 3-3-5 shows the axial ratio against elevation angle ( $\theta$ ) for the proposed antenna with different azimuthal angles of  $\varphi = 0, 45, 90, 135$  degrees. From Fig. 3.1.5, all of the 3 dB AR bandwidth for the proposed antenna at the four azimuthal angles is at least covered the range of  $\theta$  from -30 to 30 degrees, and all of the AR values at the elevation angle of zero degree are below 1dB. It is obvious that the proposed antenna demonstrates very well performance of AR space distribution.

The radiation patterns against elevation angle and against azimuthal angle are shown in Figure 3-3-6 (a) and (b) respectively. From these figures, the proposed antenna presents good LHCP radiation, and shows omni-directional radiation pattern for all of the azimuthal angles. These good radiation characteristics are very attractive to modern wireless communication applications.

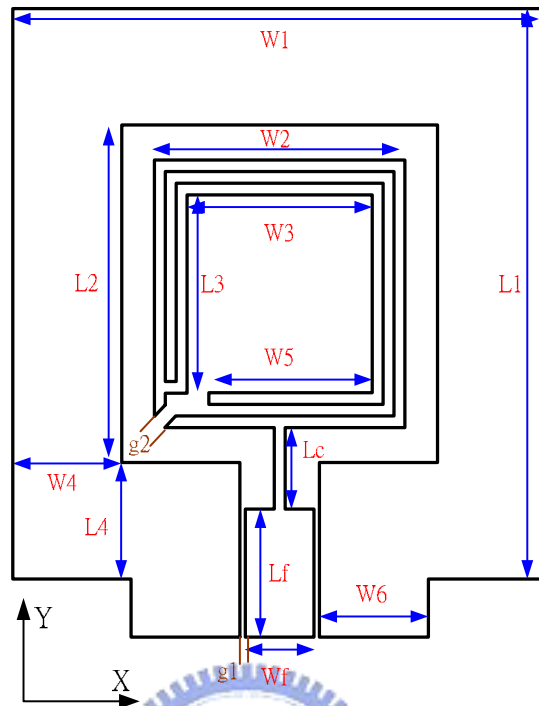


Figure 3-3-1 Geometry of the proposed CPW-fed circularly polarized slot antenna

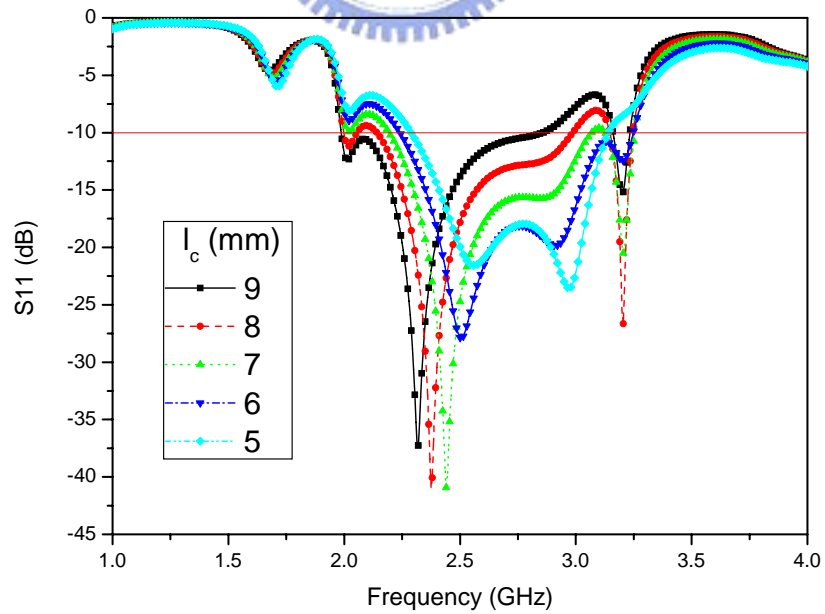
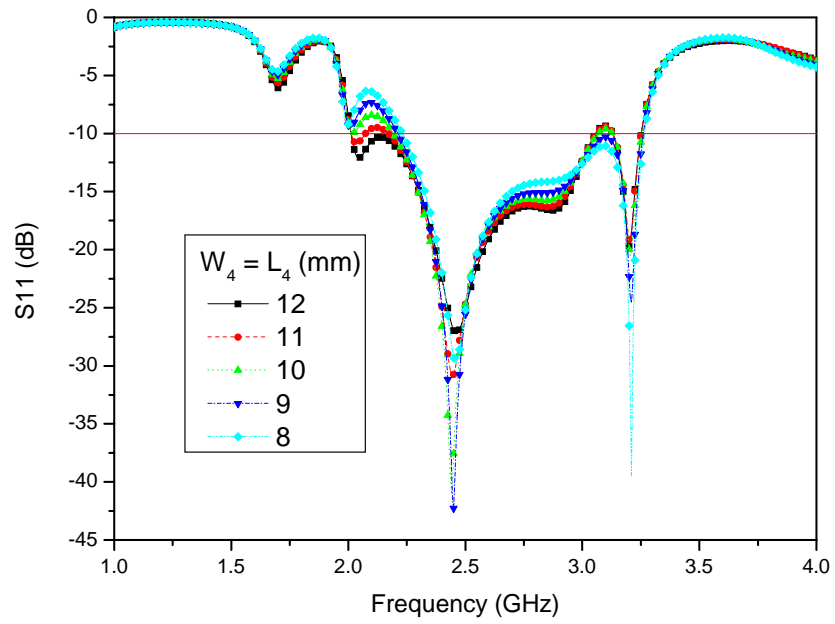
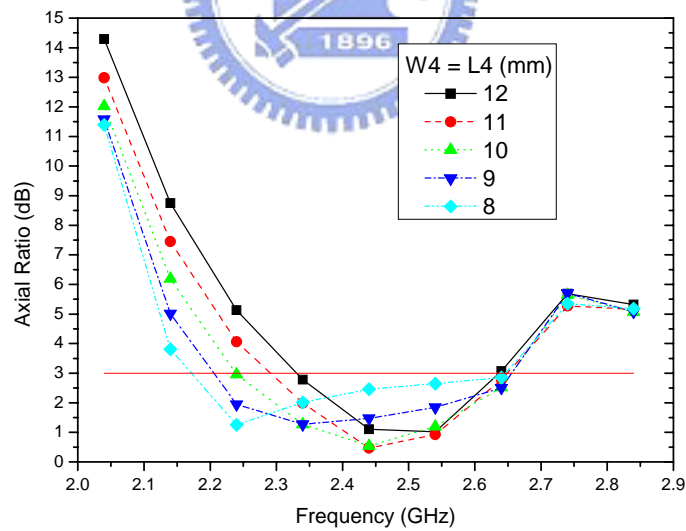


Figure 3-3-2 Return loss against frequency for the proposed antenna with different signal strip length ( $L_c$ ) as the length of  $L_4 = W_4 = 10\text{mm}$  and  $g_2 = 1.35\text{ mm}$

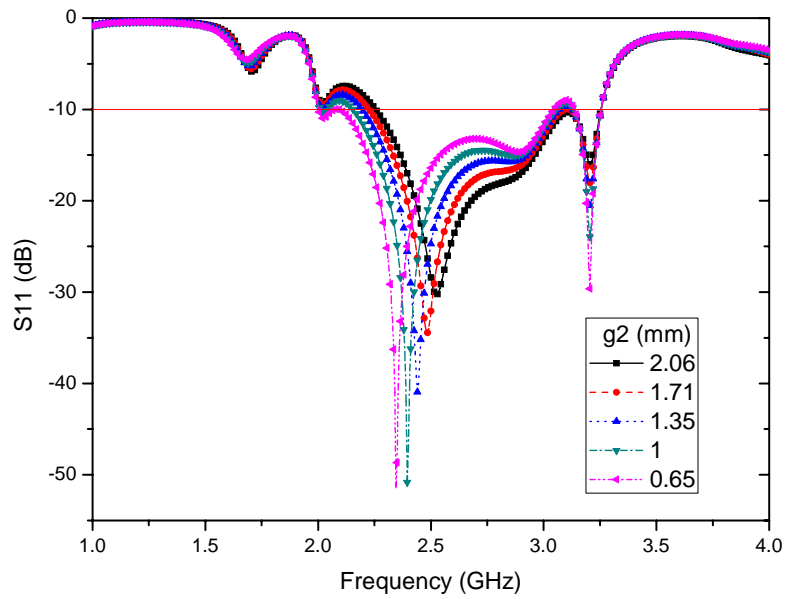


(a)

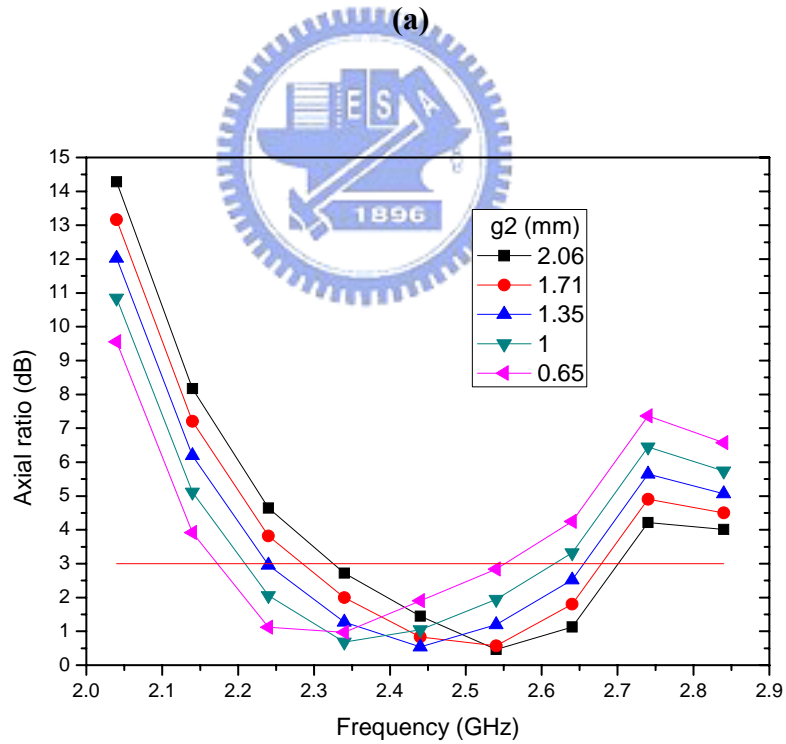


(b)

Figure 3-3-3 (a) Return loss against frequency and (b) axial ratio against frequency for the proposed antenna with different ground size ( $L_4 = W_4$ ) as the length of  $L_C = 10$  mm, and  $g_2 = 1.35$  mm.



(a)



(b)

Figure 3-3-4(a) Return loss against frequency and (b) axial ratio against frequency for the proposed antenna with different gap space ( $g_2$ ) as the length of  $L_C = 10$  mm, and  $L_4 = W_4 = 10$  mm.



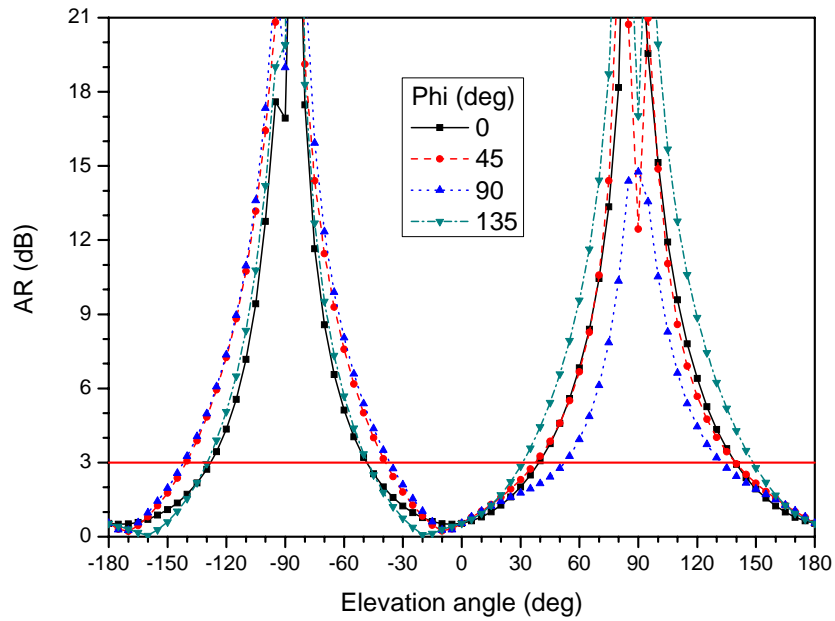
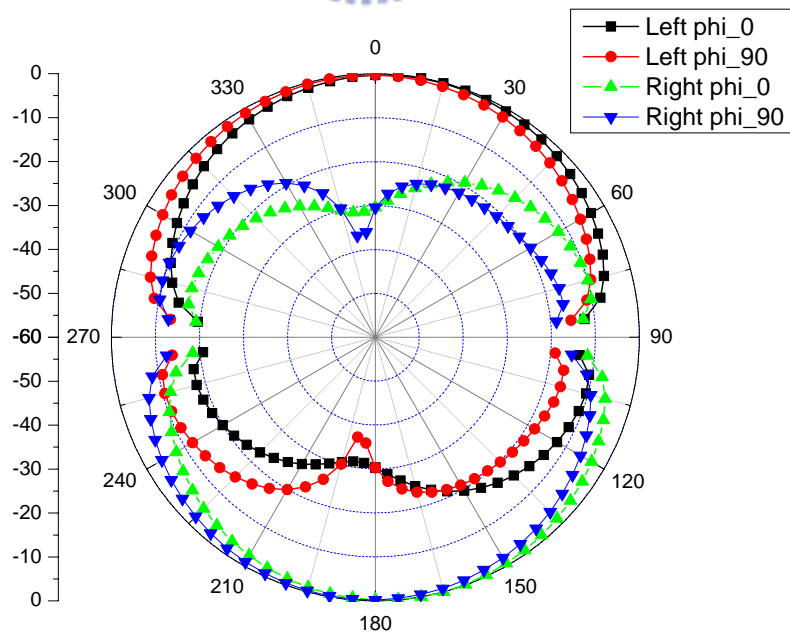
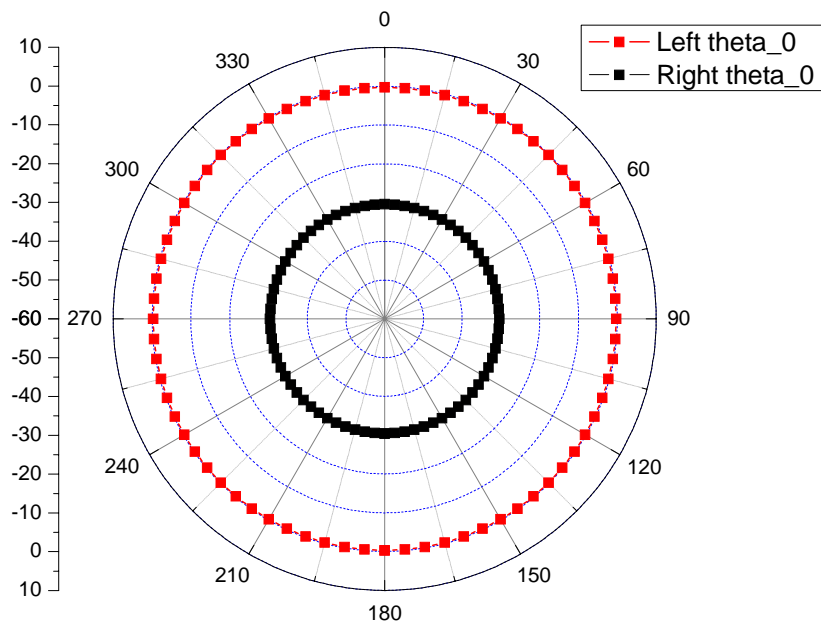


Figure 3-3-5 Axial ratio against elevation angle ( $\theta$ ) at the resonant frequency of 2.44 GHz for the proposed antenna with the different azimuthal angle as the length of  $L_C = 10$  mm,  $L_4 = W_4 = 10$  mm,  $g_2 = 1.35$  mm.

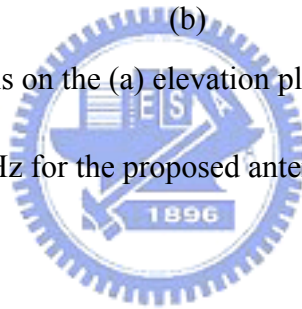


(a)



(b)

Figure 3-3-6 Radiation patterns on the (a) elevation plane and (b) azimuthal plane at the resonant frequency of 2.44 GHz for the proposed antenna as the length of  $L_C = 10$  mm,  $L_4 = W_4 = 10$  mm,  $g_2 = 1.35$  mm.



## 3.2 Type 2

### 3.2.1 Antenna Configurations

The geometry of the proposed antenna is shown in Figure 3-3-7. The proposed slot antenna is realized on an inexpensive FR4 dielectric material with a thickness ( $h$ ) of 1.6 mm, a relative permittivity ( $\epsilon_r$ ) of 4.4, and a loss tangent of 0.0245. The square slot of a side length of  $L_2$  was printed on a grounded substrate. A 50 Ohm CPW transmission line with a protruded signal strip is used to feed the proposed antenna. The 50 Ohm CPW feed has a signal strip of width  $W_f = 6.3$  mm and a gap of distance  $g_2 = 0.5$  mm between the signal strip and the ground plane. The signal strip of the CPW is narrowed to have a width of  $W_p$ , and protrudes a length of  $L_c$  to connect with a square ring located at the center of the square slot. In this proposed geometry, CP radiation can be excited by using a gap ( $g_1$ ) at the lower left or lower right corner of the square ring. If the gap is located at the lower-left corner of the square ring, the slot antenna excites a left hand circular polarization (LHCP). Conversely, if the gap is located at the lower-right corner, the slot antenna generates a right hand circular polarization (RHCP). The most important design procedure to carry out the proposed CP slot antenna is to make a decision on the square-ring circumference, because the operational frequency mainly depends on the circumference of the square ring. In order to excite CP radiation, the square-ring circumference is designed to equal one effective wavelength on the substrate at the desirable operational frequency. However, in this condition, good CP radiation and good impedance matching of the proposed antenna cannot be achieved at the same time, though we may sacrifice AR performance to attain better impedance matching. Therefore, many optimum simulations in this paper are conducted to obtain both of good CP radiation (the minimum AR value less than 1.5 dB) and good impedance matching (return loss less than -30 dB).

From many simulated results, better CP radiation and wider 3dB AR bandwidth can be obtained at the frequency of 2.45 GHz in this study as the square-ring circumference is about  $1.15 \lambda_{\text{eff}}$  ( $\lambda_{\text{eff}}$  is the effective wavelength of the operational frequency within the coplanar waveguide structure) on the FR4 substrate used here. In addition to the square-ring circumference, the impedance of the proposed slot antenna can be matched at the desirable frequency by adjusting the length of the protruded strip  $L_c$ . If the square-ring circumference does not appropriately choose, the impedance matching only using the protruded strip is hard to match well.

### 3.2.2 Results and Discussions

The goal of this study was to develop a new CP square-slot antenna including a square ring with a gap on a grounded FR4 substrate of thickness 1.6mm, relative permittivity 4.4, dielectric loss tangent 0.0245, and grounded plane size  $51 \times 42 \text{ mm}^2$ . The geometrical parameters of the proposed slot antenna are designed at the operational frequency of 2.45 GHz.

In order to easily evaluate the circumference of the square ring related to the desirable operational frequency, several simulations on three different substrates which have the relative permittivity and thickness of (4.4 and 1.6 mm), (4.4 and 20 mm), and (9 and 1.6 mm) have been done by IE3D simulator, and the geometrical parameters of these slot antennas are listed and marked as Case 1, Case 2 and Case 3 in Table 3.1. To simplify the comparisons between these cases, all of the simulations with respect to return loss and CP axial ratio are optimum to have the minimum values at the operational frequency of 2.45 GHz, and, in the proposed antenna geometry, the dimensions of  $W_2$ ,  $g_1$  and the width of the square ring are fixed to be 7 mm, 1.3 mm and 1 mm, respectively. The optimum goals in these simulations are the 3-dB AR value less than 1.5 dB at the angle of (0, 0) and the return loss less than -30 dB at the frequency of 2.45GHz. These three fixed

values obtained by many simulations can achieve good performances of return loss and axial ratio on the substrate used in Case 1. In Table I, these effective wavelengths ( $\lambda_{\text{eff}}$ ) on different substrates at the frequency of 2.45 GHz are calculated by the software of LineGauge included in IE3D simulator. It can be seen that the circumferences of these square rings are about  $1.15 \lambda_{\text{eff}}$ ,  $1.12 \lambda_{\text{eff}}$ , and  $1.12 \lambda_{\text{eff}}$  for these three different substrates, respectively. The simulated results of return loss and axial ratio against frequency for these different substrates are shown in Figure 3-3-8 (a) and (b), respectively. Besides, if we introduce  $1.12 \lambda_{\text{eff}}$  to the square-ring circumference in Case 1, we can also obtain good CP radiation and 3-dB AR bandwidth. However, the proposed antenna with the use of  $1.15 \lambda_{\text{eff}}$  can obtain better antenna performances than that of using  $1.12 \lambda_{\text{eff}}$ .

Besides, the geometrical parameters obtained from the optimum simulations on the substrate of FR4 at two different operational frequencies of 4 and 1.8 GHz are also listed and marked as Case 4 and Case5, respectively, in Table 3.2.1. It should be noted that the ratio of the square-ring circumference to the effective wavelength is also about  $1.12 \lambda_{\text{eff}}$  at each case. The simulated results of axial ratio against frequency are shown in Figure 3-3-8(c). The AR values at their desirable frequencies have the minimum values (less than 1.5 dB) within their simulated ranges.

From above discussions, if the desirable frequency and the substrate parameters are known, we can use simulator to calculate the effective wavelength. Then, the square-ring circumference is equal to the effective wavelength multiplied by 1.12. Hence, the most important parameter affecting the response of the proposed antenna is decided. The further simulations need to be conducted to achieve the desirable response of the proposed antenna on different substrates or at different frequencies. It is worth noticing that the square-slot width and grounded plane width at the frequency of 1.965 GHz are about 36 mm and 50 mm based on our antenna designs and smaller than that presented in Ref. [53].

The influences of the protruded strip length ( $L_c$ ) and the grounded plane width ( $W_1$ ) have also been simulated and discussed in the following. Figure 3-3-9(a) and Figure 3-3-9(b) show the simulated results of return loss and ratio axial against frequency with the different protruded signal strip lengths ( $L_c$ ), respectively. With the increase of the protruded strip length ( $L_c$ ), the frequency with the minimum return loss slightly increases when the length of  $L_c$  is in the ranges of 5 - 7 mm and 8 - 9 mm. However, there are large variations in frequency within the range of 7 mm to 8 mm. The 3-dB AR bandwidth and the frequency with the minimum AR value only slightly change with the variation of the length of  $L_c$ . Thus, the protruded strip length mainly affects the behavior of return loss, but slightly influences the axial-ratio response.

The axial ratio could also be affected by the substrate width. The grounded plane effect has been simulated with variation of grounded plane widths. The return loss and axial ratio against frequency with different grounded plane widths ( $W_1$ ) are demonstrated in Figure 3-3-10 (a) and (b), respectively. From simulated results, it can be seen that the grounded plane width has major influence on axial ratio response and has less effect on return loss. The frequency with the minimum return loss slightly increases as the decrease of the grounded plane width ( $W_1$ ) except for  $W_1 = 38$  mm. Besides, the impedance bandwidths with different grounded plane widths are almost the same. From Figure 3-3-10(b), it can be noted that the grounded plane effect has large influence on axial ratio response. With the increase of grounded plane width, the frequency with the minimum AR value increases. Both AR bandwidths of the proposed antenna with  $W_1$  of 40 and 42 are widest in the simulated results, but the antenna with  $W_1$  of 42 has better AR response than that with  $W_1$  of 40. Furthermore, from other simulations which did not show here, if the range of the gap width ( $g_1$ ) is between 1.1 mm and 1.5 mm, it does not nearly affects both of the impedance matching and CP radiation.

In order to present the antenna geometrical parameters with the best antenna

performances at the operational frequency of 2.45 GHz, many simulated results and optimum procedures have been done. Figure 3-3-11(a) and Figure 3-3-11(b) show the measured and simulated results of return loss and axial ratio against frequency, respectively, for the proposed antenna with the protruded strip length of  $L_c = 7$  mm, the gap ( $g_1$ ) of 1.3 mm, the length of  $L_3 = 24$  mm, and the grounded plane width ( $W_1$ ) of 42 mm. The fundamental resonant frequency is about 2.45 GHz and 2.5 GHz for the simulated and measured results, respectively. The difference between the simulation and measurement results from the fabrication inaccuracy and measured error. From the measured curve in Figure 3-3-11(a), the proposed antenna has a fundamental resonant frequency of 2.5 GHz with the minimum return loss of -39.9 dB, and the impedance bandwidth of 460 MHz (or 18.4%) including the frequency from 2.28 GHz to 2.74 GHz. In addition, Fig. 3.2.5(b) presents the measured bandwidth of 3-dB axial-ratio (AR) of 360 MHz or (14.4%) including the frequency from 2.28 GHz to 2.64 GHz, and the bandwidth of 1dB axial-ratio is about 100 MHz and the frequency from 2.42 GHz to 2.52 GHz. The minimum AR value occurs at the frequency of 2.5 GHz and is about 0.8 dB.

The circularly polarized radiation patterns against elevation angle with different azimuthal angles of  $\phi = 0$  and 90 degrees at the frequency of 2.45 GHz are simulated and demonstrated in Figure 3-3-12. As can be seen from Figure 3-3-12, the proposed antenna with a gap ( $g_1$ ) located at the lower left corner of a square ring demonstrates good LHCP radiations on both the azimuthal directions for the upper half free space. As we known, the slot antenna is a bi-directional radiator. Therefore, if we look at this antenna from the upper half free space, we can observe LHCP radiation. While we look at it from the lower half space, RHCP radiation can be observed. Figure 3-3-13 demonstrates this phenomenon.

Though this type of CP radiation pattern presented in Figure 3-3-13 can show the properties of circular polarization, it cannot be seen at a glance the space distribution of

the 3dB axial ratio. Hence, the measurement of polarization patterns in this study employs the rotating source method [54]. The measured results of polarization patterns at different frequencies of 2.4, 2.5, and 2.6 GHz are shown in Figure 3-3-14. These ripples in the polarization patterns are a consequence of the beam ellipticity, which occurs when a finite cross-polar component exists. The depth of the ripples defines the AR value. The polarization patterns at the frequencies of 2.4, 2.5, and 2.6 GHz are shown in Figure 3-3-14. They present well circular polarization and also obtain good axial-ratio values over a wide angle range. In Figure 3-3-14 (a), the AR values in the range of elevation angle from 40 to -40 degrees are lower than 3 dB at the frequency of 2.4GHz. In Figure 3-3-14(b), the polarization pattern at the operational frequency of 2.5 GHz presents that the range of elevation angle with lower 3-dB AR value is from 35 to -45 degrees. The elevation-angle range with lower 3-dB AR value at 2.5 GHz is slightly narrower than that at 2.4 GHz. In Figure 3-3-14(c), it shows the polarization pattern at the frequency of 2.6 GHz which has the lower 3-dB AR range between 23 and -45 degrees at the elevation direction. It can be seen that the space distribution of the lower 3-dB AR in each of the three polarization patterns is not symmetrical with respect to the elevation angle of 0 and 180 degrees. In order to further manifest the asymmetric distribution of axial ratio, the calculated results obtained from the depth of the ripples in these measured polarization patterns are shown in Figure 3-3-15. The 3-dB AR space distribution at the frequency of 2.5 GHz is the most symmetric in these results, and it is symmetrical with respect to the elevation angle of -5 degrees.

The symmetrical center deviated from the elevation angle of 0 can be explained by the electric-current distribution on the slot antenna shown in Figure 3-3-16. It is the simulated result of the proposed antenna at the frequency of 2.45 GHz. The arrow and color express respectively the direction and magnitude of electric current on the slot antenna. The ideal CP radiation sources only come from these parts marked B, C, E and F.



However, in order to consider the impedance matching and signal feed, the protruded strip must be added to the antenna configuration, but it deteriorates the CP radiation response due to introducing other radiation sources such as the parts marked A and D in this case. Hence, the asymmetric radiation sources make the proposed antenna generate asymmetric CP radiation with respect to 0 and 180 degrees. As we known [55-57], the diffraction from the finite ground plane edge also affects the symmetry of the AR space distribution, but here we don't discuss it.

The measured and simulated antenna gains against frequency are shown in Figure 3-3-17. The 3-dBi gain bandwidth of the measured result is about 340 MHz (or 13.6%) referred to the resonant frequency of 2.5 GHz, and the bandwidth is from 2.26 GHz to 2.6 GHz. The maximum gain of 3.74 dBi occurs at the frequency of 2.4 GHz, and the gain at the frequency of 2.5 GHz is about 3.47 dBi.



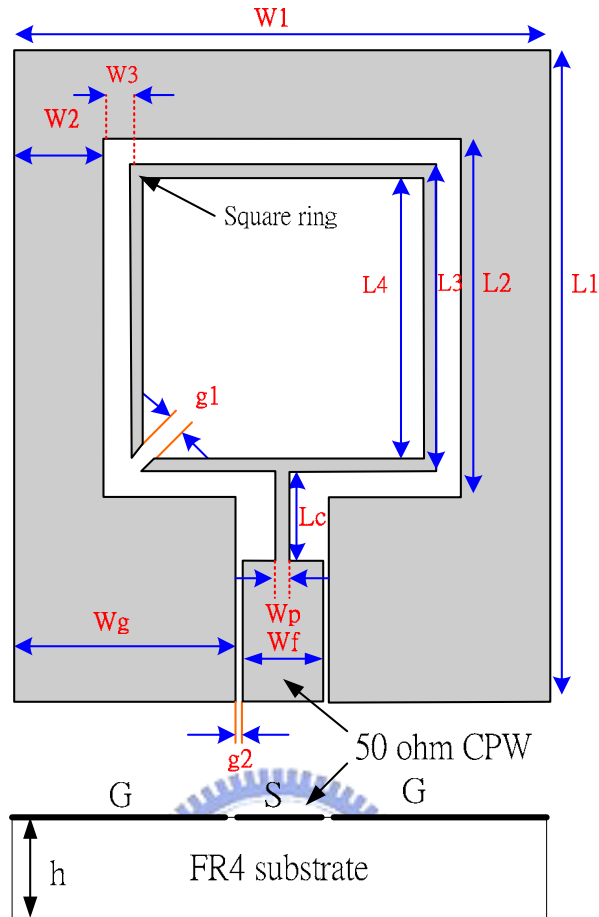
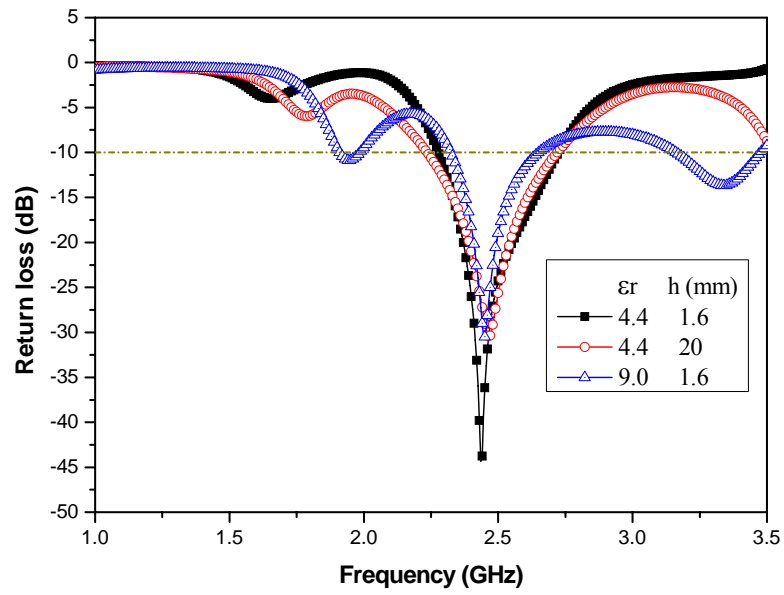


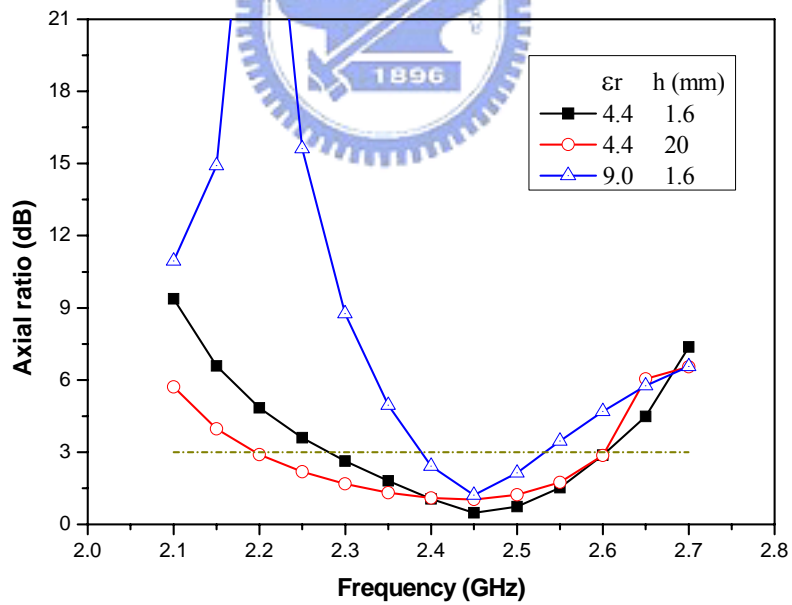
Figure 3-3-7 Geometry of the proposed CPW-fed CP square slot antenna

	Substrate parameters		(Unit : mm)							
	$\epsilon_r$	$h$	W1	W3	4*L3	Wp	Wf	Lc	$\lambda_{eff}$	4*L3/ $\lambda_{eff}$
<b>Design for 2.45 GHz</b>										
Case 1	4.4	1.6	42	2	96	1	6.3	7	82.88	1.15
Case 2	4.4	20	37	1	84	1.4	4.0	4.7	74.68	1.12
Case 3	9.0	1.6	38	4	64	0.8	14.2	7.5	56.96	1.12
<b>Design for 4 GHz</b>										
Case 4	4.4	1.6	30.2	2	57.6	1	6.3	6	50.76	1.13
<b>Design for 1.8 GHz</b>										
Case 5	4.4	1.6	49.5	2	126	1	6.3	2	112.8	1.12

**Table 3.2.1** Design parameters of the proposed antenna geometry on three different substrates and at three different frequencies.



(a)



(b)

Figure 3-3-8(a) Simulated return loss and (b) simulated axial ratio against frequency for the proposed antenna geometry on three different substrates.

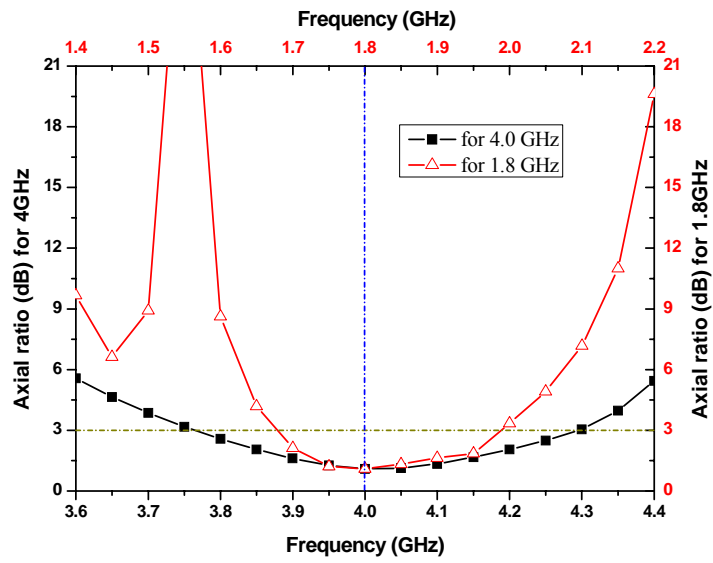
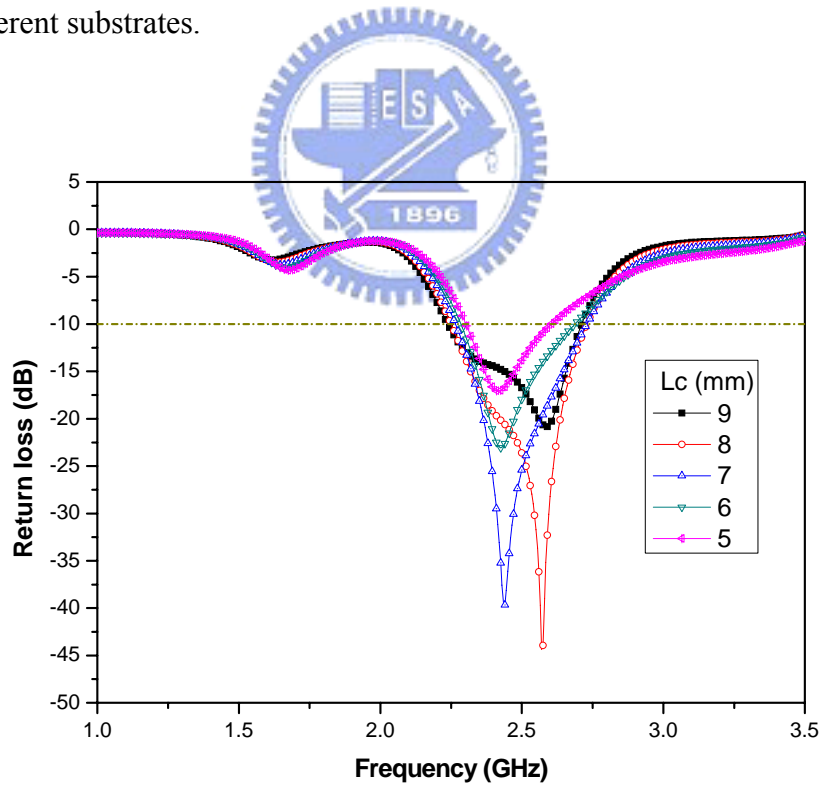
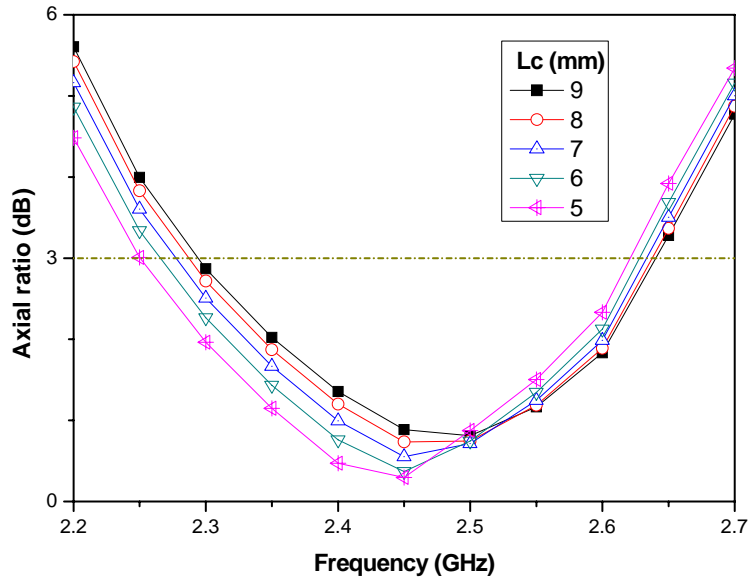


Figure 3-3-9 Simulated axial ratio against frequency for the proposed antenna geometry on two different substrates.

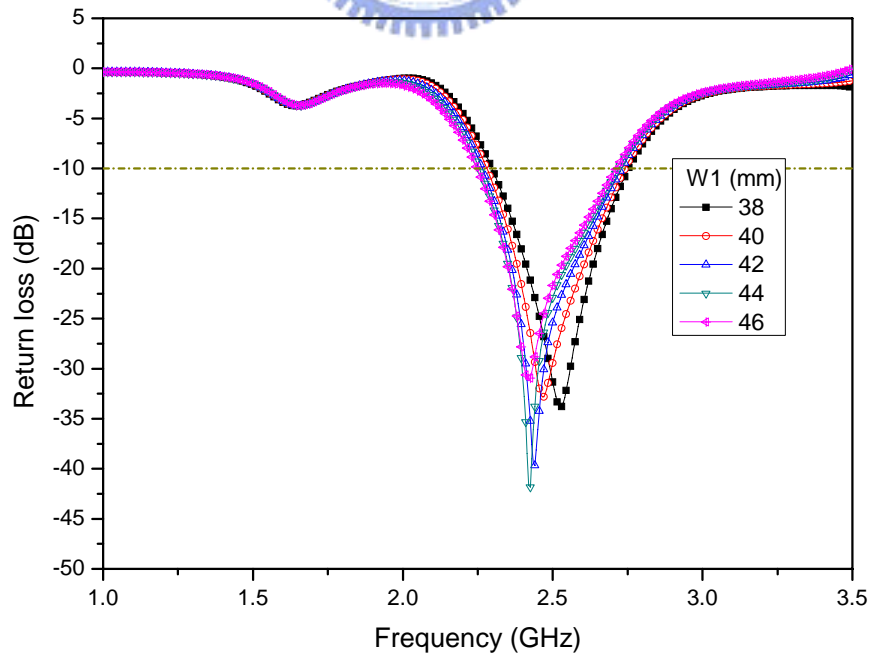


(a)

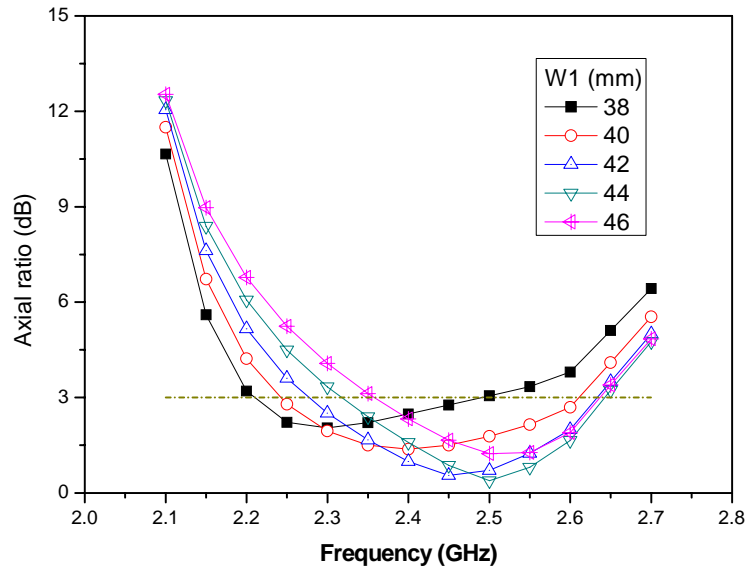


(b)

Figure 3-3-10(a) Simulated return loss and (b) simulated axial ratio against frequency for the proposed slot antenna with different protruded strip length ( $L_c$ )

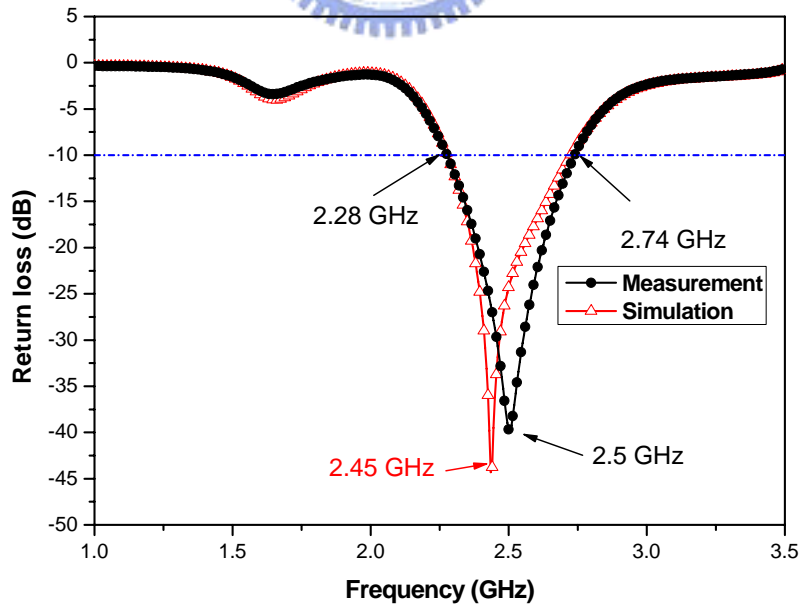


(a)



(b)

Figure 3-3-11(a) Simulated return loss and (b) simulated axial ratio against frequency for the proposed slot antenna with different grounded plane width (W1).



(a)

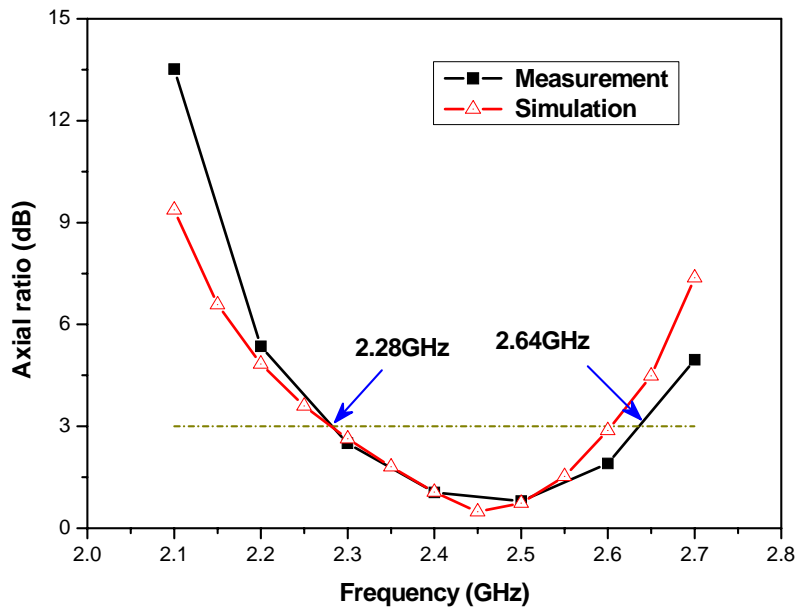


Figure 3-3-12 Measured and simulated (a) return loss and (b) axial ratio against frequency for the optimum proposed slot antenna.

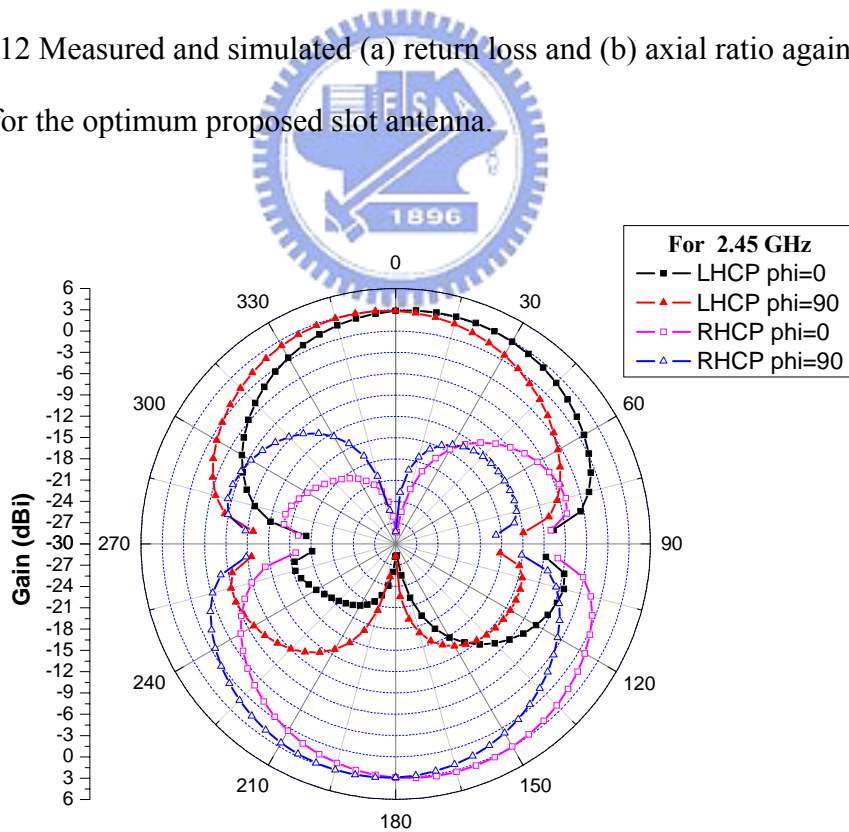
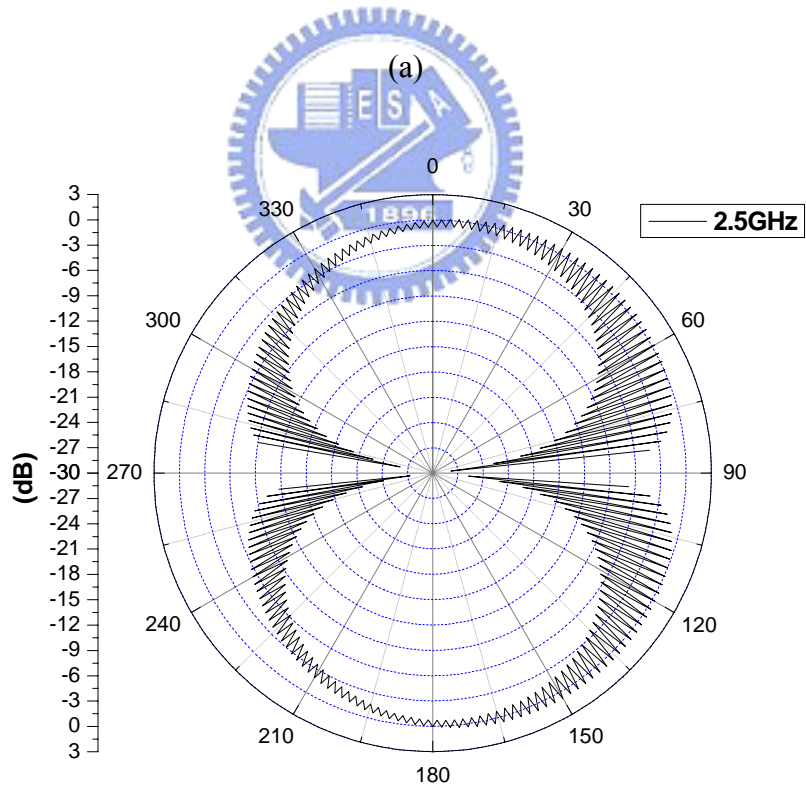
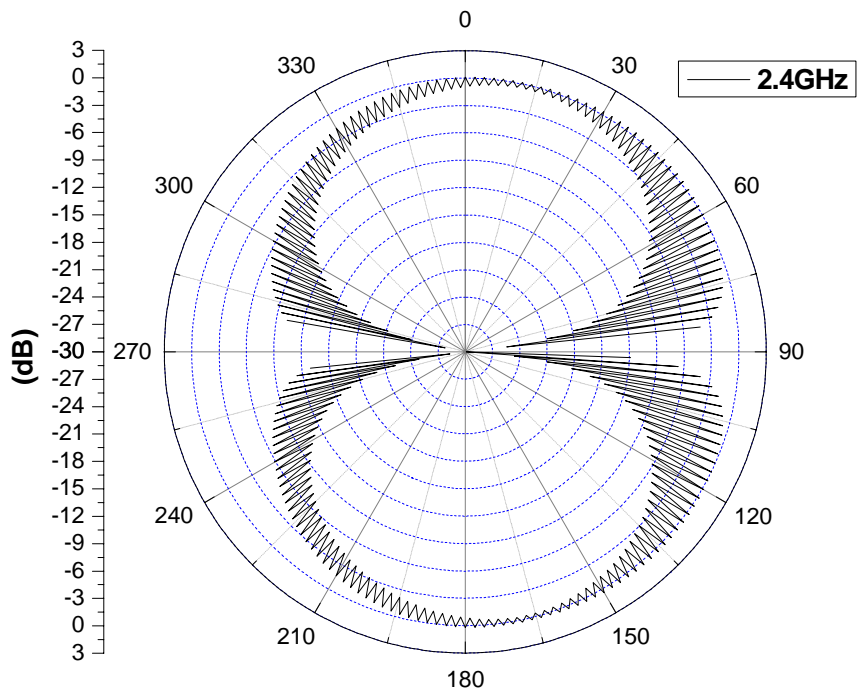
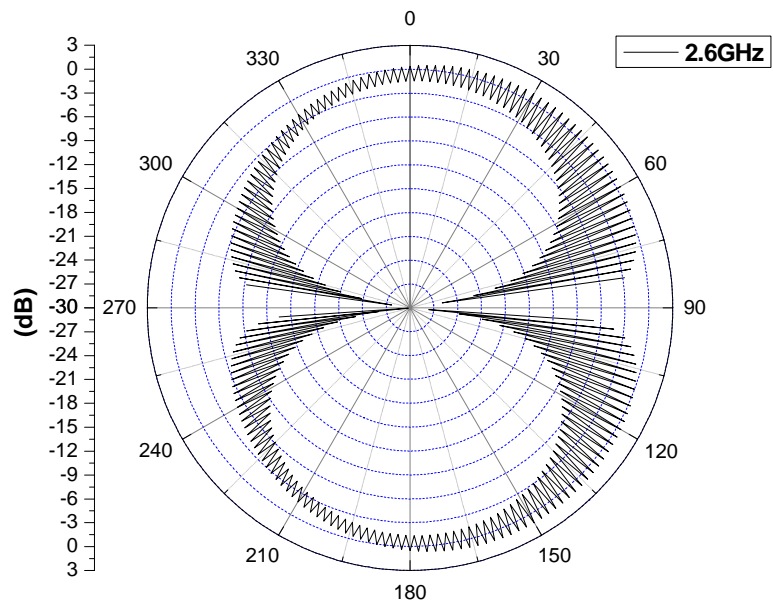


Figure 3-3-13 Simulated circularly polarized radiation patterns for the optimum proposed slot antenna at the frequency of 2.45 GHz







(c)

Figure 3-3-14 Measured radiation patterns at the frequency of (a) 2.4 GHz, (b) 2.5 GHz, and (c) 2.6 GHz by the rotating source method.

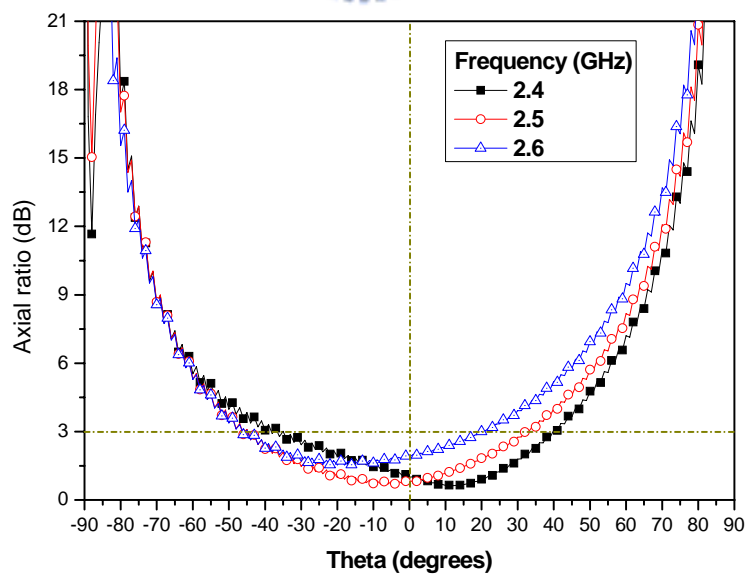
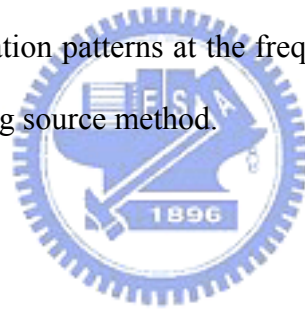


Figure 3-3-15 Axial ratio against elevation angle calculated from the measured CP radiation patterns

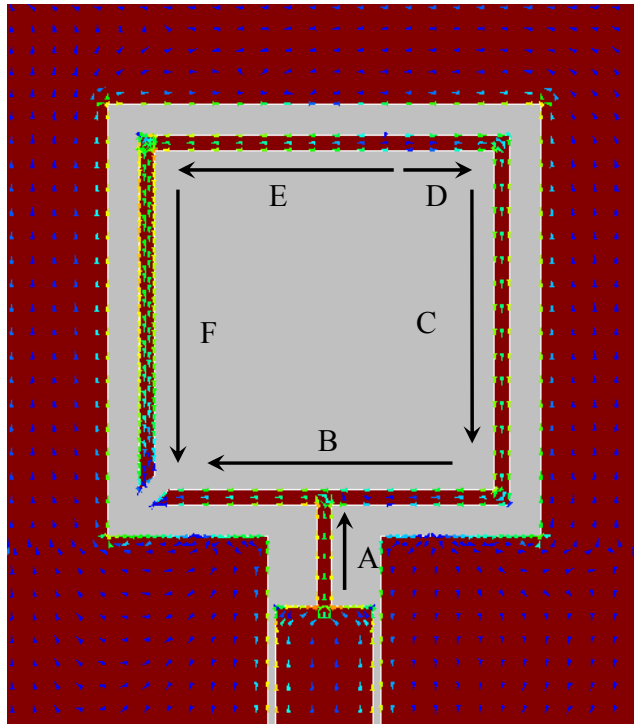


Figure 3-3-16 Simulated electric-current distributions on the proposed slot antenna at the frequency of 2.45 GHz.

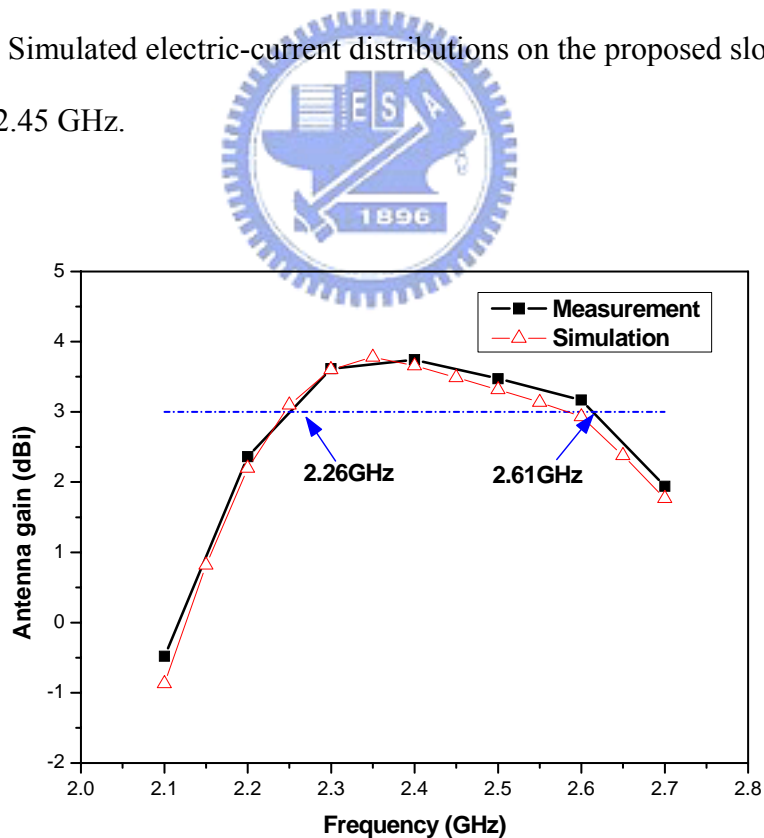


Figure 3-3-17 Measured and simulated antenna gain against frequency for the proposed antenna.

## Chapter 4

### Magnetic current excited CP slot antenna

Printed ring slot antennas have several advantages such as low profile, light weight, easy to manufacture and wide impedance bandwidth. Slot antennas also have wider circular polarization (CP) bandwidth than that of microstrip antennas. Previous report [58] shows the possibility to obtain CP radiation by using a shorted strip at an appropriate position along the ring slot. This shorted strip is applied to a cavity-backed annular slot antenna, and the antenna uses a coaxial probe feed to produce CP radiation. Several microstrip-fed ring-slot antennas producing CP radiation are proposed [59-61]. Chen et al. [59] employs the concept of [58] to achieve the 3-dB axial-ratio (AR) bandwidth of 8.4% and 8.1% for annular and square ring-slot antennas, respectively. However, the frequency at which the minimum AR value occurs does not meet the fundamental resonant frequency. In comparison with [59], the ring-slot antennas without shorted strip have the 3 dB AR bandwidths of only about 3.5% and 4.3% for annular and square ring-slot, respectively. In addition, the 2x2 ring-slot antenna array with a 3 dB AR bandwidth of 15% is presented in [61], but the frequency of the minimum AR value is not the same as the fundamental resonant frequency.

In this paper, we propose a novel design of CP slot antenna to separate the two geometric factors of controlling the fundamental resonant frequency and the frequency of the minimum AR value. In the proposed antenna, a shorted strip has an included angle of 45 degrees relative to the microstrip feedline, and this method is different from these previous studies [58-61]. Besides, our proposed antenna improves these drawbacks of these literatures for similar purposes and shows good circularly polarized radiation performances.

#### 4.1 Antenna Configurations

The configuration of the proposed microstrip-fed circularly-polarized square-ring slot antenna is depicted in Figure 3-4-1. The substrate used an inexpensive FR4 dielectric substrate with a thickness of 1.6mm, a relative permittivity of 4.4, and a loss tangent of 0.0245. The dimensions of this proposed antenna are listed in table 4.1. The ground plane of the proposed antenna has a length of  $L_1$  and a width of  $W_1$ . The shorted square-ring slot has outer and inner side lengths of  $L_2$  and  $L_3$ , respectively, and the shorted strip has an included angle of 45 degree with respect to the microstrip feedline. If the shorted strip is located at the lower left corner, the slot antenna excited a right-hand circular polarization (RHCP) radiation in the upper half free space. Similarly, the left-hand circular polarization (LHCP) radiation observed in the upper half free space can be achieved by locating the shorted strip at the lower right corner. Also note that, for the proposed antenna, the free space wavelength at the operating frequency at which the minimum AR occurs is about the mean circumference of the ring slot. A 50 Ohm input microstrip feedline with a width of  $W_f$  is connected to an impedance transformer with a width of  $W_7$ . In order to reduce the antenna size and match the 50 Ohm microstrip feedline ( $W_f = 3\text{mm}$ ), the meander impedance transformer and three tuning stubs are conducted. The three stubs only affect the return-loss value and the fundamental resonant frequency, but have less influence on the AR operating frequency. In addition, a square slot with a length of  $L_4$  is located at the center of the slot antenna. This square slot is able to make the AR operating frequency to meet the fundamental resonant frequency. Further, the three small triangles (with widths of  $c_1$ ,  $c_2$  and  $c_3$ ) located at the corners of the shorted ring slot are capable of making the radiation patterns of CP more symmetric along the elevation angle of zero degree. In the proposed antenna, the most important geometric factor in the return loss response is the meander transformer and the three tuning stubs. Besides, the mean square-ring slot circumference is the main geometric

factor impacting on the AR response. The two geometric factors separately control their individual antenna response and less influence on each other. This is convenient for the antenna design.

## 4.2 Summary

Figure 3-4-2 demonstrates the simulated and measured results of return loss against frequency for the proposed antenna. The measured result shows that the antenna has a fundamental resonant frequency of 2.4 GHz with the minimum return loss of -50.44 dB and the impedance bandwidth of 930 MHz (or 38.7%) covering the frequency range from 1.83 GHz to 2.76 GHz. The free space wavelength of 2.4 GHz is about 125 mm and approximately equals the mean circumference of square-ring slot (about 130 mm). The simulated polarization patterns are shown in Figure 3-4-3. The proposed antenna radiates right hand circular polarization (RHCP) in the upper half free space and left hand circular polarization (LHCP) in the lower half free space. Besides, the simulated results of axial ratio and CP gain against frequency for the proposed antenna are shown in Figure 3-4-4. It is shown that the 3-dB AR bandwidth is 310 MHz or 12.9%, including the frequencies range from 2.21 GHz to 2.52 GHz, and the 1-dB AR bandwidth is about 100 MHz. The minimum AR value of about 0.1 dB is located at the frequency of 2.4 GHz. Besides, the CP gains are about 3.3 dBi and almost keep constant during 3-dB AR bandwidth. The measurement of polarization patterns in this study employs the rotating source method [54]. The measured results of polarization patterns at different frequencies of 2.3, 2.4, and 2.5 GHz are shown in Figure 3-4-5. These ripples in the polarization patterns are a consequence of the beam ellipticity, which occurs when a finite cross-polar component exists. The depth of the ripples defines the AR value. They present well circular polarization and also obtain good axial-ratio values over a wide angle range. From figure

4.5, the elevation-angle ranges with respected to lower 3-dB AR are -33 to 29, -43 to 47 and -49 to 9 degrees, respectively, for 2.3, 2.4 and 2.5 GHz in the upper half free space. It can be seen that the space distribution of the lower 3-dB AR value are more symmetric at the frequencies of 2.3 and 2.4 GHz than that at the frequency of 2.5 GHz. In order to further manifest the symmetric distribution of axial ratio, the calculated results obtained from the depth of the ripples in these measured polarization patterns are shown in Figure 3-4-6. It can be observed that the AR pattern with respect to elevation angle is nearly symmetric along the elevation angle of 0 degree at the frequencies of 2.3 and 2.4 GHz. By using the three small triangles at the square-ring slot corners to perturb the magnetic current within the square-ring slot, the symmetric AR space distribution and the minimum AR position can be further controlled. In this proposed antenna, the length of  $c_3$  (4 mm) is not equal to the length of  $c_1$  and  $c_2$  (2 mm), and in this condition, a very symmetric AR space distribution can be achieved. In order to manifest this phenomenon, the simulated results of axial ratio against elevation angle for the proposed antenna with and without three small triangles at the frequency of 2.4 GHz are shown in Figure 3-4-7(a) and Figure 3-4-7(b) respectively. It can be observed that the AR distribution in the elevation direction for the proposed antenna with three small triangles is more symmetric along the elevation angle of 0 degrees than that without three triangles.

	<b>L1</b>	<b>L2</b>	<b>L3</b>	<b>L4</b>	<b>L5</b>	<b>L6</b>	<b>L7</b>	<b>c1</b>	<b>c2</b>	<b>c3</b>
(mm)	64	40	25	20	11.5	2	2.75	2	2	4
	<b>W1</b>	<b>W2</b>	<b>W3</b>	<b>W4</b>	<b>W5</b>	<b>W6</b>	<b>W7</b>	<b>Wf</b>	<b>g1</b>	
(mm)	60	40	25	20	3	3.5	1	3	1.4	

Table 4.1

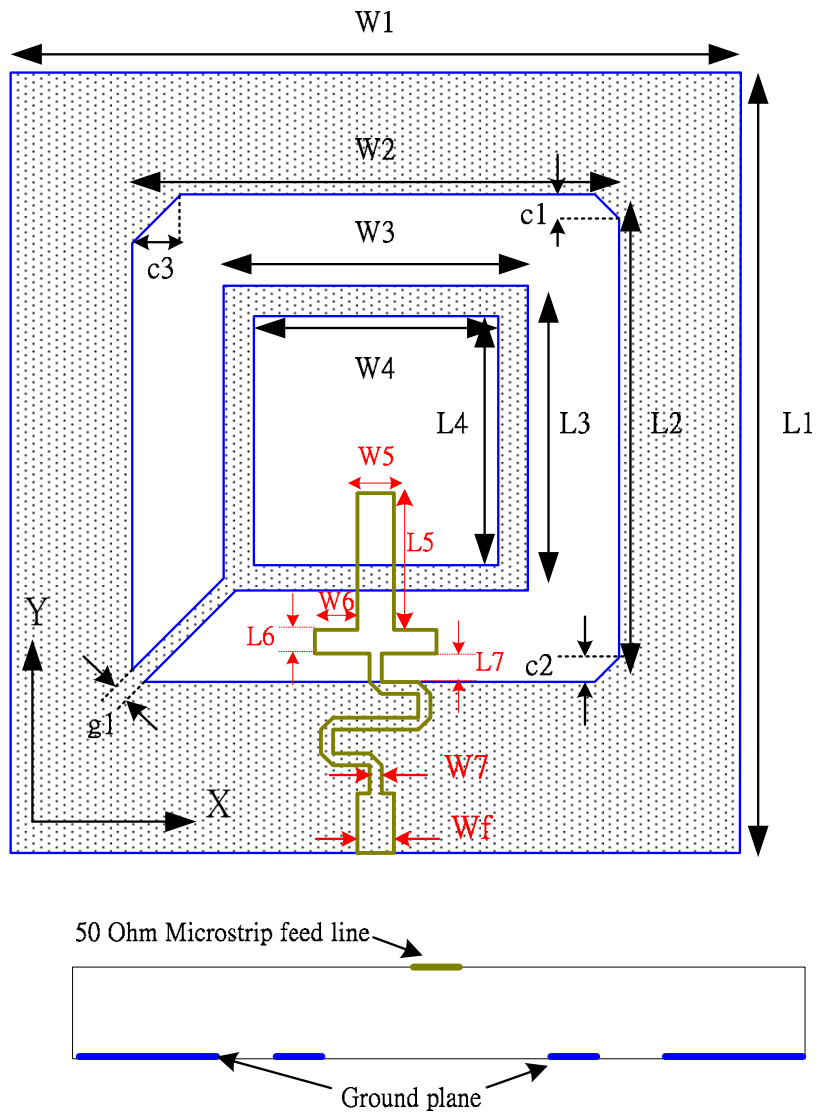


Figure 3-4-1 Configuration of the proposed microstrip-fed circularly polarized slot antenna

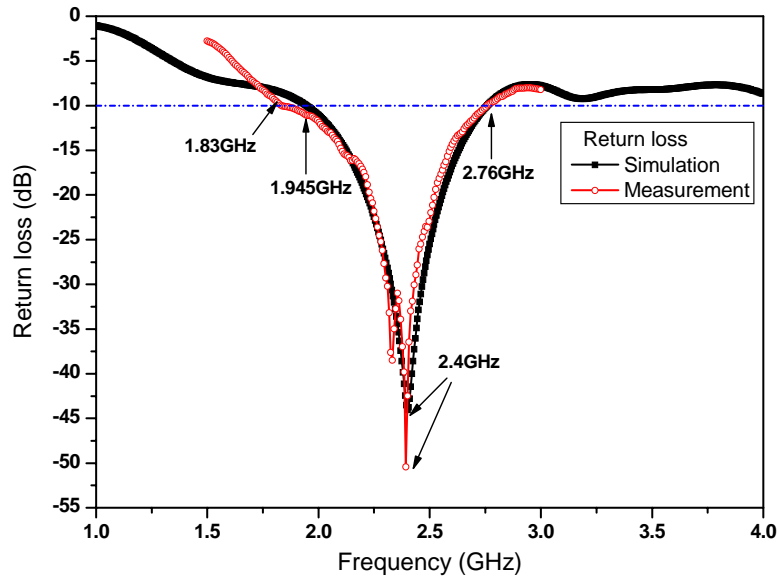


Figure 3-4-2 Simulated and measured results of return loss against frequency for the proposed antenna

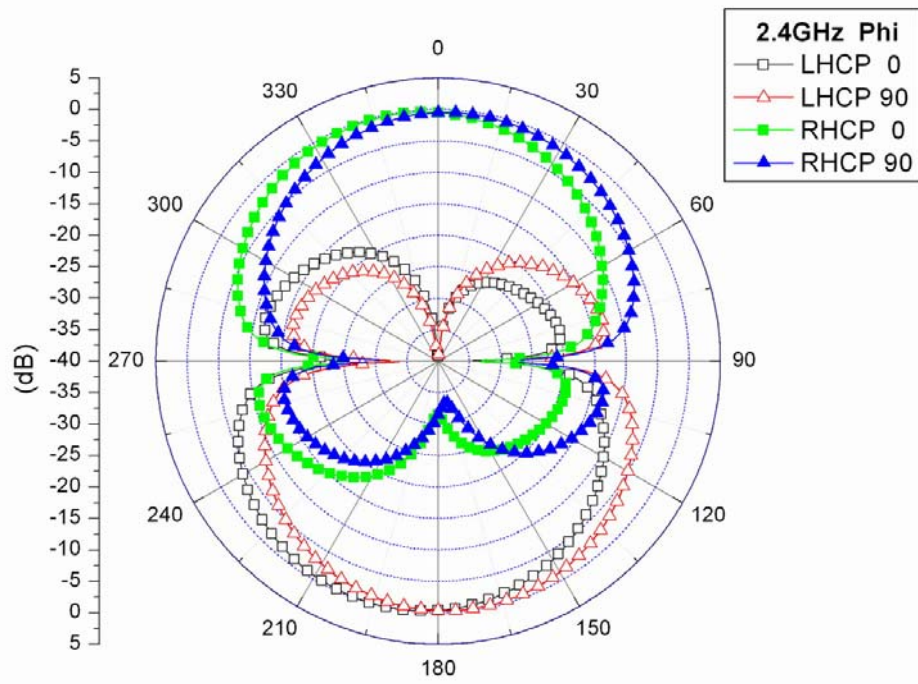


Figure 3-4-3 Simulated polarization patterns at the frequency of 2.4 GHz for the proposed antenna



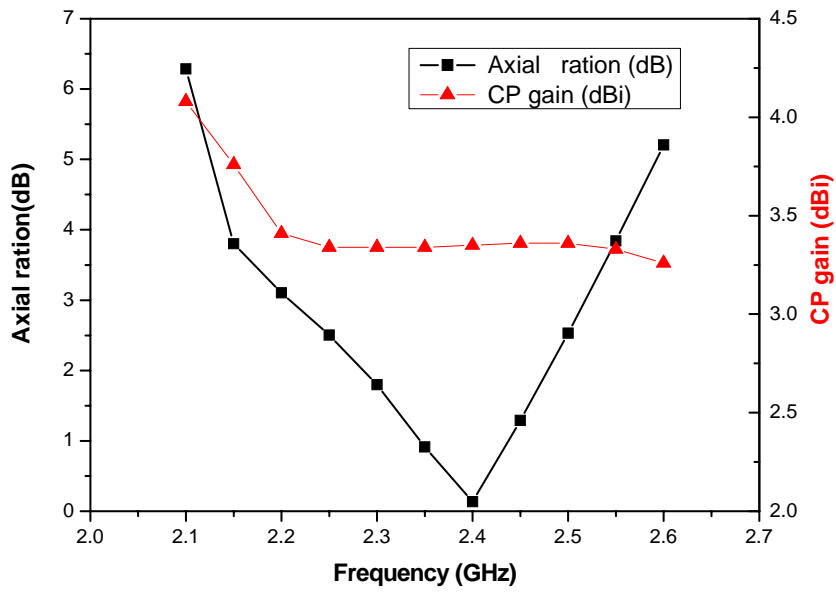
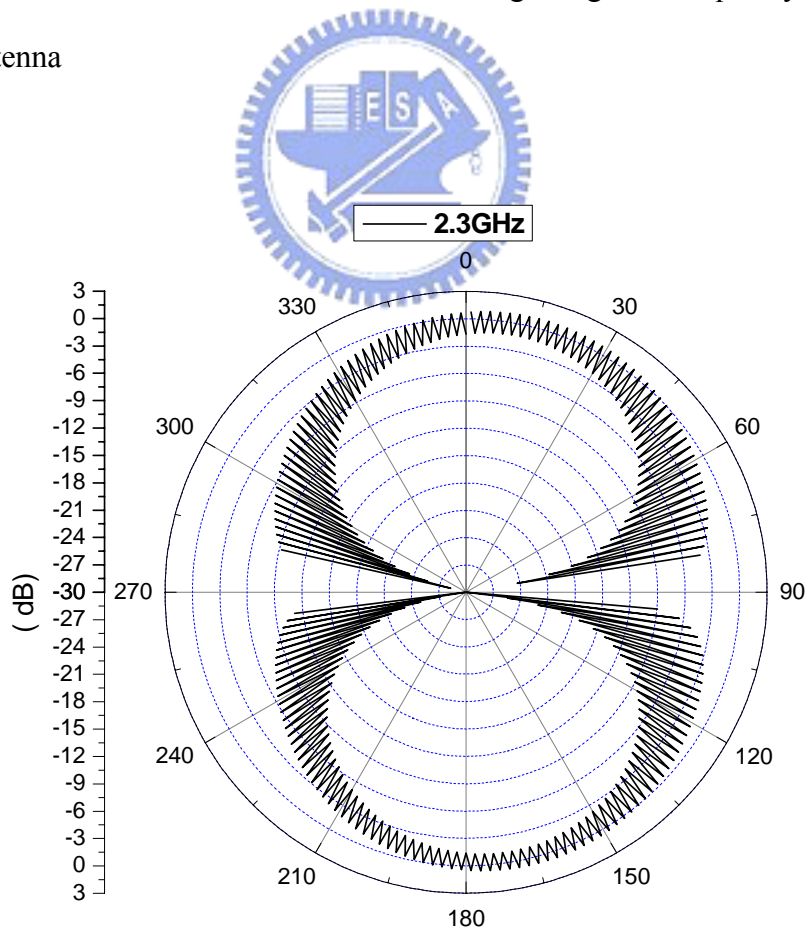
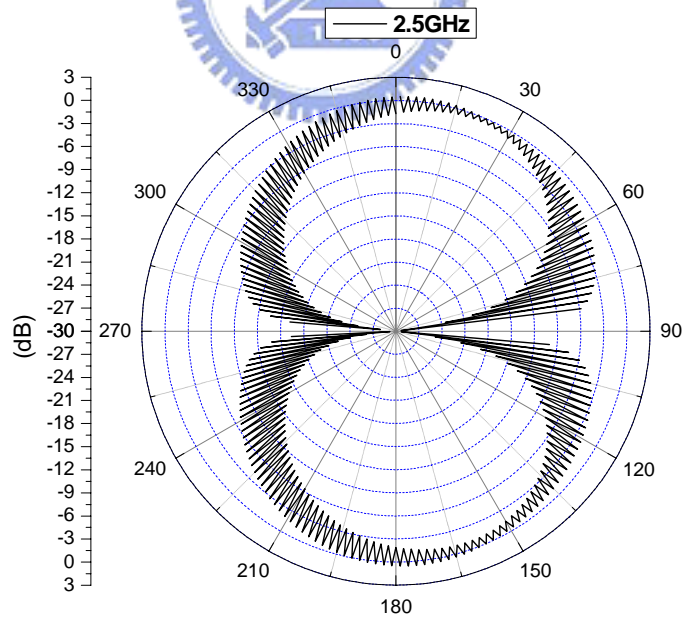
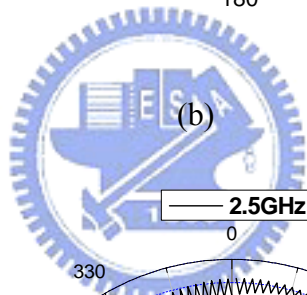
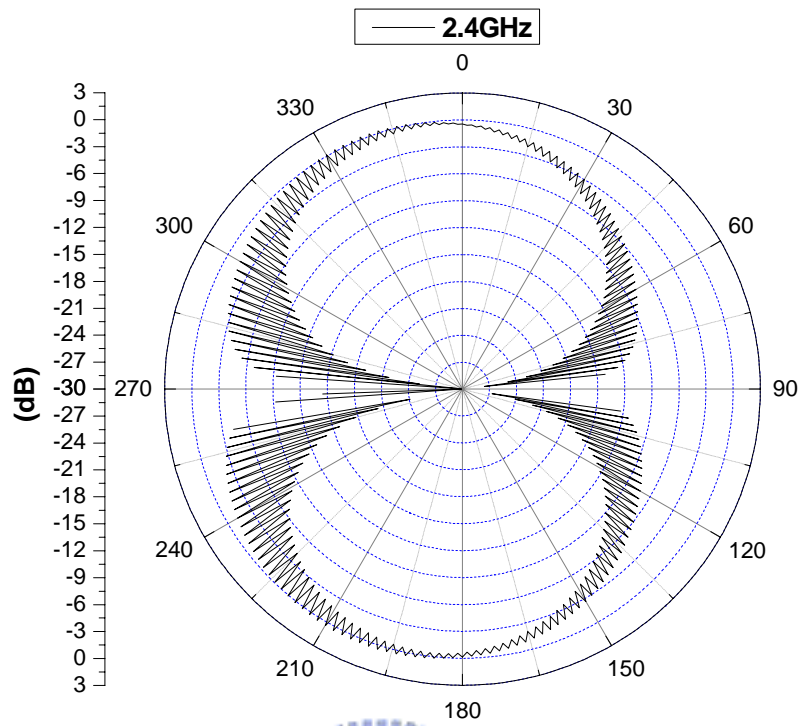


Figure 3-4-4 Simulated results of axial-ratio and CP gain against frequency for the proposed antenna



(a)



(c)

Figure 3-4-5 Measured polarization patterns at different frequencies of 2.3, 2.4 and 2.5 GHz for the proposed antenna.

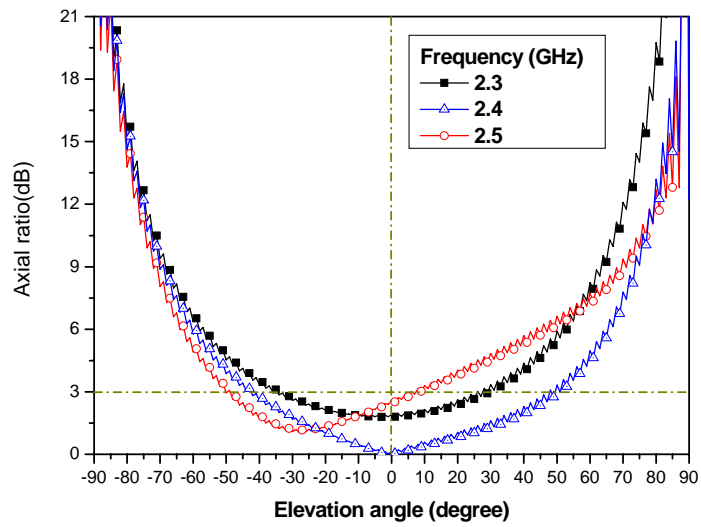
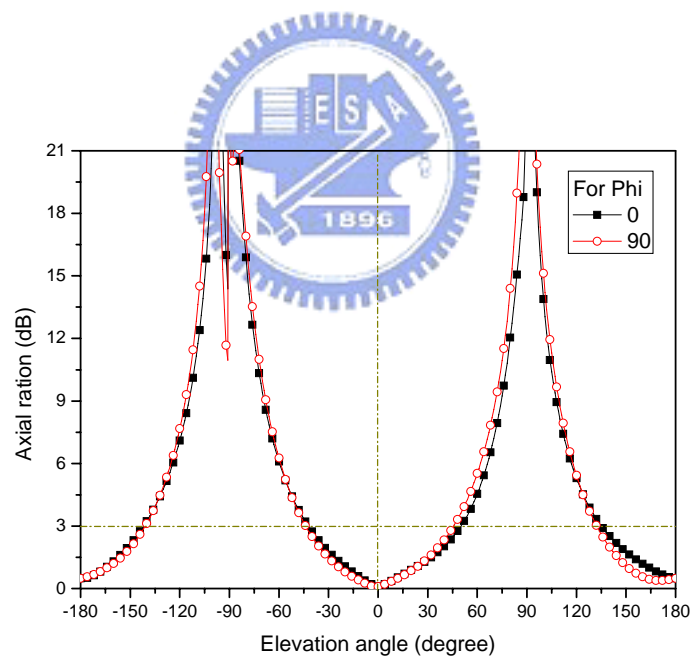
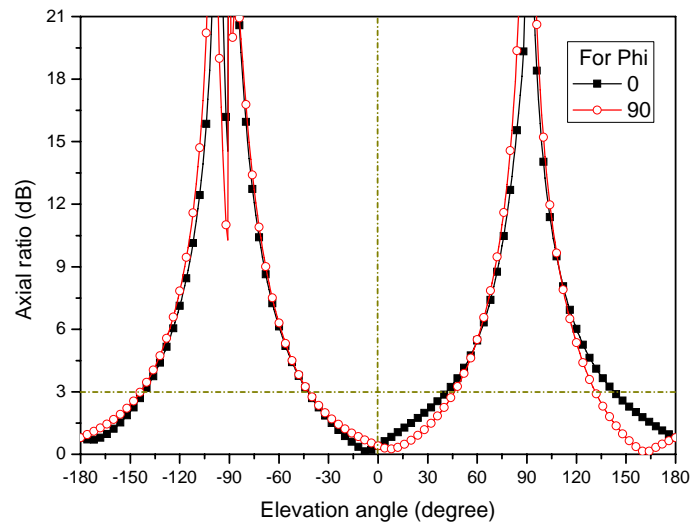


Figure 3-4-6 Axial ratio against elevation angle calculated from the measured polarization patterns

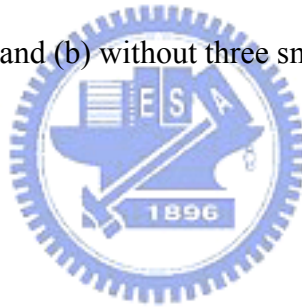


(a)



(b)

Figure 3-4-7 Simulated axial ratio against elevation angle at the frequency of 2.4 GHz for the proposed antenna (a) with and (b) without three small triangles.



## Chapter 5

### Further Discussions

In this chapter, we further discuss these circularly polarized slot antennas. According to excitation mechanism, these slot antennas can be divided into two types such as electric current excitation and magnetic current excitation. With respect to electric current excitation, the circularly polarized wave is mainly excited from the four segments of the square ring at the center of the square slot. However, for the magnetic current excitation, the CP radiation is excited from the four segments of the square-ring slot, and we can also consider the square-ring slot as a waveguide of magnetic current.

Besides, we must also consider the influence of the image effect by the ground plane. This effect has larger influence on electric-current excited slot antenna, but less influence on magnetic-current excited antenna. This is because the electric current traveling on the square-ring strip at the center of the slot induces several image antennas on the surrounding ground plane. These image antennas largely affect the polarization patterns of the original slot antenna. In addition, the slight change of feed configuration has also large influence on the radiation pattern and S parameter. Thus, the requirement of fabrication tolerance must be exactly controlled, or the S parameter and CP performance of the slot antenna have very large deviation from our design. In terms of magnetic current excitation, the image effect is very little influence on the S parameter and radiation pattern. This is because the magnetic current is confined within the square-ring slot and the confined magnetic current contributes to the most of the CP radiation. This type of slot antenna with microstrip fed and magnetic excitation is less sensitive to fabrication tolerance and feed configuration, and the main geometry factors of S parameter and radiation pattern can be separately controlled. Thus, the design flexibility is very attractive and convenient.

Figure 3-5-1 shows the photograph of the microstrip-fed square-ring square slot antenna, and (a) is back side and (b) is front side. We use 3D FEM simulator of Ansoft HFSS to simulate the slot antenna and also compare with using IE3D (which is 2.5D FEM simulator not 3D FEM simulator). The 3D solid model built by HFSS is presented in Fig. 5.2. The air box is used to monitor the space distribution of electric field and magnetic field. The boundary conditions of radiation are also applied to the surface of the air box. A wave port is loaded on the feed line. Figure 5.3 shows the simulated results of (a) scattering parameter, (b) axial ratio, and (c) radiation pattern. The simulated result of scattering parameter is in good agreement with the results shown in Figure 3-5-2. The difference between HFSS and IE3D is the higher order mode at the frequency of 3.25 GHz. The higher order mode maybe results from the waveguide mode of the substrate. The polarized radiation patterns shown in Figure 3-5-3 and Figure 3-5-3(c), which are RHCP and LHCP, also show some difference between these figures. This can be explained that the HFSS takes account of diffraction effect from substrate edge and metal plane. Figure 3-5-4 shows the measured results of polarization pattern at various frequencies. It should be noted that the slot antenna presents very good circularly polarized radiation cover wide frequency bandwidth from 2.15 GHz to 2.5 GHz. Besides, the polarization patterns show slight symmetry on the upper free half space and the lower half space, if we correct the measured error due to the alignment between the under test antenna and the source antenna. Electrical field and magnetic field distributions on the x-y plane are shown in Figure 3-5-5 and Figure 3-5-6, respectively, while feed signal phase from  $0^\circ$  to  $180^\circ$  by step of  $90^\circ$ . We can observe the electric and magnetic field rotate along anti-clockwise which excites RHCP radiation. Besides, the magnetic field presents very smooth distribution over electric field, and this phenomenon results in the very good CP radiation performance due to its magnetic excitation mechanism. Figure 3-5-7 and Figure 3-5-8 illustrate the vector plot of electric field and magnetic field

distribution on the top of the air box while the feed signal phase from  $0^\circ$  to  $180^\circ$  by step of  $90^\circ$ . The phase of the magnetic field obviously leads one of the electric field by a quadrature phase.

The CPW-fed square-ring slot antenna is fabricated as shown in Figure 3-5-9. The 3D solid model is developed by Ansoft HFSS as shown in Figure 3-5-10. The simulated results of scatter parameter, axial ratio, and radiation patterns are presented in Figure 3-5-11. The slot antenna has the return loss with the minimum value of -28 dB at the frequency of 2.42 GHz and axial ratio with the minimum value of 1.8dB at the frequency of 2.55 GHz. These antenna parameters are some different from that by using IE3D simulator. This is due to the HFSS simulator accounting for the diffraction effect by the substrate and metal plane. The measured polarization patterns are demonstrated in Figure 3-5-12 at the different frequencies from 2.4 GHz to 2.6 GHz. It can be noted that the 2.5 GHz and 2.55 GHz have the better CP performance. In general, the radiation pattern for slot antennas should be symmetry at the upper half free space and lower half free space. The non-symmetric distributions of polarization pattern along the line from 90 to 270 result from the diffraction and the measurement error. The misalignment between the source antenna and measured antenna contributes to the measurement error, and the non-fixed rotation of the measured antenna also contributes to the measurement error. Electrical field and magnetic field distributions on the x-y plane are shown in Figure 3-5-13 and Figure 3-5-14, respectively, while feed signal phase from  $0^\circ$  to  $180^\circ$  by step of  $90^\circ$ . We can observe the electric and magnetic field rotate along clockwise which excites LHCP radiation. The most of the electric and magnetic field distribution concentrate at the square-ring strips, and thus it indicates the circular polarized radiation mainly results from the square-ring strips unlike magnetic current excitation using the square slot radiating. Figure 3-5-14 and Figure 3-5-15 illustrate the vector plot of electric field and magnetic field distribution on the top of the air box while the feed signal phase from  $0^\circ$  to

180° by step of 90°. We can observe that the plane at which the feed line is located has larger electric and magnetic field than other places. It manifests this type of electric excited slot antenna are larger influenced by the feed configuration. The slight deviation of the feed configuration from original design maybe leads to large undesirable results. In order to resolve this problem, we develop a new square-ring slot antenna as shown in Figure 3-5-17. The measured and simulated results of scattering parameter are shown in Figure 3-5-18. In order to manifest the less sensitivity to feed configuration, we fabricate two antennas with slight change of feed length to measure. The measured results indeed prove the consequence of less sensitive to feed configuration. In this antenna, the circularly polarized radiation mainly excites from the electromagnetic interaction between the square ring at the feed-line side and the square ring at the ground-plane size. The simulated results of axial ratio against frequency and axial ratio against elevation angle are shown in Figure 3-5-19. Besides, the measured results of polarization patterns at the frequency of 2.45 GHz and 2.5 GHz are presented in Figure 3-5-20.

For the sake of further improving the circularly polarized response of CPW-fed square-ring slot antenna, we must make more effort to alleviate the image effect. We add two slits at the edges of the CPW feed to alleviate the image antenna forming. The proposed antenna is shown in Figure 3-5-21, and the simulated return loss is also shown in Figure 3-5-22. The minimum return loss occurs at the frequency of 2.2 GHz with the S11 value of -48.5 dB. Figure 3-5-23 presents the results of (a) axial ratio against frequency and (b) axial ratio against elevation angle at various frequencies. We can observe the AR bandwidth is very wide and the AR space distribution is very symmetry even if at different frequency. But the proposed antenna has narrower impedance bandwidth than AR bandwidth. This impedance bandwidth narrowing is incurred from the discontinuity of CPW feed line. Figure 3-5-24 demonstrates the measured polarization patterns at various frequencies. It also manifest the good CP response of the proposed



antenna

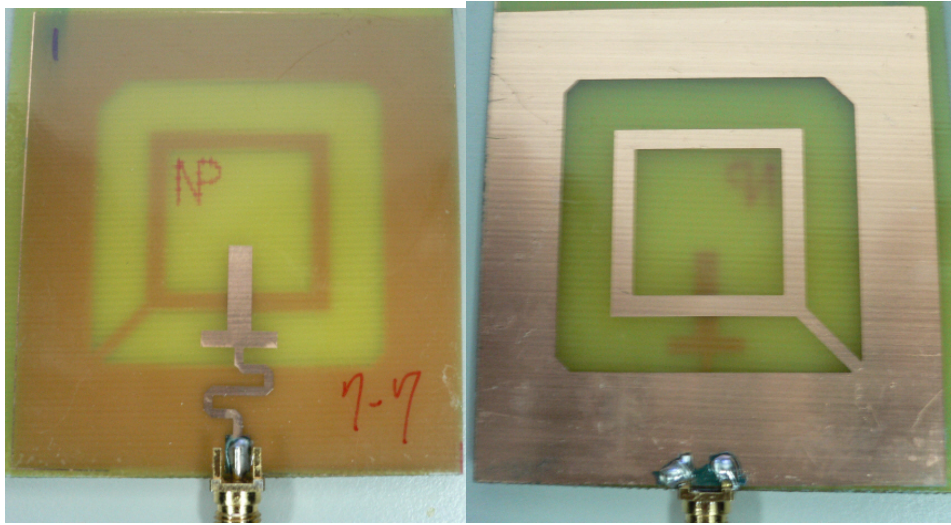


Figure 3-5-1 Photograph of microstrip fed slot antenna

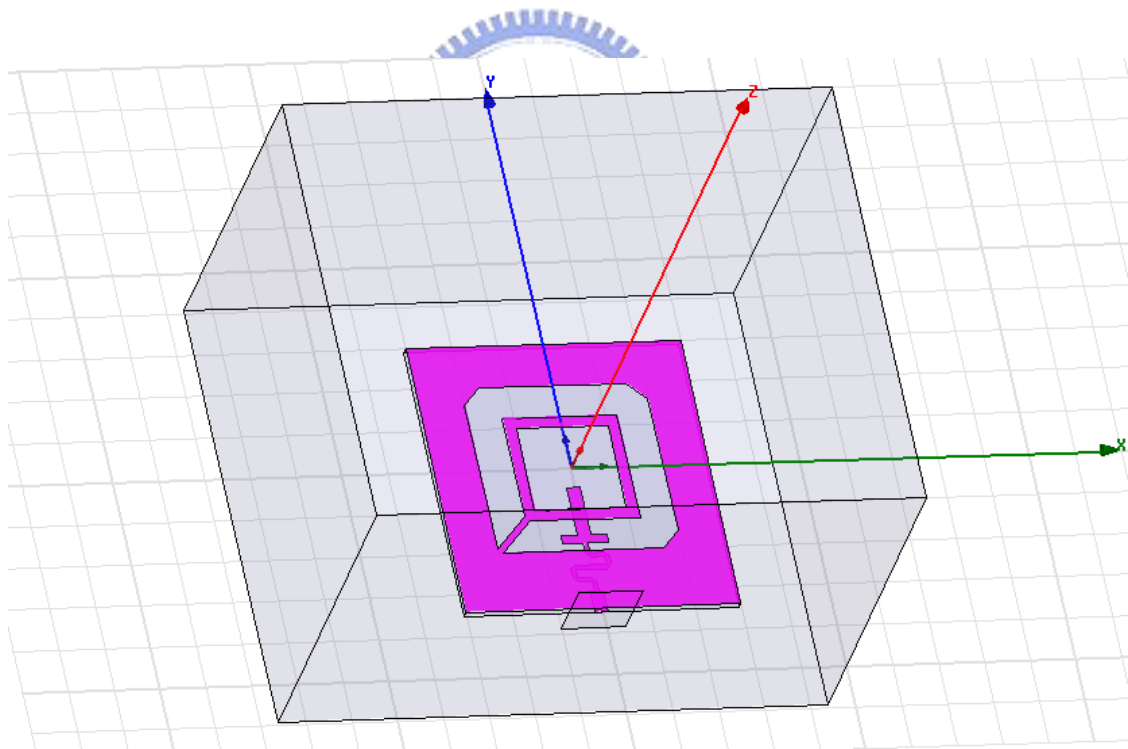
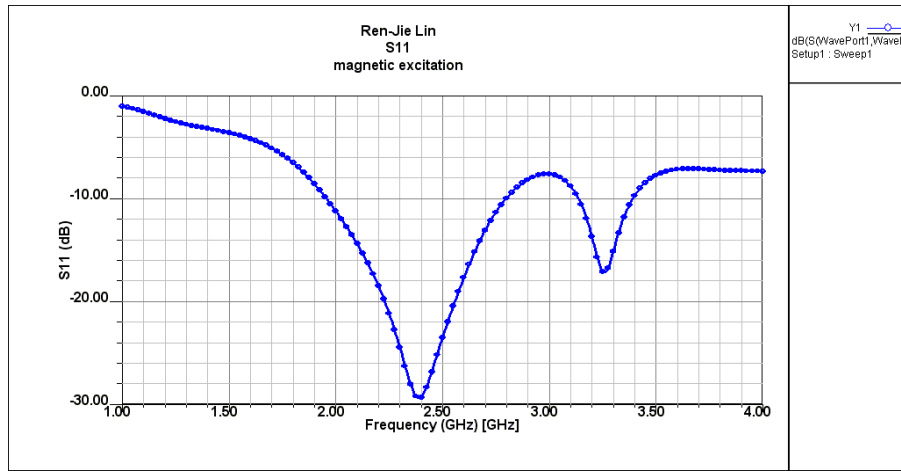
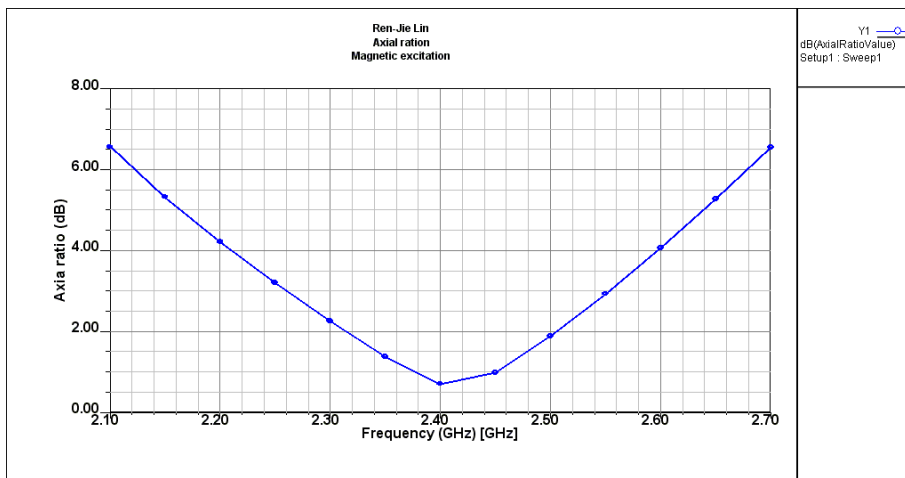


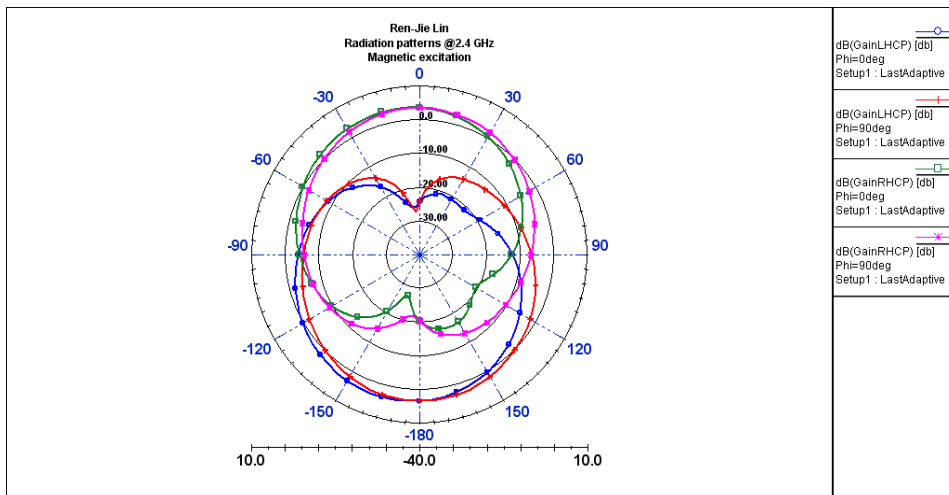
Figure 3-5-2 3D solid model of microstrip fed slot antenna



(a)

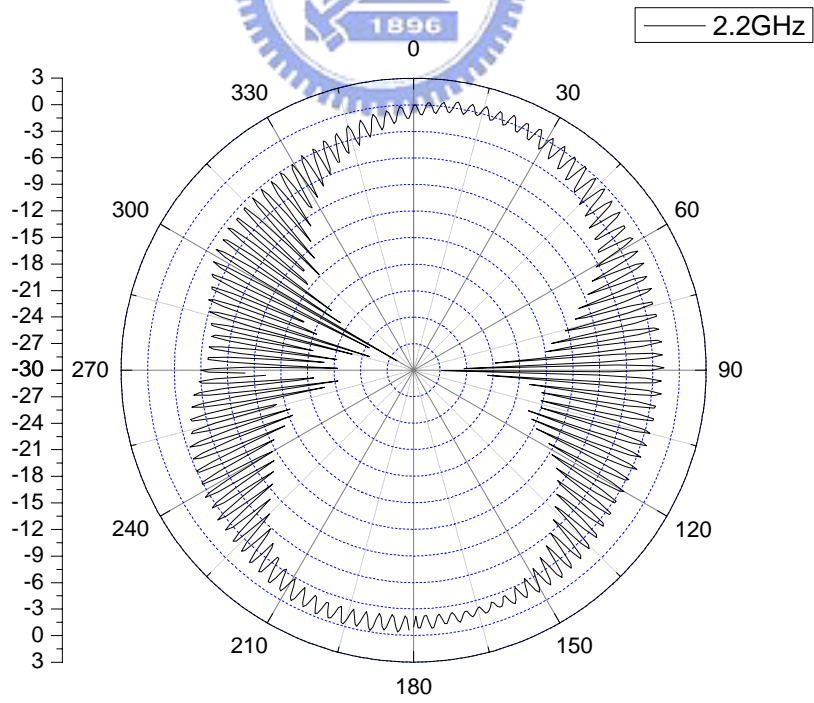
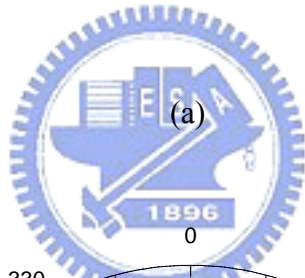
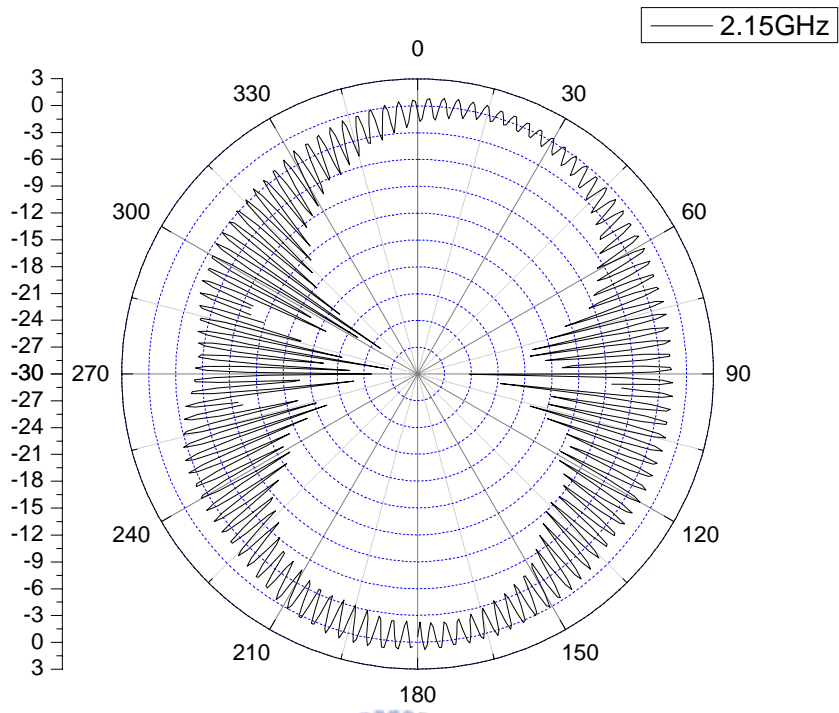


(b)

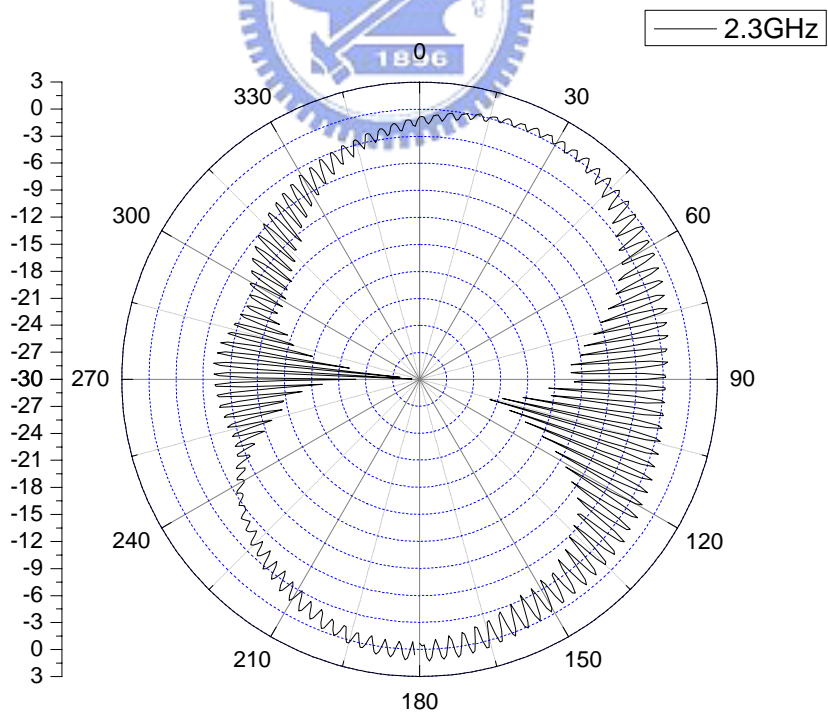
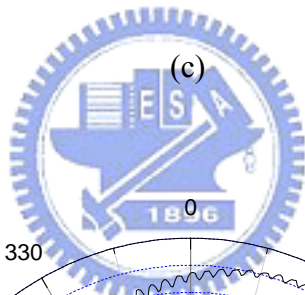
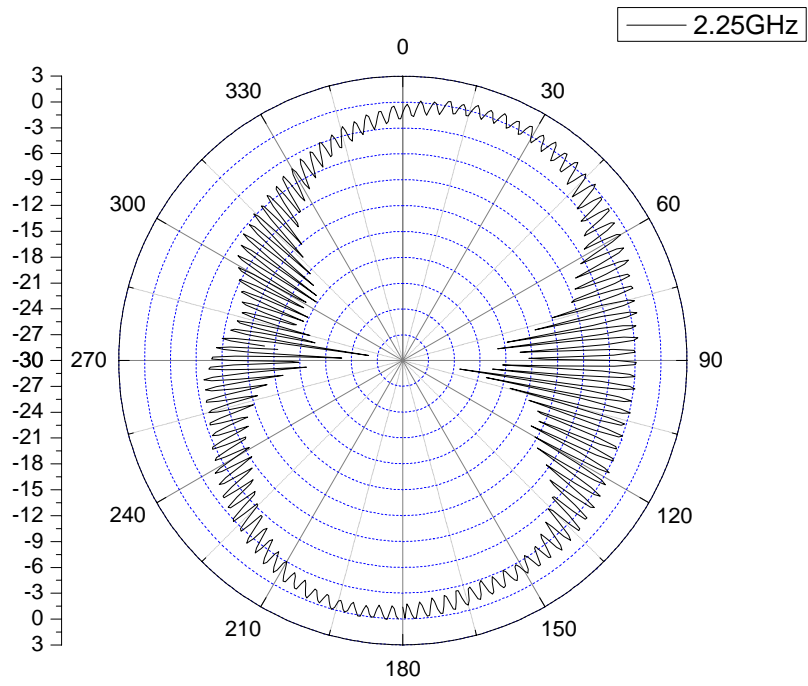


(c)

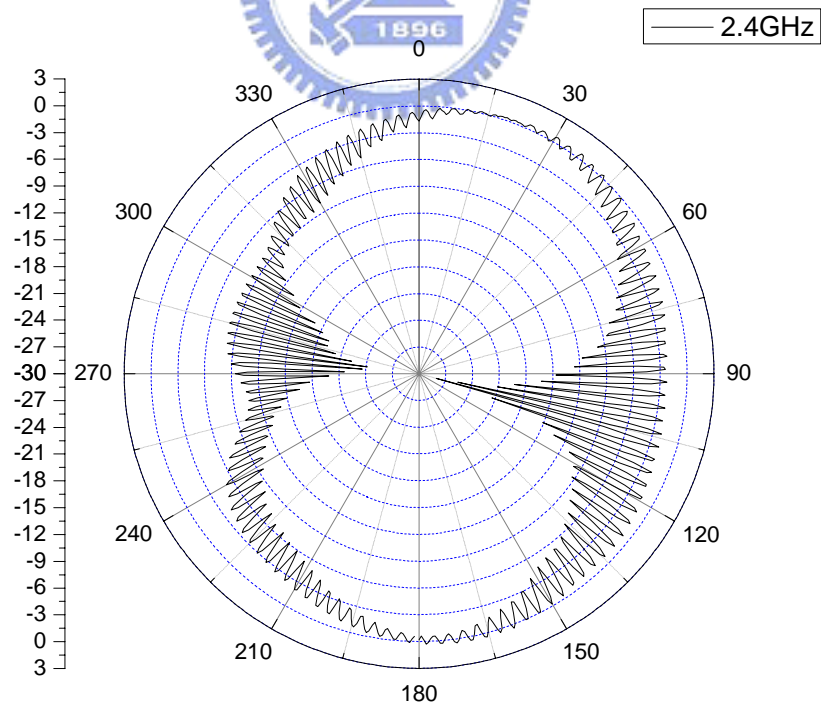
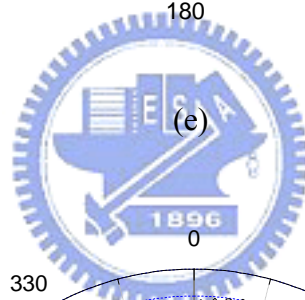
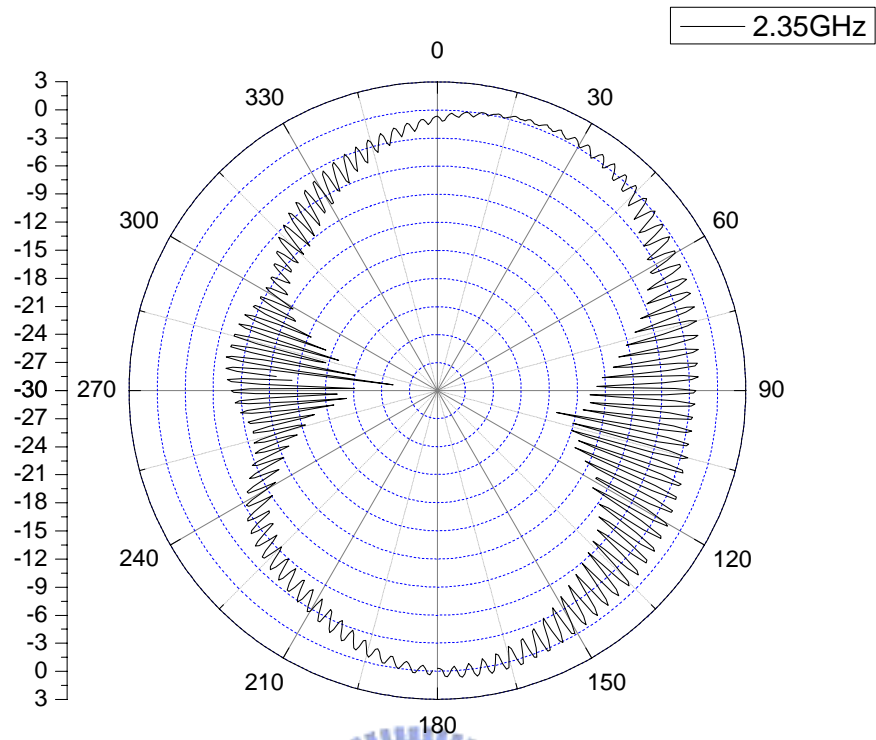
Figure 3-5-3 Simulation of (a) S parameter, (b) Axial ratio, and (c) CP radiation pattern by using Ansoft HFSS simulator



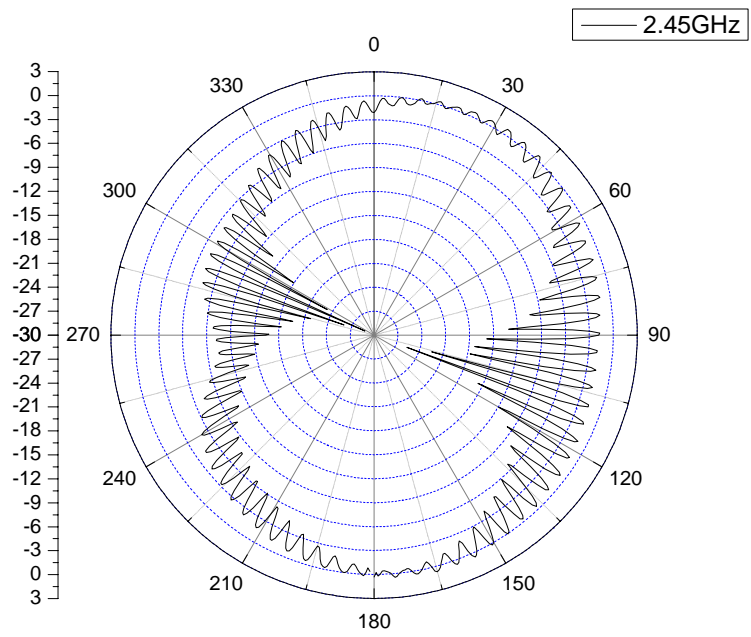
(b)



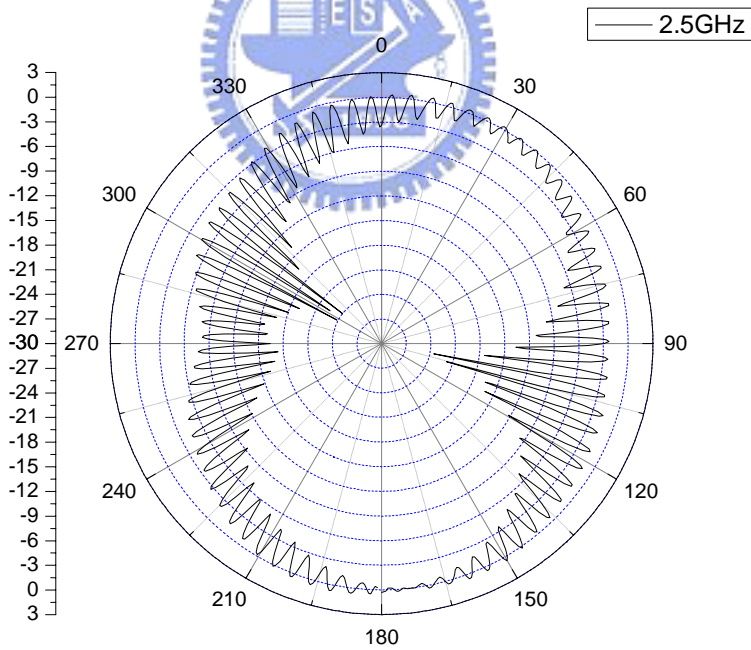
(d)



(f)



(g)



(h)

Figure 3-5-4 Measurement of polarization patterns of microstrip-fed CP slot antenna at different frequency.

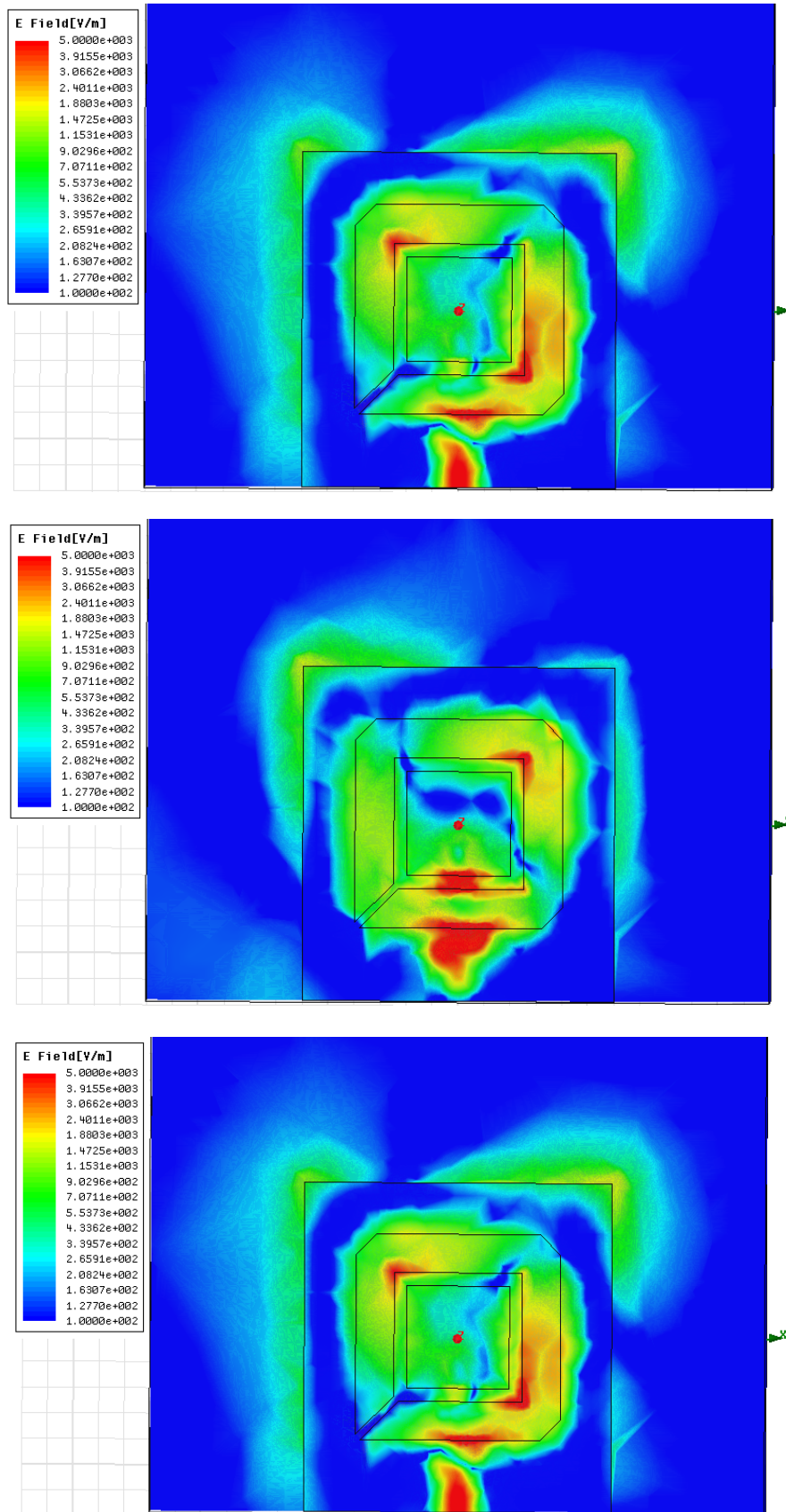


Figure 3-5-5 Electrical field distributions on the x-y plane as feed signal phase from 0 to 180 by step of 90

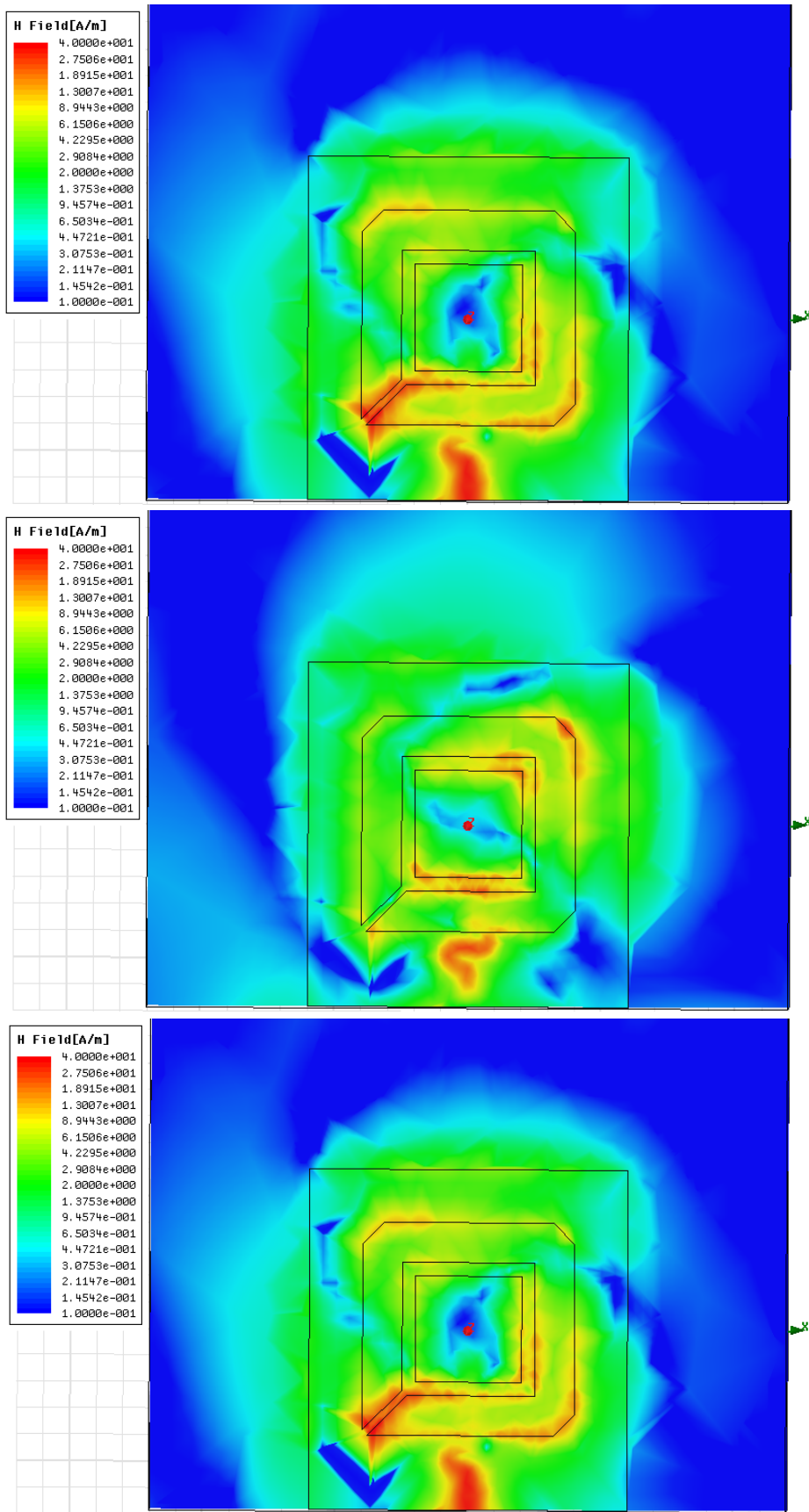


Figure 3-5-6 Magnetic field distributions on the x-y plane as feed signal phase from 0 to 180 by step of 90



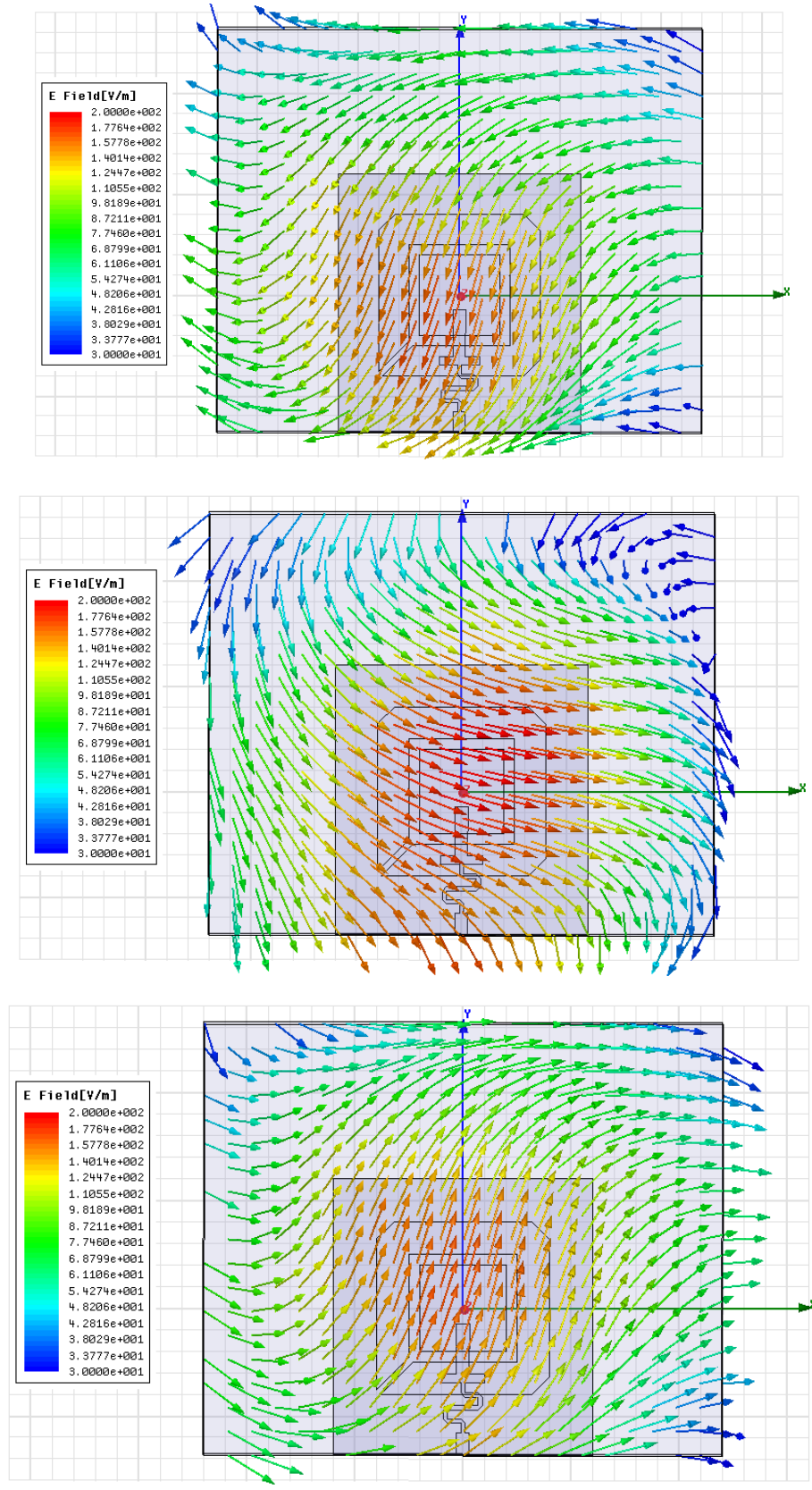


Figure 3-5-7 Vector plot of electrical field distribution on the top of Air box as the feed phase from 0 to 180 by step of 90

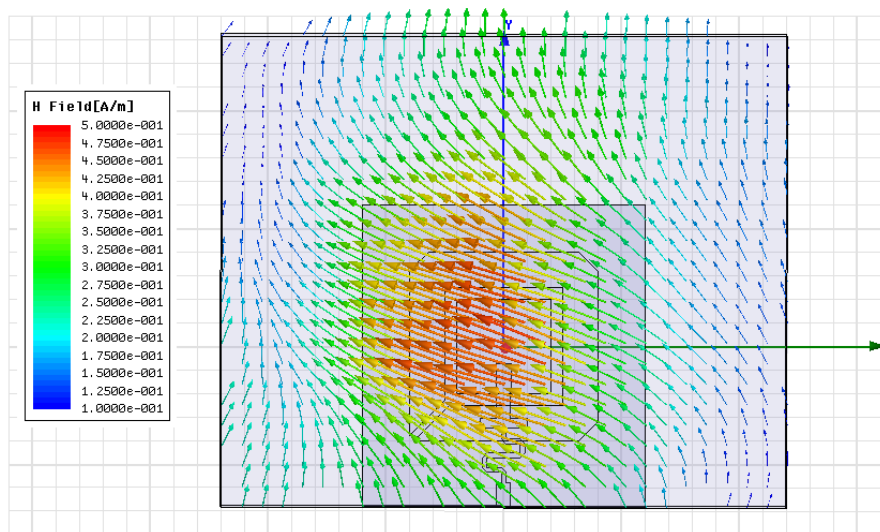
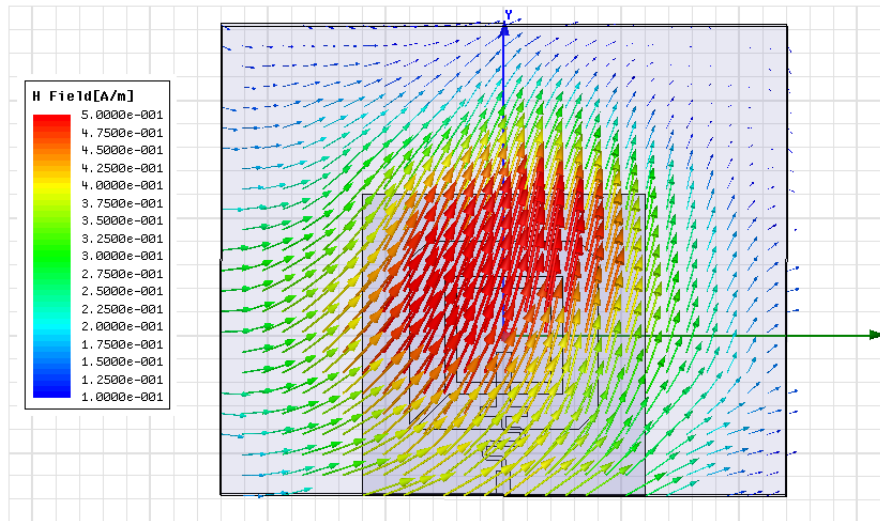
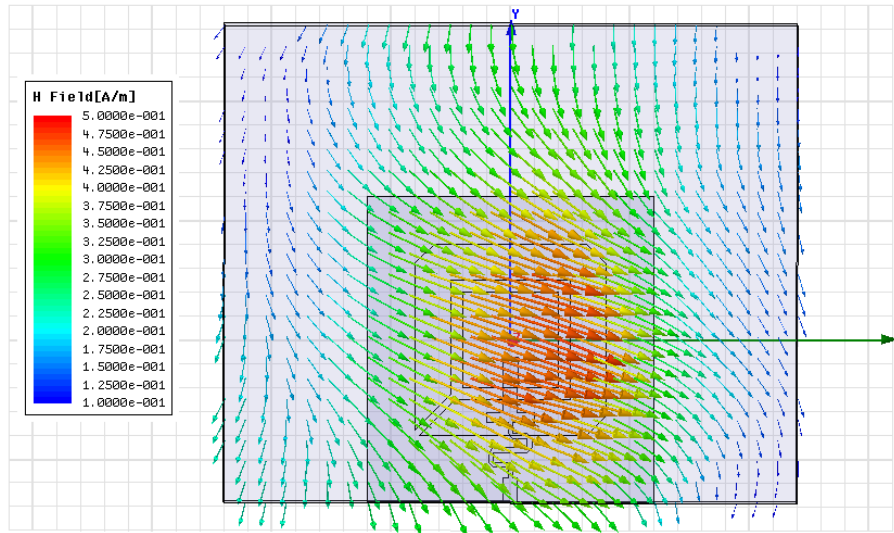


Figure 3-5-8 Vector plot of magnetic field distribution on the top of Air box as the feed phase from 0 to 180 by step of 90

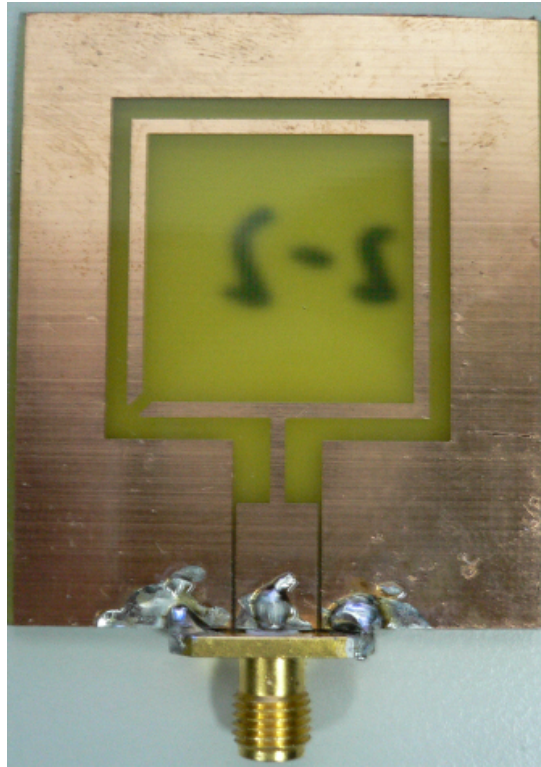


Figure 3-5-9 Photograph of CPW-fed square-ring slot antenna

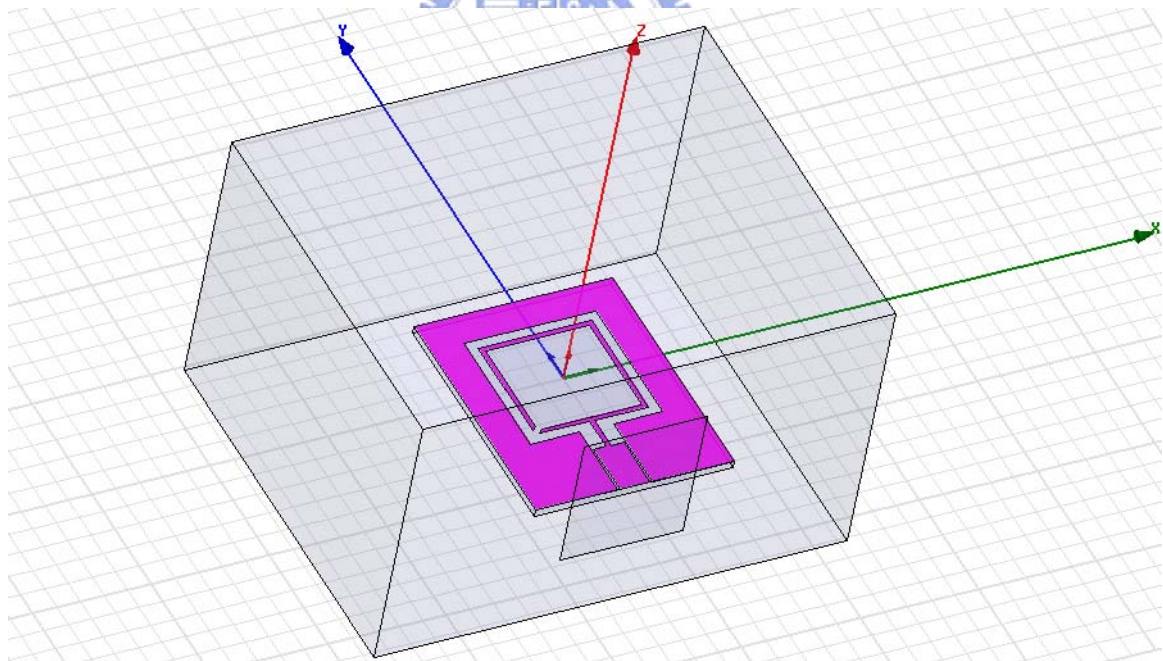


Figure 3-5-10 3D solid model of microstrip fed slot antenna

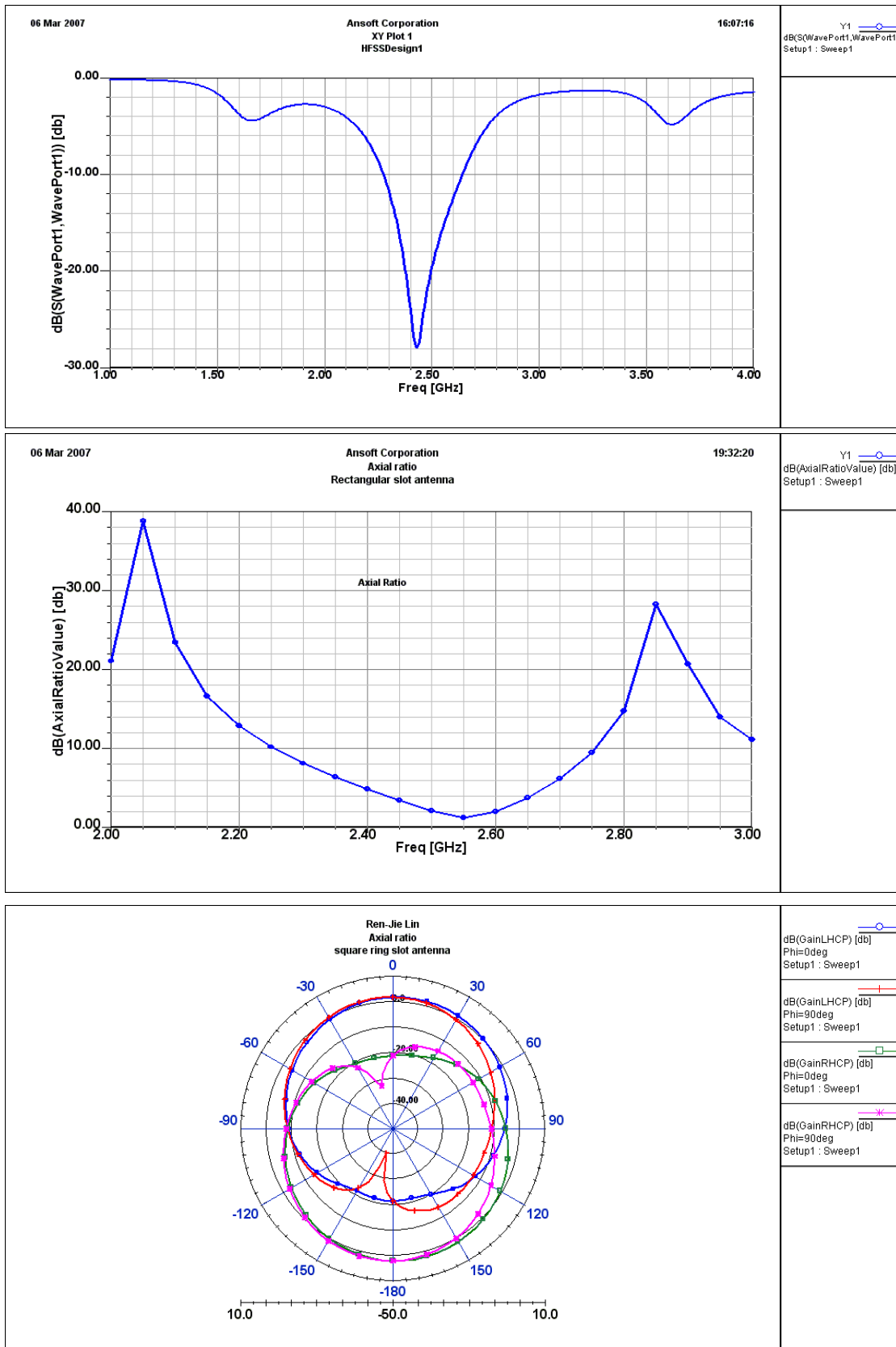
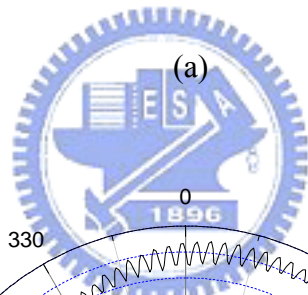
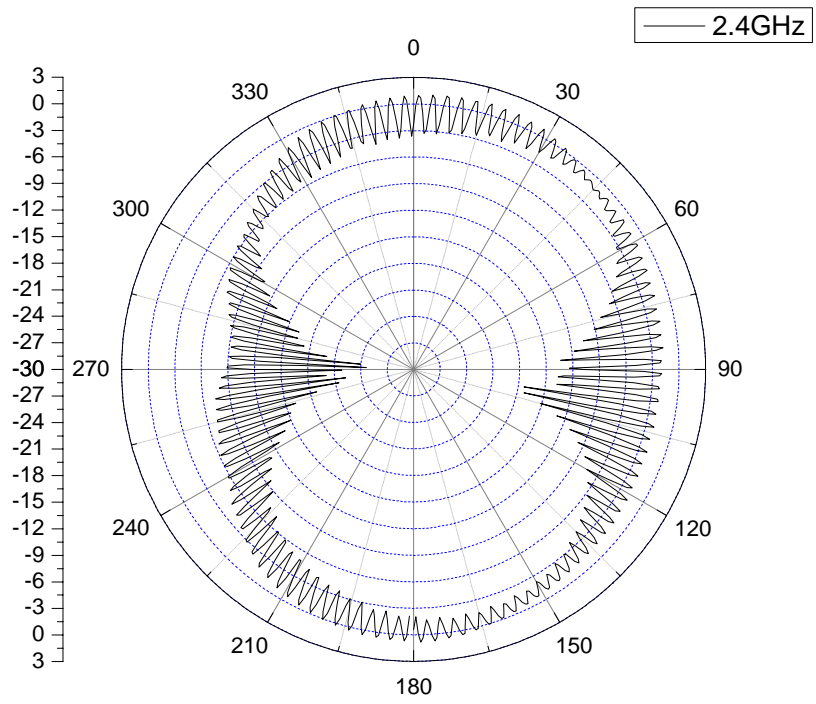
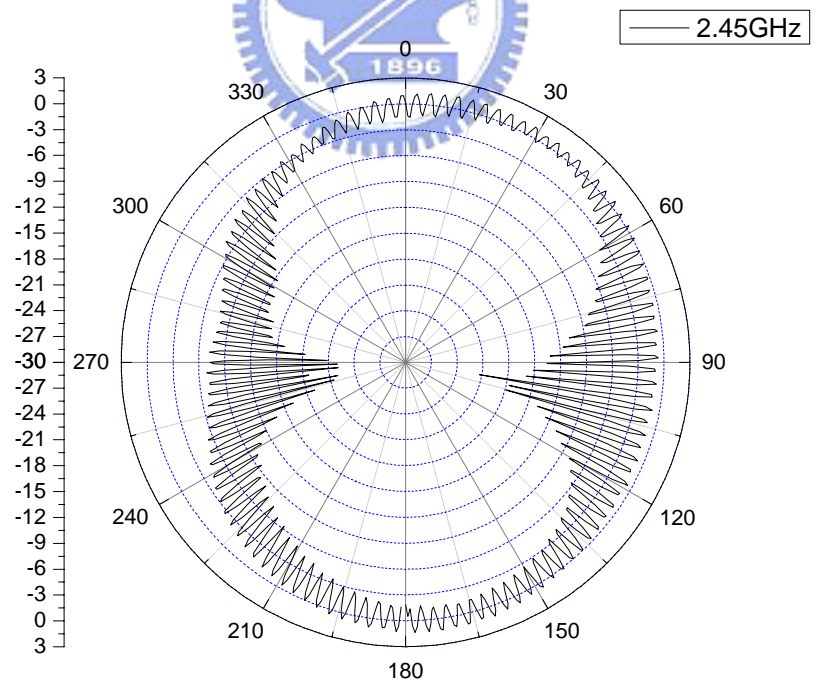


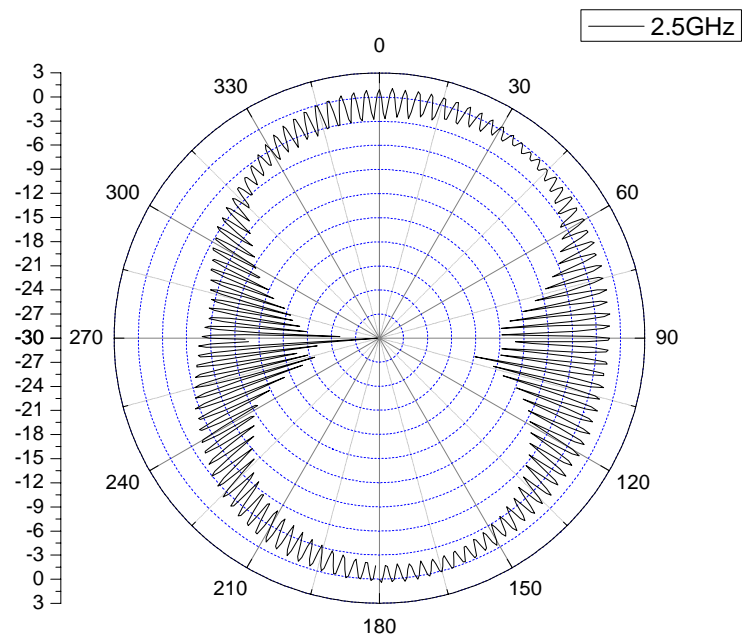
Figure 3-5-11 Simulation of (a) S parameter, (b) Axial ratio, and (c) CP radiation pattern by using Ansoft HFSS simulator



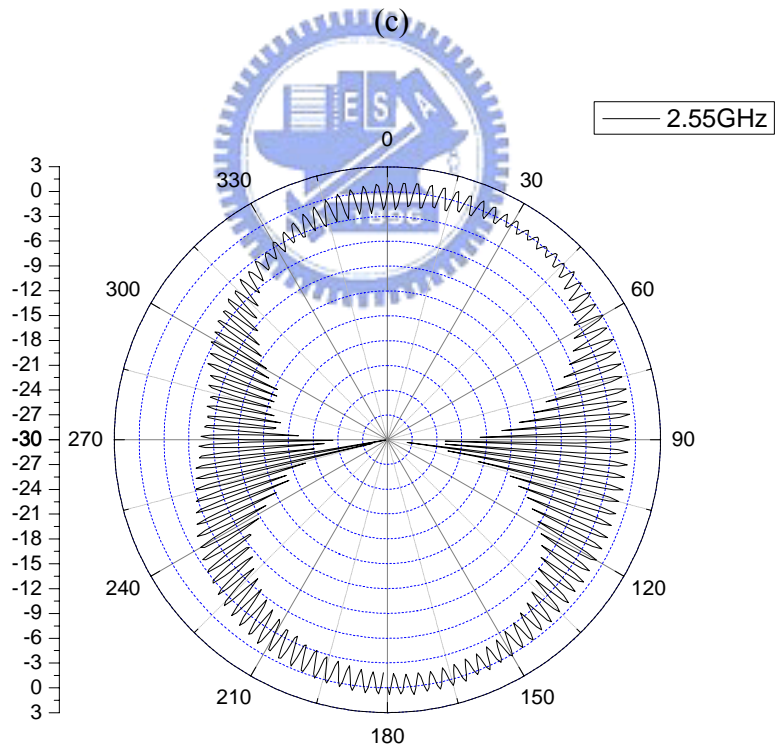
(a)



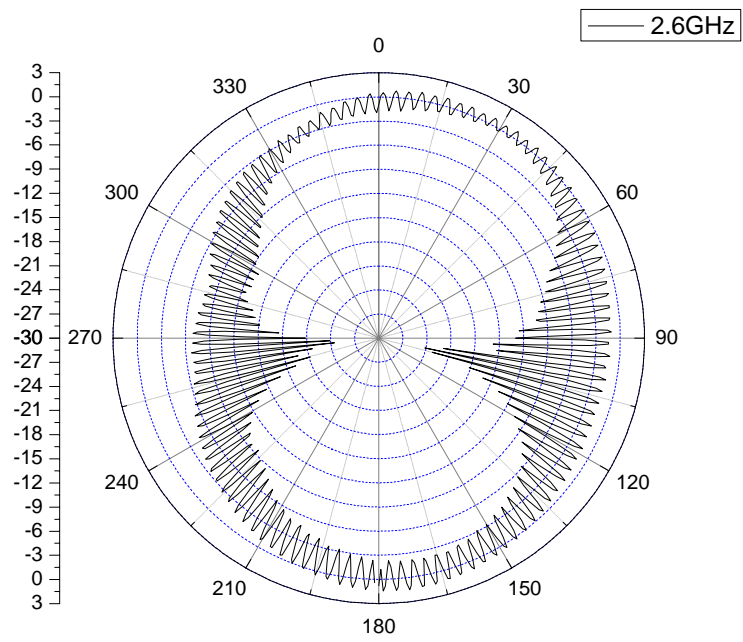
(b)



(c)

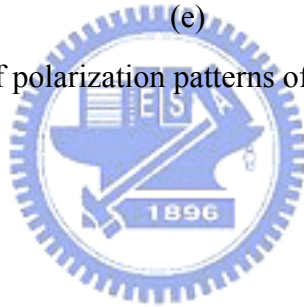


(d)



(e)

Figure 3-5-12 Measurement of polarization patterns of CPW-fed CP slot antenna at different frequency.



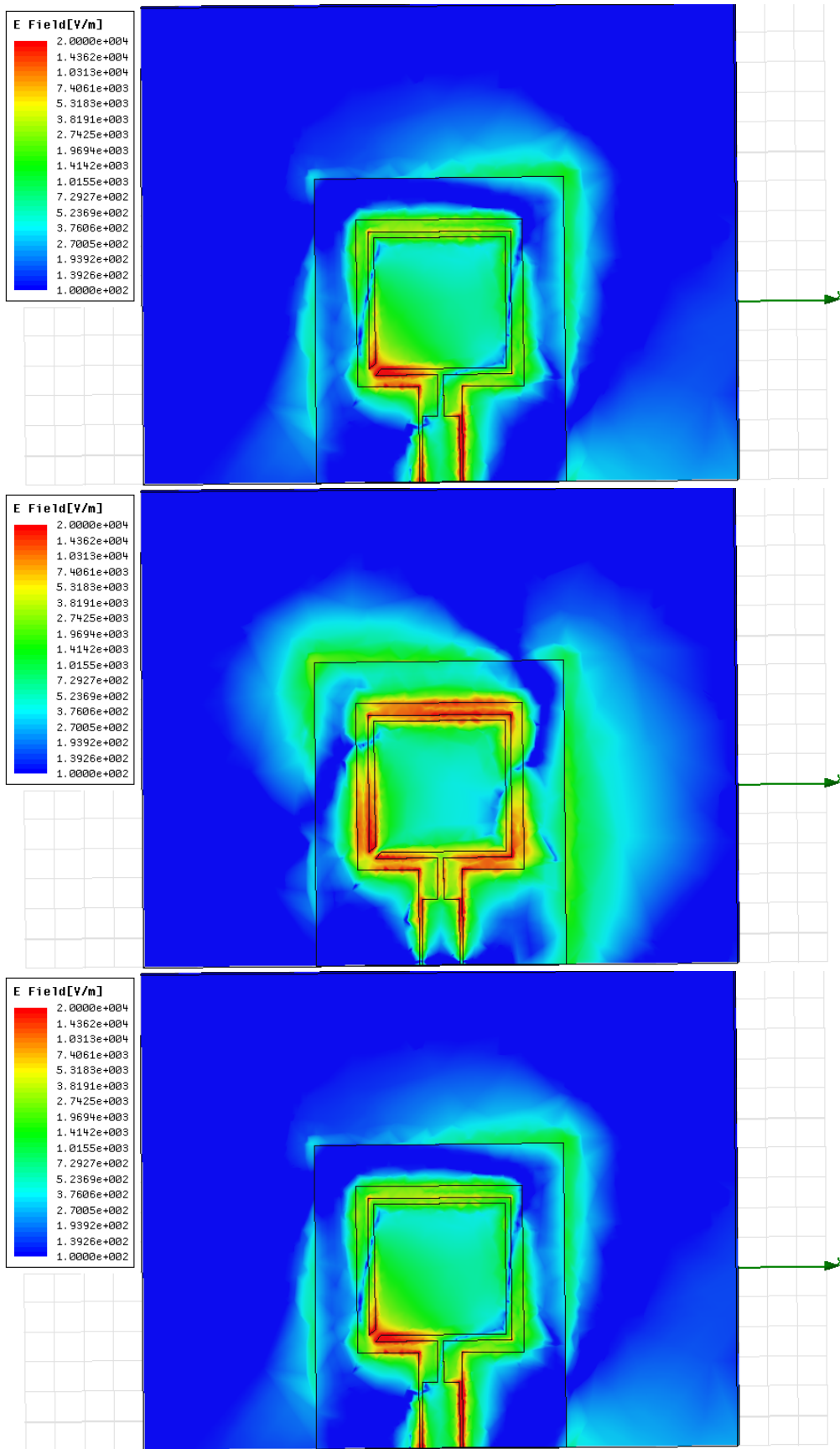


Figure 3-5-13 Electrical field distributions on the x-y plane as feed signal phase from 0 to 180 by step of 90



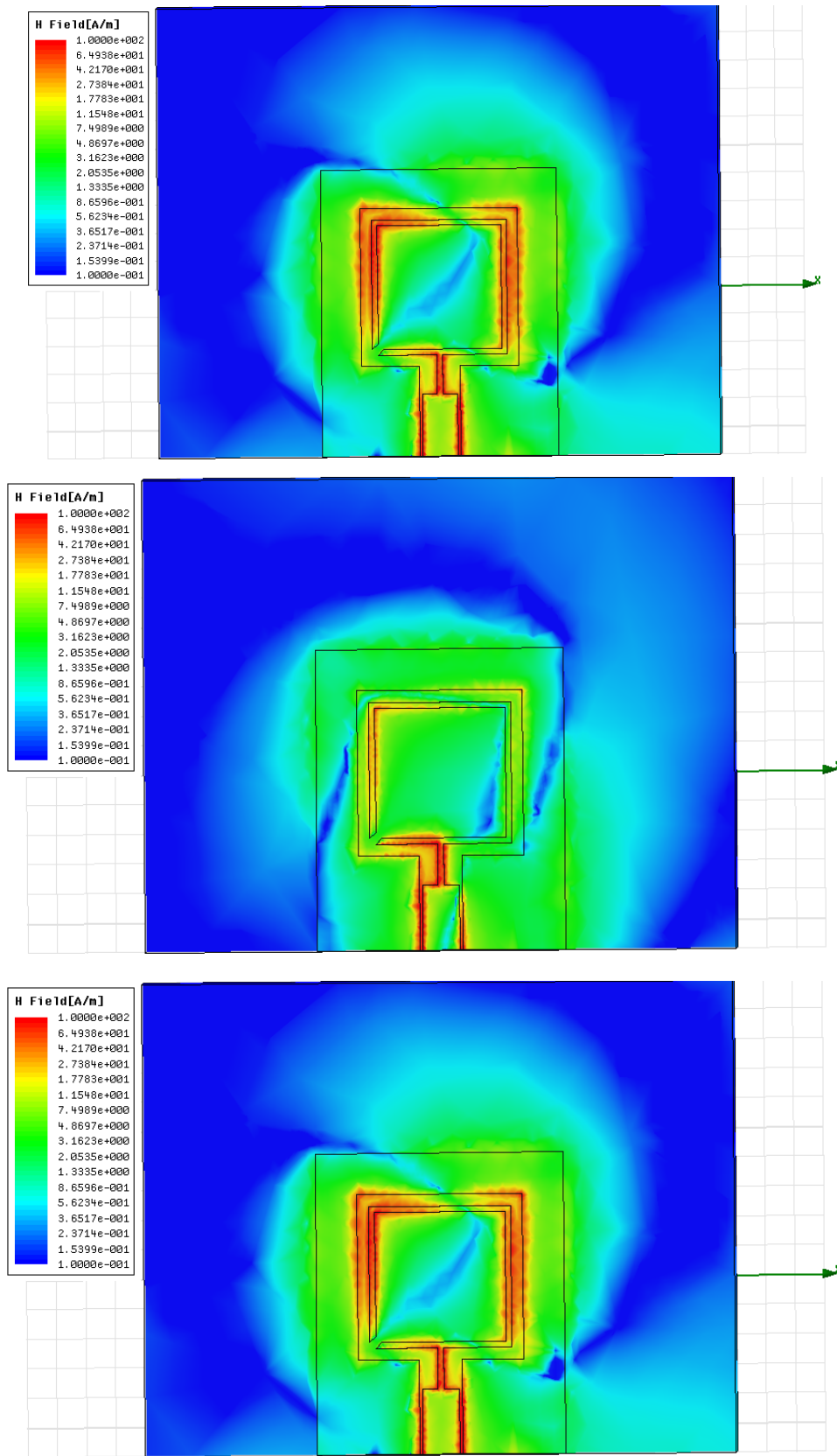


Figure 3-5-14 Magnetic field distributions on the x-y plane as feed signal phase from 0 to 180 by step of 90

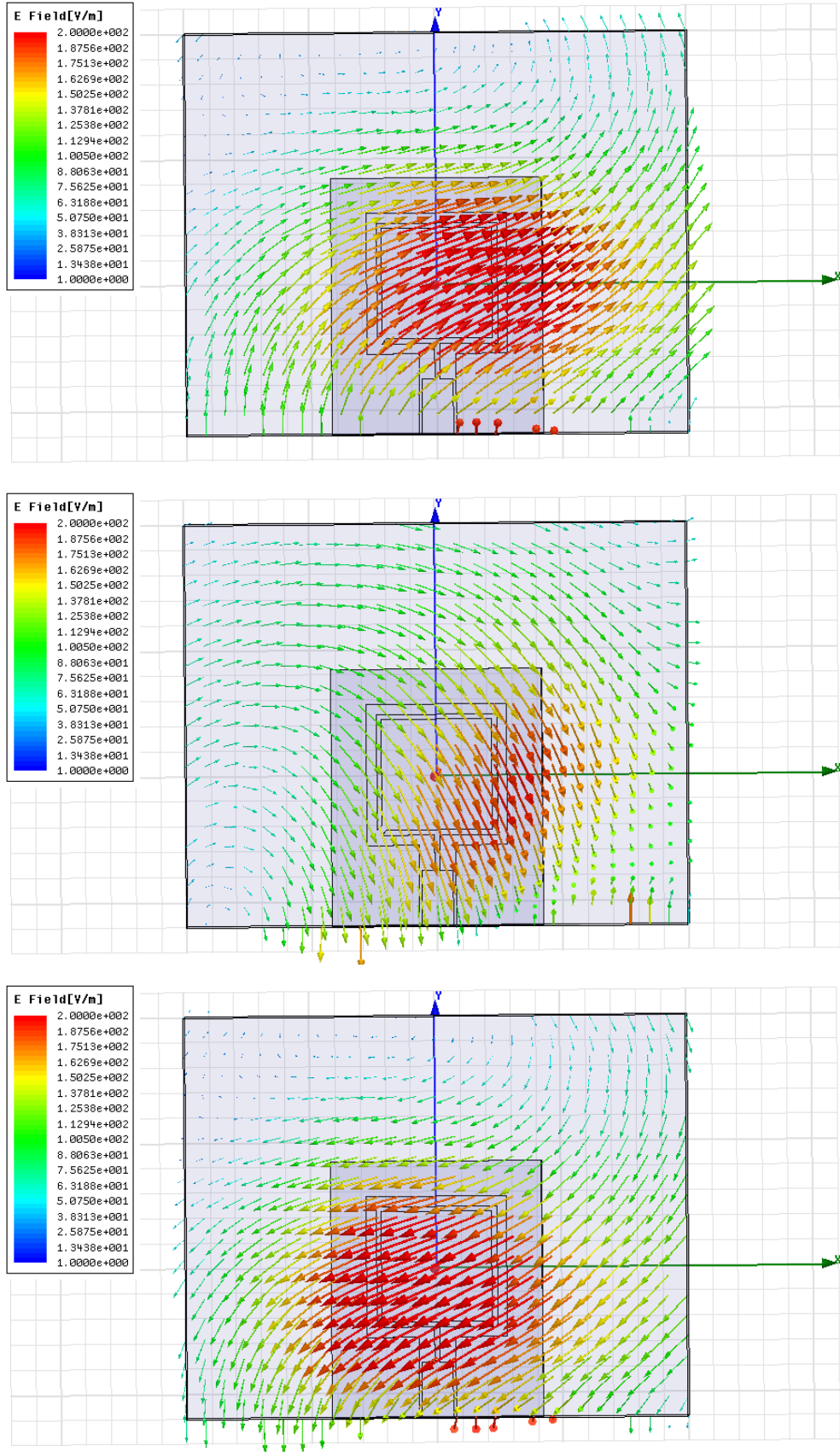


Figure 3-5-15 Vector plot of electrical field distribution on the top of Air box as the feed phase from 0 to 180 by step of 90

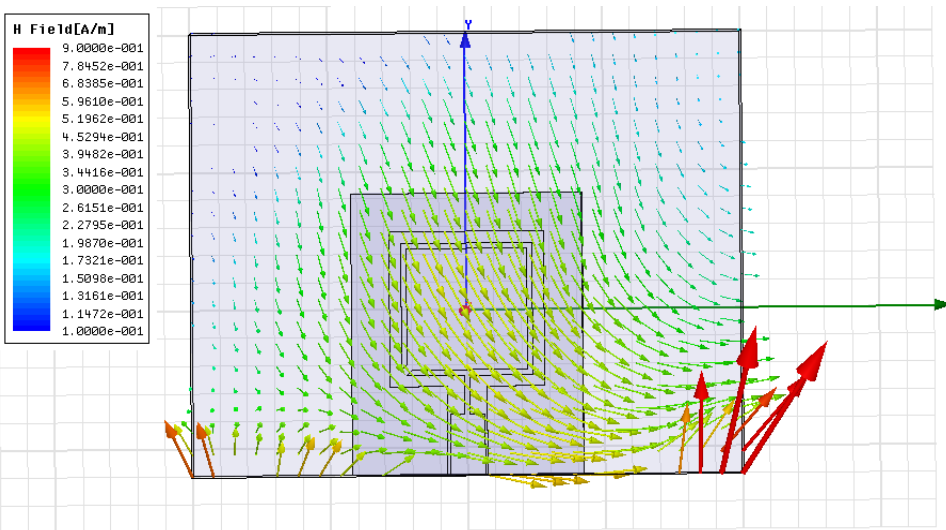
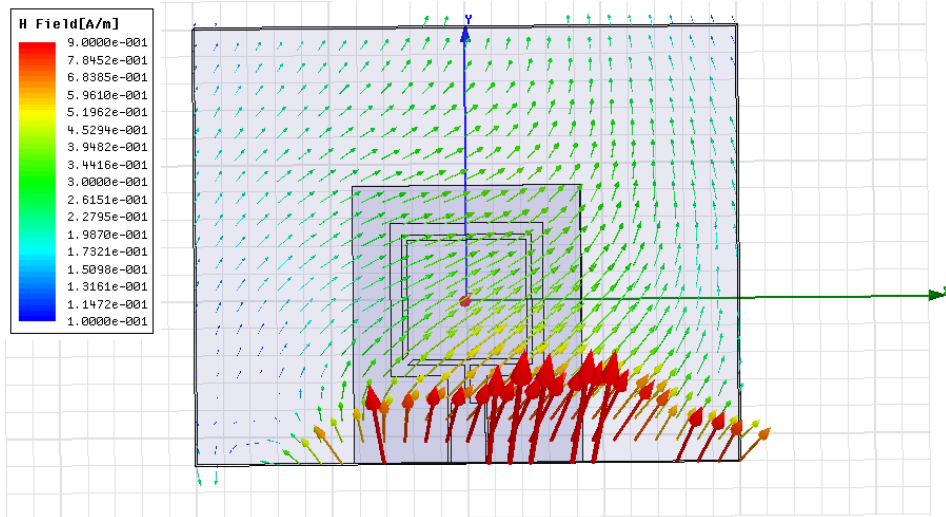
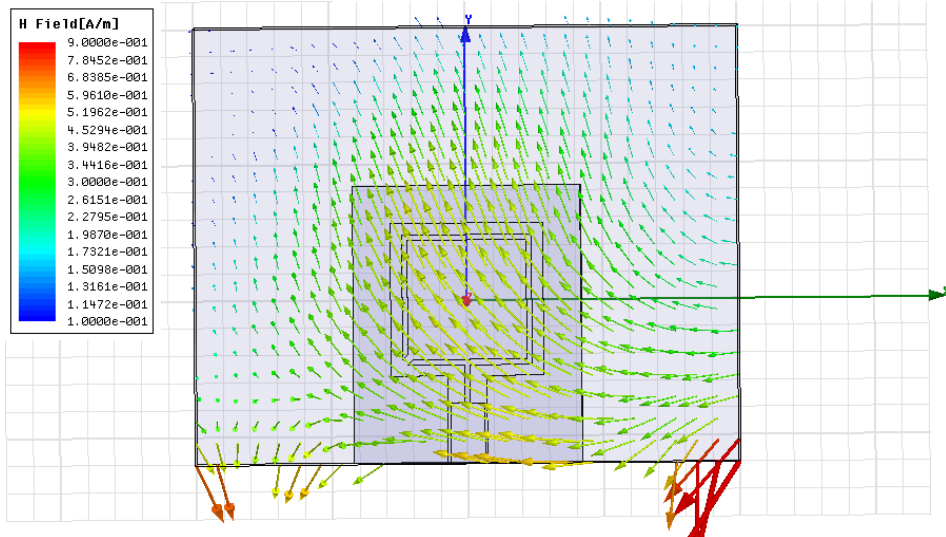


Figure 3-5-16 Vector plot of magnetic field distribution on the top of Air box as the feed phase from 0 to 180 by step of 90

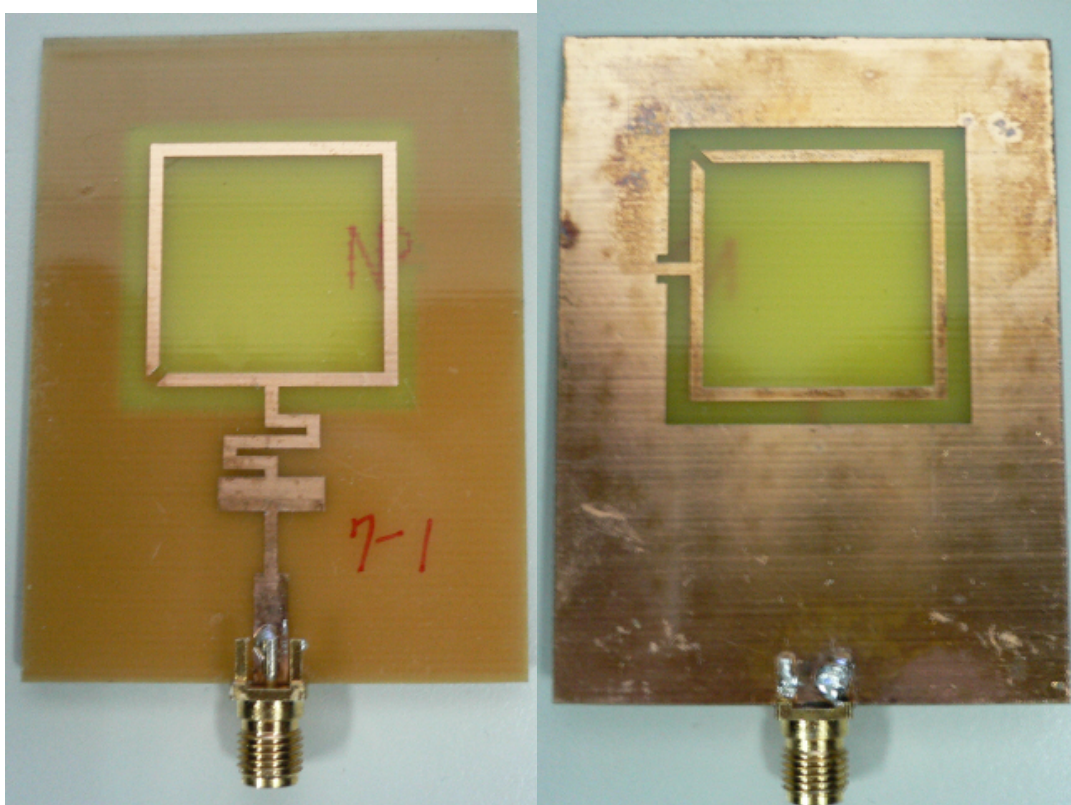


Figure 3-5-17 Photograph of microstrip-fed square-ring slot antenna

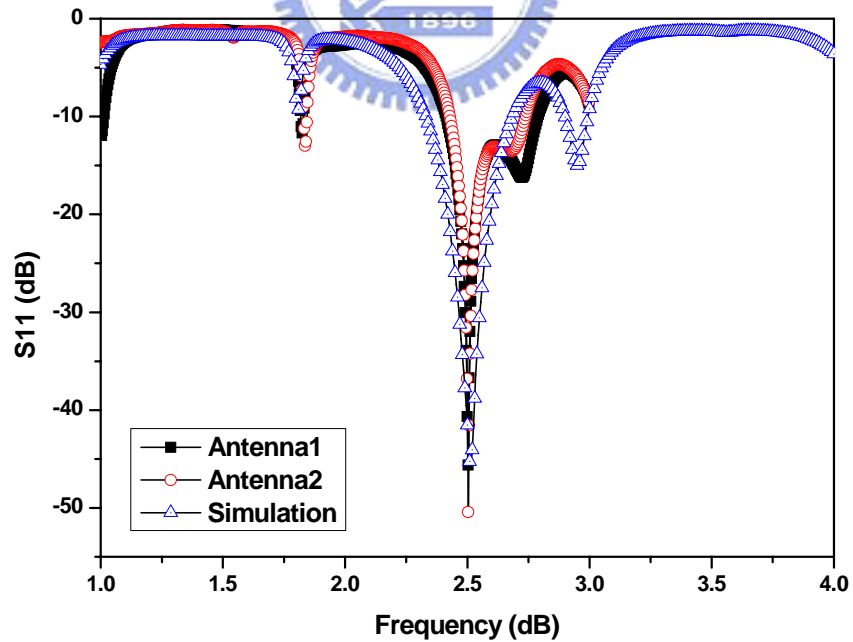


Figure 3-5-18 Measured and simulated results of the microstrip-fed square-ring slot antenna

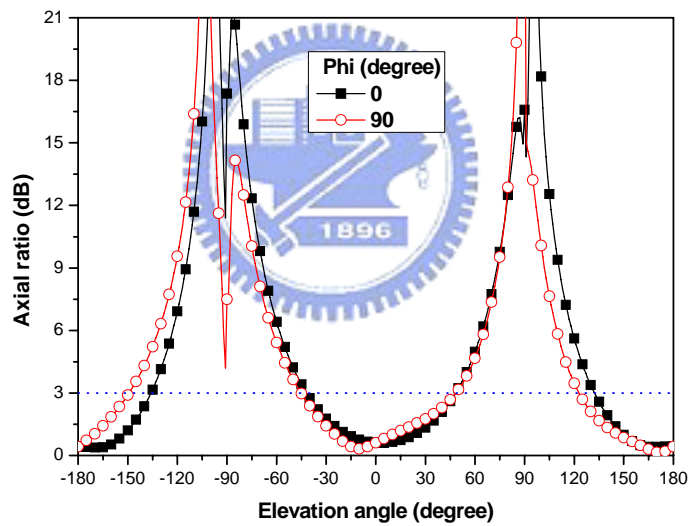
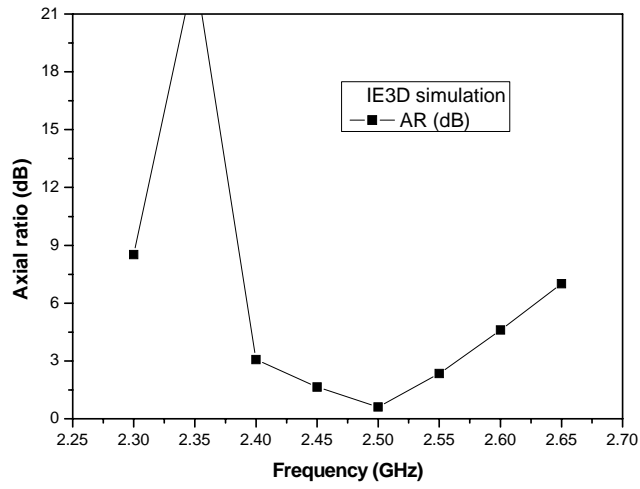


Figure 3-5-19 Simulated results of axial ratio against frequency and against elevation angle by IE3D simulator for microstrip-fed square-ring slot antenna

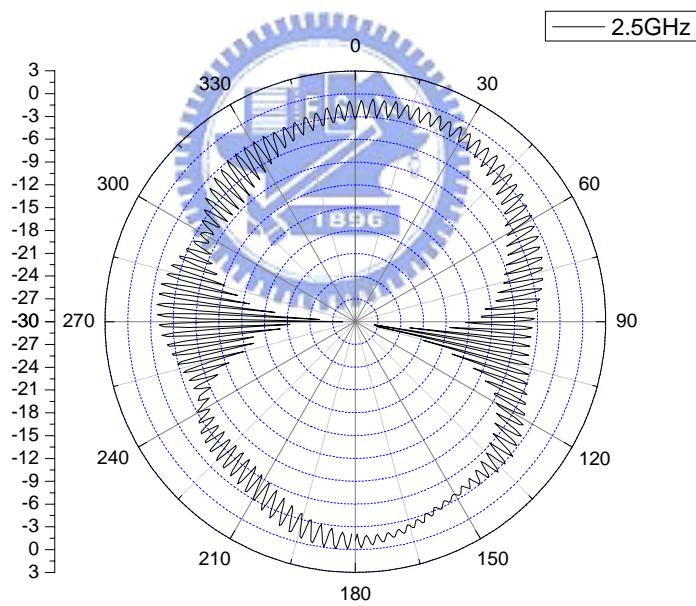
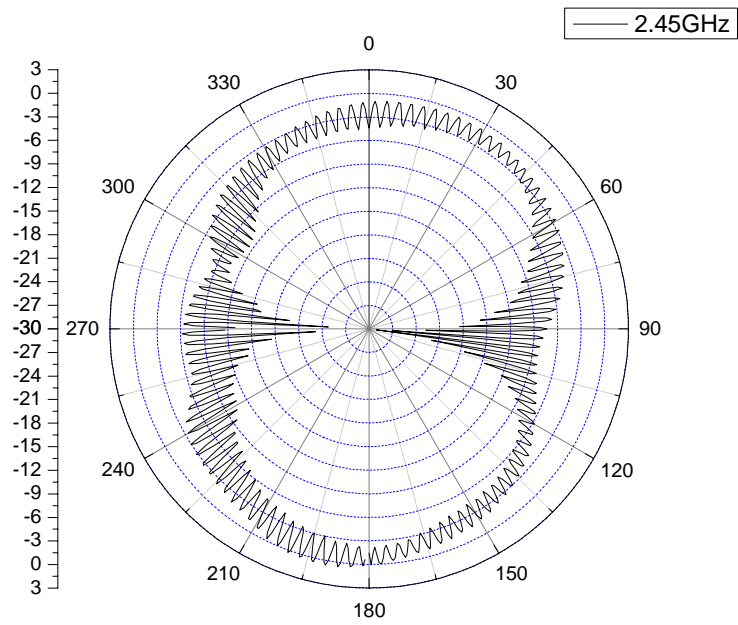


Figure 3-5-20 Measurement of polarization patterns of microstrip-fed square-ring slot antenna at different frequency.

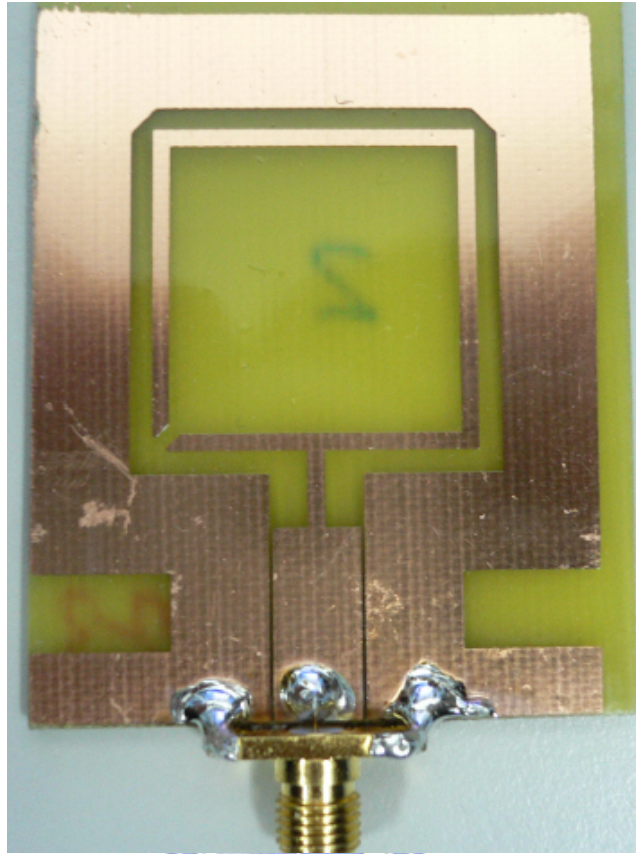


Figure 3-5-21 Photograph of CPW-fed square-ring slot antenna

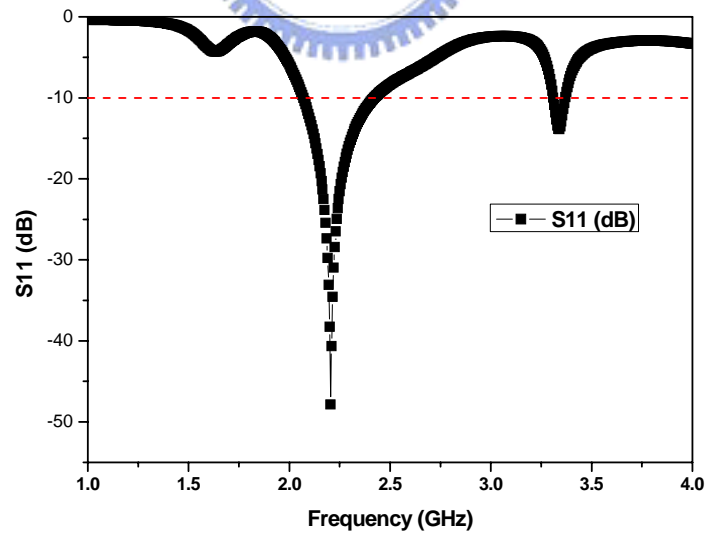
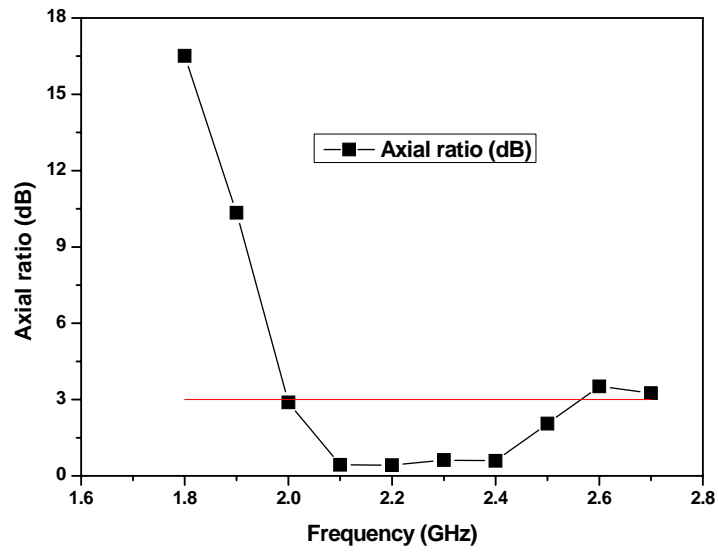
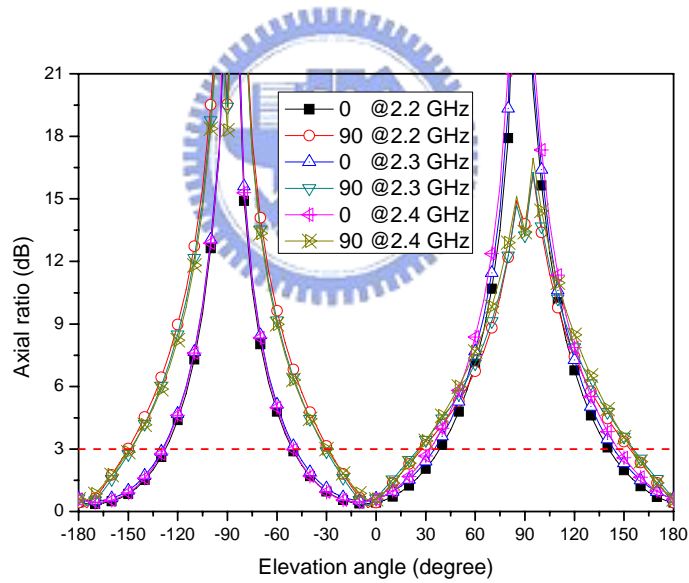


Figure 3-5-22 Simulated result of return loss for CPW-fed slot antenna with two slits



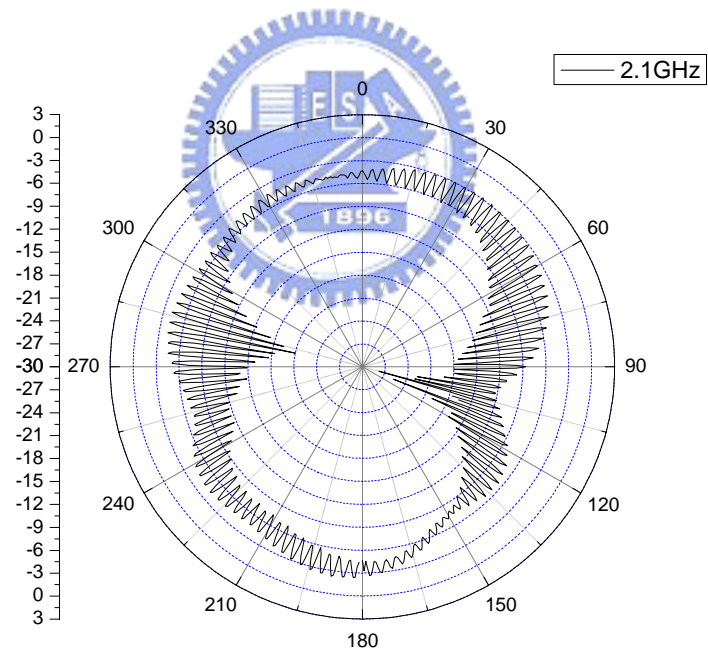
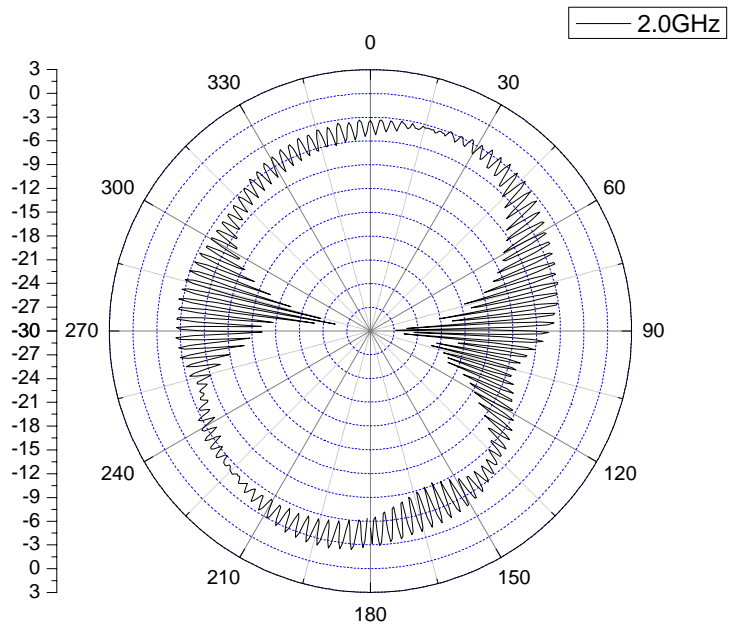
(a)



(b)

Figure 3-5-23 Simulated results of (a) axial ratio against frequency and (b) axial ratio against elevation angle





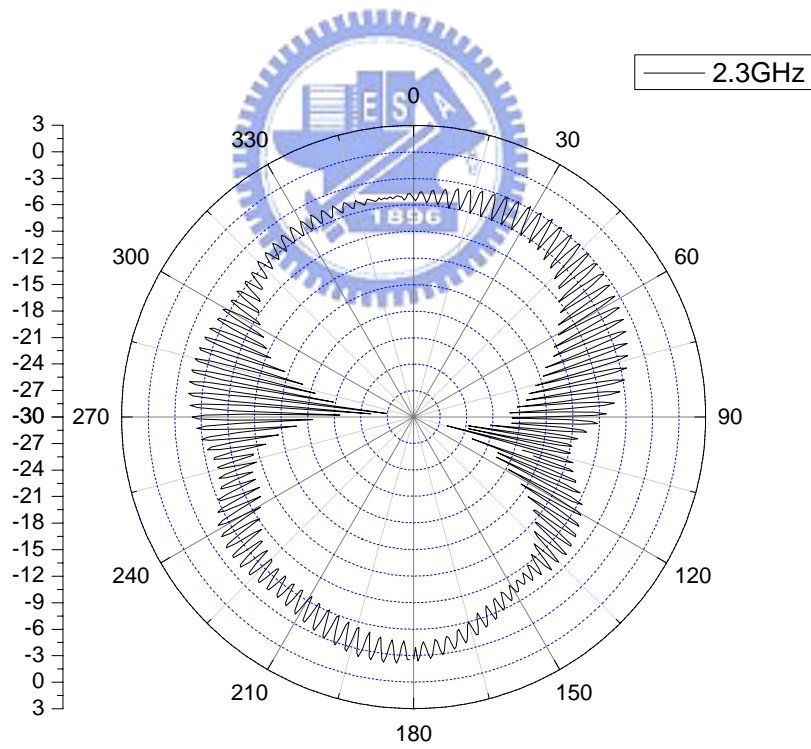
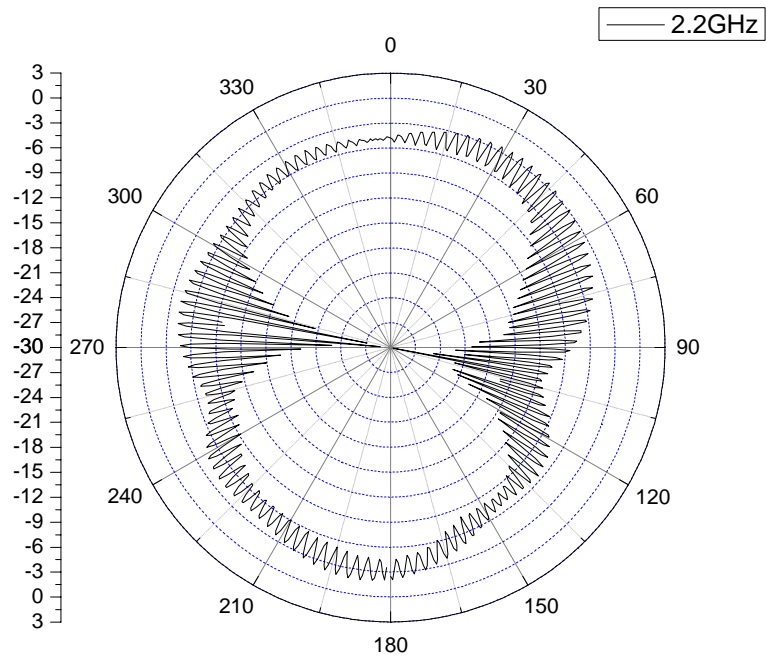


Figure 3-5-24 Measured results of polarization pattern at various frequencies.

## Chapter 6

### Summary

In this research, we have developed several types of slot antennas. Each type of slot antennas has several advantages and disadvantages. For different requirement, we can choose the appropriate type of slot antenna. In general, the CP slot antenna using magnetic current excitation has the least sensitive to the tolerance of fabrication and measurement, but it has the largest antenna area. On the contrary, the slot antenna with electric current excitation has larger sensitivity to the fabrication tolerance and measured error, but it has the least antenna area. If the slot antenna will be fabricated on silicon wafer to integrate with IC and micro-sensor, the type of electric current excitation is preferable to use for compact size applications.

In the future, we hope to actually implement the slot antenna on the silicon wafer to integrate with IC and micro-sensor to form a smart system. In addition, we consider the total size of 20mm x 20mm for CP slot antenna can be achieved. This is also our next target.

## Reference:

- [1]. J. R. James and P. S. Hall, *Handbook of Microstrip Antennas*, Peter Peregrinus, London, 1989.
- [2]. H. Iwasaki, "A circularly polarized small-size microstrip antenna with a cross slot," *IEEE Trans. Antennas Propagat.* **44**, 1399–1401, Oct. 1996.
- [3]. J. H. Lu, C. L. Tang, and K. L. Wong, "Single-feed slotted equilateral-triangular microstrip antenna for circular polarization," *IEEE Trans. Antennas Propagat.* **47**, 1174–1178, July 1999.
- [4]. K. P. Yang, K. L. Wong, and J. H. Lu, "Compact circularly-polarized equilateral-triangular microstrip antenna with Y-shaped slot," *Microwave Opt. Technol. Lett.* **20**, 31–34, Jan. 5, 1999.
- [5]. K. L. Wong, W. H. Hsu, and C. K. Wu, "Single-feed circularly polarized microstrip antenna with a slit," *Microwave Opt. Technol. Lett.* **18**, 306–308, July 1998.
- [6]. J. H. Lu, C. L. Tang, and K. L. Wong, "Circular polarization design of a single-feed equilateral-triangular microstrip antenna," *Electron. Lett.* **34**, 319–321, Feb. 19, 1998.
- [7]. H. M. Chen and K. L. Wong, "On circular polarization design of annular-ring microstrip antennas," *IEEE Trans. Antennas Propagat.* **47**, 1289–1292, Aug. 1999.
- [8]. K. L. Wong and J. Y. Wu, "Single-feed small circularly polarized square microstrip antenna," *Electron. Lett.* **33**, 1833–1834, Oct. 23, 1997.
- [9]. K. L. Wong and M. H. Chen, "Single-feed small circular microstrip antenna with circular polarization," *Microwave Opt. Technol. Lett.* **18**, 394–397, Aug. 20, 1998.
- [10]. W. S. Chen, C. K. Wu, and K. L. Wong, "Novel compact circularly polarized square microstrip antenna," *IEEE Trans. Antennas Propagat.* **49**, 340–342, March 2001.
- [11]. J. Y. Wu, C. Y. Huang, and K. L. Wong, "Compact broadband circularly polarized square microstrip antenna," *Microwave Optical Technol. Lett.* **21**, 423–425, June 20,

1999.

- [12]. J. H. Lu, H. C. Yu, and K. L. Wong, "Compact circular polarization design for equilateral-triangular microstrip antenna with spur lines," *Electron. Lett.* **34**, 1989–1990, Oct. 15, 1998.
- [13]. S. A. Bokhari, J. F. Zuercher, J. R. Mosig, and F. E. Gardiol, "A small microstrip patch antenna with a convenient tuning option," *IEEE Trans. Antennas Propagat.* **44**, 1521–1528, Nov. 1996.
- [14]. C. L. Tang, J. H. Lu, and K. L. Wong, "Circularly polarized equilateral-triangular microstrip antenna with truncated tip," *Electron. Lett.* **34**, 1277–1278, June 25, 1998.
- [15]. W. S. Chen, C. K. Wu, and K. L. Wong, "Single-feed square-ring microstrip antenna with truncated corners for compact circular polarization operation," *Electron. Lett.* **34**, 1045–1047, May 28, 1998.
- [16]. C. L. Tang and K. L. Wong, "A modified equilateral-triangular-ring microstrip antenna for circular polarization," *Microwave Opt. Technol. Lett.* **23**, 123–126, Oct. 20, 1999.
- [17]. W. S. Chen, C. K. Wu, and K. L. Wong, "Compact circularly polarized microstrip antenna with bent slots," *Electron. Lett.* **34**, 1278–1279, June 25, 1998.
- [18]. W. S. Chen, C. K. Wu, and K. L. Wong, "Compact circularly polarized circular microstrip antenna with cross slot and peripheral cuts," *Electron. Lett.* **34**, 1040–1041, May 28, 1998.
- [19]. K. L. Wong and Y. F. Lin, "Circularly polarized microstrip antenna with a tuning stub," *Electron. Lett.* **34**, 831–832, April 30, 1998.
- [20]. W. S. Chen, C. K. Wu, and K. L. Wong, "Square-ring microstrip antenna with a cross strip for compact circular polarization operation," *IEEE Trans. Antennas Propagat.* **47**, 1566–1568, Oct. 1999.
- [21]. J. H. Lu and K. L. Wong, "Single-feed circularly-polarized equilateral-triangular

- microstrip antenna with a tuning stub,” *IEEE Trans. Antennas Propagat.* **48**, 1869–1872, Dec. 2000.
- [22]. K. L. Wong and M. H. Chen, “Slot-coupled small circularly polarized microstrip antenna with modified cross-slot and bent tuning-stub,” *Electron. Lett.* **34**, 1542–1543, Aug. 6, 1998.
- [23]. W. S. Chen, K. L. Wong, and C. K. Wu, “Inset microstripline-fed circularly polarized microstrip antennas,” *IEEE Trans. Antennas Propagat.* **48**, 1253–1254, Aug. 2000.
- [24]. K.C. Gupta et al., *Microstrip Lines and Slot Lines*, 2<sup>nd</sup> ed. Norwood, MA:Artech House, 1996.
- [25]. W. Menzel and W. Grabherr, “A Microstrip patch antenna with coplanar feed line”, *IEEE Microwave Guided Wave Lett.*, Vol. 1, pp.340-342, Nov. 1991.
- [26]. R.Q. Lee and R.N. Simons, “Coplanar waveguide aperture coupled microstrip patch antenna”, *IEEE Microwave Guided Wave Lett.*, Vol. 2, pp. 138-139, Nov. 1992.
- [27]. T.J. Ellis, J.P. Raskin, G.M. Rebeiz, and L.P.B. Katehi, “A wideband CPW-fed microstrip antenna at millimeter wave frequencies”, in *Proc. IEEE MMT-S Int. Microwave Symp. Dig.*, Vol. 2, Anaheim, CA, June 1999, pp.629-632.
- [28]. J.Y. Sze, K.L. Wong, and C.C. Huang, “Coplanar waveguide Fed Square Slot Antenna for broadband Circularly Polarized Radiation”, *IEEE Trans. Antennas Propagat.*, Vol.51, pp.2141-2144, Aug. 2003.
- [29]. L.T. Wang, X.C. Lin, and J.S. Sun, “The broadband loop slot antenna with photonic bandgap structure”, *IEE Int Conf Antennas Propagat (ICAP) 2003*, pp.470-472.
- [30]. K.L. Wong, *Compact and Broadband Microstrip Antennas*. New York, NY:Wiley, 2002, ch. 5.
- [31]. K.L. Wong, C.C. Huang, and W.S. Chen, “Printed ring slot antenna for circular polarization”, *IEEE transaction on antennas and propagation*, Vol. 50, No. 1,

January 2002, pp. 75-77

- [32]. Jia-Yi Sze, Kin-Lu Wong, and Chieh-Chin Huang, "Coplanar waveguide-fed square slot antenna for broadband circularly polarized radiation", IEEE transaction on antennas and propagation. Vol.51, Issue 8, 2003 pp. 2141 – 2144.
- [33]. Y.B. Chen, X.F. Liu, Y.C. Jiao and F.S. Zhang, " CPW-fed broadband circularly polarized square slot antenna", IEEE Electronics letters, Vol. 42, No. 19, September 2006.
- [34]. H. Morishita, K. Hirasawa, T. Nagao, "Circularly polarized wire antenna with a dual rhombic loop", in Proc. IEE Microwave Antenna Propagation., Vol.145, No. 3, June 1998., pp. 219-224.
- [35]. H. Morishita, K. Hirasawa, T. Nagao, "A dual rhombic loop antenna for circular polarization", in Antenna and Propagation Conference, Apr 1995, pp. 500-503
- [36]. Song Shi, Kazuhiro Hirasawa, and Zhi Ning Chen, "Circularly polarized rectangular bent slot antennas blacked by a rectangular cavity", IEEE transaction on antennas and propagation, Vol. 49, November 2001, pp. 1517-1524
- [37] Balanis, C.A., "Antenna analysis and design", John Wiley & Sons, New York, 1997
- [38] Stutzman, W.L., and G.A. Thiele," Antenna theory and design", John Wiley & Sons, New York, 1981
- [39] Hall, P.S., and J.S. Dahele," Dual and circularly polarized microstrip antennas," in advances in microstrip and printed antennas, K.F. Lee and W. Chen., John Wiley & Sons, New York, 1997
- [40] Polzar, D.M.," Microwave engineering", John Wiley & Sons, New York, 1998
- [41] Haneishi, M., and S. Yoshida," A design method of circularly polarized rectangular microstrip antenna by one-point feed", Artech House, Norwood, MA, 1998, pp.313~321
- [42] T. T. Wu, "Theory of thin circular loop antennas," *J. Math. Phys.*, vol. 3, pp.

1301–1304, 1962.

- [43] B. R. Rao, “Far field patterns of large circular loop antennas: Theoretical and experimental results,” *IEEE Trans. Antennas Propag.*, vol. 16, no. 2, pp. 269–270, Mar. 1968.
- [44] W. L. Stutzman and G. A. Thiele, *Antenna Theory and Design*. New York: Wiley, 1998, pp. 205–210.
- [45] R. S. Elliott, *Antenna Theory and Design*. Piscataway, NJ: IEEE Press, 2003, pp. 71–73.
- [46] H. Nakano, N. Tsuchiya, T. Suzuki, and J. Yamauchi, “Loop and spiral line antennas at microstrip substrate surface,” in *Proc. 6th Int. Conf. Antenna and Propagation (ICAP)*, 1989, pp. 196–200.
- [47] E. E. Altshuler, “The Traveling-wave linear antenna,” *IRE Trans. Antennas Propag.*, vol. 9, pp. 324–329, Jul. 1961.
- [48] S. Okuba and S. Tokumaru, “ Reactively loaded loop antennas with reflectors for circular polarization,” *Trans. IECE Jpn.*, vol. J65-B, pp. 1044–1051, Aug. 1982.
- [49] RongLin Li, Nathan A. Bushyager,, Joy Laskar,” Determination of Reactance Loading for Circularly Polarized Circular Loop Antennas With a Uniform Traveling-Wave Current Distribution”, *IEEE transactions on antennas and propagation*, vol. 53, 2005, pp.3920~3929
- [50] R. C. Johnson and H. Jasik, *Antenna Engineering Handbook*. New York: McGraw-Hill, 1984.
- [51] IEEE Standard Test Procedures for Antennas, IEEE Standard 149, 1979.
- [52] Bee Yen TOh, Robert Cahil,” Understanding and measuring circular polarization”, *IEEE transactions on education*, vol. 46, 2003, pp. 313~318
- [53] Jia-Yi Sze, Kin-Lu Wong, and Chieh-Chin Huang, “Coplanar waveguide-fed square slot antenna for broadband circularly polarized radiation”, *IEEE transaction on*



- antennas and propagation. Vol.51, Issue 8, 2003, pp. 2141 – 2144.
- [54] Bee Yen Toh, Robert Cahill, and Vincent F, Fusco, “Understanding and measuring circular polarization”, IEEE transactions on education, Vol. 46, NO. 3, August 2003, pp.313-318.
- [55] John Huang, “The finite ground plane effect on the microstrip antenna radiation patterns”, IEEE transactions on antennas and propagation, Vol. 31, No.4, July 1983, pp. 649-653.
- [56] Boyu Zheng, and Zhongxiang Shen,” Effect of a finite ground plane on circularly polarized microstrip antennas”, IEEE antenna and propagation, Vo. 2A, July 2005. pp. 238-241.
- [57] M. Miao, B.L. Ooi, and P.S. Kooi,” Broadband CPW-fed wide slot antenna”, Microwave and optical letters, Vol. 25, No. 3, May 2000, pp. 206-211.
- [58] H. Morishita, K. Hirasawa, and K. Fujimoto, “Analysis of a cavity backed annular slot antenna with one point shorted”, IEEE Trans Antennas Propagation, Oct. 1991, Vol.39, pp.1472-1478,
- [59] Chen, W.S., Huang, C.C., Wong, K.L., “Microstrip-line-fed printed shorted ring-slot antenna for circular polarization”, Microwave and optical technology letter, 2001, Vol.3, No.2, pp. 137–140.
- [60] Wong, K.L., Huang, C.C., Chen, W.S., “Printed ring slot antenna for circular polarization”, IEEE Trans. Antennas Propagation, Jan. 2002, Vol.50, pp.75-77
- [61] J.S. Row, C.Y.D. Sim, K.W. Lin “Broadband printed ring-slot array with circular polarization”, Electronics Letter, Feb. 2005, Vo.41, No.3, pp.110-112.

## *Total Conclusions*

In this dissertation, a wireless microsensor with an infrared temperature sensor, a circularly polarized antenna and rectenna circuit is developed. In addition, the electromagnetic power transmission of a wireless microsensing system is calculated and simulated. The RF power signal conversion of the rectenna is also calculated and simulated. The approach of predicting the wireless microsensor performances by many simulation tools can be used for other wireless applications such as RFID sensor, wireless temperature sensor, pressure, health or environment monitoring sensor. This method can save much time to develop a wireless microsensing system.



## 個人學經歷資料表

姓名：林稔杰 出生地：台南市 生日：64/04/15

教育：高中 台南一中

大學 交大電機與控制系

碩士 交大電子研究所

博士 交大電子研究所

工作經歷：

曾任國家同步輻射研究中心 RF 小組之專案助理研究員 十個月

在校經歷：

1. 協助交大奈米中心光罩設計與製作流程硬體和軟體的建置
2. 協助交大奈米中心與NDL製程機台的維護與管理



研究領域：

1. 半導體元件物理與製程技術
2. 半導體感測器之元件與製程設計以及模擬分析
3. 高功率半導體元件模擬與製程模擬
4. 微小機電元件設計、模擬與製程技術
5. 高頻電磁模擬分析與量測技術
6. 天線設計、模擬與量測技術